AD-A032 128 DAYTON UNIV OHIO DEPT OF PHYSICS F/G 20/12
IDENTIFICATION OF DEFECTS IN COMPOUND SEMICONDUCTORS.(U)
OCT 76 D C LOOK, J M MEESE, M M KREITMAN F33615-71-C-1877
UNCLASSIFIED AFAL-TR-76-139 NL

1 OF 3
AD
AD32128

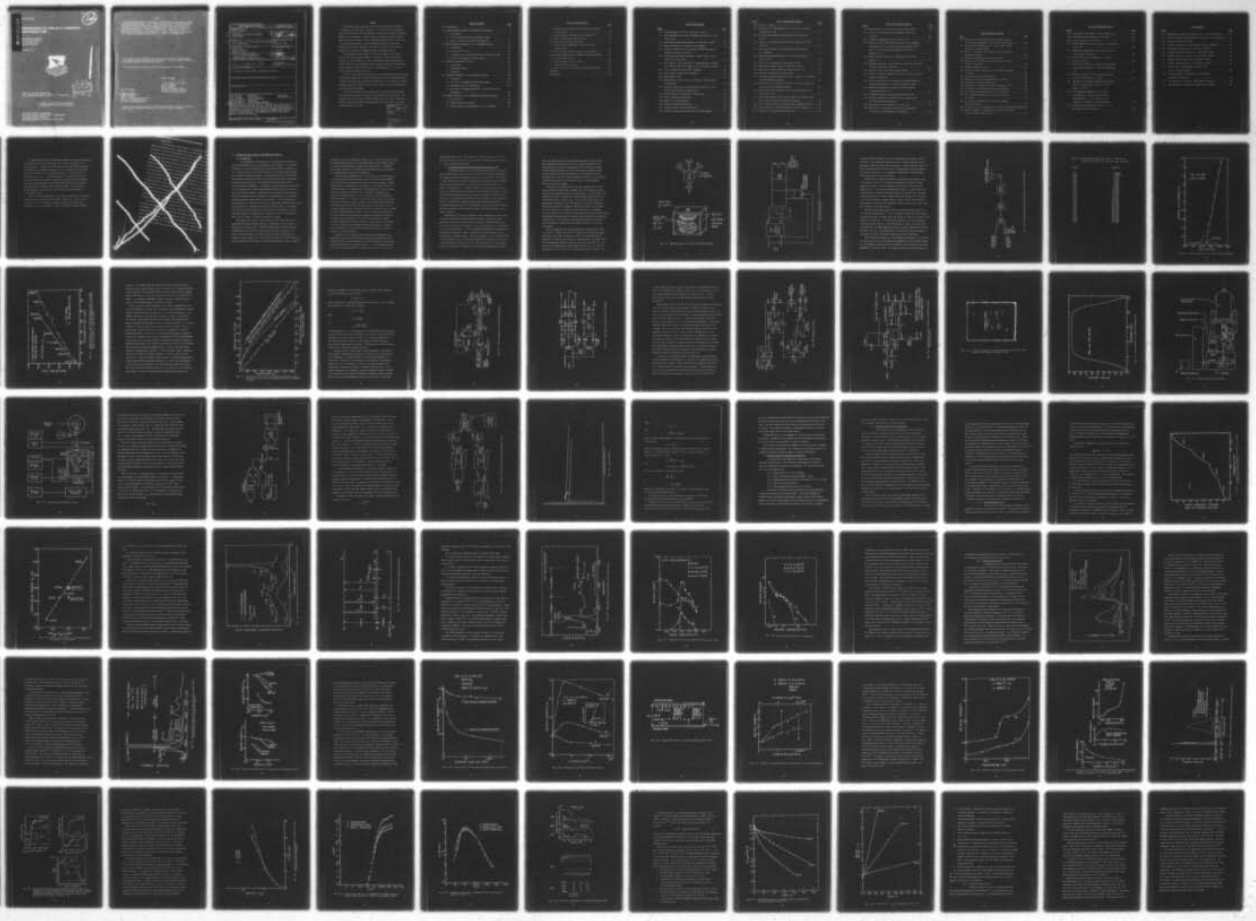

AD A032128

AFAL-TR-76-139

FG 12

IDENTIFICATION OF DEFECTS IN COMPOUND SEMICONDUCTORS

UNIVERSITY OF DAYTON
PHYSICS DEPARTMENT
300 COLLEGE PARK
DAYTON, OHIO 45469

OCTOBER 1976

DDC
RECEIVED
NOV 17 1976
B

TECHNICAL REPORT AFAL-TR-76-139
FINAL REPORT FOR PERIOD 1 JULY 1971 - 31 MARCH 1976

Approved for public release; distribution unlimited

AIR FORCE AVIONICS LABORATORY
AIR FORCE WRIGHT AERONAUTICAL LABORATORIES
AIR FORCE SYSTEMS COMMAND
WRIGHT-PATTERSON AIR FORCE BASE, OHIO 45433

NOTICE

When Government drawings, specifications, or other data are used for any purpose other than in connection with a definitely related Government procurement operation, the United States Government thereby incurs no responsibility nor any obligation whatsoever; and the fact that the government may have formulated, furnished, or in any way supplied the said drawings, specifications, or other data, is not to be regarded by implication or otherwise as in any manner licensing the holder or any other person or corporation, or conveying any rights or permission to manufacture, use, or sell any patented invention that may in any way be related thereto.

This report has been reviewed by the Information Office (OI) and is releasable to the National Technical Information Service (NTIS). At NTIS, it will be available to the general public, including foreign nations.

This technical report has been reviewed and is approved for publication.

PROJECT ENGINEER

Donald C. Reynolds

DONALD C. REYNOLDS
Senior Scientist
Electronics Research Branch
Electronic Technology Division
Air Force Avionics Laboratory

For the Commander

Robert D. Larson

ROBERT D. LARSON
Chief, Electronics Research Branch
Electronic Technology Division
Air Force Avionics Laboratory

Copies of this report should not be returned unless return is required by security considerations, contractual obligations, or notice on a specific document.

AIR FORCE - 8 NOVEMBER 76 - 125

SECURITY CLASSIFICATION OF THIS PAGE *(When Data Entered)*

REPORT DOCUMENTATION PAGE

READ INSTRUCTIONS BEFORE COMPLETING FORM

1. REPORT NUMBER: AFAL-TR-76-139	2. GOVT ACCESSION NO.
3. RECIPIENT'S CATALOG NUMBER	
4. TITLE *(and Subtitle)*: IDENTIFICATION OF DEFECTS IN COMPOUND SEMICONDUCTORS.	5. TYPE OF REPORT & PERIOD COVERED: Final Report. 1 Jul 71 — 31 Mar 76,
	6. PERFORMING ORG. REPORT NUMBER
7. AUTHOR(s): David C. Look, Jon M. Meese, Marshall M. Kreitman, Jose C. Manthuruthil	8. CONTRACT OR GRANT NUMBER(s): F33615-71-C-1877
9. PERFORMING ORGANIZATION NAME AND ADDRESS: Physics Dept. University of Dayton Dayton, OH 45469	10. PROGRAM ELEMENT, PROJECT, TASK AREA & WORK UNIT NUMBERS: 78850613
11. CONTROLLING OFFICE NAME AND ADDRESS: Air Force Avionics Laboratory/DHR Wright-Patterson AFB, OH 45433 Contract Monitor: Donald C. Reynolds	12. REPORT DATE: Oct 1976
	13. NUMBER OF PAGES: 214 (12) 217 p.
14. MONITORING AGENCY NAME & ADDRESS *(if different from Controlling Office)*: (16) 7885 (17) 06	15. SECURITY CLASS. *(of this report)*: Unclassified
	15a. DECLASSIFICATION/DOWNGRADING SCHEDULE

16. DISTRIBUTION STATEMENT *(of this Report)*

A - Approved for public release; distribution unlimited.

17. DISTRIBUTION STATEMENT *(of the abstract entered in Block 20, if different from Report)*

18. SUPPLEMENTARY NOTES

19. KEY WORDS *(Continue on reverse side if necessary and identify by block number)*

III-V Compounds	Luminescence	Solar Cells
II-VI Compounds	Optical Absorption	Photoconductivity
I-III-VI Compounds	Thermal Conductivity	
Semi-insulating GaAs	Hall-effect	
Radiation Damage	Nuclear Magnetic Resonance	

20. ABSTRACT *(Continue on reverse side if necessary and identify by block number)*

Radiation-damaged, ion-implanted, doped, and as-grown semiconducting materials, including CdS, CdSe, CdTe, CdO, ZnS, ZnSe, ZnTe, ZnO, HgS, $CuInS_2$, In_2Te_3, GaAs, GaAlAs, Si, and Ge, have been examined by photoluminescence, cathodoluminescence, optical absorption, thermal conductivity, magnetic susceptibility, Hall effect, photoconductivity, photomagnetoelectric effect, and nuclear magnetic resonance techniques.

DD FORM 1 JAN 73 1473 EDITION OF 1 NOV 65 IS OBSOLETE

UNCLASSIFIED

SECURITY CLASSIFICATION OF THIS PAGE *(When Data Entered)*

401 556

FOREWORD

The contract effort described in this report represents approximately 17 man-years of effort, from 1 July 1971, to 31 March 1976. At the beginning of this period the work was primarily concerned with electron-irradiation damage in II-VI compounds. Toward the end of the period the chief interest was in the characterization of III-V compounds, especially GaAs. Thus, much of our time has been spent in establishing new techniques and becoming familiar with different materials. In spite of this, the effort has been productive, resulting in 30 published papers in refereed journals.

The personnel who have served in a full-time capacity, for at least part of the contract period, include: Dr. David C. Look, Mr. Marshall M. Kreitman, Dr. Jon M. Meese, Dr. Jose C. Manthuruthil, and Miss Mary Turner. Readers who desire more information about a particular section of this report should contact Dr. Meese (Section II), Dr. Look (Sections III, IV, and V), or Mr. Kreitman (Sections VI and VII).

We wish to thank our many colleagues at the Aerospace Research Laboratories (now disestablished), and the Avionics Laboratory, who have unselfishly helped to make our experience here pleasant and productive. We hope that our research has aided, and will continue to aid, Air Force efforts to solve relevant semiconductor materials problems.

This work was performed by the University of Dayton Physics Department, 300 College Park, Dayton, Ohio, 45469, under Contract F33615-71-C-1877. The project, task, and work unit number was 78850613, and the project engineer was Donald C. Reynolds, AFAL/DHR, Wright-Patterson AFB, Ohio, 45433. The report was submitted on 1 May 1976.

ACCESSION for
NTIS White Section
DDC Buff Section
UNANNOUNCED
JUSTIFICATION
BY
DISTRIBUTION/AVAILABILITY CODES
Dist. AVAIL. and/or SPECIAL
A

TABLE OF CONTENTS

		Page
1.0	INTRODUCTION	1
2.0	ELECTRON RADIATION DAMAGE IN SEMICONDUCTING COMPOUNDS	3
	2.1 Introduction	3
	2.2 Facilities Modifications and Equipment Design	5
	2.3 Radiation Effects in Compound Semiconductors	36
3.0	NUCLEAR MAGNETIC RESONANCE IN II-VI COMPOUNDS AND GaAs	132
	3.1 Introduction	132
	3.2 A Study of Co^{2+} in CdS	132
	3.3 A Measurement of the Conduction-Electron g-Factor in CdTe	133
	3.4 Studies of Paramagnetic Dopants in GaAs	133
4.0	ELECTRICAL PROPERTIES OF $CuInS_2$	134
	4.1 Introduction	134
	4.2 Experimental Results	134
	4.3 Conclusions	136
5.0	ELECTRICAL PROPERTIES OF GaAs SUBSTRATE MATERIALS	139
	5.1 Introduction	139
	5.2 Hall-Effect and Magnetoresistance Measurements	141
	5.3 Photomagnetoelectric Measurements	151
	5.4 Photo-Hall, Photomagnetoresistance, and Photoconductivity Measurements	153
6.0	THERMAL PROPERTIES OF II-VI COMPOUNDS AND RELATED MATERIALS	159
	6.1 Introduction	159
	6.2 Thermal Properties Equipment	161
	6.3 Thermal Conductivity Measurements on II-VI Compounds	162

TABLE OF CONTENTS (CONT'D)

Page

6.4 Thermal Conductivity Results from Comparator Measurements on CdTe Crystals 164

6.5 Thermal Comparator Measurements on Ion-Implanted CdS 171

6.6 Thermal Conductivity of Support Materials. 173

6.7 Some Notes on the Comparator Method. 175

6.8 Linear-Heat-Flow Measurements of ZnSe and Type 316 Stainless Steel. 176

6.9 Debye θ and Heat Capacity Studies in II-VI Compounds 177

7.0 OPTICAL INVESTIGATIONS IN II-VI COMPOUNDS AND RELATED MATERIALS 179

7.1 Raman Scattering in ZnTe 179

7.2 Infrared Absorption in ZnS and ZnSe. 180

7.3 Infrared Absorption in α-HgS 181

7.4 Characterization of *GaAs Samples by Infrared Spectroscopy*. 185

REFERENCES. 192

PUBLICATIONS. 202

LIST OF ILLUSTRATIONS

Figure		Page
2-1	Switching-magnet (~1 kG) for 1 MeV Van de Graaff	7
2-2	Switching-magnet power supply and degaussing circuit for 1 MeV Van de Graaff	8
2-3	Beam-energy stabilization schematic for 1 MeV Van de Grafff	10
2-4	Range measurement for a single Al foil thickness	12
2-5	Internal conversion electron spectrum of ^{207}Bi source used to calibrate accelerator and foils	14
2-6	Calibration-foils range (thickness) - energy curves. Solid curve is the correct one	15
2-7	Beam energy vs. dial setting and vs. switching magnet currents. Also shown is proper focus-magnet current as function of energy	17
2-8	Circuit diagram for beam-current integrator	19
2-9	Power supply for beam-current integrator	20
2-10	Beam-scanner circuit	22
2-11	Modifications to input circuits of commercial amplifier used in beam scanner	23
2-12	Lissajous' figure at low scan-frequency produced by a 1 MeV electron beam striking a phospher screen	24
2-13	Optical density of irradiated microscope slide	25
2-14	Typical luminescence experiment	26
2-15	Diagram of irradiation dewar	28
2-16	Double-pass monochromator system	29
2-17	Integrator preset accelerator shut-off	31
2-18	Circuit to measure solar cell carrier diffusion lengths	33

LIST OF ILLUSTRATIONS (CONT'D)

Figure		Page
2-19	J_{SC}/J_B vs. fluence	34
2-20	Increase in the 5325Å luminescence as a function of electron irradiation near L.He	40
2-21	Low-resolution cathodoluminescence spectra near band edge in ZnTe	41
2-22	Square root of production rate vs electron energy of 2.320 eV transition	42
2-23	Cation-recoil energy vs. lattice-bond energy for several II-VI compounds	43
2-24	High-resolution photoluminescence of ZnTe edge emission at 4.2°K and 77°K	45
2-25	Model for the zinc-vacancy energy levels in ZnTe	46
2-26	Edge emission showing effects of 300°C argon anneal	48
2-27	Annealing of various transitions defined in Fig. 2-26	49
2-28	Temperature dependence of A-transitions	50
2-29	IR cathodoluminescence spectra for CdS as a function of irradiation and room-temperature annealing	53
2-30	Production of the 1.03μm band in CdS as a function of fluence for various electron-irradiation energies	55
2-31	Square root of the production rate vs. electron energy for the 1.03μm band in CdS	56
2-32	Pre-irradiation spectra near the band edge for (a) excess sulfur, and (b) excess cadmium or undoped CdS platelets	58
2-33	Decay of bound-exciton line intensity with irradiation in CdS	59
2-34	Typical photo- and cathodo-luminescent decay with fluence	61
2-35	Production of I_R bound exciton line in CdS	62

LIST OF ILLUSTRATIONS (CONT'D)

Figure		Page
2-36	Energy-level model for two edge-emission series in CdS	63
2-37	Growth of cathodoluminescent edge emission in CdS with irradiation	64
2-38	Isochronal annealing of I_R and I_1 lines in CdS	66
2-39	Production of the 7200Å luminescence band (a) by isochronal annealing, and (b) as a function of fluence before a 200°K anneal. Also, the radiation annealing of this band is displayed in (c).	67
2-40	Thermal neutron production of 7200Å band in CdS at room temperature	68
2-41	Isochronal annealing of the 1.03μm and 1.65μm bands for samples irradiated above the Cd-threshold	70
2-42	Annealing stages in CdS seen by other workers	71
2-43	Increase in carrier concentration in CdS for 1 MeV and 250 keV electron irradiations	73
2-44	Carrier concentration vs. temperature for samples which are unirradiated, irradiated at 1 MeV, and annealed at 260°C	74
2-45	Temperature dependence of mobility for same conditions as specified in Fig. 2-44	75
2-46	Isochronal annealing and energy-level diagram in CdS	76
2-47	Isothermal annealing of additional carrier concentration for three annealing temperatures	78
2-48	Second-order fit to annealing data in Fig. 2-47	79
2-49	Square root of the carrier removal rate vs. beam energy for ZnO after a room-temperature irradiation	84

LIST OF ILLUSTRATIONS (CONT'D)

Figure		Page
2-50	EPR spectrum of ZnO irradiated at 300°K by 600 keV electrons after a previous irradiation at 1 MeV and 300°C thermal anneal	86
2-51	Square root of the production rate of ionized oxygen vacancies (F^+ Centers) versus beam energy	87
2-52	Decay of F^+ resonance at room temperature after the removal of white-light excitation	89
2-53	Electrical properties of In_2Te_3 before irradiation	97
2-54	EPR spectrum at 77°K before irradiation and after irradiation with 10^{17} - 1 MeV e/cm^2	98
2-55	Isochronal annealing of In_2Te_3	100
2-56	Processes and defect charge states for low-temperature annealing in n-type Ge	104
2-57	Kinetics equations for annealing models	105
2-58	Comparison of calculated and experimental rate constants	106
2-59	Calculated fit to thermal annealing data	107
2-60	Calculated fit to extrinsic-light optical annealing at 4.5°K	108
2-61	Calculated fit to 30°K intrinsic-light optical annealing	109
2-62	Fit to 30°K optical annealing data in Ge for 80% recovery	114
2-63	Fit to radiation annealing data in n-type Si for a float-zone sample	116
2-64	Fit to radiation annealing data for a pulled Si sample (no adjustable parameters)	117
2-65	I-V curves for typical GaAs-GaAlAs solar cell for various concentration ratios	120
2-66	Injection annealing of irradiated GaAs laser diode as a function of time for various forward currents	122

LIST OF ILLUSTRATIONS (CONT'D)

Figure		Page
2-67	Forward-current annealing for various temperatures	123
2-68	1 MeV degradation of GaAlAs-GaAs solar cell	126
2-69	V_{mp} and I_{mp} versus 1 MeV fluence	127
2-70	500 keV degradation of cell, similar to one described in Fig. 2-69	129
2-71	Comparison of GaAlAs-GaAs and Si solar cells after 1 MeV electron irradiation	130
4-1	The hole mobility vs. temperature for a single crystal of $CuInS_2$	135
4-2	The electron mobilities vs. temperature for several $CuInS_2$ crystals annealed at different temperatures in In	137
5-1	The Hall coefficient R vs. the magnetoresistance $\Delta\rho/\rho_o$ for GaAs:Cr Sample A at 370°K	144
5-2	The square of the inverse magnetic field strength $1/B^2$ vs. $R_o/(R_o-R)$ and vs. $\rho_o/\Delta\rho$ for GaAs:Cr Sample A at 370°K	145
5-3	The temperature dependences of the carrier concentrations, n and p, and the intrinsic concentration, n_i. (The curvature at low temperature is caused by surface conduction)	146
5-4	A proposed energy diagram for GaAs:Cr at T = 0. The energy levels are tentative	147

LIST OF TABLES

Table		Page
2-1	Range-energy values for electrons in Al by Katz and Penfold.	11
2-2	Various displacement thresholds in CdS reported in the literature. .	13
2-3	Physical properties of In_2Te_3	95
2-4	Physical properties of other possible In_xTe_{1-x} compounds	96
5-1	Electrical parameters in various GaAs:Cr samples	150
6-1	Thermal resistance behaviors of various defect types	160
6-2	Thermal-comparator results on Zn compounds at 300°K.	165
6-3	Thermal conductivities of Zn compounds at 300°K.	166
6-4	Thermal conductivities of Cd compounds at 300°K.	167
6-5	Descriptions of CdTe samples measured by the thermal comparator method.	169
6-6	Thermal comparator measurements on CdTe samples described in Table 6-5	170
7-1	Low-temperature I-R data on α-HgS phonon frequencies	185
7-2	Photoconductivity results in several GaAs:Cr samples	189

LIST OF ILLUSTRATIONS (CONT'D)

Figure		Page
5-5	The photoconductivity and photo-Hall mobility ($R\sigma$) vs. light energy for GaAs:Cr Sample F at 300°K.	154
5-6	The photoconductivity, electron mobility (μ_n), and hole concentration (p) vs. light energy for GaAs Sample G at 300°K.	156
5-7	The photoconductivity, photo-Hall mobility ($R\sigma$), electron mobility (μ_n), electron concentration (n), and hole concentration (p) vs. light energy for Sample B at 300°K	157

1.0 INTRODUCTION

Semiconductor devices play a major and increasingly important role in many catagories of Air Force systems. Thus, it is important to understand the materials out of which these devices are made, and our contract effort has primarily been concerned with the investigations of impurities and defects in as-grown, doped, radiation-damaged, and ion-implanted crystals. The semiconductor materials we have investigated include CdS, CdSe, CdTe, CdO, ZnS, ZnSe, ZnTe, ZnO, HgS, $CuInS_2$, In_2Te_3, GaAs, GaAlAs, Si, and Ge, while the techniques we have employed include photoluminescence, cathodoluminescence, optical absorption, thermal conductivity, magnetic susceptibility, Hall effect, photoconductivity, photomagnetoelectric effect, and nuclear magnetic resonance.

During the first 2-3 years of this contract effort a primary goal was the solution of radiation-damage problems in II-VI compounds, and this work is described in Section II. During this period, several important atomic-displacement threshold energies were measured. In Section III we describe some nuclear-magnetic-resonance investigations of the properties of free and bound electrons in CdS, CdTe, and GaAs. Among the accomplishments here was the measurement of the effective g-factor of the conduction electrons in CdTe, an important parameter for tunable, spin-flip Raman lasers.

One of the promising new solar-cell materials is $CuInS_2$ and we were able to grow perhaps the largest single crystals presently available. Furthermore, we carried out the first extensive investigation of the electrical properties of this material, both n- and p-type. This work is discussed in Section IV. In Section V we consider the problems associated with GaAs substrate materials. We have devised a scheme for determining the donor and deep acceptor (Cr) concentrations from the mixed-conductivity electrical data.

The thermal conductivity of a semiconductor material is an important parameter, especially for cases in which the device will be used at very high or very low temperatures. A relatively fast and convenient instrument which has recently been developed is the thermal comparator, and we have studied its applicability to the II-VI compounds and other related materials. It has proved to be a useful and effective tool, as shown in Section VI. In Section VII we look at the optical properties of several materials, including HgS and high-resistivity GaAs. HgS has great potential in non-linear optics applications, and we have grown and studied some large, single crystals of α-HgS. In the GaAs effort we have been able to clear up some recent problems in the interpretation of photoconductivity data.

Since most of the work described in this report is already in the published literature we have not gone into great detail in many areas. However, we have attempted to carefully document the research so that the interested reader can either refer to the literature or contact the authors for more information.

2.1 Introduction

At the beginning of this contract, the accelerator facil
AFARL (now AFAL/DHR) were to a large degree, non-functional. This
consisted of a 150 keV Cockroft-Walton accelerator which had not be
for at least five years and from which most of the beam line vacuum eq
and electronics had been stripped, a 1 MeV electron-beam Van de Graaf
would produce a maximum beam energy of only about 4 MeV after consid
arcing and vacuum excursions, and a 400 keV electron beam Van de Graaff
which was largely disassembled. Furthermore, a small machine shop was
in the accelerator area causing considerable difficulty from its associa
dust, metal chips and debris. Shielding for the accelerators was inadequ
in that 10-20 mR/hr radiation leakage could be detected near the vault doo
(maximum permissible human exposure is 100 mR/week). If the machines had
been operating on a continuous 40 hour basis, a considerable radiation hazard
existed for the operating personnel near the vault doors. Furthermore,
the vault walls did not extend up to the ceiling and approximately 10 mR/hr
radiation bounce over the wall made it impossible to work in the Cockroft-
Walton vault either of the Van de Graaffs was running.

The accelerator only a single beam port each, so there were no
beam-switching magnets installed, making it impossible to set up multiple
experiments on the beam line. Accelerator-beam-energy calibration had been
accomplished only approximately by measuring the range of electrons in Al
foil of various thickness. Although a sound technique in principle, the
theoretical calculations of A. T. Nelms (N.B.S.-Circular 577) had been used for
energy calibration rather than the Katz-Penfold experimental values, leading to

2.0 ELECTRON RADIATION DAMAGE IN SEMICONDUCTING COMPOUNDS

2.1 Introduction

At the beginning of this contract, the accelerator facilities at AFARL (now AFAL/DHR) were to a large degree, non-functional. This facility consisted of a 150 keV Cockroft-Walton accelerator which had not been run for at least five years and from which most of the beamline vacuum equipment and electronics had been stripped, a 1 MeV electron-beam Van de Graaff which would produce a maximum beam energy of only about 400 keV after considerable arcing and vacuum excursions, and a 400 keV electron-beam Van de Graaff which was largely disassembled. Furthermore, a small machine shop was located in the accelerator area causing considerable difficulty from its associated dust, metal chips and debris. Shielding for the accelerators was inadequate in that 10-20 mR/hr radiation leakage could be detected near the vault doors (maximum permissible human exposure is 300 mR/week). If the machines had been operating on a continuous 40 hr week, a considerable radiation hazard would have existed for the operating personnel near the vault doors. Furthermore, the vault walls did not extend up to the ceiling and approximately 10 mR/hr radiation bounce over the walls made it impossible to work in the Cockroft-Walton vault if either of the Van de Graaffs was running.

The accelerators had only a single beam port each, since there were no beam-switching magnets installed, making it impossible to set up multiple experiments on the beam lines. Accelerator-beam-energy calibration had been accomplished only approximately by measuring the range of electrons in Al foil of various thickness. Although a sound technique in principle, the theoretical calculations of A. T. Nelms (N.B.S.-Circular 577) had been used for energy calibration rather than the Katz-Penfold experimental values, leading to

experimental errors in beam energy as large as 15%. Since none of the accelerators had beam-scanning circuits, it was nearly impossible to define fluence (number of incident electrons/cm^2) due to beam-profile nonuniformities. Furthermore, beam current integrators, a universally accepted fluence measuring instrument for charged-particle beams, were not being used.

From these meager beginnings and in the time span of the present contract, the accelerator-based materials-research program and facilities at WPAFB have become internationally recognized in the areas of radiation damage in compound semiconductors, ion implantation in semiconductors, and radiation effects in semiconductor devices as evidenced by the many acceptances of refereed publications at international radiation effects conferences, international ion-implantation conferences, and the I.E.E.E. Annual Space and Nuclear Radiation Effects conferences. As a result of the efforts of both military and civilian personnel in this group, contract personnel from Systems Research Laboratories, and personnel from the University of Dayton employed on the present contract, a research program has been established which will be a valuable asset in solving Air Force materials problems for years to come. A broad base of experience has been developed in the research group ranging from elemental-semiconductor irradiation problems through the III-V and II-VI semiconductor materials, areas where industrial and military experience is still maturing. Furthermore, the work has extended from vary basic research problems, such as annealing-kinetics studies, to extremely pertinent and applied areas such as radiation hardening of GaAs and Si devices.

In addition to the sometimes necessarily dull and dry reporting of the experimental facts, we are hopeful that this report will capture some of the excitement which we all have experienced during the development of this group under conditions which were frequently adverse. It is further hoped that the results of the present program will stimulate the desire in others to pursue

with renewed vigor those elusive semiconductor defect structures which tend more often than not to play havoc with the best of electronic systems exposed to a hostile radiation environment.

2.2 Facilities Modifications and Experimental Equipment Design

Considerable modification of the accelerator facilities at WPAFB has been performed under this contract both directly and by means of suggestions and planning originated by personnel supported by this contract. The purpose of these modifications has been to systematically broaden the basis of experimental materials problems which require accelerator usage at WPAFB. As a result of these efforts by ourselves and others in the group, the accelerator facility at AFAL/DHR represents perhaps the most versatile and complete facility in the mid-west devoted exclusively to materials problems of interest to the Air Force. The facilities are now suitable for a variety of tasks from basic research on point-defect interactions and defect-production mechanisms to the applied research areas of device fabrication by ion implantation, radiation testing and hardening of semiconductor devices, and accelerator-based trace-impurity analysis.

Considerable effort has been expanded on the maintenance and repair of the accelerators by personnel supported by this contract. The initially poor performance of the 1 MeV Van de Graaff in achieving a maximum energy of only 400 keV before arcing was attributed to a lack of accelerator-tube conditioning or a dirty accelerator tube. After a systematic conditioning by operating the machine in the instability range of energies just before breakdown, at high beam currents, a maximum energy of 850 keV was achieved. It was determined that a dirty accelerator tube was the primary limitation in achieving a 1 MeV beam. A physical inspection indicated that the tube was covered with a layer of Hg, probably as a result of contamination from the Hg-diffusion vacuum pump which

had at one time been used as the primary pumping system for the beam line. This contamination problem was due either to improper maintenance of the diffusion-pump cold trap or a vacuum rupture of the Al-foil beam windows, although improper maintenance is the more likely since a properly trapped diffusion pump should have stopped nearly all the Hg migration into the accelerator tube. The Hg was actually standing in puddles in the acceleration tube, shorting out many of the acceleration planes. A new accelerator tube was procured and installed.

In addition to the installation of the new accelerator tube, the belt-charging system was changed from a charging comb, which depended upon establishing a corona between the belt and the comb points, to a wiper screen. This modification allowed a stiffening of the insulating-gas-mixture dielectric by the addition of about 5 lb/in^2 of SF_6. After all these modifications, the maximum energy obtained from the 1 MeV machine was 1.50 MeV, a million-volt gain from the accelerator's original condition at the start of the contract, and a 500 keV gain over its maximum nominal voltage rating. The maximum voltage attainable is now limited by arcing between the acceleration planes inside the accelerator tube and cannot be increased without lengthing the acceleration column and tank. It is possible to make these modifications if additional funds are provided, at which point beam energies in excess of 2 MeV should be obtainable.

Once the accelerator was functioning properly, consideration was given to the other limitations, such as lack of beam scan, lack of accurate energy calibration, lack of beam steering, and the lack of a sufficient number of beam ports to accommodate the accelerator usage envisioned. A homebuilt beam-switching magnet was installed on the end of the drift tube (Fig. 2-1). The circuit for the magnet-current power supply is shown in Fig. 2-2. The coils were wound on two 6 1/2" dia. x 2 1/2" spools with #16 wire. The 25Ω - 50 W

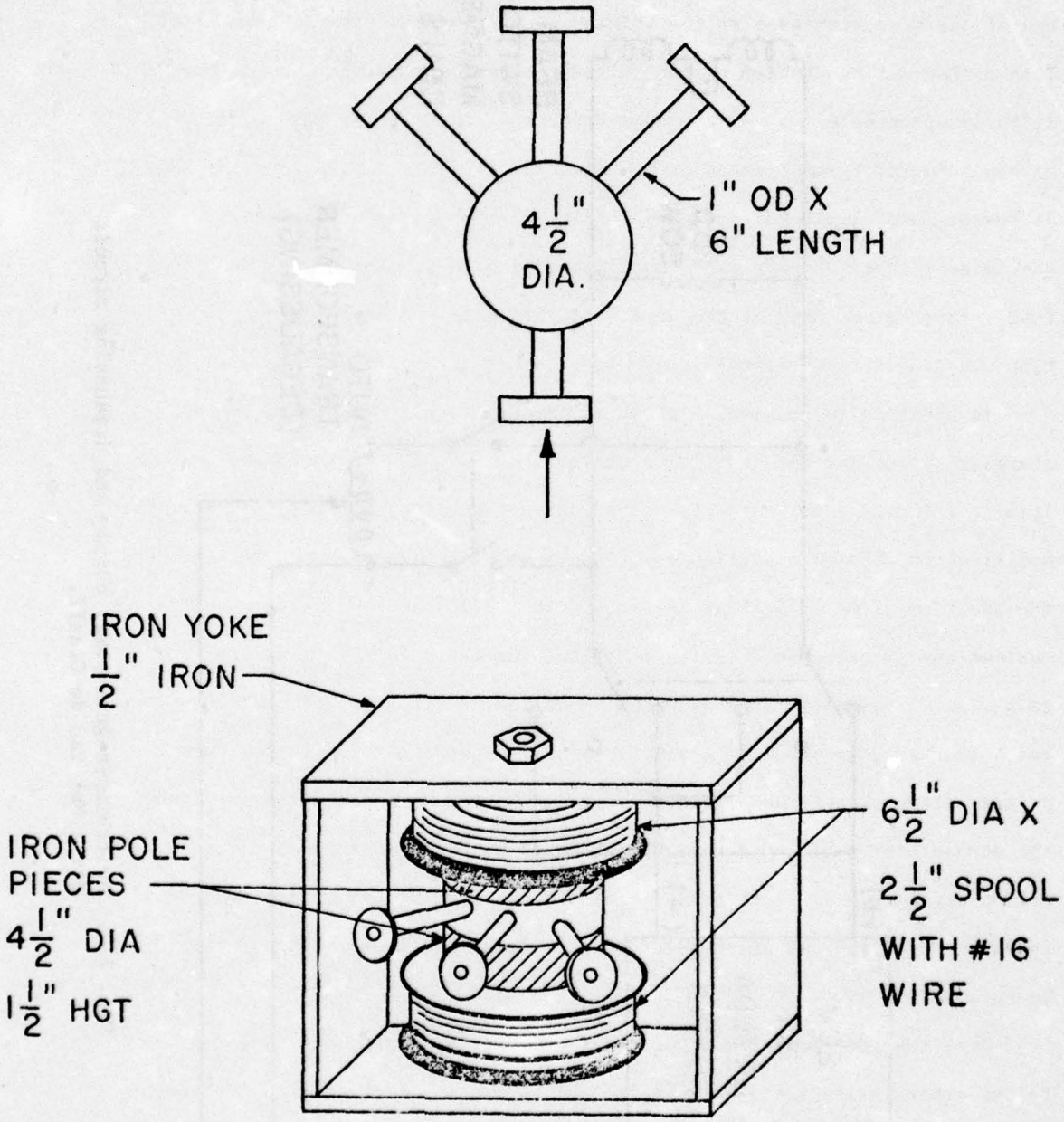

Fig. 2-1. Switching magnet (~1kG) for 1 MeV Van de Graaff.

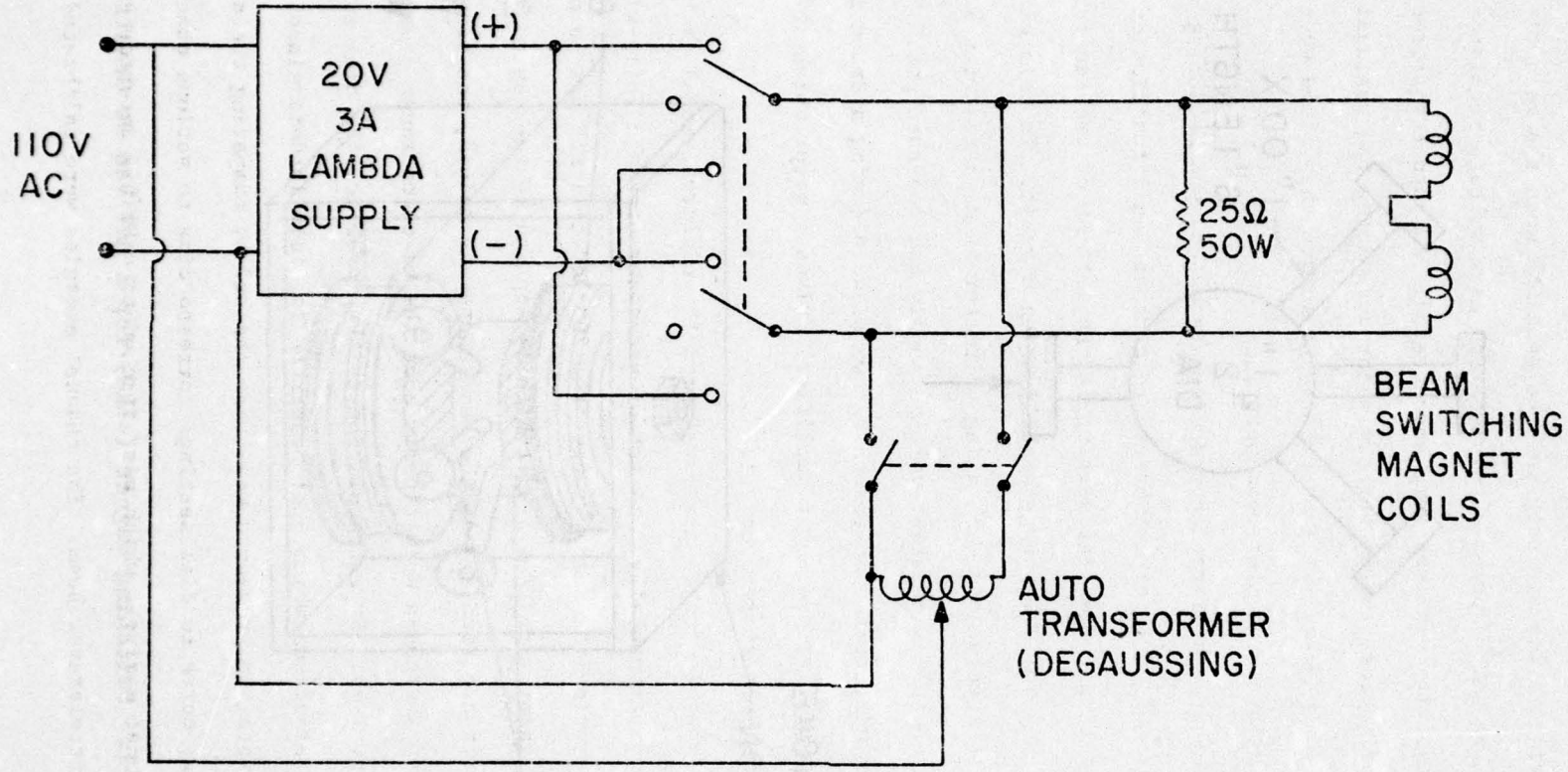

Fig. 2-2. Switching-magnet power supply and degaussing circuit for 1 MeV Van de Graaff.

resistor provides a leakage path for the back-EMF when the magnetic field is collapsed. The Lambda power supply was run as a voltage regulator since no temperature stability problems were encountered. An auto transformer (Fig. 2-2) can be switched across the magnet coils for degaussing the residual magnetism in the pole iron pieces. It is necessary to remove this field when making irradiations using the center beam port.

The beam-energy calibration procedure is based upon measuring the range of electrons in Al foils of calibrated thicknesses as a function of beam-energy dial setting. The dial setting is the setting of the ten-turn pot shown in Fig. 2-3 for the energy stabilization circuit. In this circuit the signal from the accelerator generating voltmeter is compared with a reference voltage obtained from a constant-voltage supply and ten-turn pot. The output of the voltage difference between these two signals (using a Brown recorder differential amplifier and power amplifier) drives a motor which in turn drives the accelerator belt-charge control.

The Katz-Penfold range-energy relation for electrons in Al (Table 2-1) is well known experimentally.[1] A set of secondary standard foils with various thicknesses covering the energy range from 200 keV to 1 MeV can be mounted in the window of a Faraday cup. A 375-volt bias is applied to the cup to suppress secondary-electron currents. As the beam energy is raised, the current from the Faraday cup increases dramatically once the electron range exceeds the foil thickness (Fig. 2-4). By extrapolation to the baseline, the dial setting for the energy of electrons which just penetrate the foil is determined.

This calibration procedure was cross checked by comparing the dial setting vs. beam energy curve to dial settings corresponding to various channel numbers of a multichannel analyser which was attached to a Si(Li) detector and pre-amp sampling the accelerator beam. The channel energies were calibrated using the

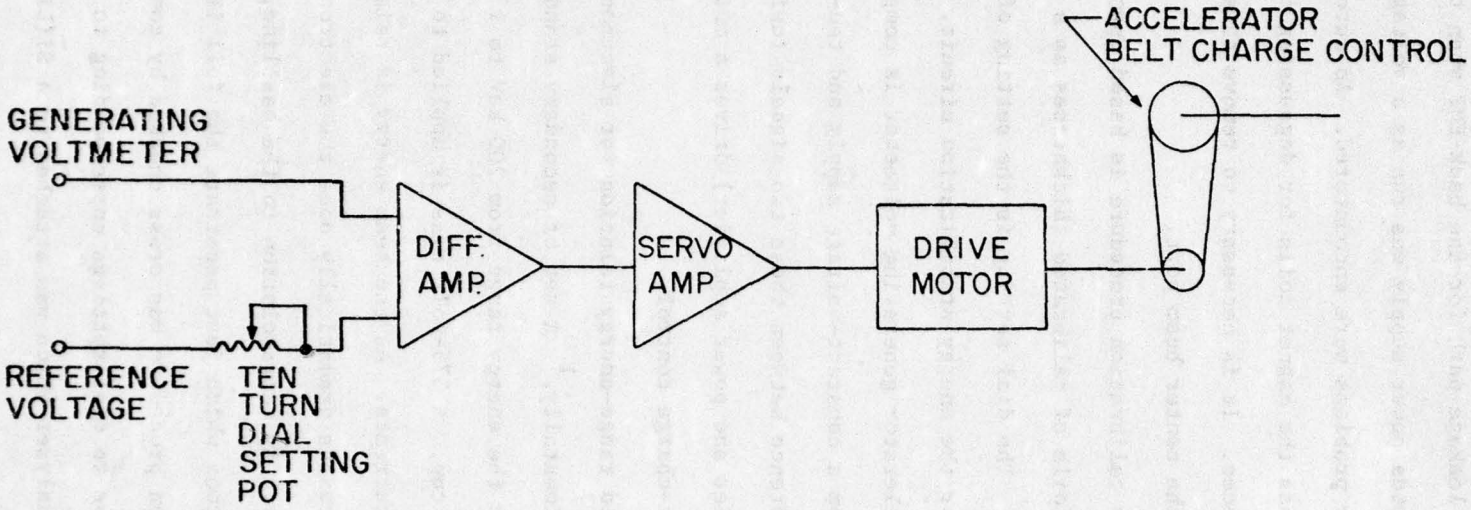

Fig. 2-3. Beam-energy stabilization schematic for 1 MeV Van de Graaff.

Table 2-1. Katz-Penfold range-energy values for electrons in Al [Katz and Penfold, Rev. Mod. Phys. 24, 28 (1952)].

E(MeV)	R(mg/cm^2)
0.01	0.016078
0.02	0.067863
0.03	1.5101
0.04	2.6135
0.05	3.9561
0.06	5.5121
0.07	7.2603
0.08	9.1833
0.09	11.2664
0.10	13.4968
0.15	26.5178
0.20	42.0126
0.25	59.3837
0.30	78.2345
0.35	98.2834
0.40	119.3211
0.45	141.1866
0.50	163.7526
0.55	186.9166
0.60	210.5946
0.65	234.7167
0.70	259.2241
0.75	284.0670
0.80	309.2025
0.85	335.4379
0.90	360.2086
0.95	386.0189
1.00	412.0000

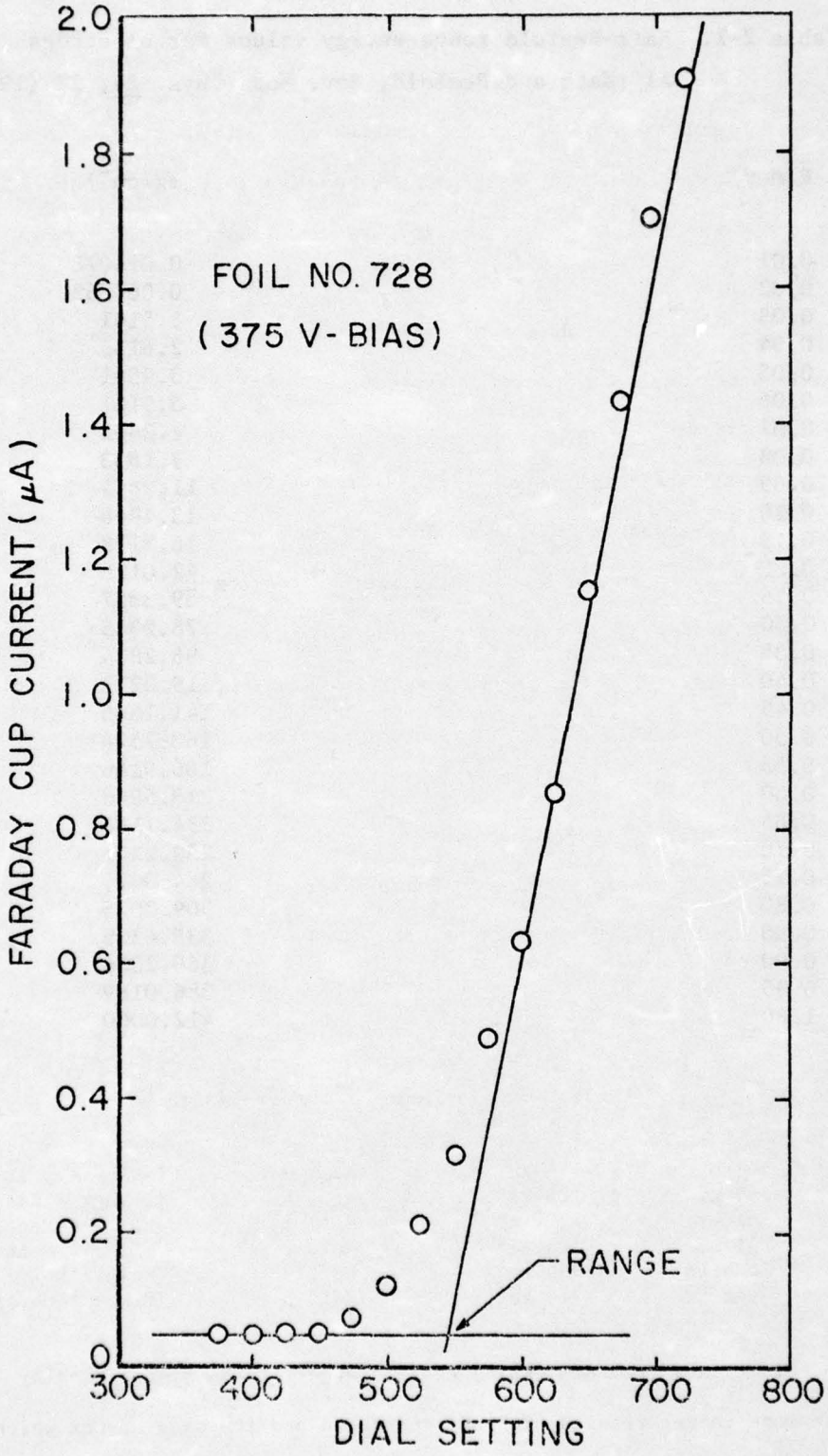

Fig. 2-4. Range measurement for a single Al foil thickness.

same detector and the known emission energies of internal-conversion electrons from ^{207}Bi A typical ^{207}Bi spectrum is shown in Fig. 2-5. The agreement between these two calibration procedures was within one channel number (3 keV) or less than ± 1/2% at 1 MeV.

Figure 2-6 shows the agreement between the beam energy as measured using the multichannel analyser and solid state detector (solid line) and the energy calibration obtained by using the Katz-Penfold[1] experimental range-energy relationship and the ranges as determined in Fig. 2-4 for various foil thicknesses. The agreement is excellent and we believe essentially correct since the energies are determined by two separate and independent experiments.

Also shown in Fig. 2-6 is the calculated range-energy relation by A. T. Nelms[2] (broken line) along with the energy labels found on the Al foils at the beginning of this contract. It is apparent that someone had calibrated the accelerator prior to this contract using the theoretical Nelms curves rather than the experimental Katz-Penfold curves. As a result of this error, it is likely that the displacement thresholds reported in the literature by Kulp, et. al, prior to 1971 are in error. Figure 2-6 can be used to correct these values. As a result of this error the displacement thresholds in CdS have been remeasured on this contract. The results are summarized in Table 2-2.

Table 2-2 Displacement thresholds in CdS

Sulfur	115 keV	Ref. 3	(Kulp, et.al.)
Sulfur	125 keV	Ref. 4	(Bryant & Cox)
Sulfur	125 keV	Ref. 5	(Elsby & Meese)
Sulfur	125 keV	Ref. 6	(Elsby & Meese)
Cadmium	290 keV	Ref. 7	(Kulp)
Cadmium	314 keV	Ref. 5	(Elsby & Meese)

The older data from ARL (Kulp, et.al.) appear to be systematically lower than the more recent results of Elsby and Meese and the data of Cox which are in

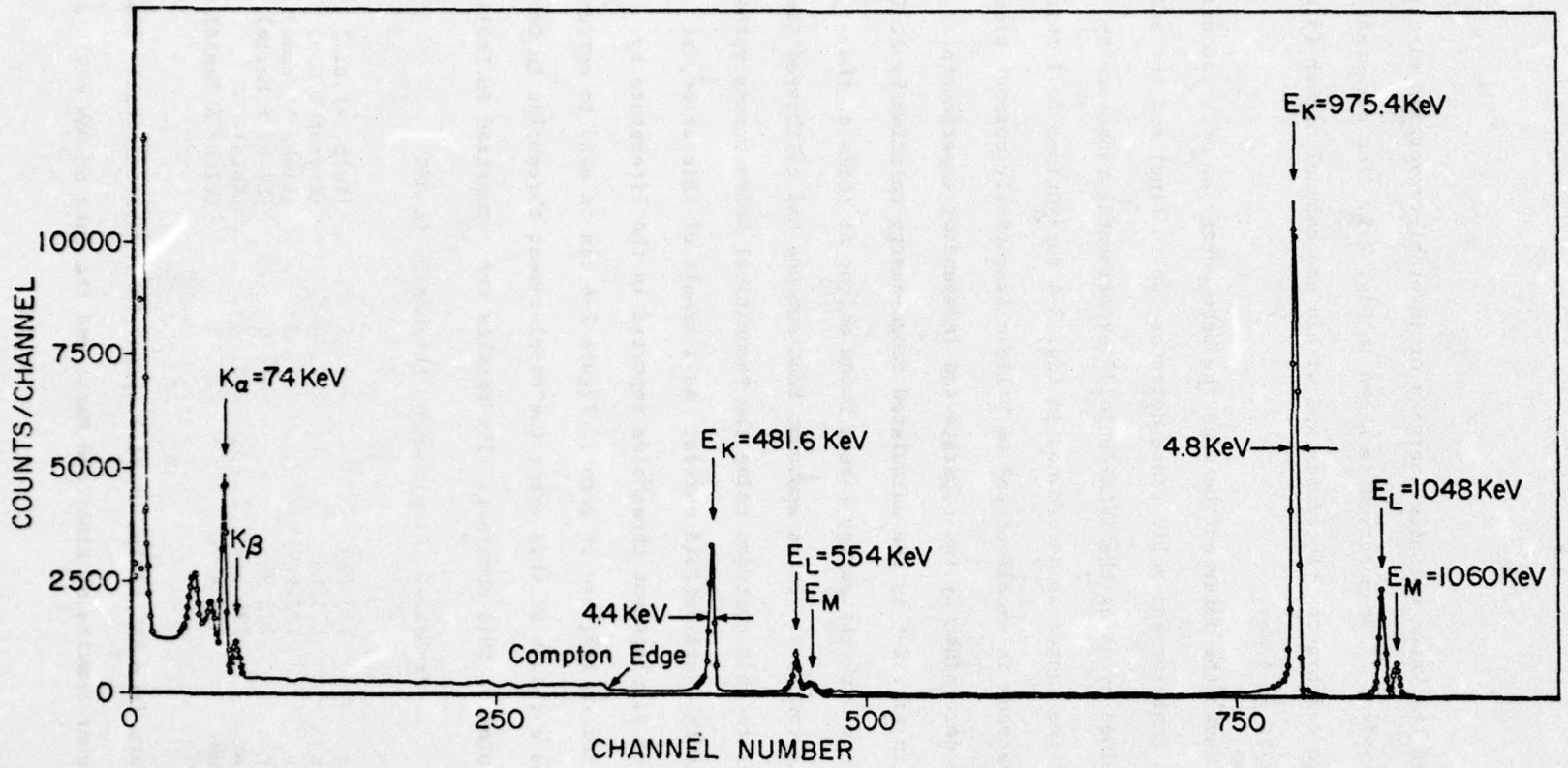

Fig. 2-5. Internal conversion electron spectrum of ^{207}Bi source used to calibrate accelerator and foils.

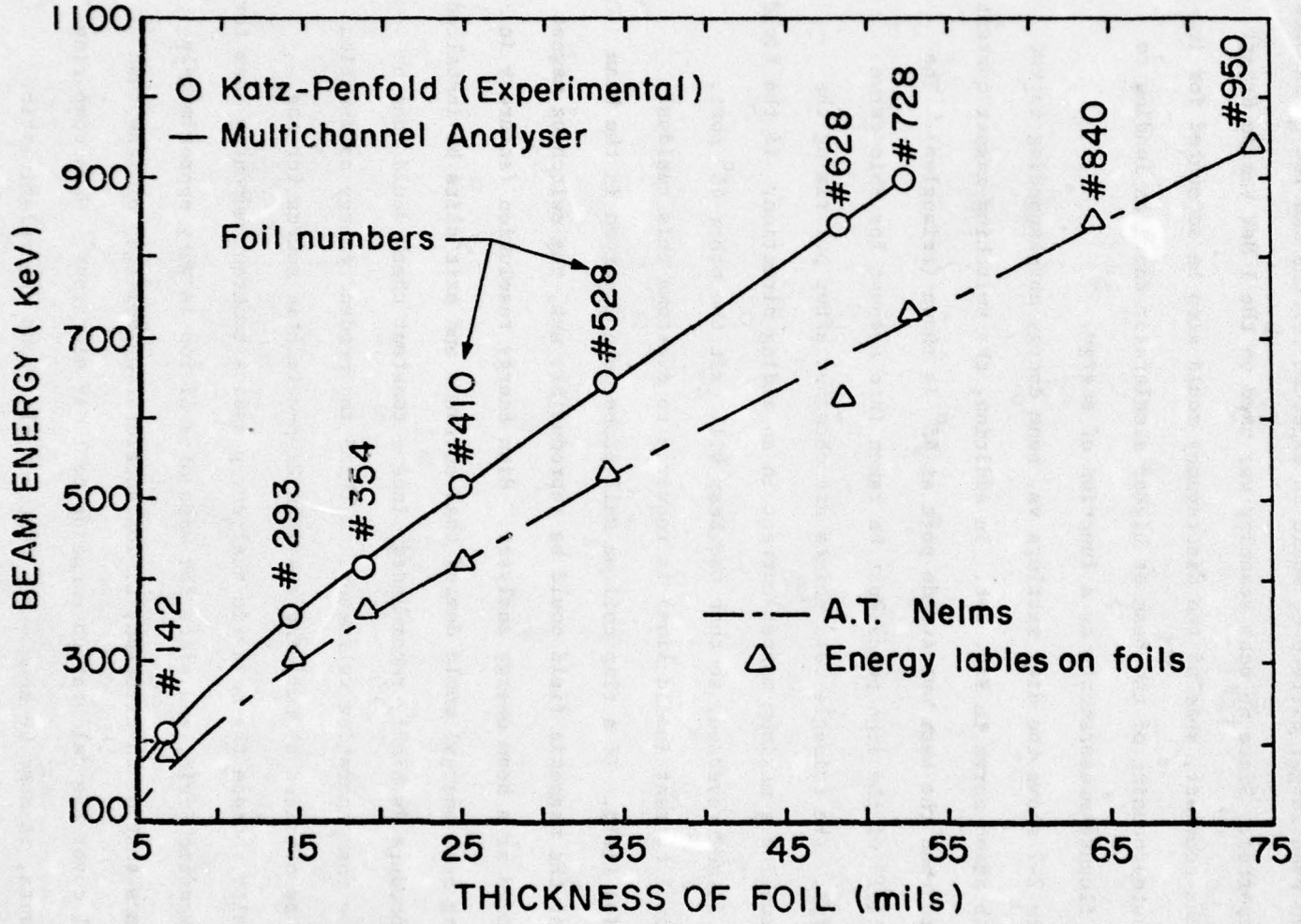

Fig. 2-6. Calibration-foils range (thickness)-energy curves. The solid curve is the correct one. The Katz-Penfold data may be found in Ref. 1, and the A. T. Nelms data, Ref. 2.

agreement. This agrees reasonably well with the curves shown in Fig. 2-6, although an even larger difference would be expected for the cadmium thresholds than is reported. Since no beam scanning was used on the 1 MeV Van de Graaff prior to the contract, some of the discrepancy could also be accounted for in terms of auto-focusing of the beam at higher accelerator energies leading to errors in fluence measurements as a function of energy.

Figure 2-7 shows the dial settings vs. beam energy corresponding to the solid calibration curve in Fig. 2-6. In addition, the switching-magnet current required to bend the beam out a side port at 45^{o} is shown (triangles). The residual field of the iron poles must be taken into account for this curve to be useful. The triangle data points are obtained after polarizing the poles by running a maximum magnet current in an aiding direction. If the field direction is now reversed, so that the beam will exit the other 45^{o} port, an additional current (solid line) is required to overcome this residual polarization field. If a flip coil or Hall probe were inserted in the beam can so that the magnetic field could be reproducibly set, the switching magnet could be used as a beam energy analyser. High energy resolution (accuracy in determining beam energy) would demand that entrance and exit slits be installed. Such a procedure is highly recommended since a constant check would then be possible on the generating voltmeter. A third independent energy calibration check can be obtained by building a simple Li β-eutechtic source for the entrance slit. Since the magnetic analyser passes a constant momentum beam for a fixed magnetic field, and since the mass of a Li ion is very approximately 14,000 times that of an electron, Li-ion accelerating voltages of less than 500 V will cover the calibration range up to 1 MeV electrons. When comparing equal momenta, it must be remembered that the electrons are relativistic.

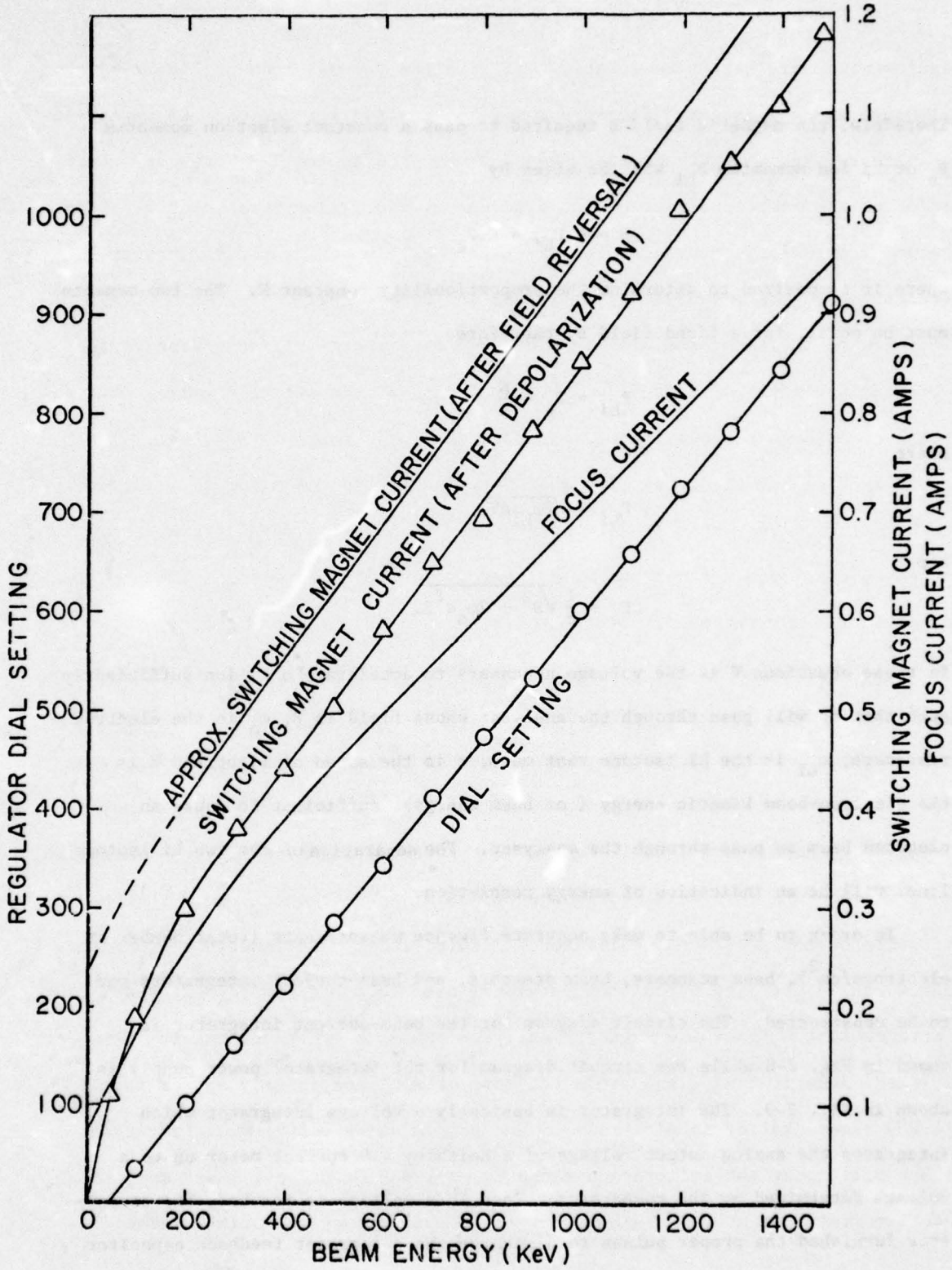

Fig. 2-7. Beam-energy vs dial setting and switching-magnet current. Also shown is the proper focus-magnet current as a function of energy.

Therefore, the magnetic field B required to pass a constant electron momentum P_e or Li ion momemtum P_{Li} will be given by

$$B = K P_{Li} = K P_e$$

where it is desired to determine the proportionality constant K. The two momenta must be equal, for a fixed field B; therefore

$$P_{Li} = P_e = \frac{B}{K}$$

where

$$P_{Li} = \sqrt{2m_{Li}eV}$$

and

$$P_e = \frac{1}{c}\sqrt{E^2 + 2m_o c^2 E}.$$

In these equations V is the voltage necessary to accelerate a Li ion sufficiently such that it will pass through the analyzer whose field is B, m_o is the electron rest mass, m_{Li} is the Li isotope rest mass, c is the speed of light, and E is the electron-beam kinetic energy (or beam energy) sufficient to cause an electron beam to pass through the analyser. The separation of the two Li isotope lines will be an indication of energy resolution.

In order to be able to make accurate fluence measurements (total number of electrons/cm^2), beam scanners, beam steerers, and beam-current integrators had to be constructed. The circuit diagram for the beam-current integrator is shown in Fig. 2-8 while the circuit diagram for the integrator power supply is shown in Fig. 2-9. The integrator is basically a voltage integrator which integrates the analog output voltage of a Keithley 410 current meter up to a voltage determined by the comparator. Once this voltage is reached, the comparator furnished the proper pulses to discharge the integrator feedback capacitor and also pulses the electromechanical counter to give one count. The process

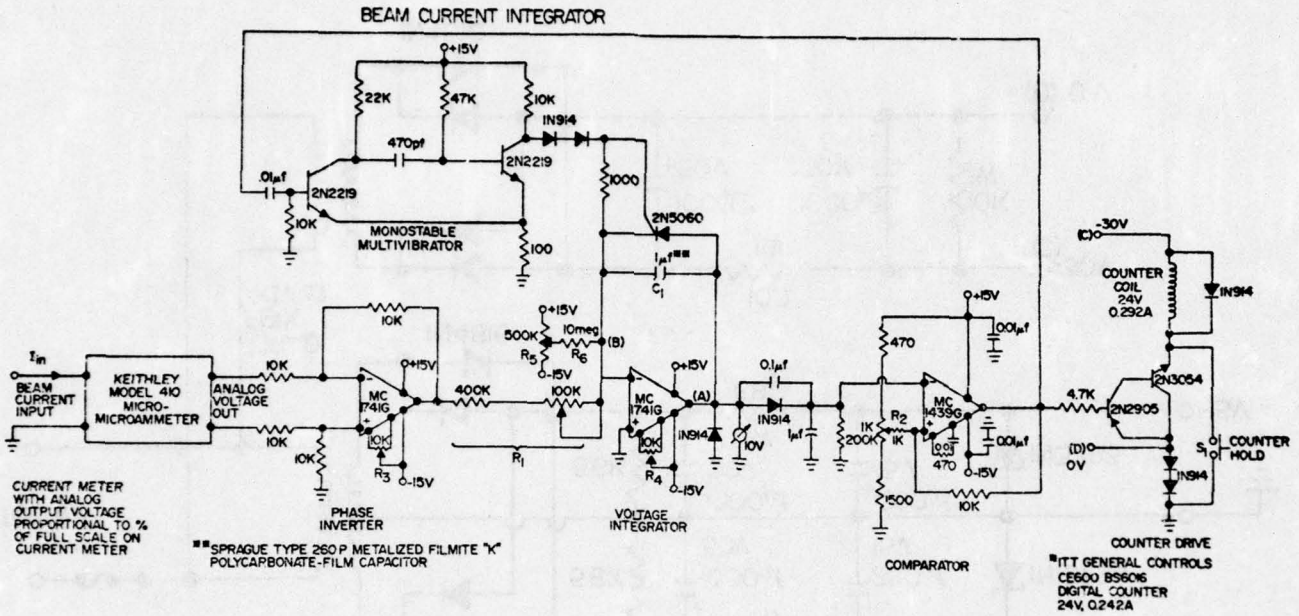

Fig. 2-8. Circuit diagram for beam-current integrator.

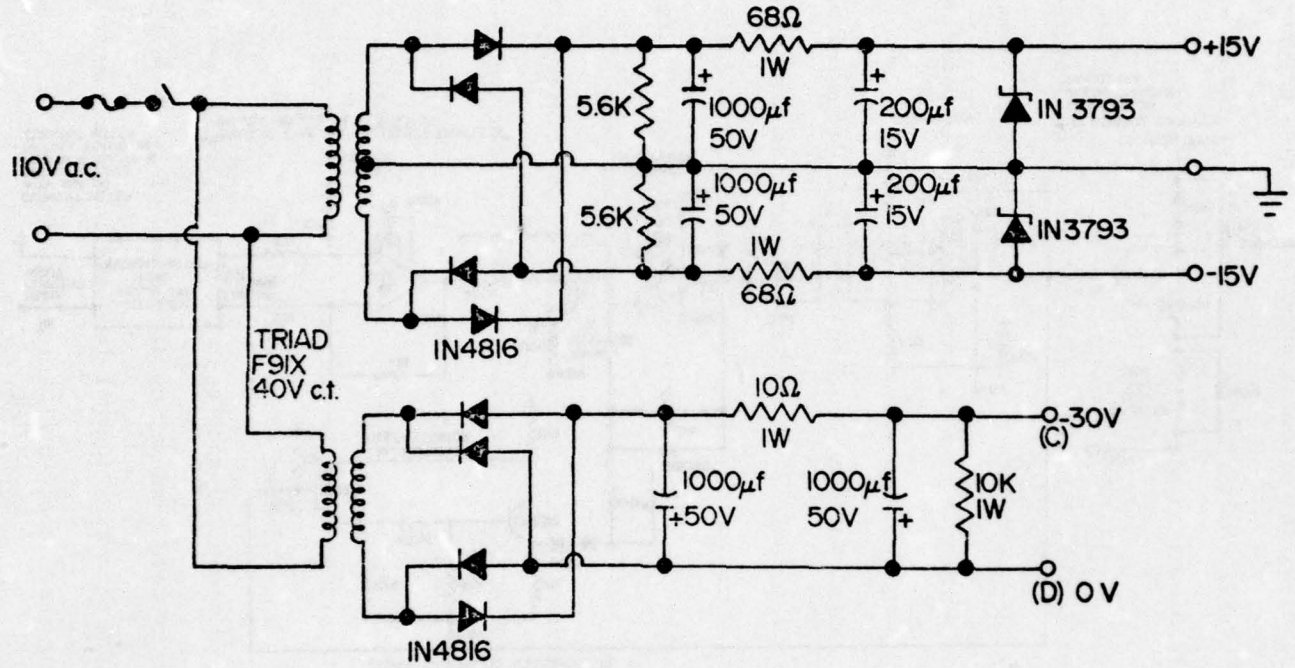

Fig. 2-9. Power supply for beam-current integrator.

is then repeated. The accuracy of the integrator can be adjusted to better than ± 0.2% by selecting the proper current at pt. B by adjusting R_5 so as to just counterbalance the offset voltage of the 1741G op amp. A complete description of the operation and adjustment of this integrator has been published.[8]

Beam scanners for the 1 MeV Van de Graaff were also designed and constructed under this project and have been published.[9] Figure 2-10 shows the basic circuit to provide a triangular wave form to the driver power amplifiers. The basic circuit was constructed from modules. A Wavetek triangular wave generator module for each channel was used. R_1 selects the frequency of oscillation while a 5K gain control and 1714G op amp determine the amplitude. Audio power amplifiers were used to amplify this signal and power the deflection coils (TV yoke). The front end of the power amplifier (Universal Tiger-175A) was redesigned so that (+) or (-) dc offset could be provided (Fig. 2-11) to furnish beam steering. Figure 2-12 demonstrates the linearity of the sweep. This figure was made with a 1 MeV electron beam striking an Al foil coated with CdS powder. Figure 2-13 demonstrates the excellent beam-scan uniformity. This figure shows the optical density produced in an irradiated microscope slide which is proportional to the number of electrons striking the glass. Uniformity of scan is estimated to be better than ± 1%.

In addition to the above accelerator modifications, several different types of experiments have been set up at the end of the beam line at various times during this contract. Figure 2-14 shows the accelerator vault set up for a luminescence-band defect-production experiment. Electrons from the Van de Graaff are accelerated and shot down the beam tube to irradiate the sample of interest which is mounted at the tip of the cold finger of the

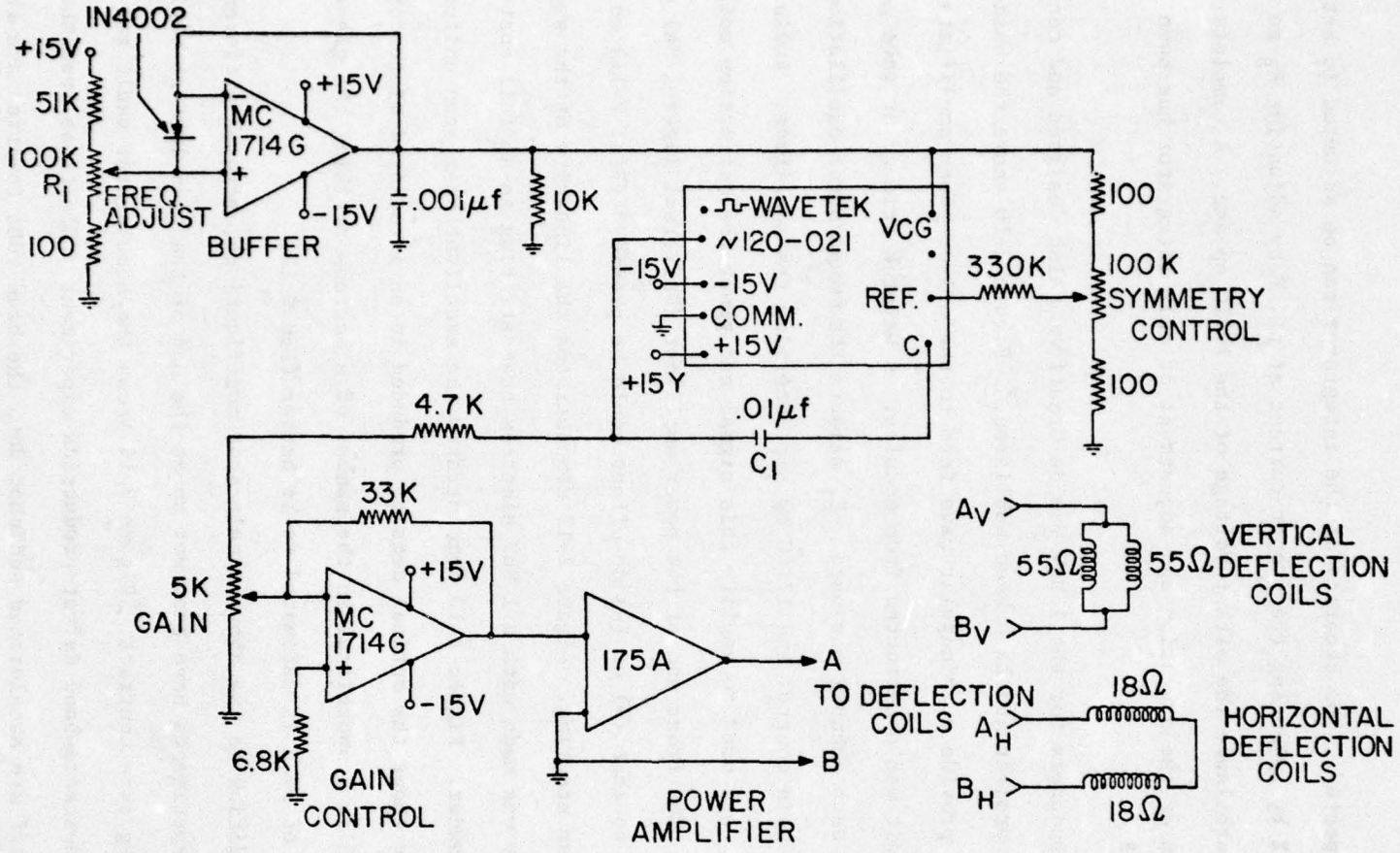

Fig. 2-10. Beam-scanner circuit.

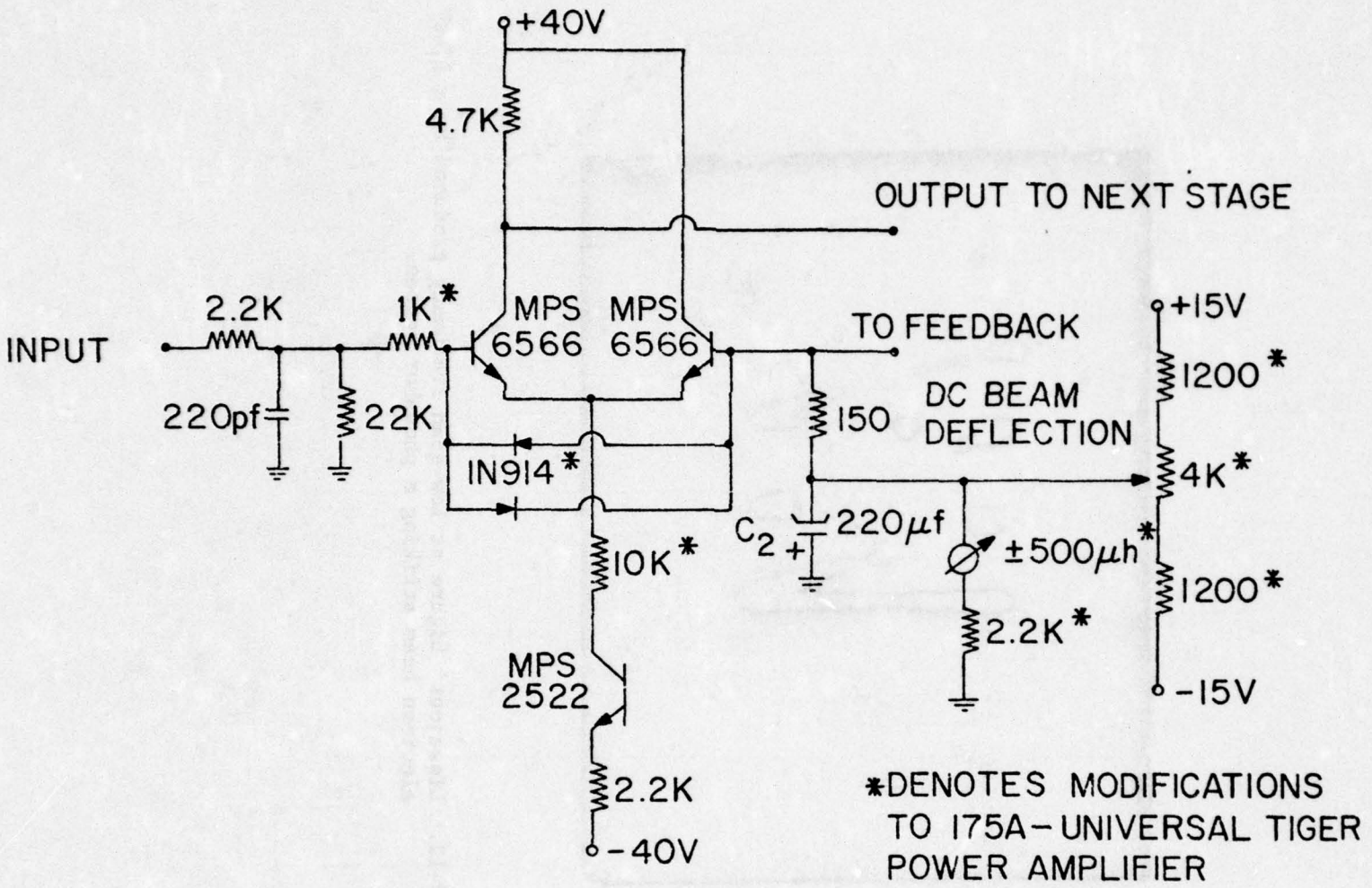

Fig. 2-11. Modifications to input circuits of commercial amplifier used in beam scanner.

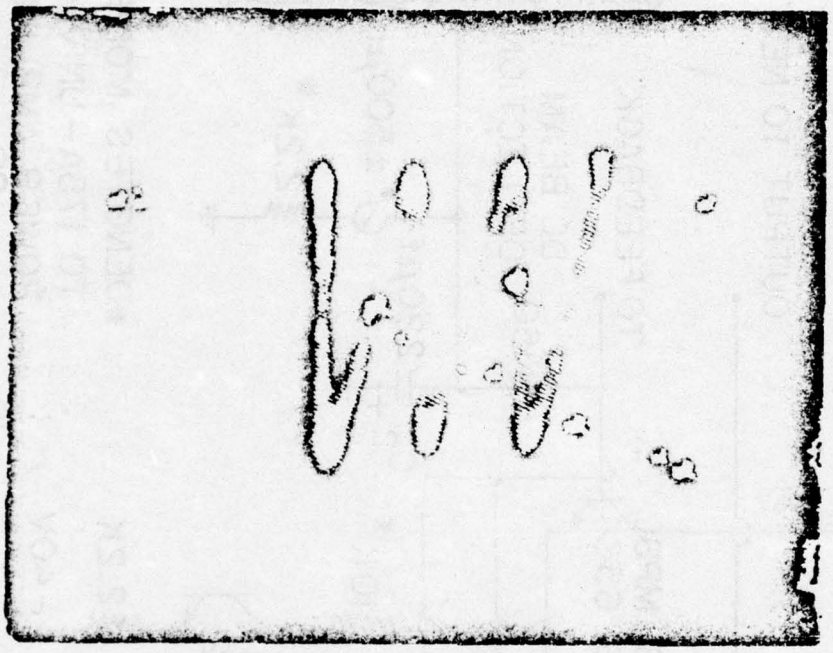

Fig. 2-12. Lissajous' figure at low-scan frequency produced by a 1 MeV electron beam striking a phosphor screen.

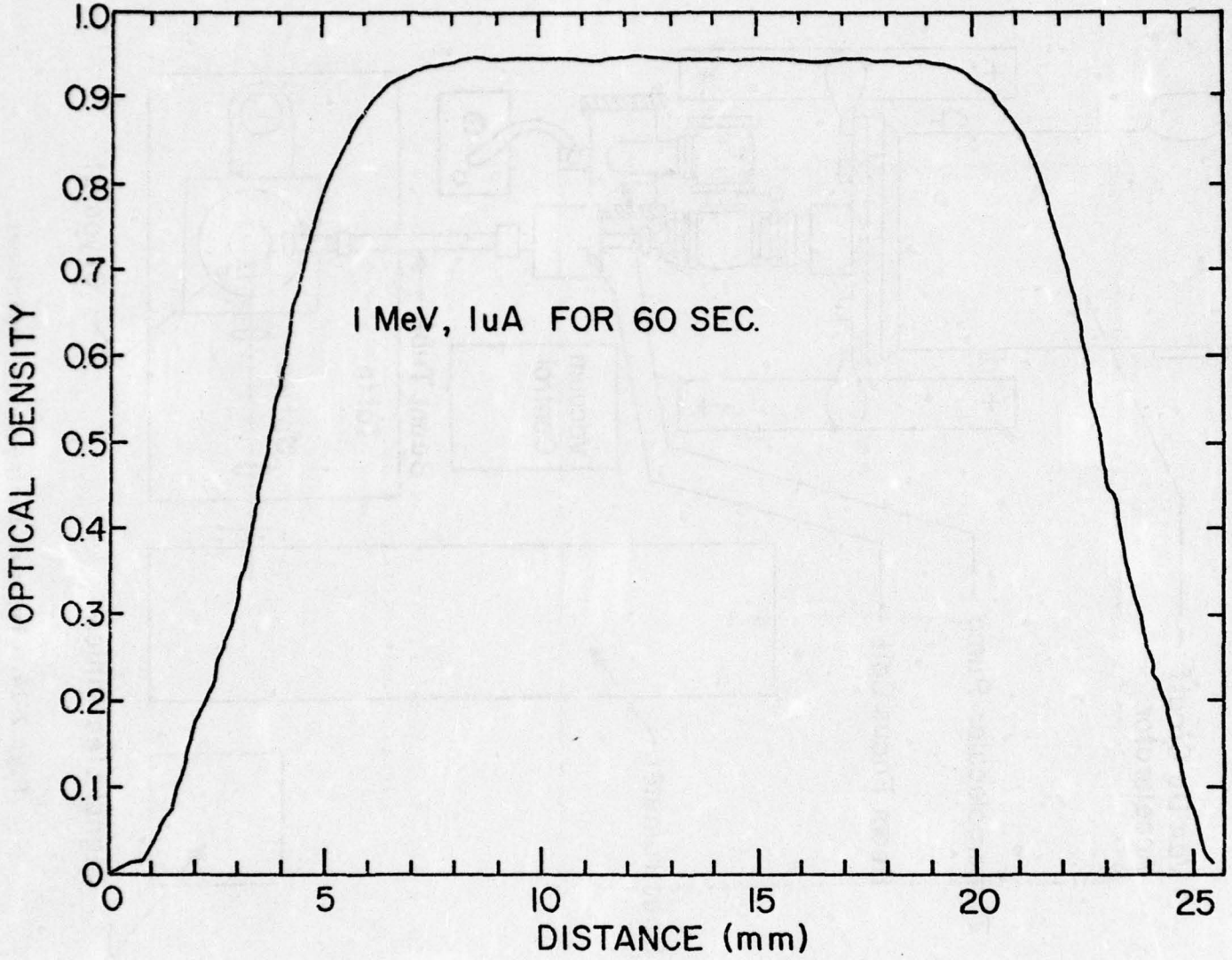

Fig. 2-13. Optical density of irradiated microscope slide.

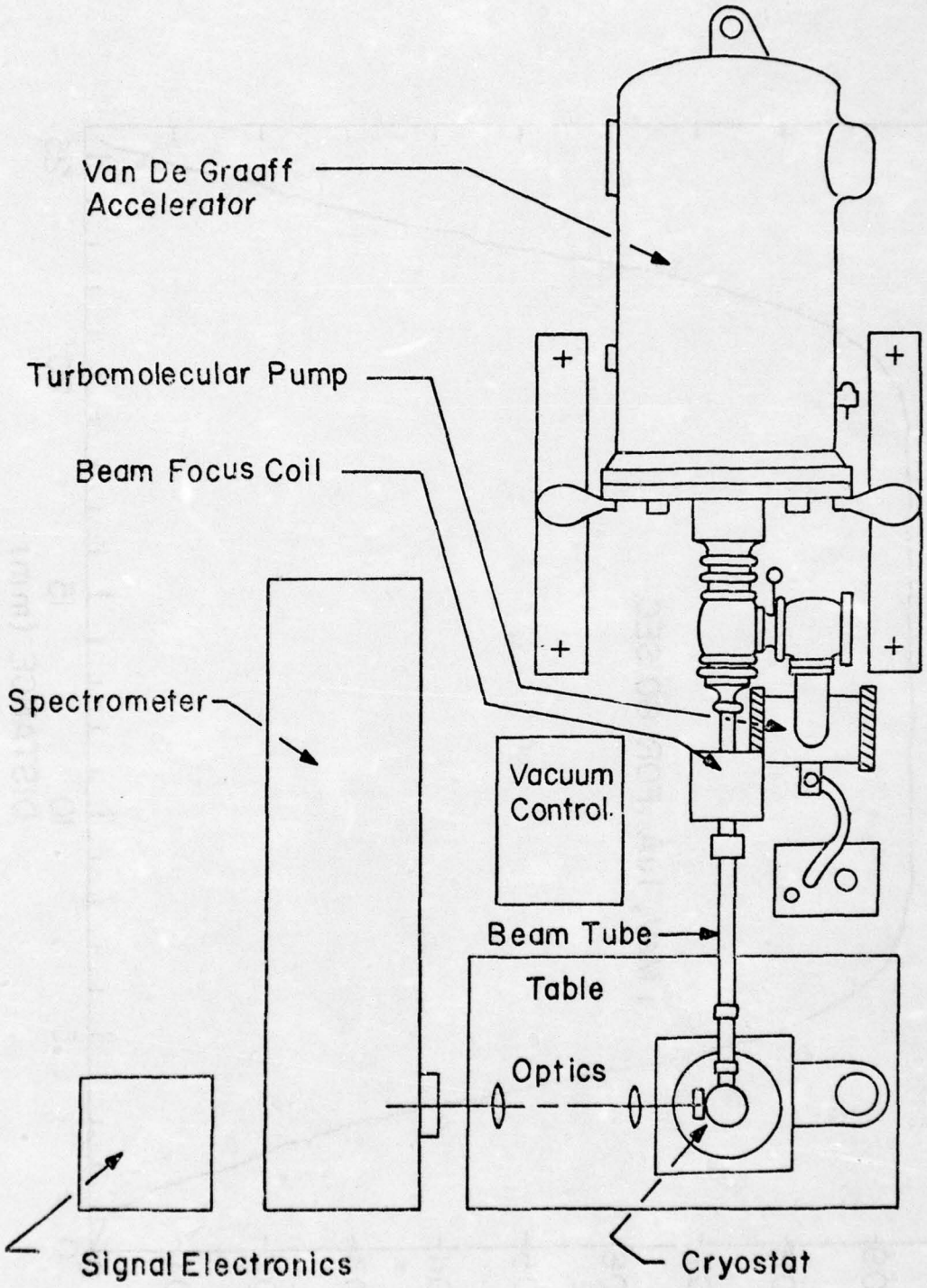

Fig. 2-14. Typical luminescence experiment.

cryostat (Dewar). The cold tip makes an angle of 45° with both the beam direction and the optical axis of the spectrometer and lens system. Since the electron beam penetrates thin samples completely the electron-hole pairs are created deep in the sample. This cathodoluminescence therefore has the advantage over photoluminescence in not being surface sensitive. Figure 2-15 is a diagram of the vaiable-temperature irradiation dewar. The Al window on the LN_2 shield scatters the beam slightly for uniformity. In later experiments where fluence accuracy was a requirement, the scattering foil was moved up into the beam tube. An insulated beam-defining aperature was mounted on the LN_2 cold shield and grounded. The rest of the Dewar, which is insulated from ground, then served as a Faraday cup. Quartz windows allowed the luminescence to be collected by the optical system. Electrical measurements were also made in this Dewar by making use of the feedthroughs at the top. Thermometry was accomplished using carbon-resistor and Pt-resistance themometers.

For IR optical measurements, a double-pass monochrometer was assembled from several junked Perkin-Elmer IR systems to provide an operating doublepass prism monochrometer which could cover the spectral range from 3000Å to 2.5μm using a RCA Quanticon photomultiplier tube and a PbS photoconductor as detectors. This experimental system is shown in Fig. 2-16. The irradiation Dewar is shown at the top of this figure. Photoluminescence could be compared with cathodoluminescence by illuminating the sample with light from a high-pressure Hg lamp.

EPR samples were irradiated in an immersion Dewar. The samples were mounted on the end of a stainless steel tube with clips which could be opened from the top. The tube was keyed so that orientation could be maintained. A substitute

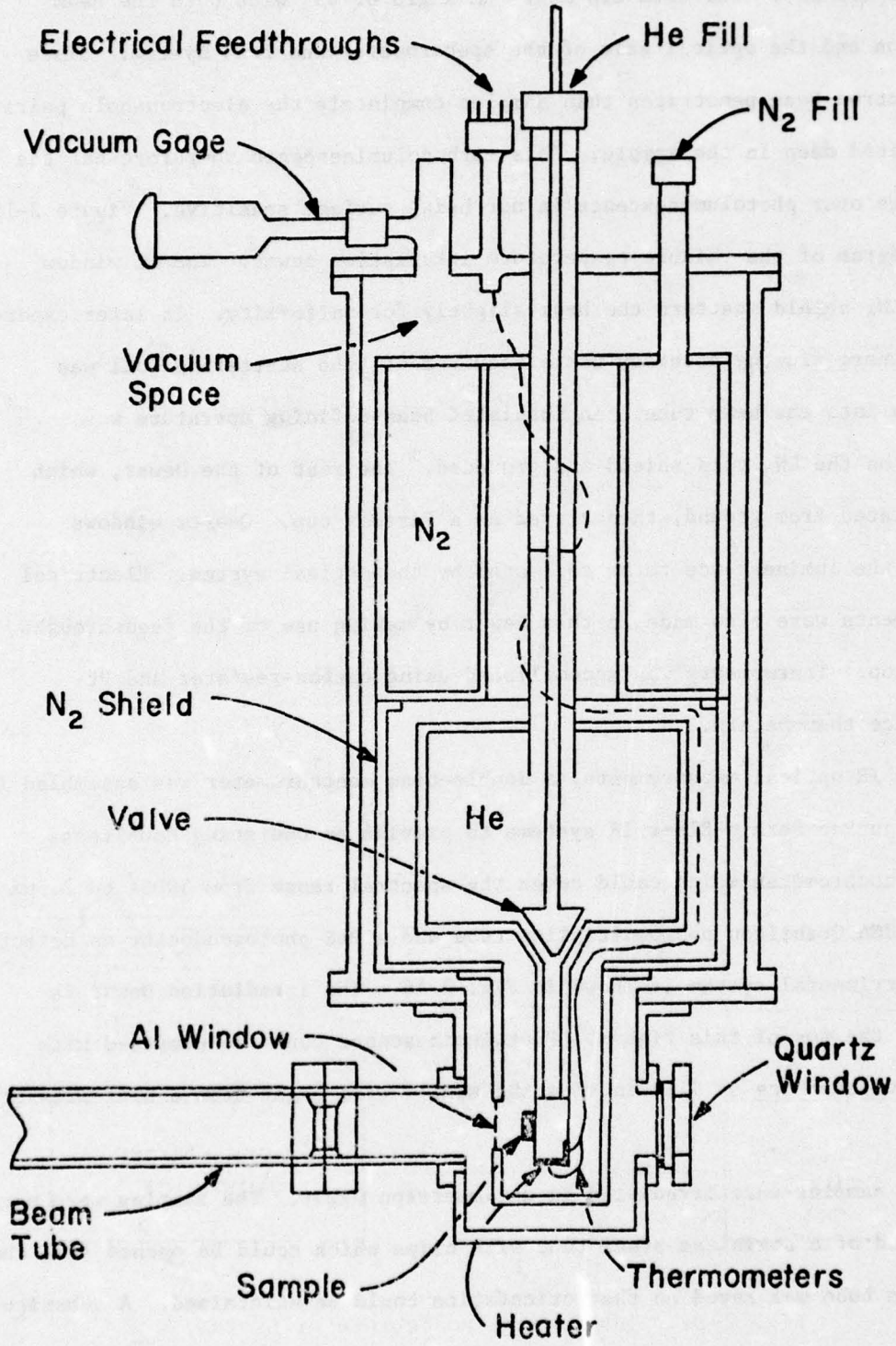

Fig. 2-15. Diagram of irradiation dewar.

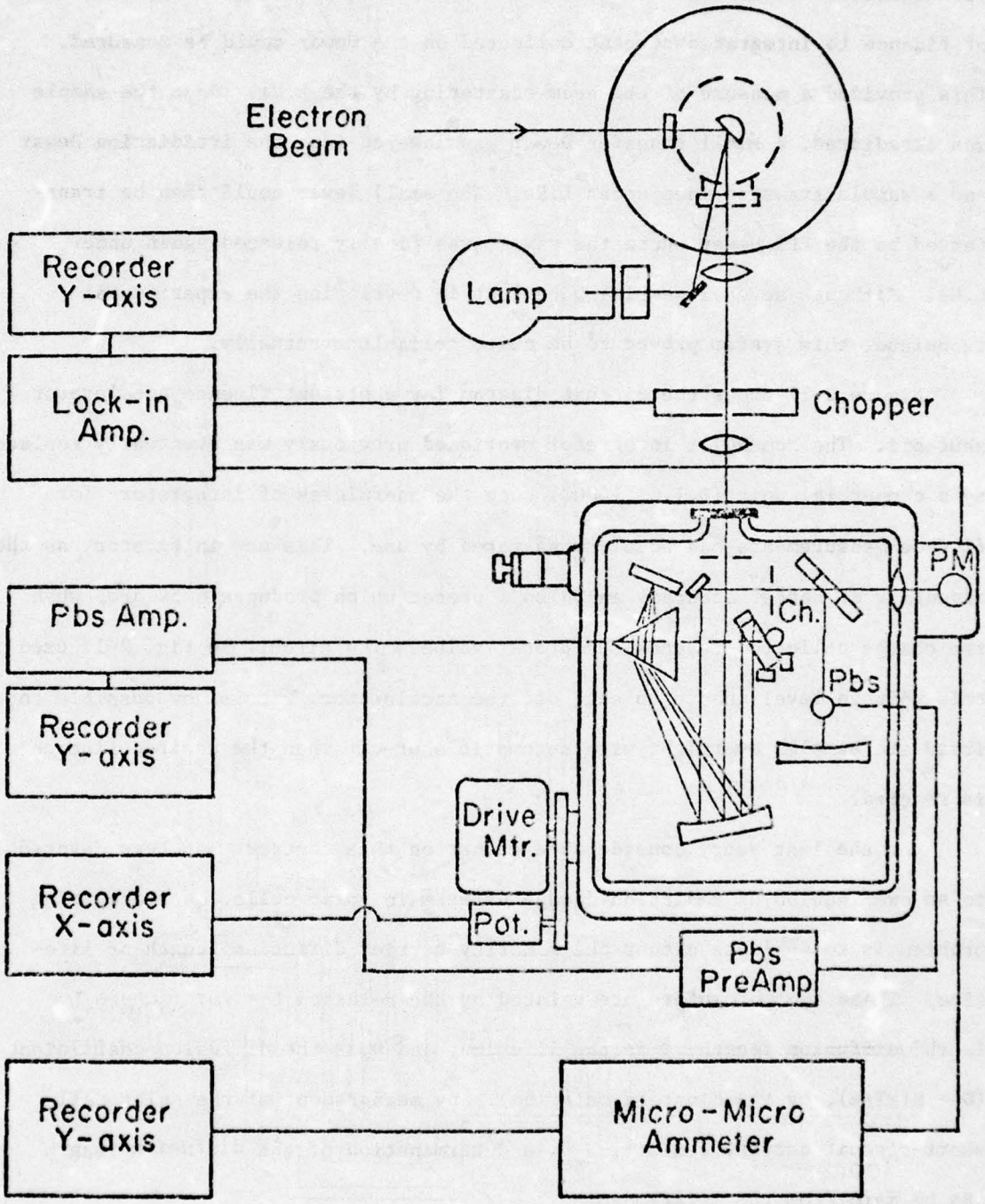

Fig. 2-16. Double-pass monochrometer system.

flux collector could also be inserted in the sample position so that the ratio of fluence to integrated current collected on the Dewar could be measured. This provided a measure of the beam scattering by the L.He. Once the sample was irradiated, a small transfer Dewar was lowered into the irradiation Dewar and a sample transfer made under L.He. The small Dewar could then be transferred to the EPR Dewar where the sample was finally released again under L.He. Although several samples were lost in developing the experimental technique, this system proved to be quite reliable eventually.

Figure 2-17 shows the circuit diagram for a present fluence accelerator shut-off. The homebuilt integrator mentioned previously was eventually replaced by a commercial unit (B.I.C. 1000C) once the usefulness of integrators for fluence measurements had been demonstrated by use. This new integrator has the advantage of better accuracy and also a preset which produces a 5V drop when the charge collected reaches the preset value. The circuit in Fig. 2-17 used this voltage level change to shut off the accelerator. It is now possible to irradiate samples overnight with automatic shut-off when the desired fluence is reached.

For the last year, considerable effort on this contract has been devoted to an examination of radiation-damage effects in solar cells. A reoccurring problem is to evaluate either the minority-carrier diffusion length or lifetime. These two parameters are related by the relation $L = \sqrt{D\tau}$ where L is thd diffusion length, τ is the lifetime, and D is the diffusion coefficient ($D = \mu(kT/e)$, by the Einstein relation). By measurement of the solar cell short-circuit current denisty, J_{sc}, a determination of the diffusion length can be made from the relationship

$$J_{sc} = S_o L J_B$$

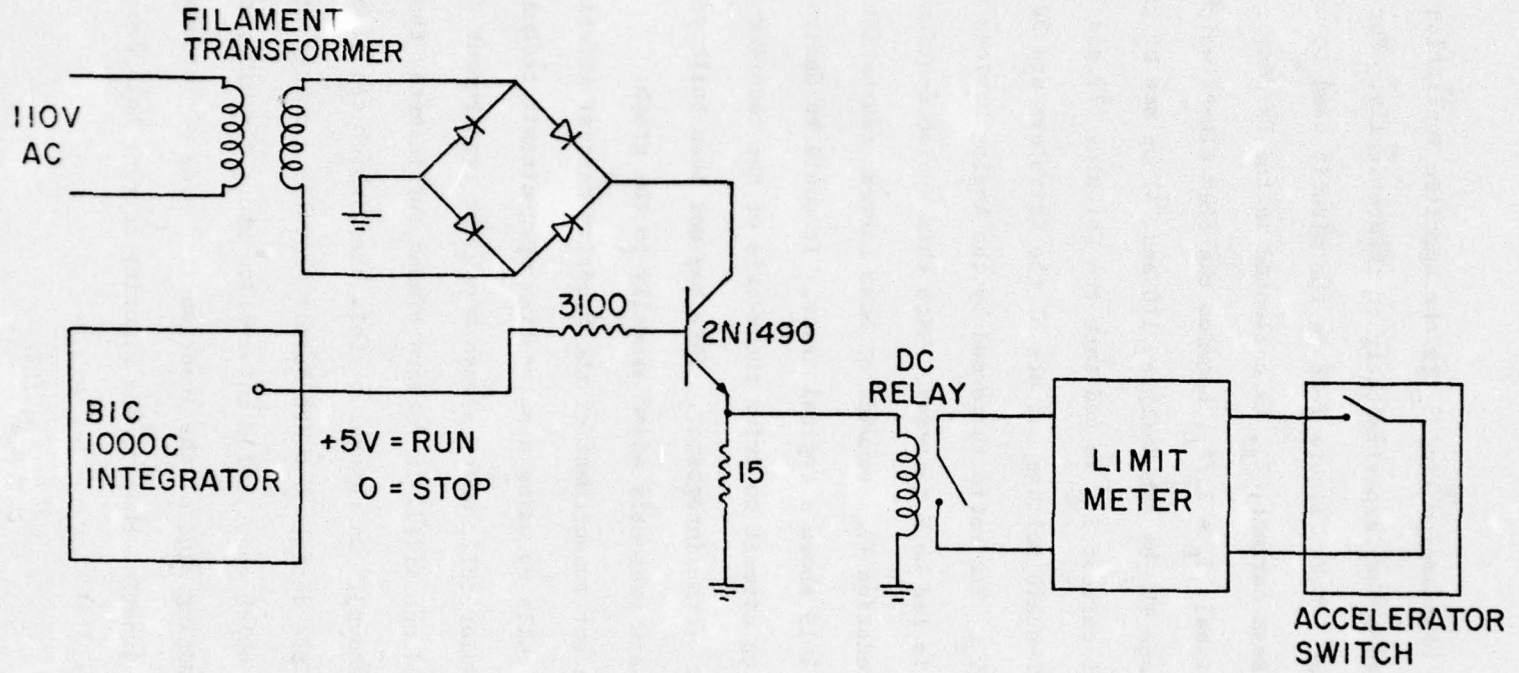

Fig. 2-17. Integrator preset accelerator shut-off.

where J_{sc} is the beam flux(amp/cm^2) and S_o is the specific ionization factor which can be determined either experimentally or theoretically. For Si, S_o = 225 e-h pairs/μ at 1 MeV. Figure 2-18 is the cirucit used to make these measurements. Beam current, I_B, is collected in the Faraday cup of aperature A_B. This signal, $J_B = I_B/A_B$, becomes the flux signal which is converted to the voltage $+V_y$ by the Keithley 110 and 741 op amp of gain = 5/3. The cell short-circuit current I_{sc} is fed into the Keithley 419 and 741 op amp of gain = 1. The full-scale voltage outputs of the Keithleys are 3V and 5V. This signal becomes $-V_x$. The ratio is formed by the Analog Devices voltage divider whose output is fed to a recorder. With this system, continuous diffusion-length degradation (independent of beam current fluxuations) may be observed. Figure 2-19 shows a typical trace. It would be desirable to use a digital-to-analog circuit to drive the x-axis of the recorder using the flux counting circuit of the integrator. This has not been built yet. Fluence measurements are presently added manually to the graph.

A second independent measurement of the minority carrier lifetime has also been made on Si cells by using a pulse-bias open-circuit technique. In this measurement, a solar cell, which always meets the requirement that the junction is abrupt and one sided, is forward biased sufficiently that the depletion width is removed. On removal of this bias, which can also be obtained by a pulse of light, the depletion width formed produces a change in the diode open-circuit voltage which then yields information about the minority-carrier lifetime in the low-doping side of the junction (the side of interest here).

From simple p-n junction theory, the minority carrier hole density in the n-region is given by

$$p = p_n e^{qV/kT} .$$

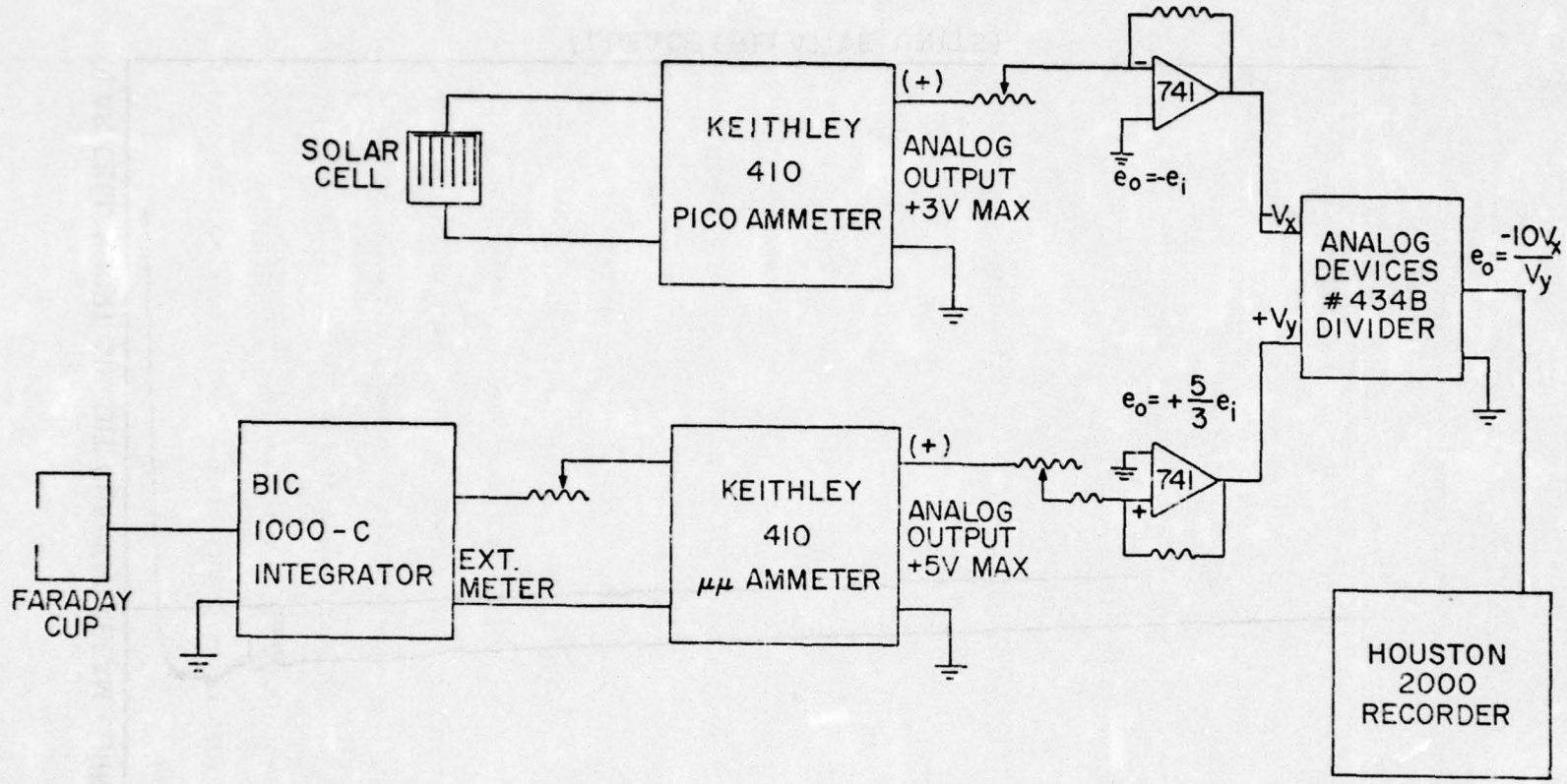

Fig. 2-18. Circuit to measure solar-cell carrier-diffusion lengths.

Fig. 2-19. J_{SC}/J_B vs. fluence.

Since

$$p = p_n + \Delta p,$$

then

$$V = \frac{kT}{q} \ln(1 + \Delta p/p_n).$$

Also, the excess carrier density, Δp, decays on the removal of the forward bias by the equation

$$\Delta p = \Delta p_o e^{-t/\tau}$$

where τ is the minority carrier lifetime and Δp_o is the excess minority carrier density at $t = 0$ when the bias is removed. If V_o is the value of the open circuit voltage at $t = 0$, then

$$V_o = \frac{kT}{q} \ln(1 + \Delta p_o/p_n)$$

and

$$V(t) = \frac{kT}{q} \ln[1 + (e^{qV_o/kT} - 1)e^{-t/\tau}].$$

For $t \ll \tau$ and $V_o \gg kT/q$, the last equation yields

$$\frac{dV}{dt} = \frac{kT}{q} \frac{1}{\tau}$$

or

$$\tau = -\frac{q}{kT} \frac{1}{(dV/dt)}.$$

Therefore, a measurement of the slope of the decay of the open-circuit voltage vs. time yields the lifetime directly.

We have used both of the above techniques on a variety of Si solar cells and have obtained good agreement between the two techniques.

In addition to the Van de Graaff facility work and the design and construction of experimental equipment already described, considerable effort has been spent on the rest of the accelerator facility. New and safer accelerator vaults

for all the machines were planned under this contract and have now been installed. The 400 keV Van de Graaff was moved from an unshielded open position to a new vault. Help was furnished from this contract in converting this accelerator to protons. This machine now resides in approximately the same place as the old Cockroft-Walton which we also helped remove.

Considerable effort was also expended in setting up the ion-implantation accelerator, aligning the beam, repairing the analyzing-magnet-winding shorts, etc., as well as training personnel to operate the machine.

This concludes the experimental equipment section of this report relating to radiation effects experiments. The following sections describe results of experimental studies of radiation damage in compound semiconductors.

2.3 Radiation Effects in Compound Semiconductors

In this section, brief summaries of experimental work concerned with defect identification, defect production mechanisms, and irradiation effects in semiconductor devices will be described. The work will be broken down into the following areas:

2.3.1 Radiation Effects in II-VI Compounds

2.3.2 Defect Semiconductor Radiation Damage - In_2Te_3

2.3.3 Annealing Kinetics and Radiation Annealing in Si, Ge, and GaAs

2.3.4 Solar Cell Radiation Effects

2.3.5 Proton-Induced Characteristic X-ray Analysis.

Since most of this work has been published, only brief summaries of the major conclusions will be presented here. Since the development of scientific models contains an evolutionary element, attempts will be made to summarize our present understanding of these problems in terms of the prospective we have been able to develop during the period of this contract. Attempts

will also be made to suggest the areas in which understanding is still lacking and to indicate fruitful avenues of future research.

2.3.1 Radiation Effects in II-VI Compounds

In the early 70's, at the beginning of this contract, very little was understood concerning the nature of the defects produced by irradiation in II-VI compounds and how to identify them by their electrical and optical properties, etc. The displacement thresholds had been measured for a number of the II-VI's and some luminescence bands produced; however, the correlation of these bands with particular defects was sketchy in most cases, the results being inferred only from one kind of measurement.

Radiation damage had been studied extensively in Si and Ge and it had been discovered that vacancies in these materials migrate at temperatures near L.N_2. The interstitials were thought to migrate near or below L.He temperature. Since most of the semiconductor-radiation-effects scientists had cut their teeth on these materials, there was a general belief in this community that the rest of the semiconductors should behave like Si and Ge. The rather obvious point that defects in a compound semiconductor should move on their own sublattices (requiring considerably more thermal energy than in the elemental semiconductors) was missed by most. The literature of the 60's is full of speculation suggesting that new low-temperature annealing stages remained to be found in the II-VI semiconductors. Very few took the trouble to look, however.

Some controversy existed concerning the displacement thresholds also. Although many of the II-VI and III-V displacement energies had been found to be in the 5-10 eV range, it was felt that these numbers were too low compared with the values of 15-30 eV from C, Si, and Ge. To complicate matters, estimates

of the displacement thresholds in ZnO had placed the value for the displacement energy of Zn in ZnO above 600 keV.[10] When later EPR experiments[11] showed that the defect produced by these very high energy electron irradiations was the oxygen vacancy, and not a Zn defect, the conclusion was drawn that T_d should be larger for ZnO than diamond, a difficult point to defend for long. Furthermore, in CdS, Kulp[7] had identified the Cd displacement threshold at 290 keV by the production of a luminescence band at 1.03μm. Bryant and Cox had reported forming this band at 125 keV suggesting that sulfur displacements were involved.[12] The situation was far from clear concerning the displacement energies. A knowledge of these energies is essential, however, to an understanding of the association of various annealing stages with defects on particular sublattices and to physical property changes associated with defects on the two sublattices.

One other point should be mentioned. Most of the II-VI compounds are usually n-type and strongly resist attempts to dope them p-type. It has been observed in Ge and Si that defect stability is affected by the defect charge state, thereby producing radiation effects which are quite different in n- and p type samples of the same materials. Exploring these differences in the II-VI system is impossible. It is possible, however, to gain some understanding of the charge-state effects by studying ZnTe, the only II-VI which is strongly p-type. Furthermore, at the beginning of this work effort, no radiation effects had been performed on this substance. We therefore will begin this section with a discussion of the work done under this contract on ZnTe. This will be followed by a discussion of radiation effects studies on CdS, ZnO and ZnS.

2.3.1.1 Radiation Damage in ZnTe

Since ZnTe had not been previously investigated, it was important to determine the displacement thresholds. This was done by irradiating single-crystal samples, which were cooled to near L.He temperature, with electrons

of various energies and measuring the effect of this irradiation by monitoring changes in the ZnTe cathodoluminescence.[13] The near-band-edge cathodoluminescent intensity was observed to increase with increasing beam energy as shown in Fig. 2-20. Figure 2-21 shows a typical low-resolution cathodoluminescent spectrum before and after 249 keV electron irradiation to a fluence of 1.2×10^{18} e/cm^2.

A displacement threshold can be derived from the data in Fig. 2-20 by using the relation

$$\frac{dI}{d\phi} \propto \bar{n}(E) \propto (E - E_d)^2$$

where $dI/d\phi$ is the initial slope in Fig. 2-20 at each irradiation-electron-beam energy E, $\bar{n}(E)$ is the average number of displaced atoms per electron, and E_d is the electron-beam energy corresponding to the threshold. From the above relation, a plot of $(dI/d\phi)^{1/2}$ vs E yields a straight line as shown in Fig. 2-22. We take the intercept, $E_d = 185 \pm 5$ keV, as the displacement threshold. This electron-beam energy corresponds to an atomic lattice-atom recoil energy of 7.35 eV for a Zn displacement, or 3.75 eV for Te displacements. We can identify the atomic species displaced as Zn for the reasons outlined below.

(1) The mass of the Te atom is approximately twice that of the Zn atom. We would expect, therefore, that the lowest threshold observed should belong to the Zn atom.

(2) Recoil energies for anions in the other II-VI compounds fall between 7.8 and 8.7 eV.[14] If the observed threshold corresponded to Te displacements, then the Te recoil energy would be approximately a factor of 2 too low as compared to other II-VI compounds.

(3) The energy required to displace an atom in a lattice should be related to the lattice bond energy since this energy is the dominant term in any calculation of displacement thresholds from first principles. Figure 2-23 shows a graph of estimated bond energy vs. cation recoil energy, T_d, for a number of

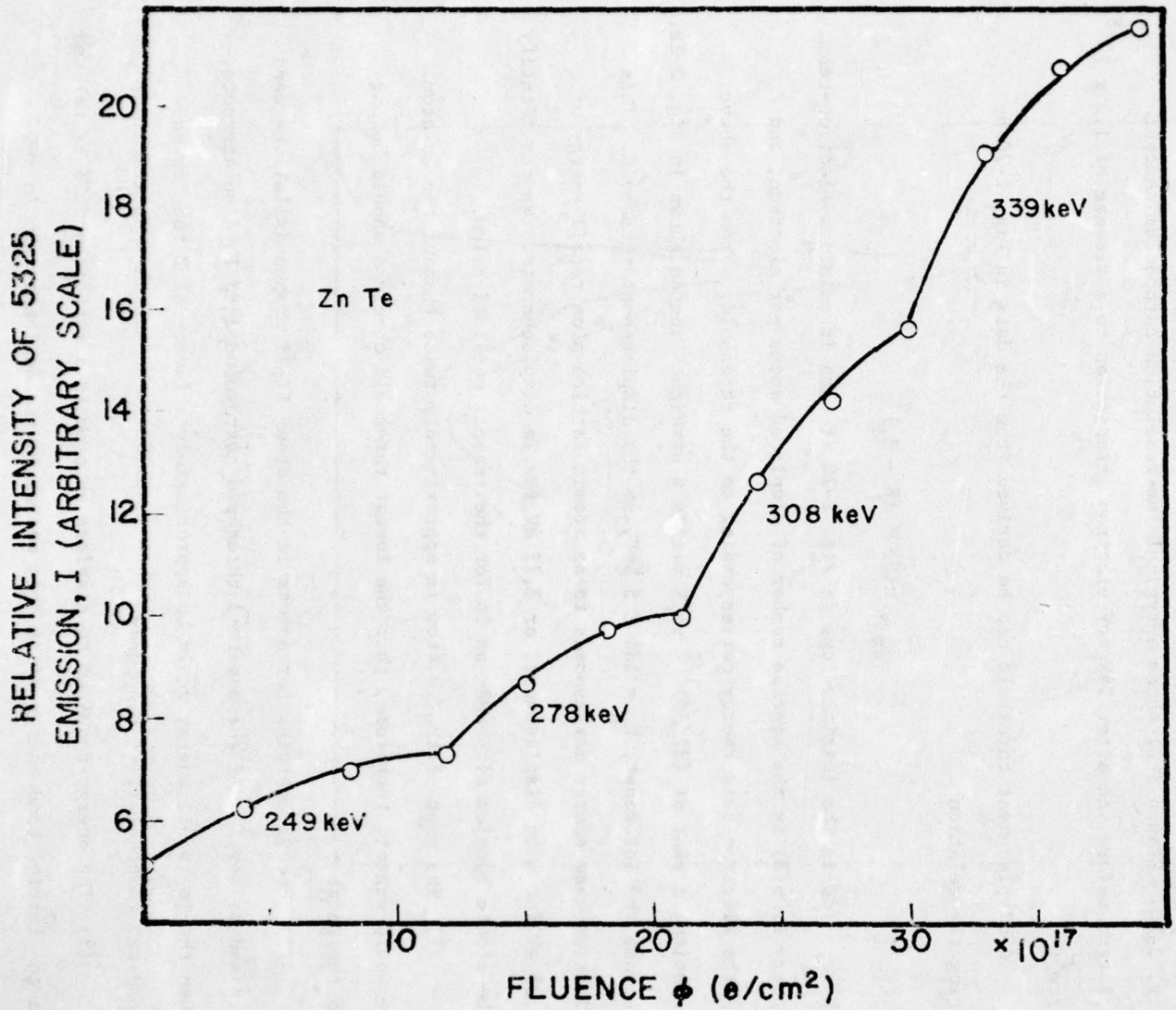

Fig. 2-20. Increase in the 5325Å luminescence as a function of electron irradiation near L.He. temperature.

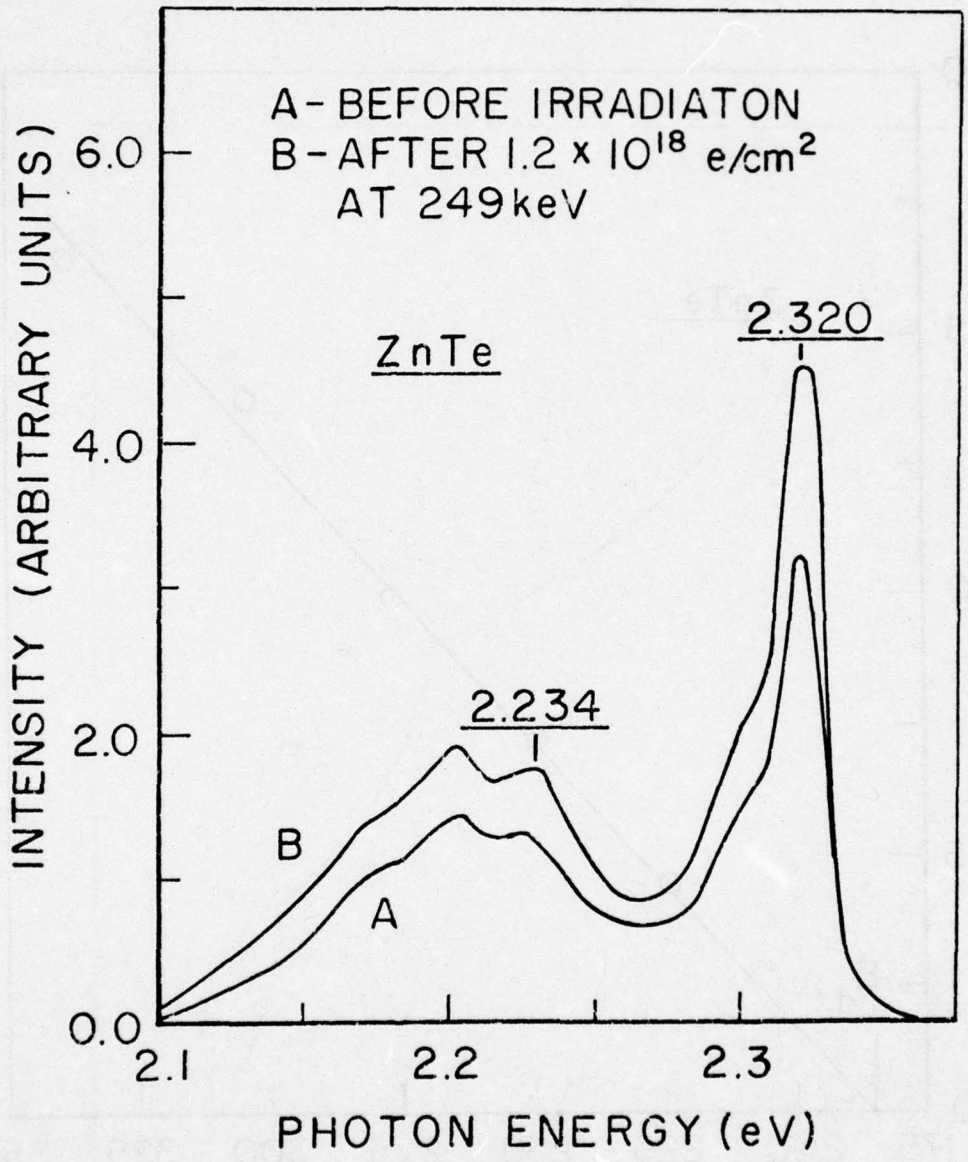

Fig. 2-21. Low-resolution cathodoluminescence spectra near band edge in ZnTe.

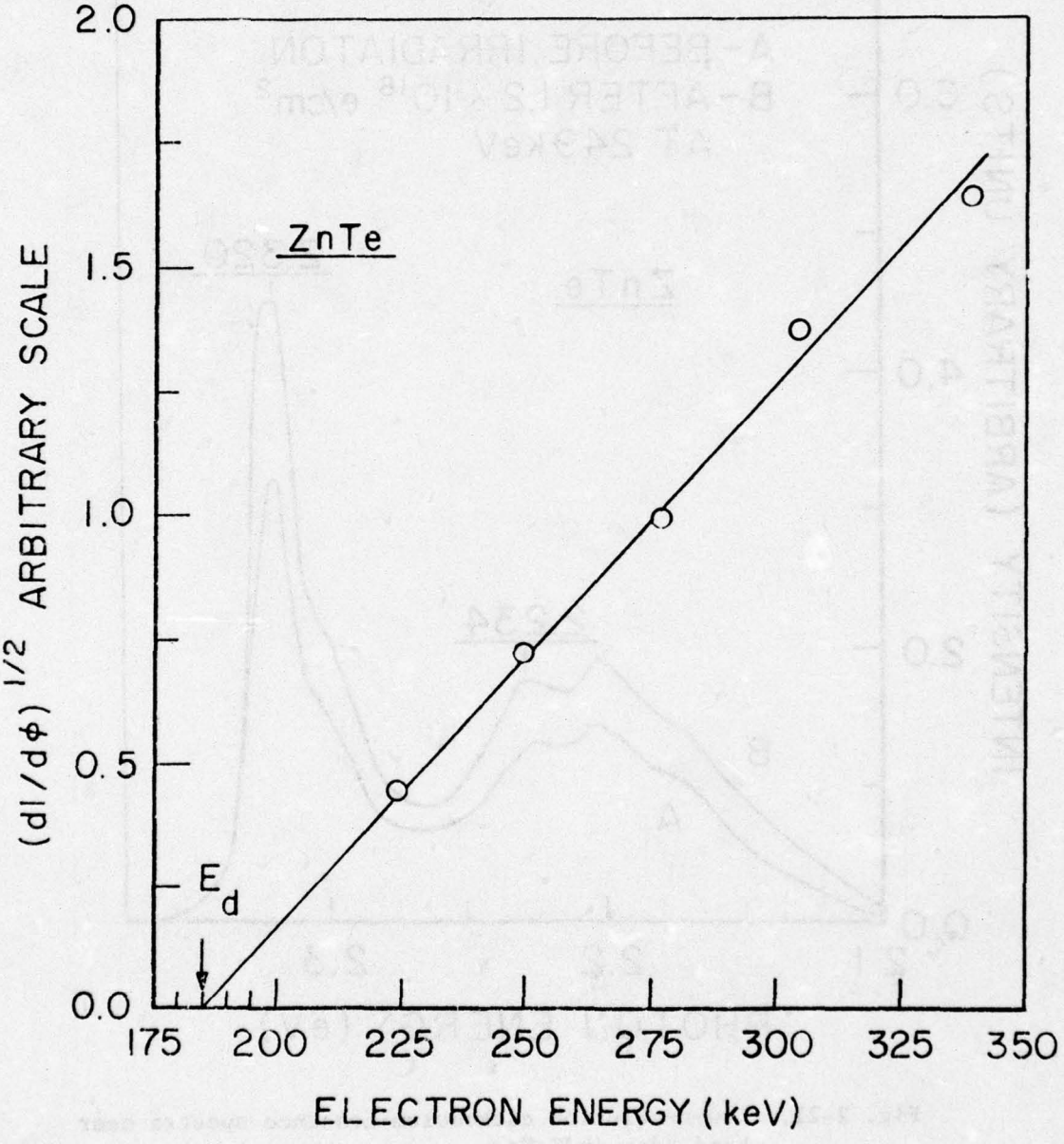

Fig. 2-22. Square root of production rate vs. electron energy of 2.320 eV transition.

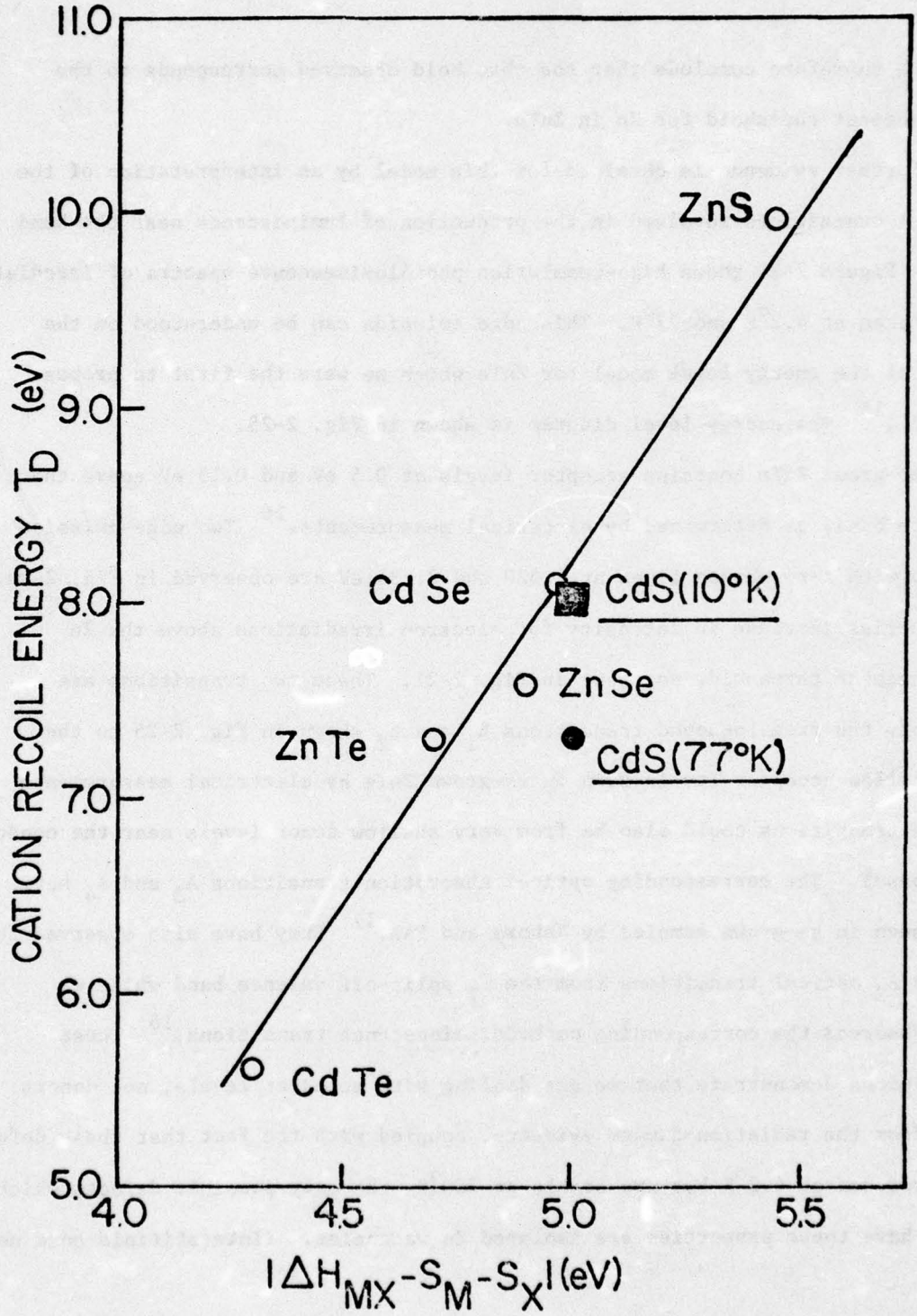

Fig. 2-23. Cation-recoil energy vs. lattice-band energy for several II-VI compounds.

II-VI compounds. Our value of 7.35 eV for Zn displacements fits this trend well.

We therefore conclude that the threshold observed corresponds to the displacement threshold for Zn in ZnTe.

Further evidence is obtained for this model by an interpretation of the optical transitions involved in the production of luminescence near the band edge. Figure 2-24 shows high-resolution photoluminescence spectra of irradiated ZnTe taken at 4.2°K and 77°K. This edge emission can be understood on the basis of the energy level model for ZnTe which we were the first to propose in 1971.[15] The energy level diagram is shown in Fig. 2-25.

As-grown ZnTe contains acceptor levels at 0.5 eV and 0.15 eV above the valence band, as determined by electrical measurements.[16] Two edge-emission series with zero phonon lines at 2.320 and 2.234 eV are observed in Fig. 2-24. Both series increase in intensity for electron irradiations above the Zn displacement threshold, as shown in Fig. 2-21. These two transitions are probably the free-to-bound transitions E_1 and E_2 shown in Fig. 2-25 to the two shallow acceptor levels seen in as-grown ZnTe by electrical measurements. (These transitions could also be from very shallow donor levels near the conduction band). The corresponding optical absorption transitions A_3 and A_4 have been seen in as-grown samples by Nahory and Fan.[17] They have also observed the A_1 and A_2 optical transitions from the Γ_7 split-off valence band while we have observed the corresponding cathodoluminescence transitions.[18] These transitions demonstrate that we are dealing with acceptor levels, not donors.

From the radiation-damage evidence, coupled with the fact that these defects are produced at 4.2°K but are stable at 300°K, the only possible defects which could have these properties are isolated Zn vacancies. (Interstitials have now

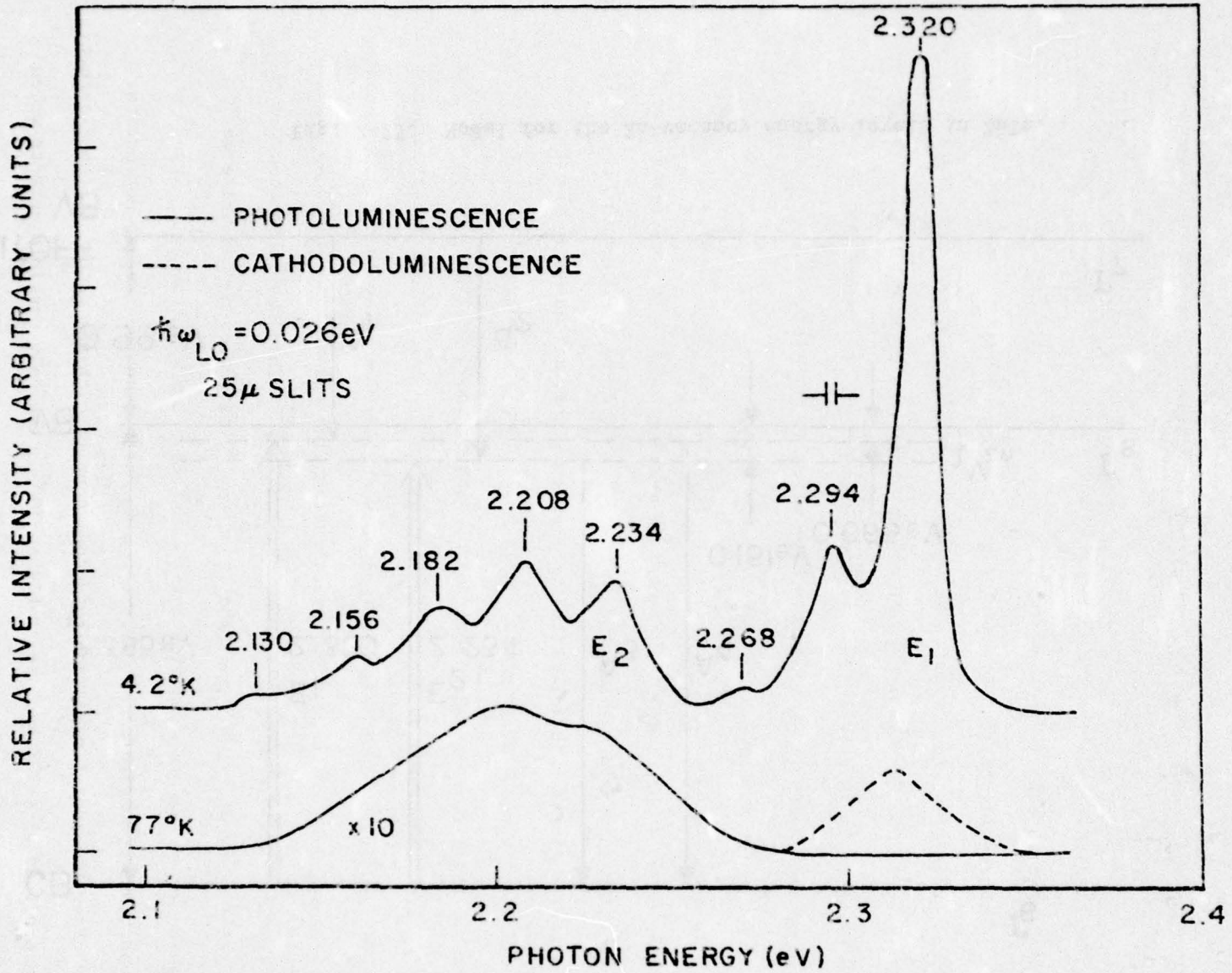

Fig. 2-24. High-resolution photoluminescence of ZnTe edge emission at 4.2°K and 77°K.

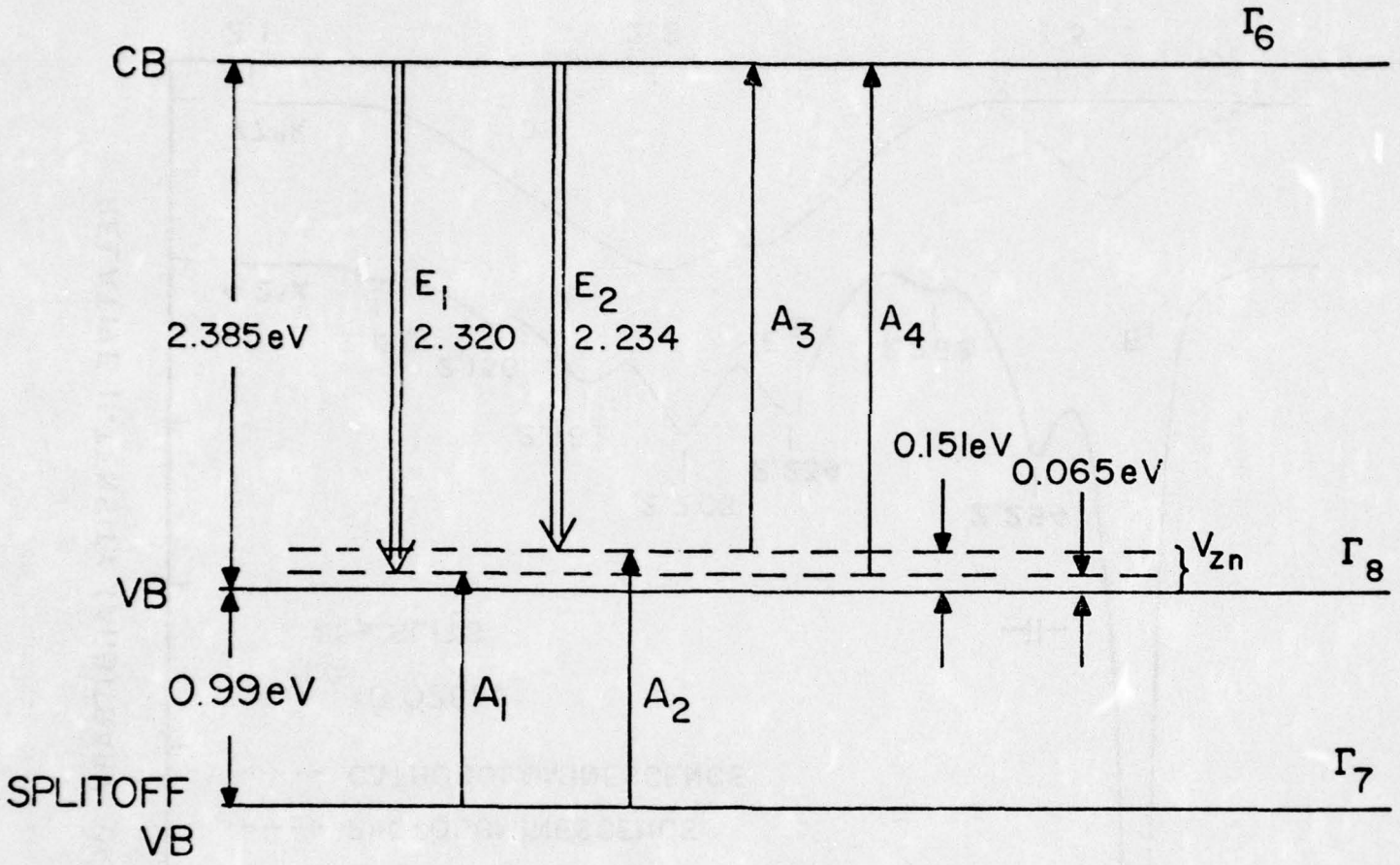

Fig. 2-25. Model for the Zn-vacancy energy levels in ZnTe.

been shown to migrate above 77°K but below room temperature in most of the II-VI compounds).

We can now make the following important conclusions about ZnTe:

(1) ZnTe is always p-type due to an excess of Zn-vacancy shallow acceptor levels (double acceptor with both levels near the valance band) which exist in as-grown ZnTe.

(2) Electron irradiation above the Zn displacement threshold of 185 keV (T_d = 7.35 eV) increases the concentration of these Zn vacancies and hence the room-temperature hole conductivity (as we have observed).

(3) The green edge-emission, which dominates the luminescence spectra of ZnTe at 4.2°K, is due to the presence of Zn vacancies in the lattice after crystal growth.

(4) The zinc vacancy in ZnTe is stable at room temperature in contrast to the behavior of vacancies in the elemental semiconductors which generally migrate below room temperature.

Subsequent studies on ion-implanted ZnTe have modified the above model in detail but not in substance.[19-21] The 4.2°K photoluminescence of ZnTe was monitored as a function of isochronal annealing in an argon atmosphere. Typical spectra before and after 300°C ischronal annealing is shown in Fig. 2-26. The relative intensities of the luminescence transitions as a function of anneal temperature is shown in Fig. 2-27. The temperature dependence of these transitions is shown in Fig. 2-28. All as-grown samples exhibit a strong exciton line at 5320Å(I_1) and two edge emission series, the first at 5318Å(A_1) and the second at 5543Å(B). The A_1 and B transitions are related to the two transitions described above.

After 300°C annealing, a marked increase is noted in the intensity of I_1 and the B series transitions. In addition, all samples exhibit a new A-series line (A_o) at 5300Å. The temperature dependence of the A-series

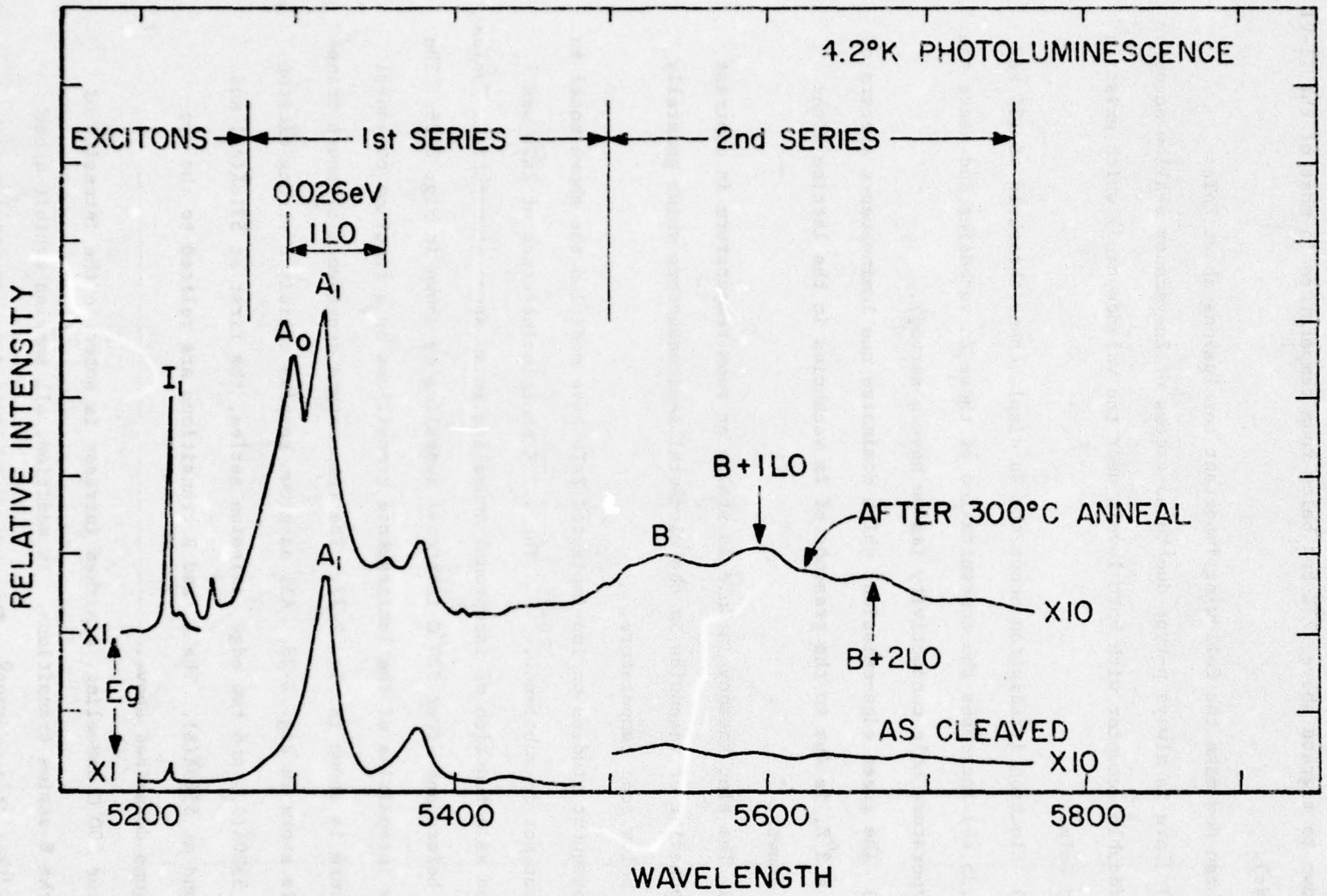

Fig. 2-26. Edge emission showing effects of 300°C argon anneal.

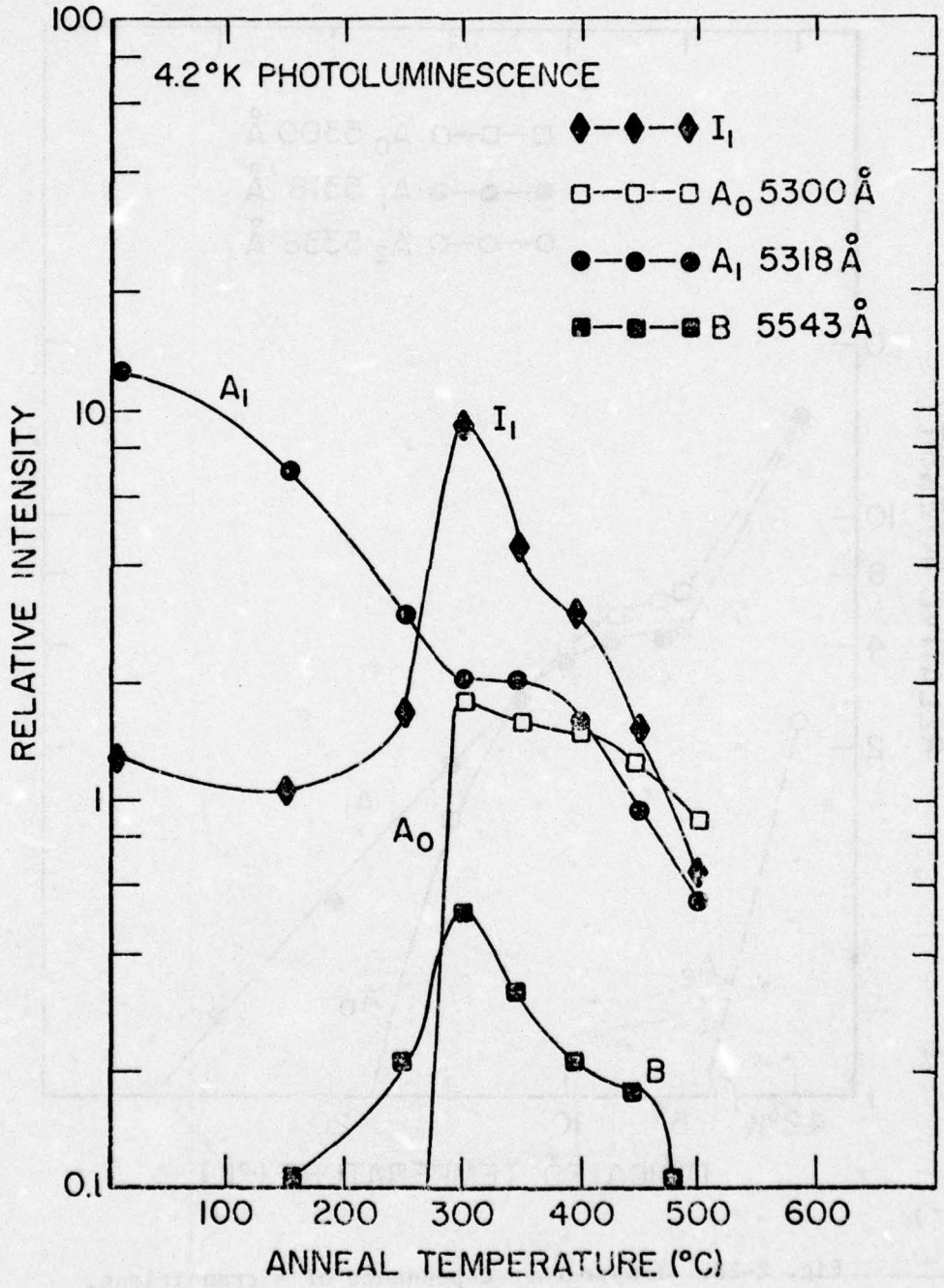

Fig. 2-27. Annealing of various transitions defined in Fig. 2-26.

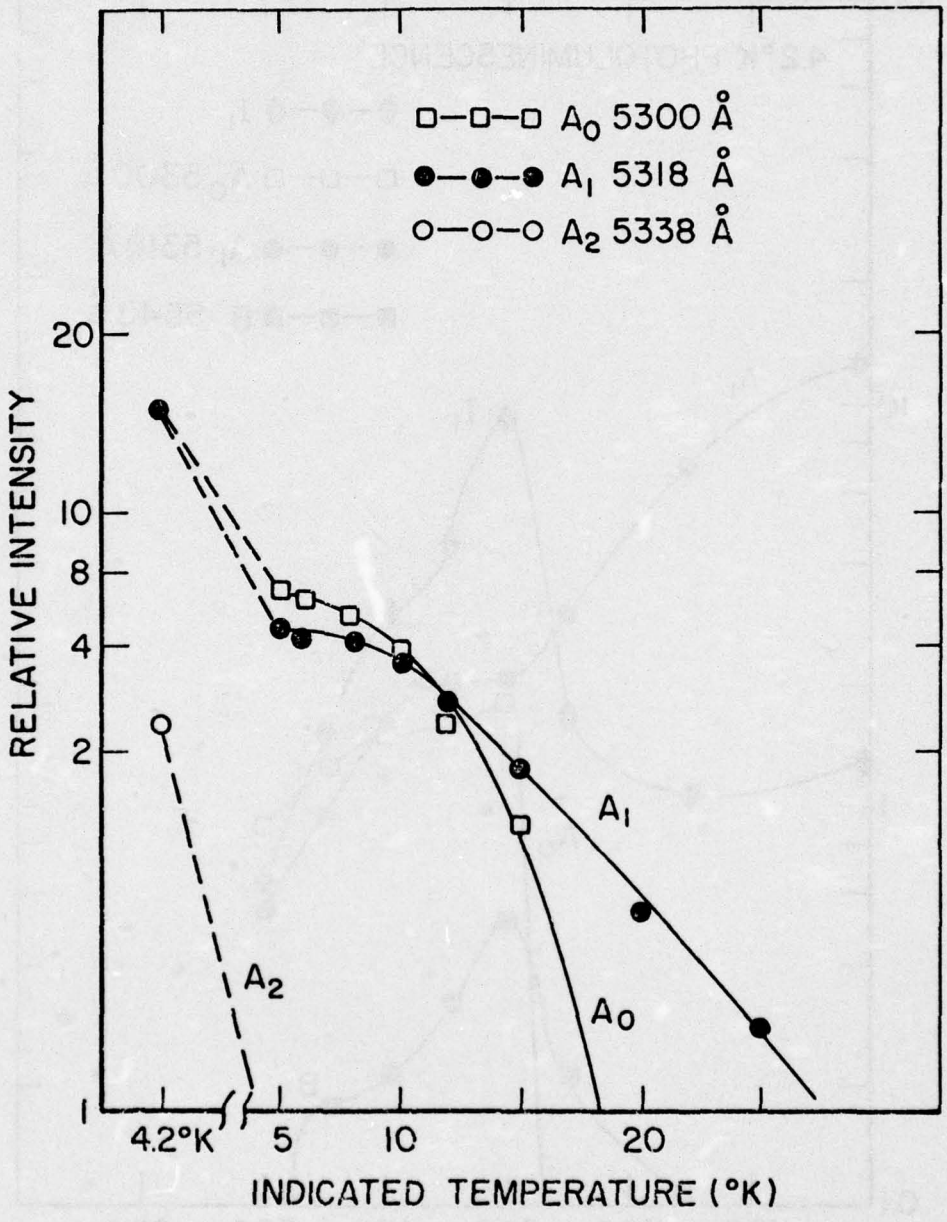

Fig. 2-28. Temperature dependence of A transitions.

transitions, and a possible exciton line at 5218Å, indicate that two shallow acceptors are involved (corresponding to the 0.05 eV level mentioned previously) with ionization energies of 0.052 eV and 0.060 eV. These values correspond to those found by electrical measurements which have been attributed to the first ionization level of the zinc vacancy and to a Group I substitutional acceptor. This close proximity of vacancy shallow levels and substitutional impurity levels of the same electrical type (donor and acceptor), will be shown to be a reoccurring theme in the nature of isolated lattice defects in II-VI compounds. This proximity has led to considerable confusion in the II-VI literature when dealing with the separate identification of isolated lattice defects and substitional impurities.

ZnTe samples, ion implanted with 90 keV Cd, Ar, and Xe ions at room temperature with fluences from 10^{12} to 10^{15} ions/cm^2, have also been investigated. Photoluminescence was measured at 4.2°K as a function of 10 min. isochronal anneals in flowing Ar. None of the samples show luminescence after a dose of 3×10^{12} ions/cm^2. Complex recovery of the edge emission is observed between 300-500°C. A broad band at 5900Å was produced at the low end of this temperature range but disappeared completely after annealing to 500°C. Samples implanted with 3×10^{13} to 4×10^{14} Cd^{112}/cm^2 exhibit exciton emission at 5293Å after 300-400°C anneals; this was not found in any of the cleaved samples or in those samples implanted with Ar or Xe. Samples implanted with Cd^{114} suggest another exciton line at 5287Å which appears to be an isotope shift of unexplained nature.

The appearance of the Cd exciton lines, the broad radiation-damage band at 5900Å, and the two shallow acceptor levels in the 0.05 eV range, which are enhanced as a result of annealing in an inert atmosphere, all suggest that

considerably more information concerning the nature of acceptor levels in II-VI compounds can be obtained by further study of ZnTe.

2.3.1.2 Radiation Damage in CdS

A considerable effort on this contract has been devoted to understanding the nature of radiation produced defects in CdS. The reasons for this effort are twofold. First, CdS is a useful device material both as a thin-film photodetector in the visible and also as a thin-film solar-cell material. Second, the understanding of the materials properties of CdS is far advanced over that of most of the II-VI's. It therefore holds an important place in obtaining a general understanding of II-VI semiconductors.

As mentioned in a previous section, a discrepancy existed between the displacement threshold measurements of Kulp et. al.[7] and those of Bryant and Cox.[12] Both groups had observed the production of a luminescent band at 1.03μm by electron irradiation but Kulp claimed that the threshold for this production was at 290 keV and represented Cd displacements while Bryant and Cox supported the view that the threshold for the production of the 1.03μm band was 125 keV and represented S displacements.

These experiments cast considerable doubt concerning the measurement of the energy required for cadmium displacements in CdS. For these reasons additional experiments were undertaken.[5] These measurements were made near L.He temperature in contrast to Kulps work, which was near L.N_2 temperature. Typical before- and after-irradiation cathodoluminescence spectra, taken at $5^{o}K$, are shown in Fig. 2-29. Figure 2-29(A) is the spectrum before irradiation, Fig. 2-29(B) the spectrum after 400 keV irradiation to a fluence of $1.89 \times 10^{17} e/cm^2$, and Fig. 2-29 (C), after a room-temperature anneal. The 1.03μm band is apparent after irradiation but shows considerable annealing at room temperature. The series of bands in the 1.6-2.2μm region have been attributed to the internal transitions between levels of substitutional Cu^{2+}.[22]

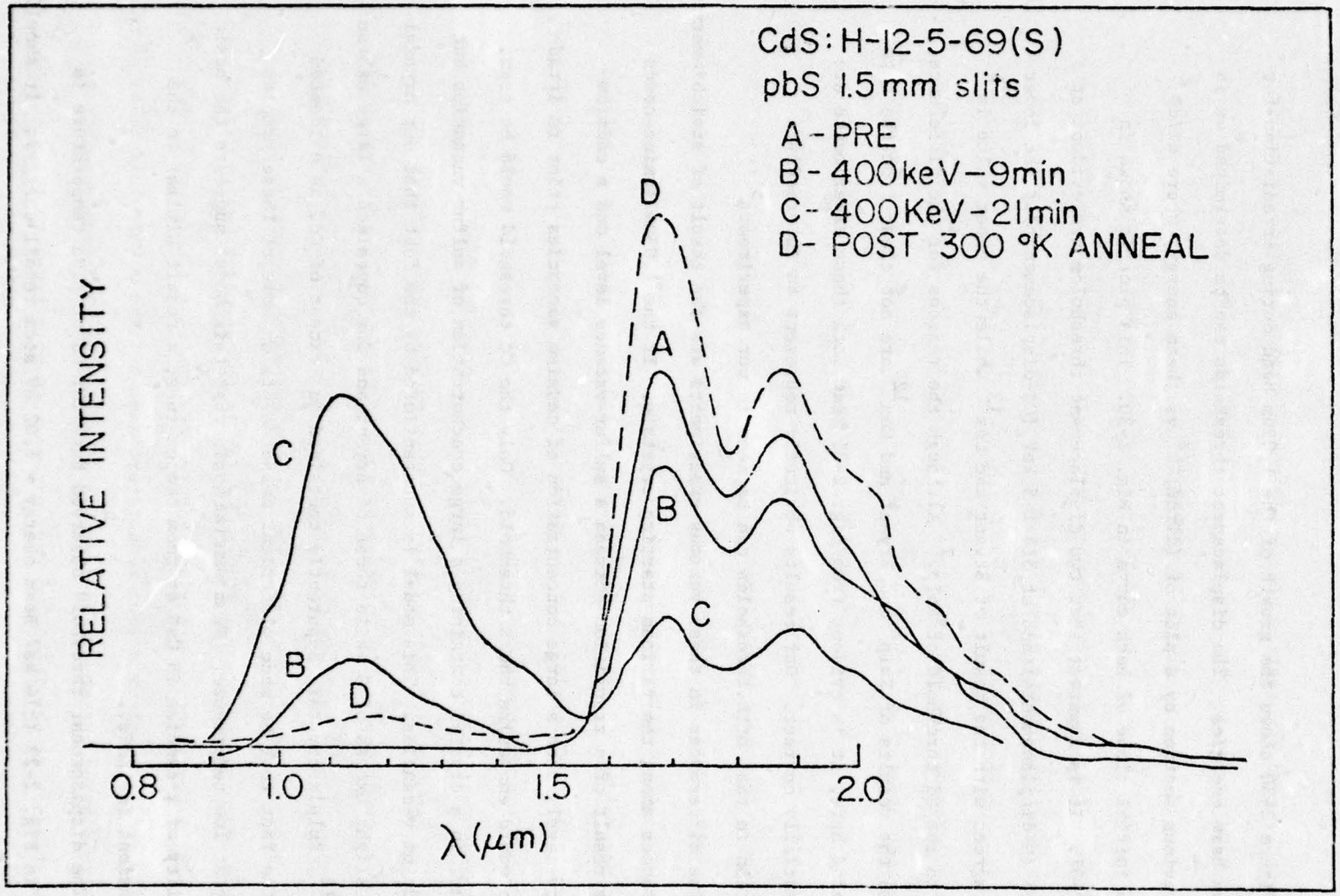

Fig. 2-29. IR cathodoluminescence spectra for CdS as a function of irradiation and room-temperature annealing.

Figure 2-30 shows the growth of the 1.03μm band during irradiation for various beam energies. The displacement thresholds can be determined as in the previous section by a plot of $(dI/d\phi)^{1/2}$ vs. beam energy, where $dI/d\phi$ is the initial slope of each curve in Fig. 2-30. This plot is shown in Fig. 2-31. It is apparent that two displacement thresholds are evident at 125 keV (S-displacements) and at 314 ± 5 keV (Cd-displacements). The lower value agrees with the result of Bryant and Cox[12] while the upper value is close to the Cd threshold of Kulp.[7] Although the reasons for the difference between the results of Kulp[7] and Bryant and Cox[12] are not clear from the data presented here, it is evident from Fig. 2-31 that both these experiments are substantially correct. Our results obviously represent an intermediate situation in that both thresholds can be seen in our experiment.[5]

The differences in these various experiments are the result of stoichiometry differences among the various starting crystals. If the 1.03μm luminescence is the result of a transition between a sulfur-vacancy level and a cadmium-vacancy level, then a large concentration of cadmium vacancies prior to irradiation would emphasize the S threshold. Only the Cd threshold would be seen, however, in a crystal containing a large concentration of sulfur vacancies but no cadmium vacancies. This model is substantiated by the fact that our crystal had a slight excess of S while those of Bryant and Cox contained a large excess of S.[12] Kulp's crystals apparently contained an excess of Cd, as evidenced from the fact that he made electrical measurements on some of these samples easily at low temperaure. We emphasize again that this model suggests the basic stability of vacancies in CdS at room temperature, a result similar to the conclusions for ZnTe.

The displacement threshold observed here for Cd at L.He temperature is shown in Fig. 2-23 (314 keV Beam energy = 8.02 eV atom recoil energy). It should

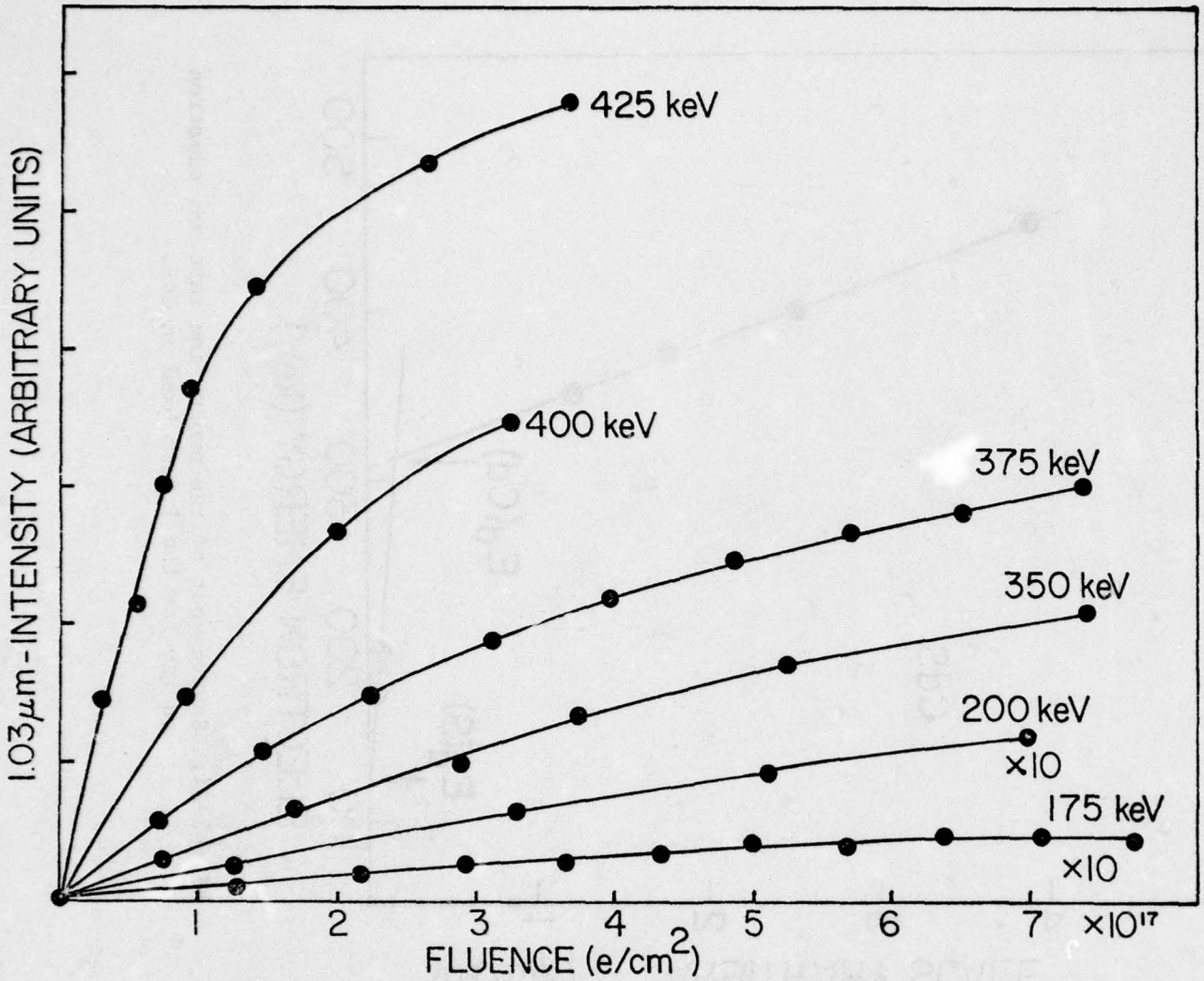

Fig. 2-30. Production of the 1.03μm band in CdS as a function of fluence for various electron-irradiation energies.

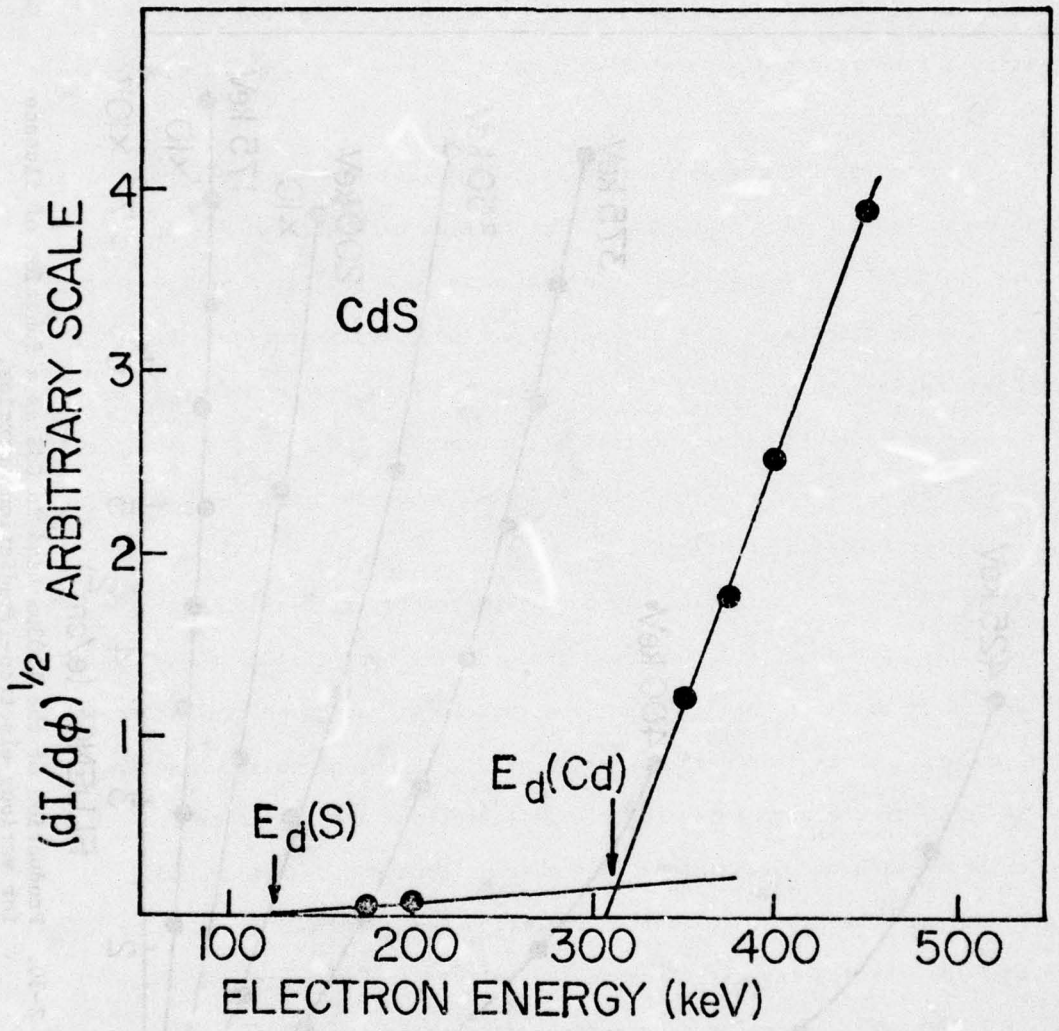

Fig. 2-31. Square root of the production rate vs. electron energy for the 1.03μm band in CdS.

be noted that both Kulp's old value at 77°K and our newer one fit the lattice bond model well. The 77°K threshold is lower, however, than that at 10°K, suggesting a temperature-dependent displacement threshold as has been observed in other semiconductors.

The above model for the production of 1.03μm luminescence presupposes that cadmium vacancies are deep acceptors (this has been demonstrated for Zn vacancies in ZnSe[23]) and that the sulfur vacancies are shallow donors. Further evidence for the donor nature of the sulfur vacancy, its migration energy, thermal ionization energy, etc., will be presented from low-temperature luminescence experiments and electrical measurements. A defect misidentification by Kulp and Kelley[3] for the 7200Å band will also be demonstrated as well as a second misidentification by Kikuchi.[24]

Figure 2-32 shows typical emission spectra, before irradiation, near the CdS band edge for undoped (U), Cd-doped (Cd), and S-doped (S) CdS platelets, taken at 7°K. The I_1, I_2 and I_3 lines are excitons bound to neutral acceptors, neutral donors, and ionized donors respectively. The broad emission series at 5140Å is known as the edge emission (see ZnTe section) and is due to free-to-bound or bound-to-bound transitions in general. Both photo- and cathodo-luminescence have been used to monitor radiation damage in CdS at 10°K for electron-beam energies capable of producing sulfur displacements only ($125 \leq E \leq 300$ keV), or sulfur plus cadmium displacements ($E \geq 300$ keV).

Plots of the 10°K bound-exciton luminescence in general show that the intensity decays according to the relation $I/I_o \propto \phi^{-1}$ for large fluence, ϕ (see Fig. 2-33). This decrease is probably due either to a disturbance of the surface states by irradiation or an increase in optical-absorption band tailing. Also seen in Fig. 2-33 is an increase in the intensity of a new bound-exciton line, I_R at 4867Å, for 250 keV irradiations at < 10°K (between the thresholds),

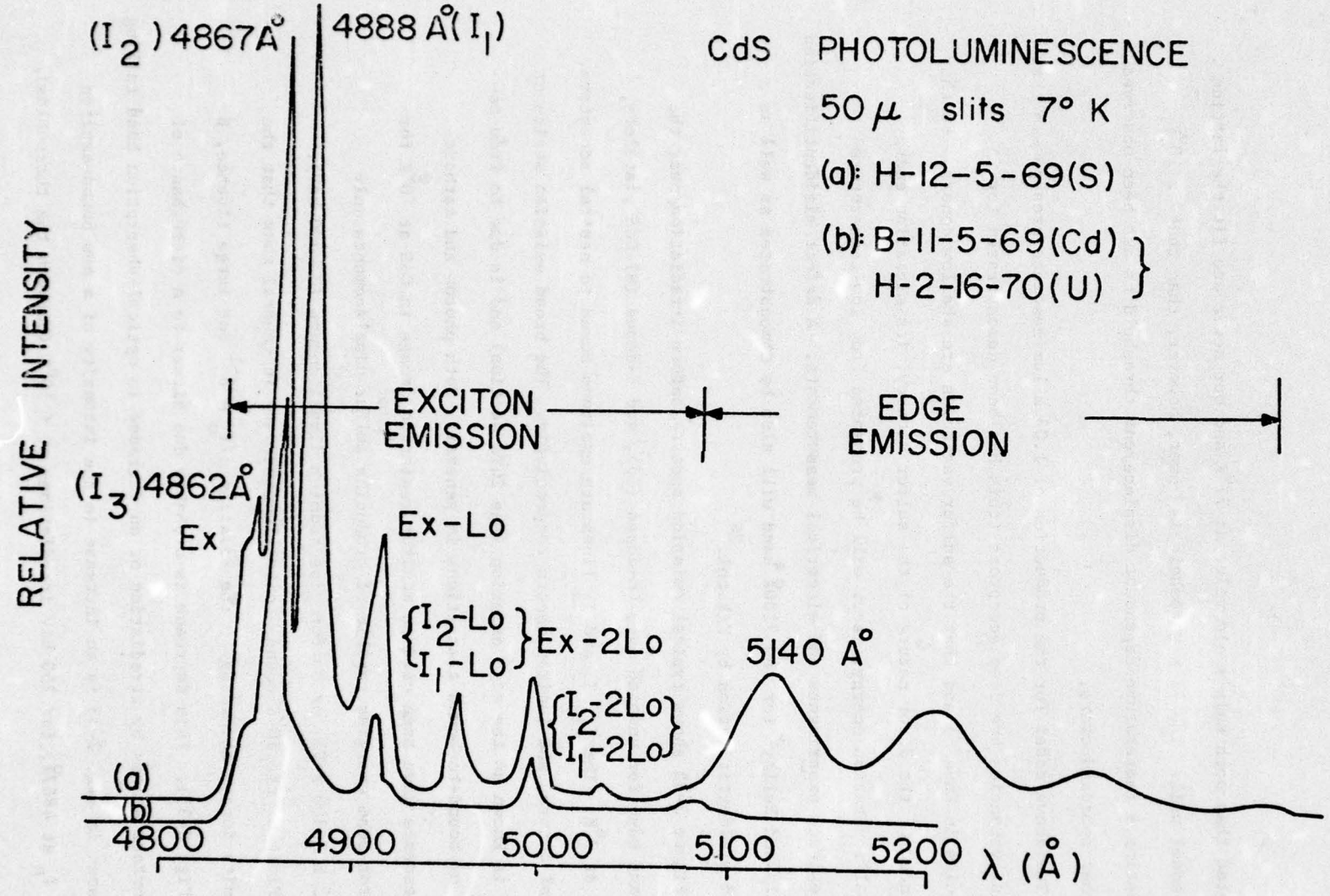

Fig. 2-32. Pre-irradiation spectra near the band edge for (a) excess sulfur, and (b) excess cadmium or undoped CdS platelets.

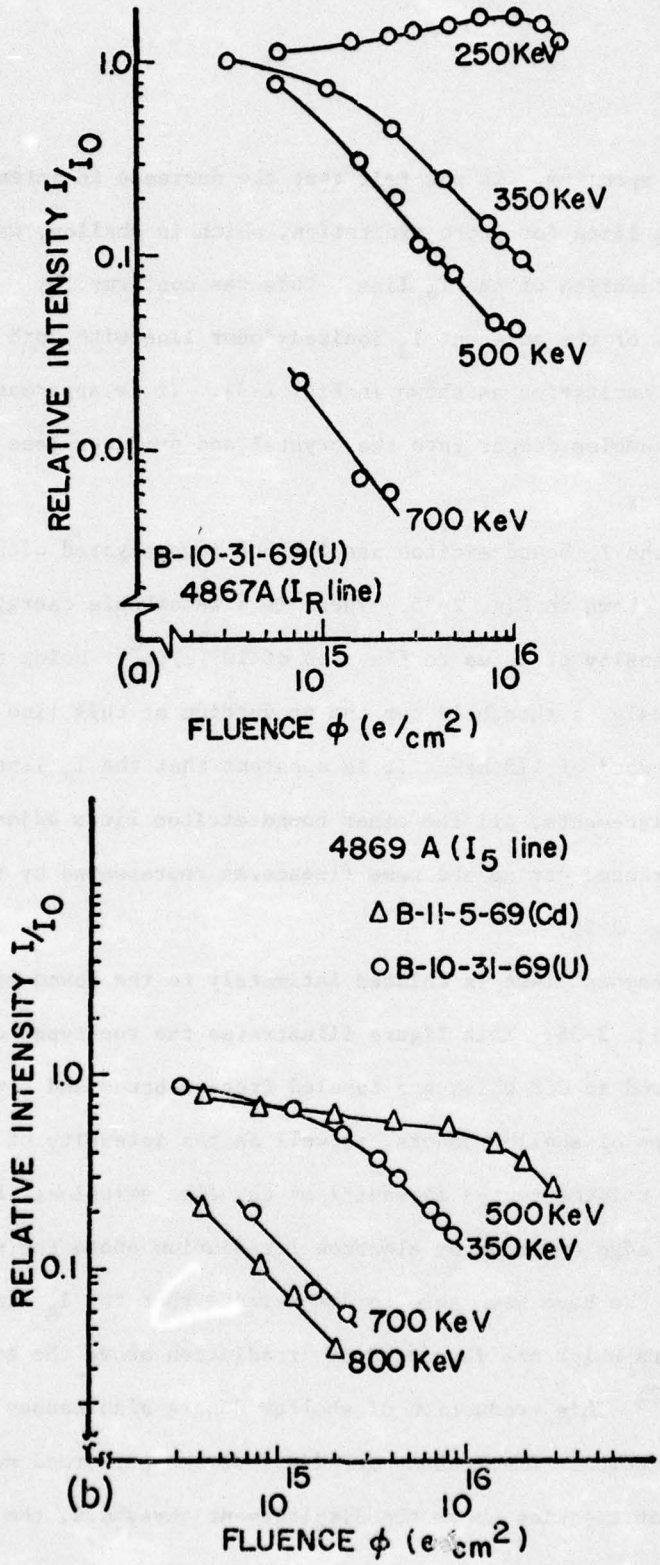

Fig. 2-33. Decay of bound-exciton line intensity with irradiation in CdS.

in the photoluminescent spectrum. It was felt that the decrease in intensity of all the bound exciton lines for photo excitation, which is shallow, was probably masking the production of the I_R line. This was confirmed by monitoring the intensity of the adjacent I_3 ionized-donor line with both electron-beam and photo excitation as shown in Fig. 2-34. It is apparent that the electron beam samples deeper into the crystal and produces less pronounced intensity decay.

The production of the I_R bound exciton was further investigated with cathodoluminescence, as shown in Fig. 2-35. There is a remarkable energy-dependent growth in intensity of I_R up to fluences of $10^{16} e/cm^2$. Using the same analysis as previously, a threshold for the production of this line is observed in the neighborhood of 115 keV. It is apparent that the I_R line is a result of sulfur displacements; all the other bound-exciton lines adjacent to the I_R line have decreased during the same fluence, as represented by the I_1 line intensity in Fig. 2-35.

The edge emission beyond 5140Å is related intimately to the bound-exciton emission, as shown in Fig. 2-36. This figure illustrates the two types of edge emission series found in CdS which are labeled free-to-bound and bound-to-bound. The concentration of shallow donors, as well as the intensity of bound-exciton donor lines, is related to the intensity of the edge emission. Figure 2-37 shows the growth of the edge emission by electron irradiation above the sulfur-displacement threshold. We have been able to demonstrate that the I_R line is related to shallow donors which are increased by irradiation above the sulfur-displacement threshold.[25] This production of shallow donors also causes an increase in the edge emission. Since these irradiations are performed near L.He temperature, and for energies above the displacement threshold, the sulfur

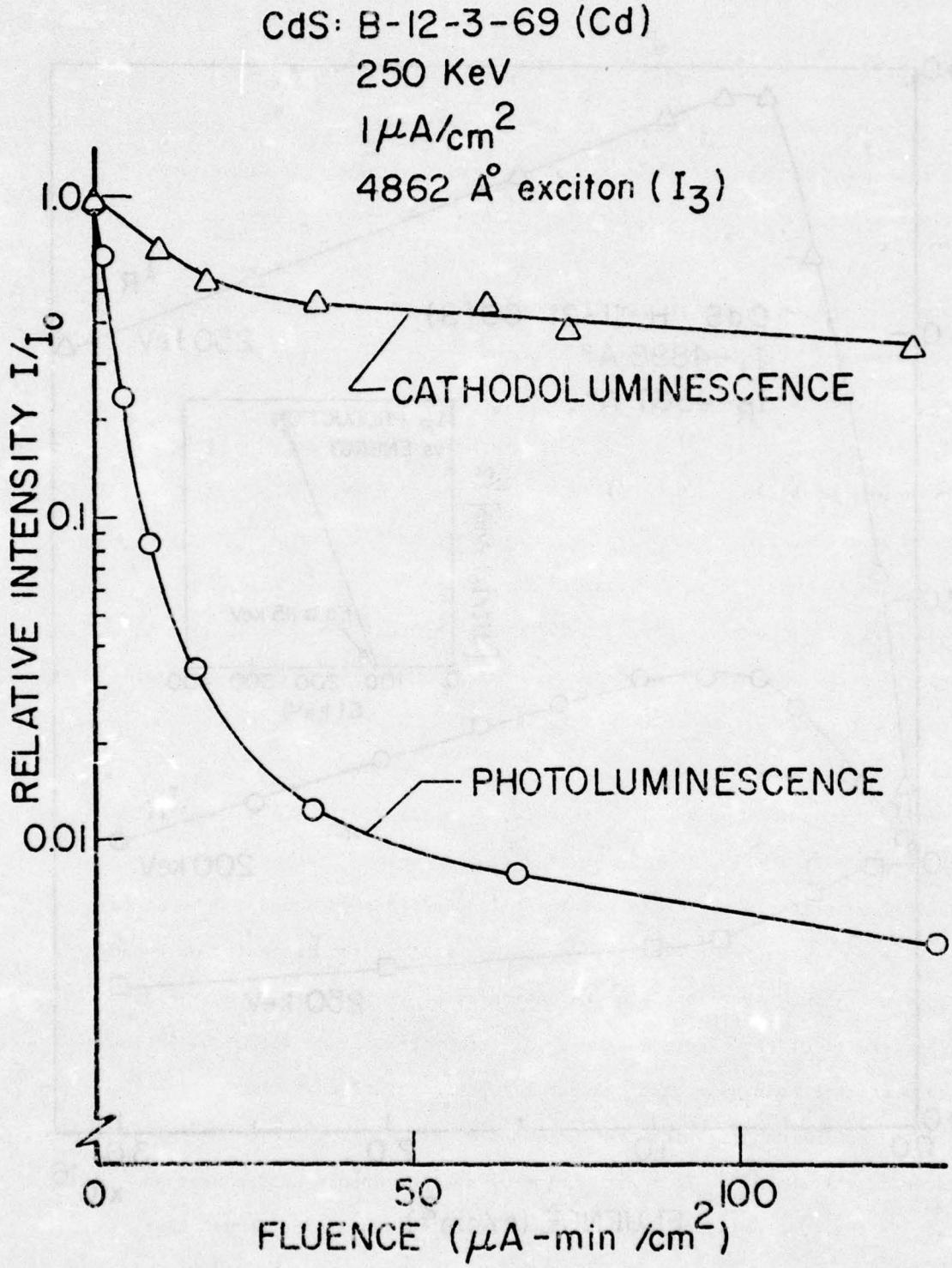

Fig. 2-34. Typical photo- and cathodo-luminescent decay with fluence.

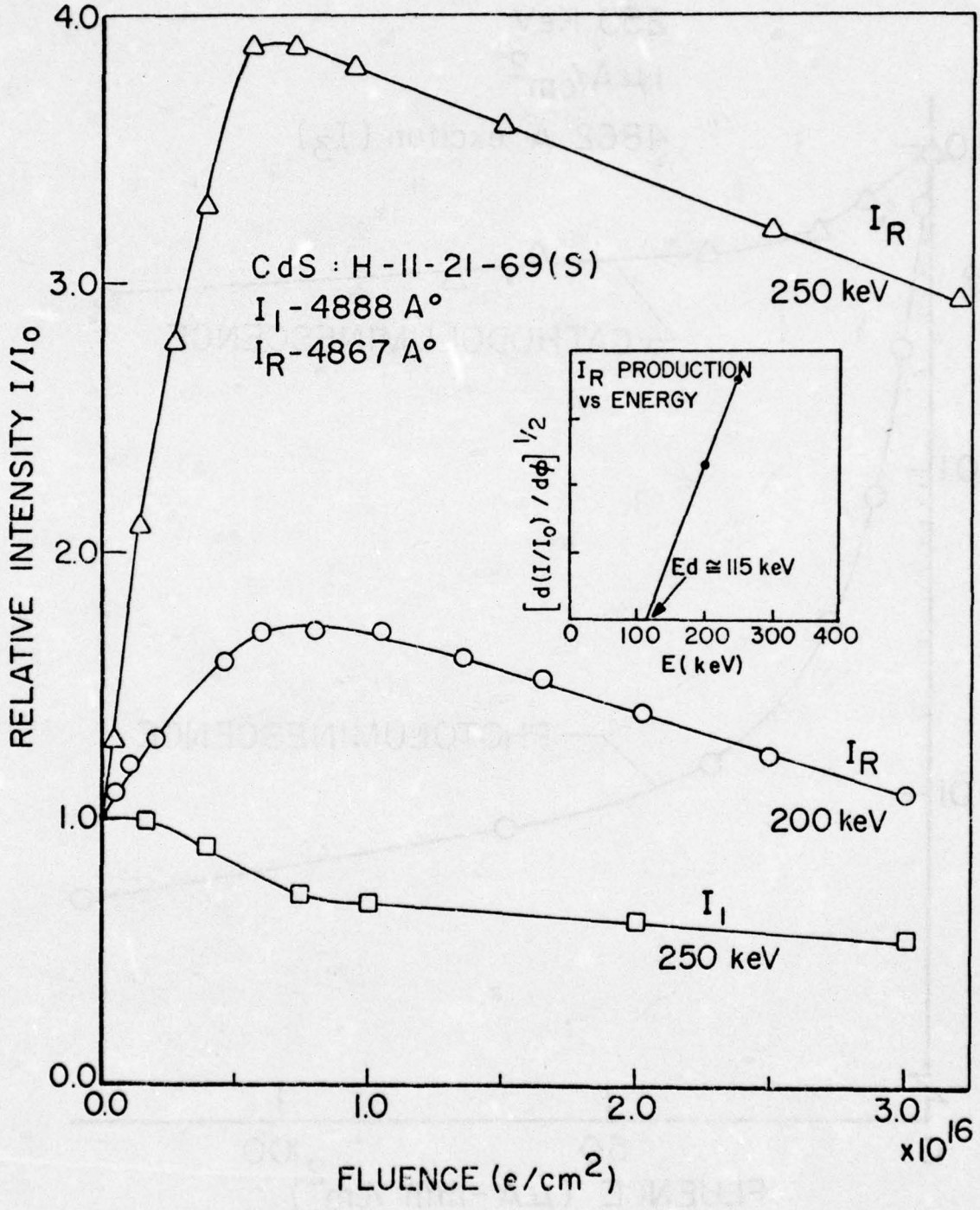

Fig. 2-35. Production of I_R bound exciton line in CdS.

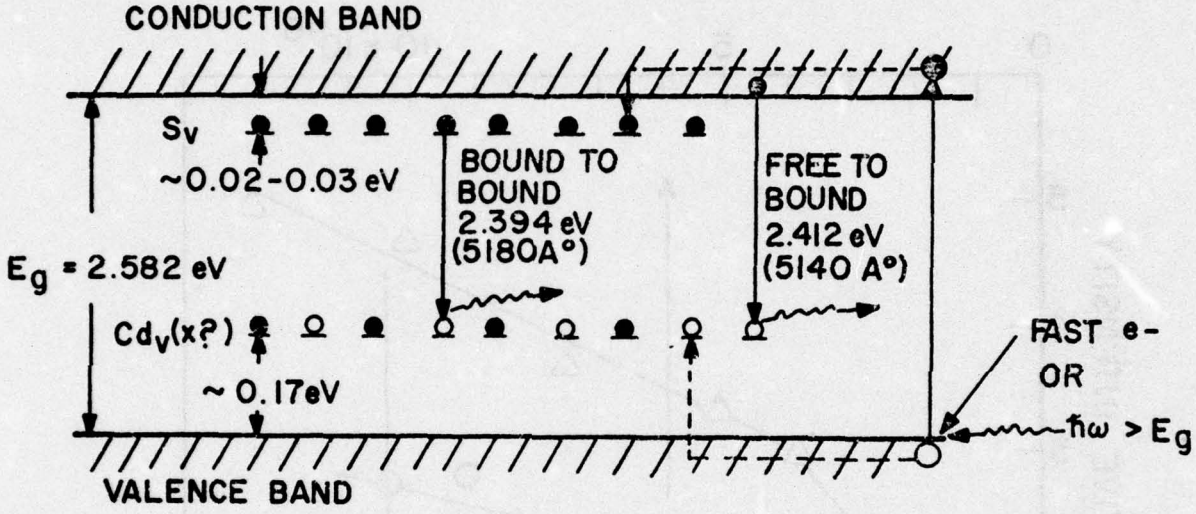

Fig. 2-36. Energy-level model for two edge-emission series in CdS.

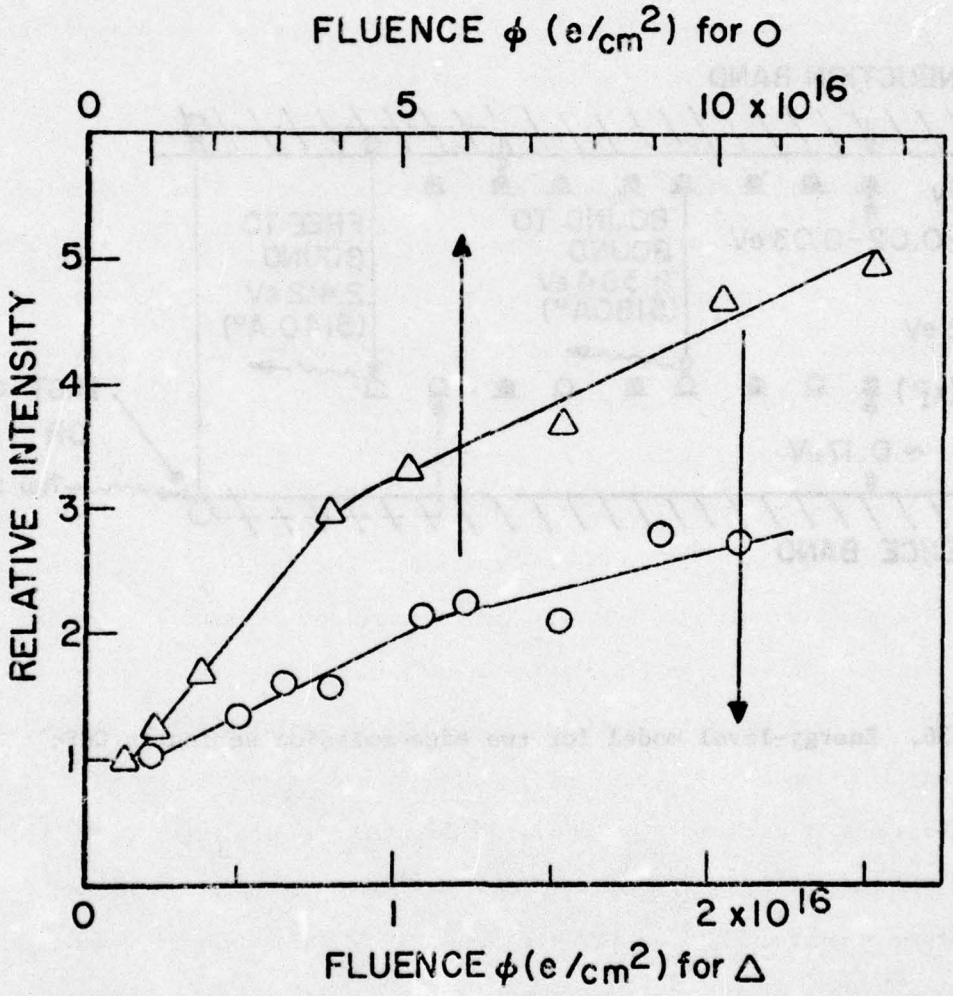

Fig. 2-37. Growth of cathodoluminescent edge emission in CdS with irradiation.

vacancy appears to be the best candidate for the shallow donor level (the S-interstitial should be neutral or an acceptor). An analysis of the exciton spectrum suggests that the donor level is about 0.03 eV below the conduction band.[25] It has further been observed by optical measurements that the production of the I_R line is possible at room temperature. Zeeman-effect studies on this line indicate that it is indeed a donor level line.

Several annealing stages have been studied in irradiated CdS.[25] Figure 2-38 indicates a recovery stage for the intensity of the bound-exciton line intensity at 180°K which can be shown to be related to the migration of sulfur sublattice defects (irradiation energy was less than Cd-threshold). In addition, a luminescence band at 7200Å is observed to be formed during this stage as shown in Fig. 2-39(a). This 7200Å band is again related to sulfur sublattice defects since it can be produced below the Cd threshold. The defect responsible for this emission appears to be a sulfur sublattice defect complexed in some way with impurities or other sites near the surface of the sample.[25] Its intensity is high for photoluminescence but very low for cathodoluminescence. Furthermore, it can be broken up by irradiation at 10°K and 200 keV as shown in Fig. 2-39(b). Kulp has attributed the 7200Å band to isolated sulfur vacancies.[3] This identification clearly is in error since the band cannot be produced at 4.2°K and since it is found as a result of annealing (defect migration). Kikuchi has suggested, on the basis of thermal neutron irradiation at room temperature, that the 7200Å band is the result of Cd vacancies, as shown in Fig. 2-40.[24] This clearly is also incorrect since this band is produced at energies below the Cd-displacement threshold, as seen in Fig. 2-39(b). The best evidence to date suggests the sulfur interstitial in a complex is the cause of this defect band.[25]

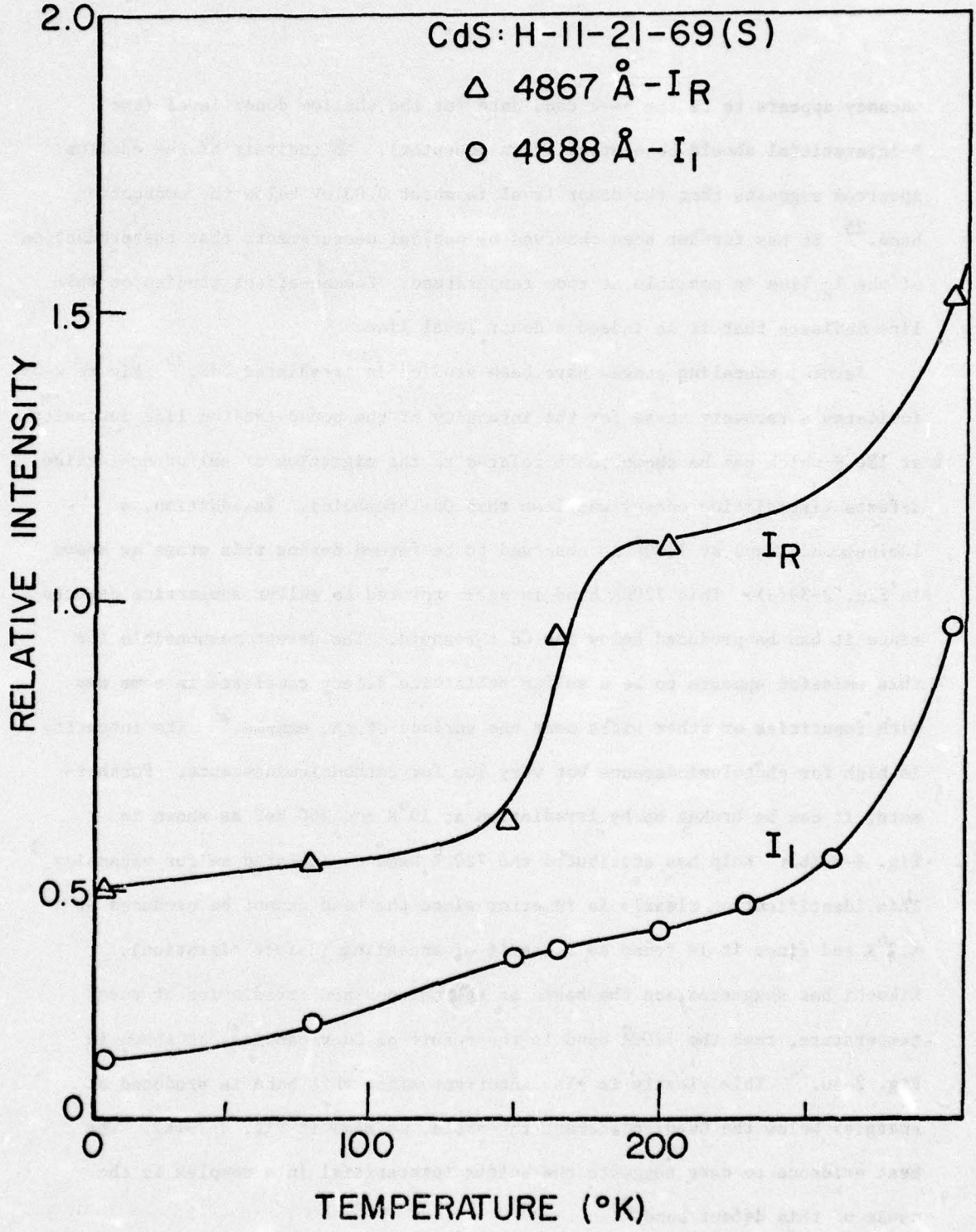

Fig. 2-38. Isochronal annealing of I_R and I_1 lines in CdS.

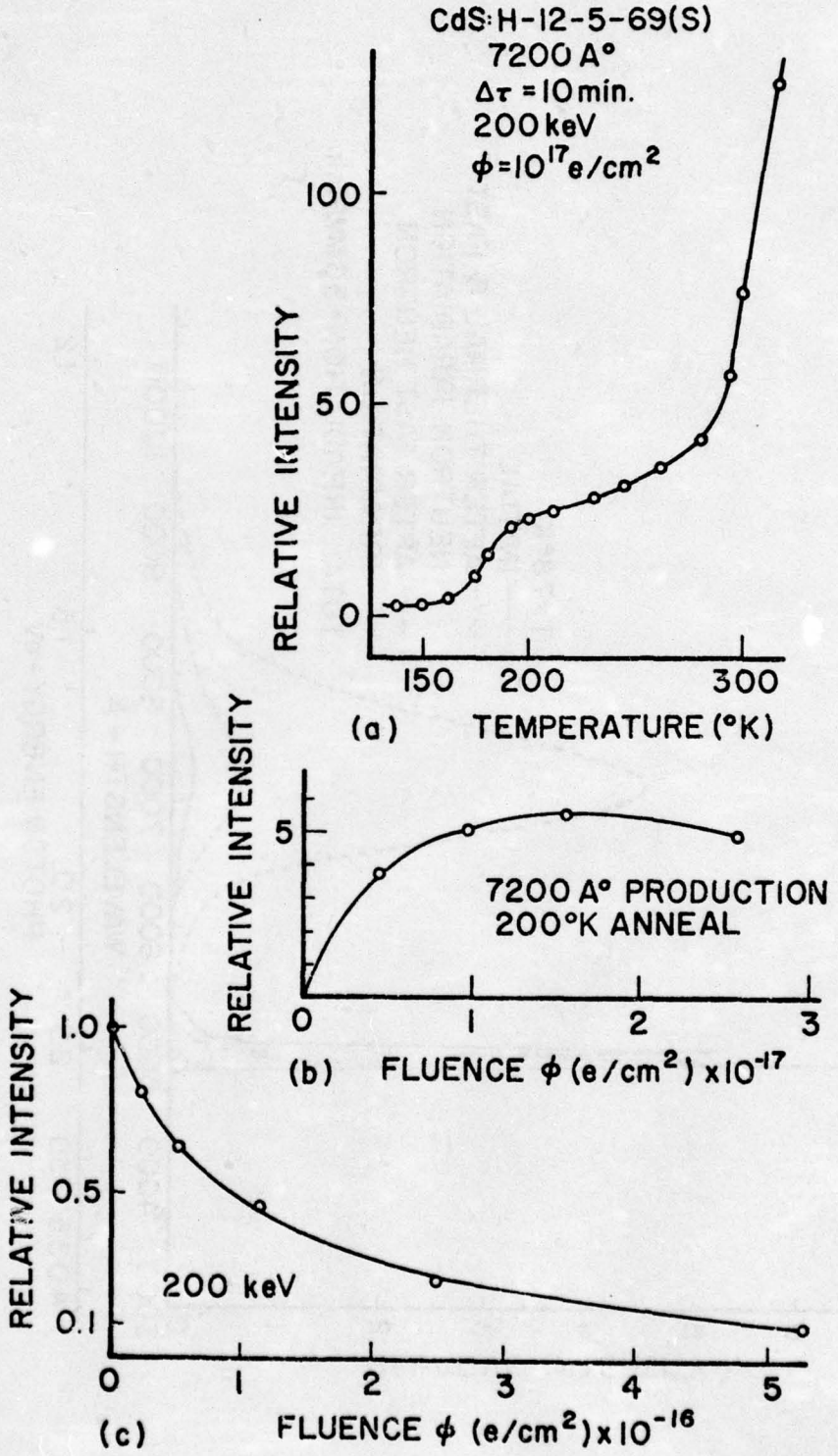

Fig. 2-39. Production of the 7200Å luminescence band (a) by isochronal annealing, and (b) as a function of fluence before a 200°K anneal. Also, the radiation annealing of this band is displayed in (c).

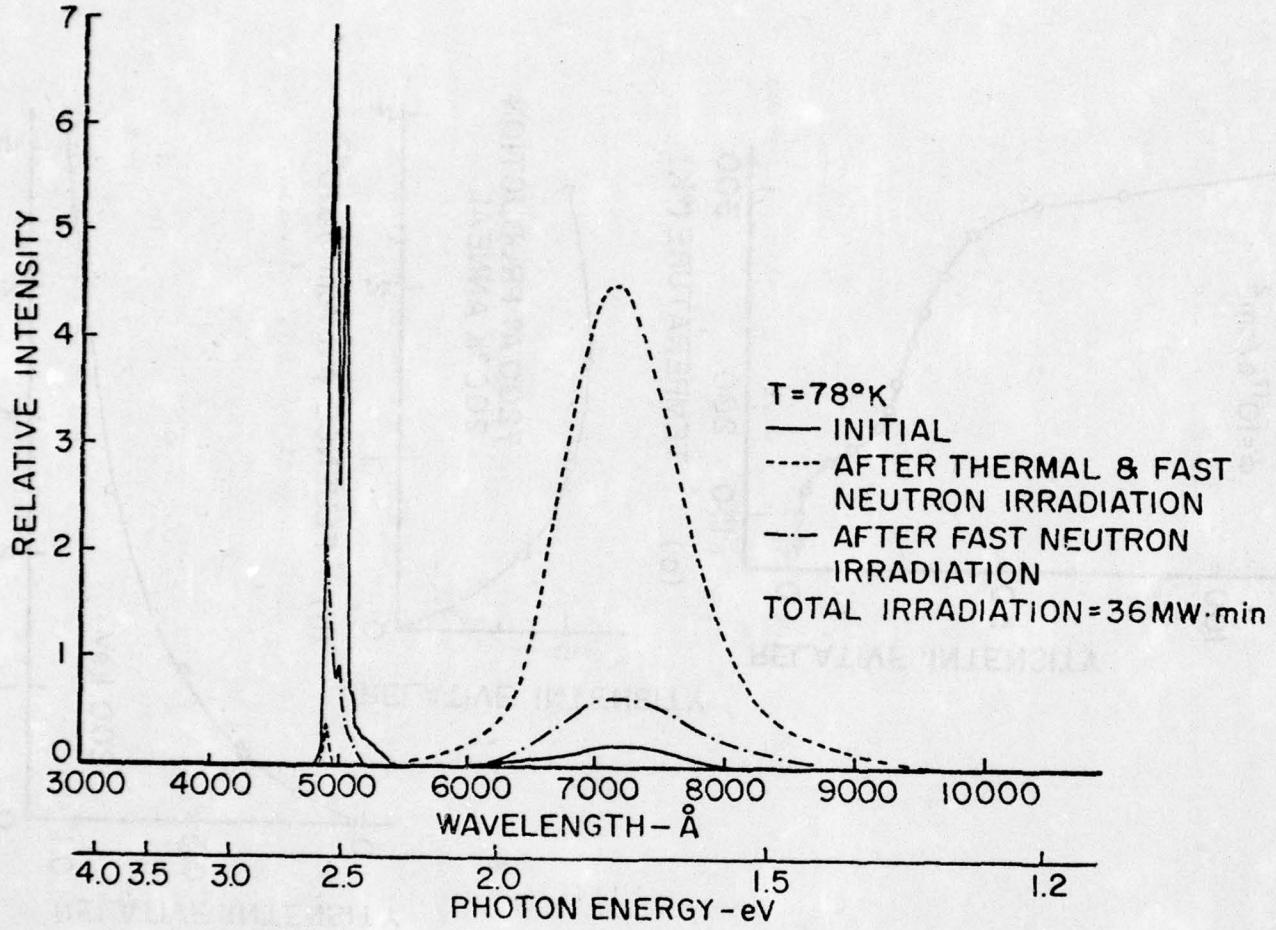

Fig. 2-40. Thermal neutron production of 7200Å band in CdS at room temperature.

Another annealing stage, at 230°K, has been observed for platelets irradiated above the Cd threshold, as shown in Fig. 2-41. This stage and the 180°K stage are seen by observing the recovery of the 1.03μm bands. Minor annealing stages are also observed below 150°K; these have also been reported by Vook[26] for the recovery of radiation-induced thermal resistance. This thermal resistance data is seen in Fig. 2-42(c). Vook has observed an increase in anisotropic thermal conductivity produced by annealing from 60 to 150°K, followed by a loss of this anisotropy in a stage at 180°K, followed by a nearly complete recovery in a broad stage extending from 210-270°K after 2 MeV irradiation. He attributes the formation of this anisotropic thermal conductivity to a re-orientation of defects along the c-axis. If we assume that these defects are Frenkel pairs, then the annihilation of these pairs at 180°K is consistent with the loss of the anisotropic thermal conductivity, with the larger percentage recovery observed with electrical measurements,[27] shown in Figs. 2-42(a) and 2-42(b), and with the large thermal conductivity recovery in this same annealing stage. Also, since from EPR results[28-30] it is unlikely that vacancies migrate in CdS below room temperature, we attribute the 180°K annealing stage to the migration of sulfur interstitials, as is consistent with the displacement energies. The annealing stage at 230°K is then most likely to be the onset of Cd-interstitial migration since the cadmium vacancy is known to be stable at room temperature from EPR.[28]

An additional annealing stage has been observed by us in room-temperature electron irradiated CdS.[31,32] Information concerning the position of the defect energy levels from electrical measurements is also in agreement with the optical measurements above. In the experiment to be described, 250 keV irradiations (between the Cd and S displacement thresholds) and 1 MeV irradiations

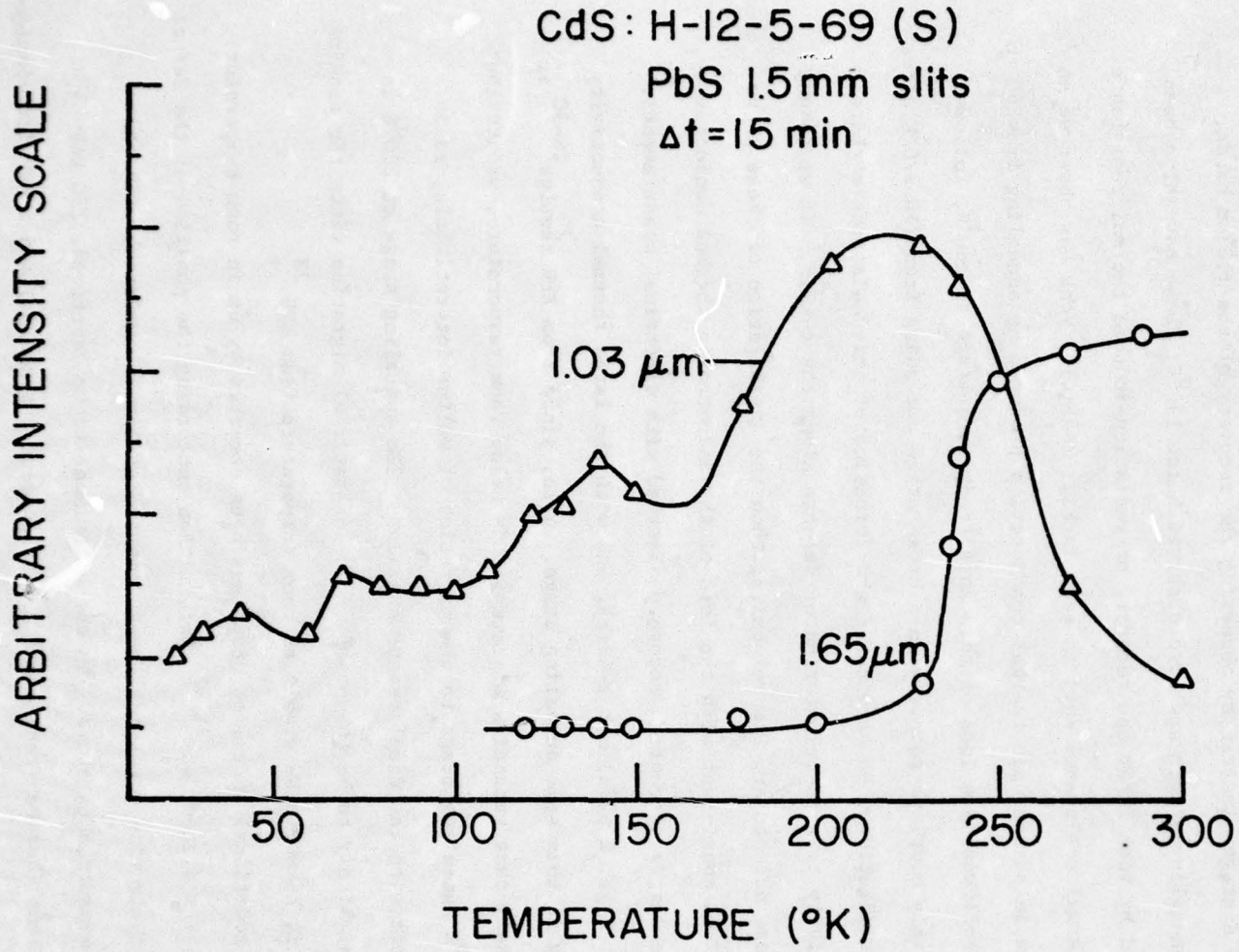

Fig. 2-41. Isochronal annealing of the 1.03μm and 1.65μm bands for samples irradiated above the Cd-threshold.

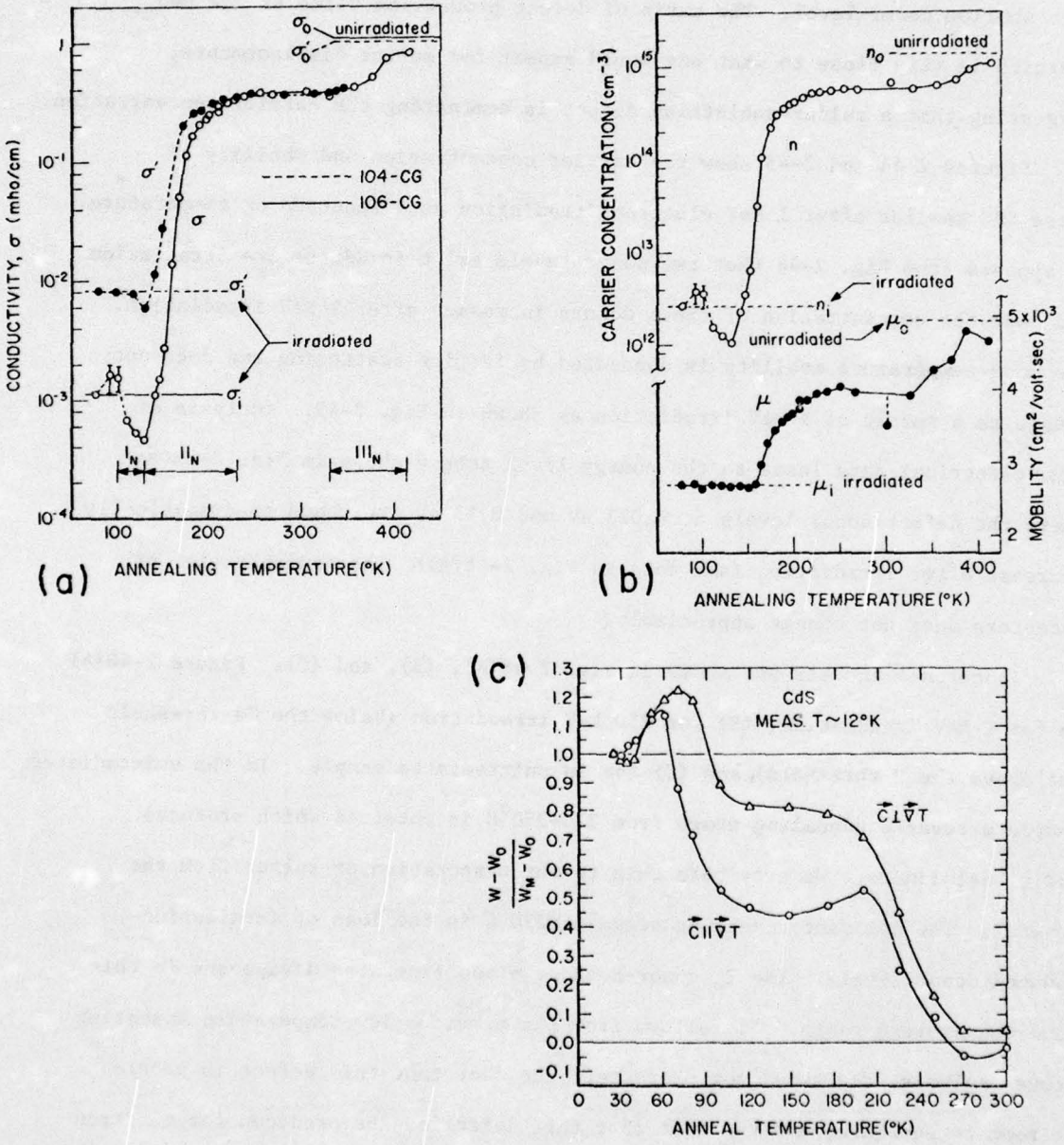

Fig. 2-42. (a) Isochronal annealing in high-conductivity CdS crystals after irradiation by 10 MeV electrons near LN_2 temperature; (b) isochronal annealing in sample 106-CG ((a) and (b) from Ref. 27); (c) fraction of the additive thermal resistivity at 12°K that remains after successive 15 min. anneals. (from Ref. 26).

(above both thresholds) are compared. Figure 2-43 shows that both energy electrons produce an increase in carrier concentration, suggesting the production of a shallow donor level. The ratio of defect production rates at the two energies is very close to what one would expect for sulfur displacements, suggesting that a sulfur-sublattice defect is dominating the carrier concentration.

Figures 2-44 and 2-45 show the carrier concentration and mobility of these CdS samples after 1 MeV electron irradiation as a function of temperature. It appears from Fig. 2-44 that two donor levels exist in CdS before irradiation and that the concentration of these donors increases after 1 MeV irradiation. The room-temperature mobility is dominated by lattice scattering and does not change as a result of 1 MeV irradiation as shown in Fig. 2-45. Analysis of these electrical data leads to the energy level scheme shown in Fig. 2-46(D) where the defect donor levels at 0.022 eV and 0.13 eV are shown to dramatically increase after irradiation (see data in Fig. 2-46(E)). The concentration of acceptors does not change appreciably.

Isochronal anneals are shown in Fig. 2-46(A), (B), and (C). Figure 2-46(A) is for 1 MeV irradiation, (B) for 250 keV irradiation (below the Cd threshold but above the S threshold), and (C) for an unirradiated sample. In the unirradiated sample a reverse annealing stage from 270-350°C is obtained which produces additional donors. We attribute this to the evaporation of sulfur from the crystal. The dominant annealing stage at 250°C is the loss of irradiation-induced donor levels. The I_R donor-bound-exciton line also disappears in this same temperature range. It follows from the previous low-temperature annealing stage analysis, the two-donor character, the fact that this defect is stable at room temperature, and the fact that this defect can be produced for electron irradiation energies just above the S displacement threshold, that the only possiblity for the identification of this defect is the sulfur vacancy.

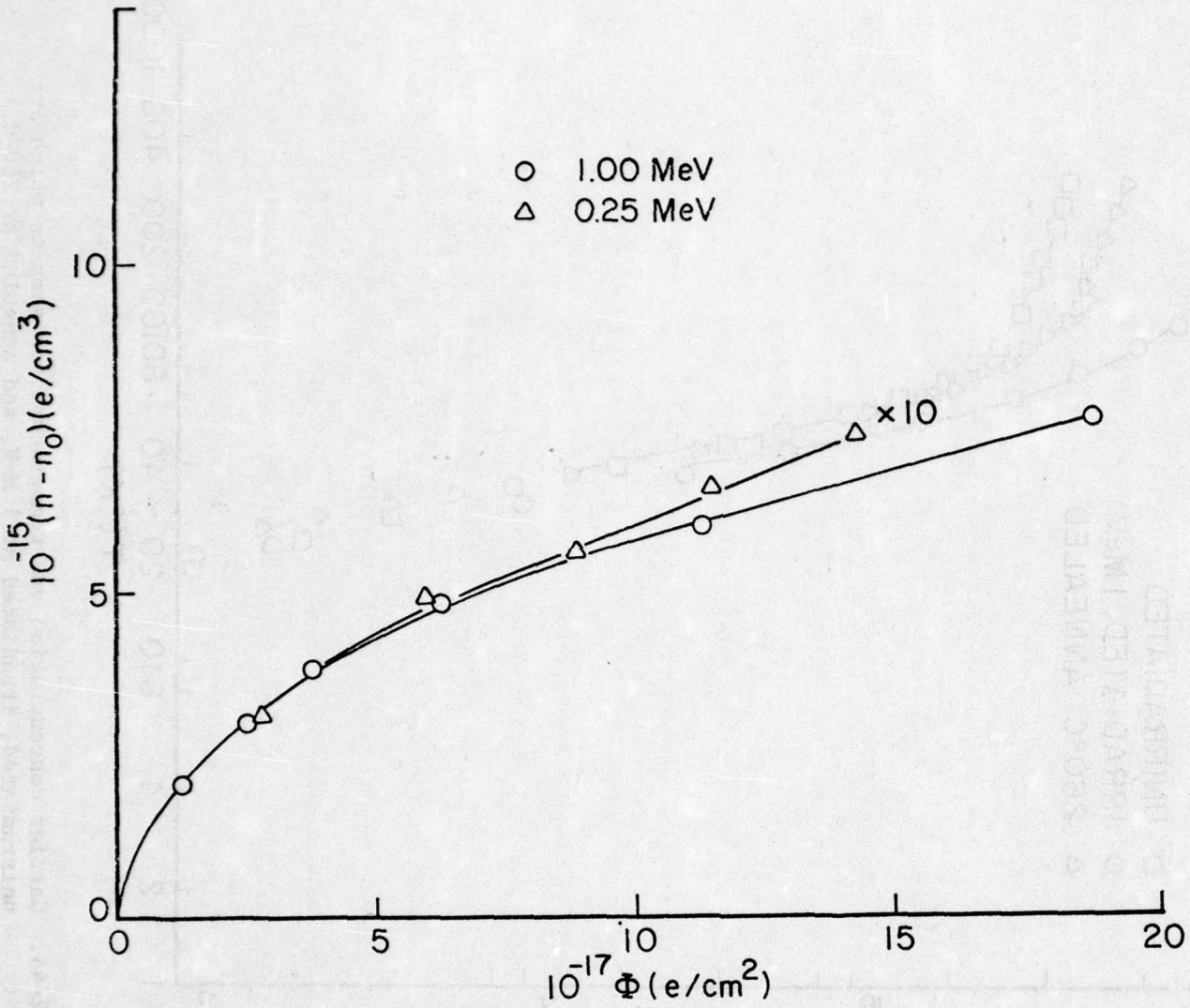

Fig. 2-43. Increase in carrier concentration in CdS for 1 MeV and 250 keV electron irradiations.

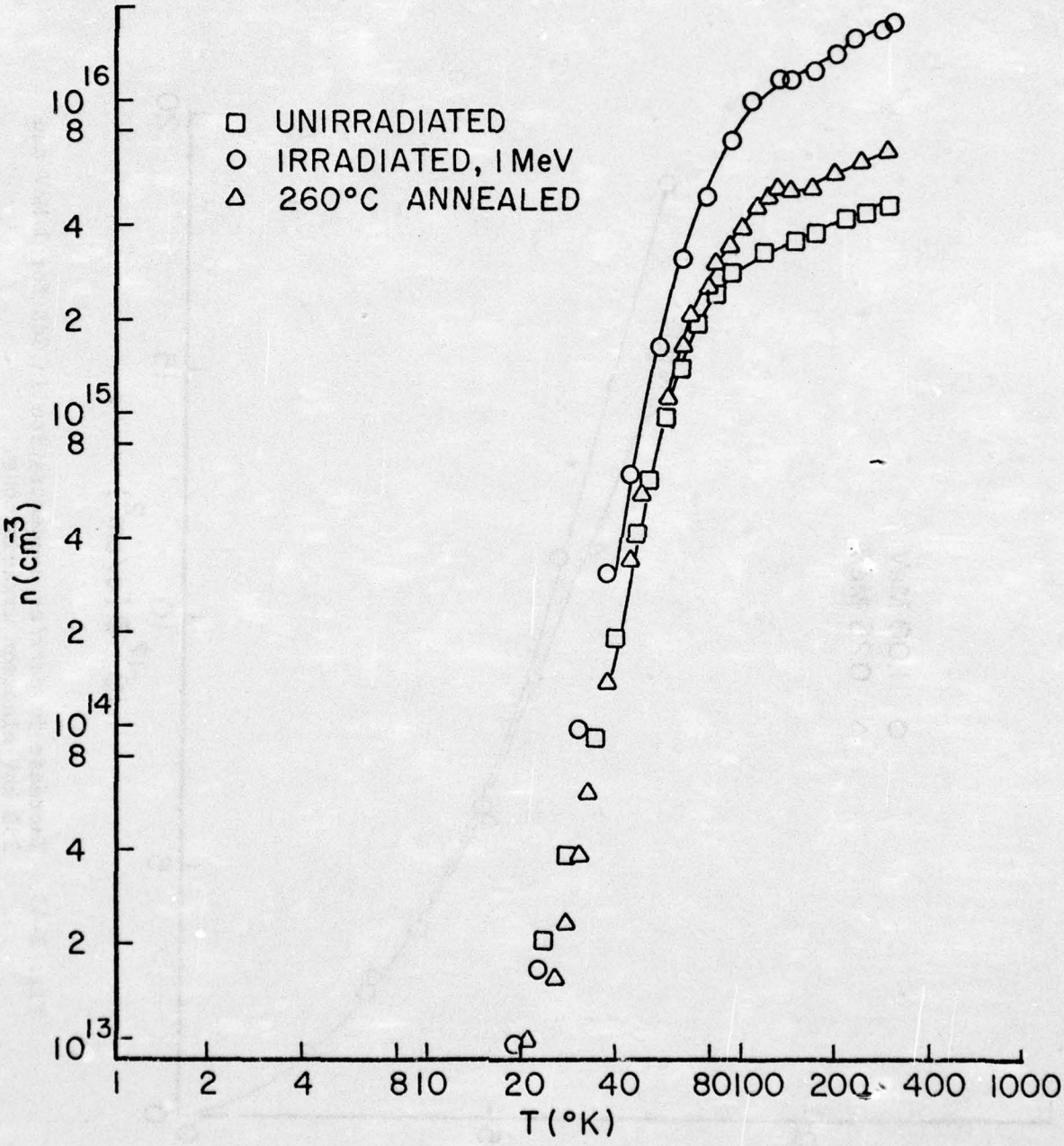

Fig. 2-44. Carrier concentration vs. temperature for samples which are unirradiated, irradiated at 1 MeV, and annealed at 260°C.

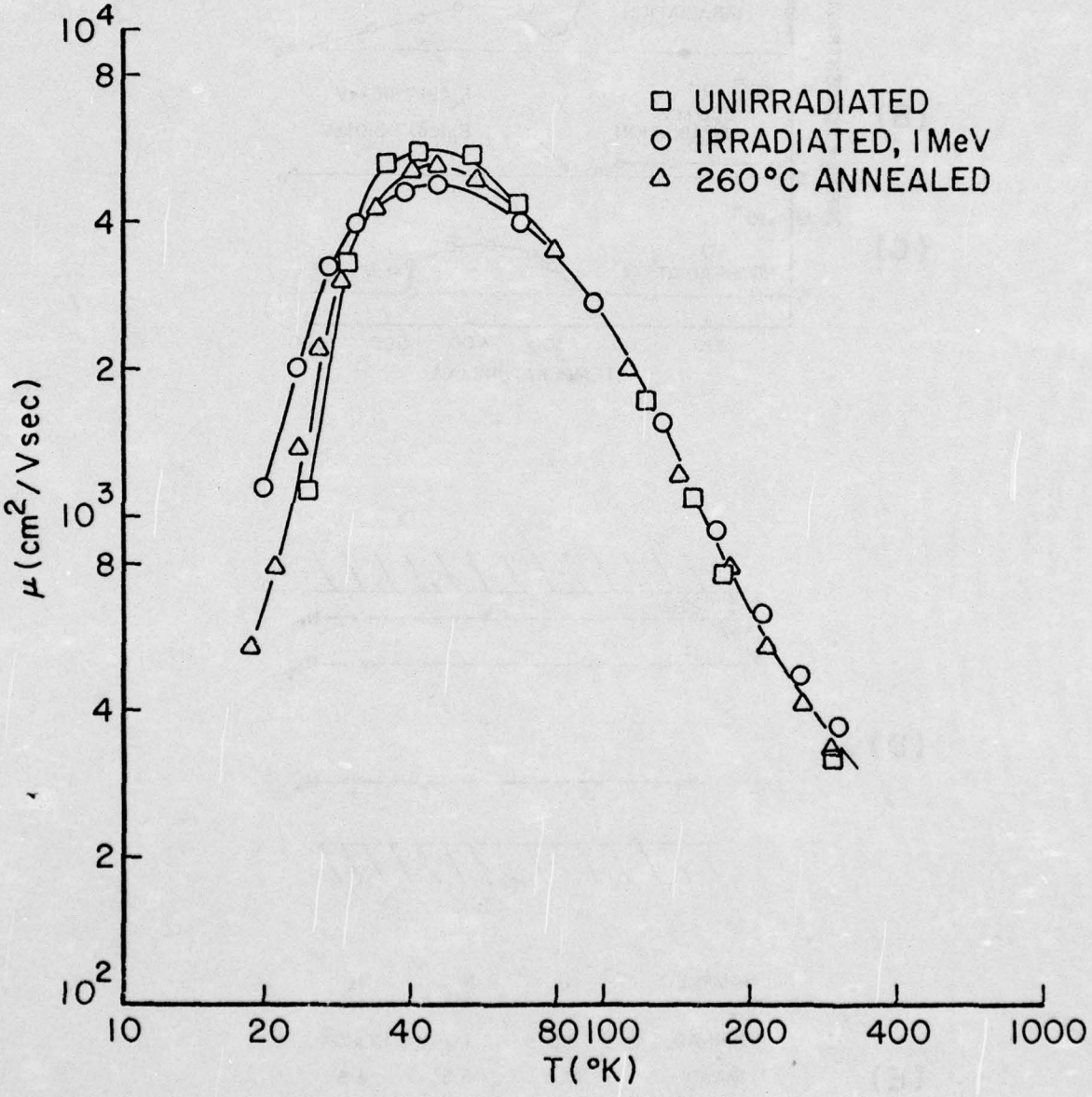

Fig. 2-45. Temperature dependence of mobility for same conditions as specified in Fig. 2-44.

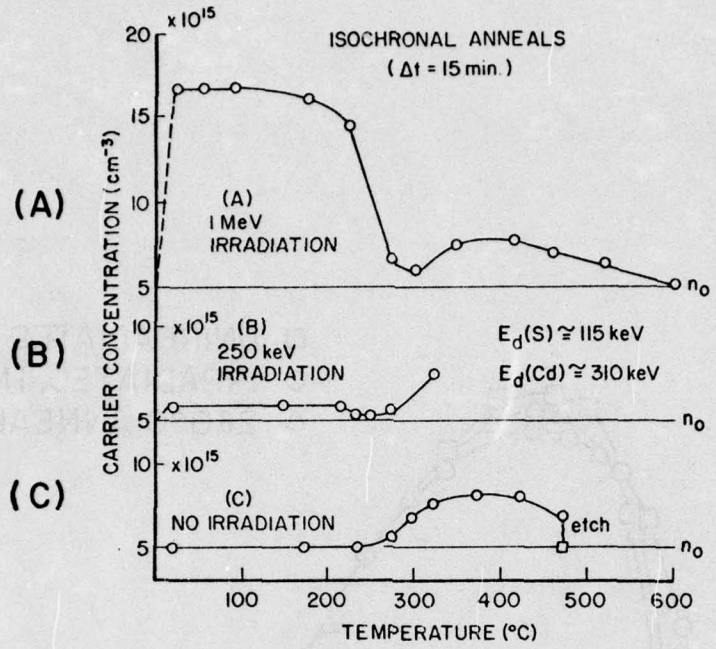

(A)

(B)

(C)

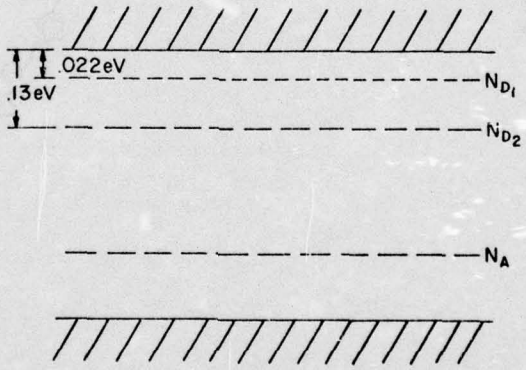

(D)

(E)

SAMPLE	N_{D_1}	N_{D_2}	N_A
UNIRRAD.	5.5	1.0	1.7×10^{15}
IRRAD.	17.5	6.5	2.5
260°C ANNEAL	9.0	1.8	3.3

$E_{D_1} = 0.022$eV

$E_{D_2} = 0.130$eV

Fig. 2-46. Isochronal annealing and energy-level diagram in CdS.

Isothermal anneals of the 250°C annealing stage add support to this argument.[32] Figure 2-47 shows these isothermal anneals at 250°C, 275°C and 300°C. An analysis of these data indicates that the annealing kinetics are second order.[32] In Fig. 2-48 the data are fitted according to the equation

$$\eta_i = \eta_i^o[1 + \eta_i^o \nu_o zvt \exp(-E/kT)]^{-1}$$

where η_i is the concentration of defects at time t, η_i^o is the initial concentration, ν_o is the jump frequency of the defect, z is the number of sites from which a jump can take place, v is the volume per lattice site, and E is the defect migration energy.

The best fit to the data yields E = 1.4 ± 0.1 eV, and $\nu_o zv = 10^{-7} - 10^{-8}$. For an order-of-magnitude estimate of $\nu_o zv$ we may take $\nu_o \simeq 10^{13}$ sec^{-1}, $z \simeq 10$, and $v \simeq 10^{-22}$ cm^{-3} to get $\nu_o zv \simeq 10^{-8}$. The same annealing kinetics are observed for the extra donors created by heating the sample above the reverse annealing stage and quenching. The activation energy of 1.4 eV is typical of vacancy motion. We therefore feel that this annealing stage represents sulfur-vacancy motion and annihilation while the reverse stage represents sulfur evaporation.

We can summarize the results of radiation damage effects in CdS as follows:

1. The displacement threshold for S in CdS is about 120 ± 5 keV.
2. The displacement threshold for Cd is about 314 ± 5 keV.
3. Irradiation at 10°K produces a shallow donor level near 0.03 eV (I_R bound-exciton line) and a deep level, probably an acceptor (1.03μm luminescence band).
4. This shallow donor level, as well as a deeper donor level at 0.13 eV, are associated with the S vacancy. The 1.03μm band is associated with a defect on the Cd sublattice, probably the Cd vacancy.
5. In the temperature range of 60-150°K, Frenkel pairs tend to align along a preferential axis.

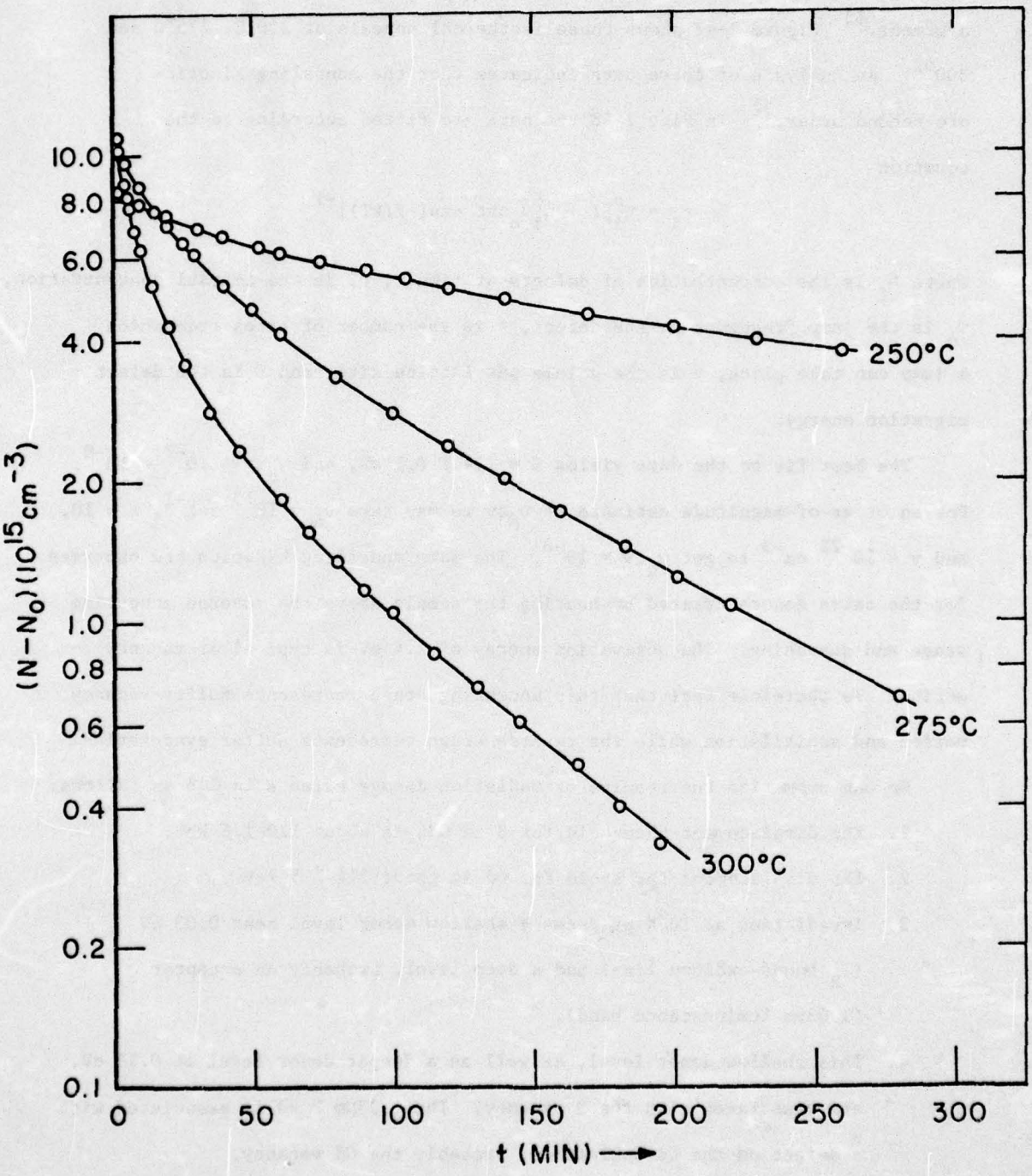

Fig. 2-47. Isothermal annealing of additional carrier concentration for three annealing temperatures.

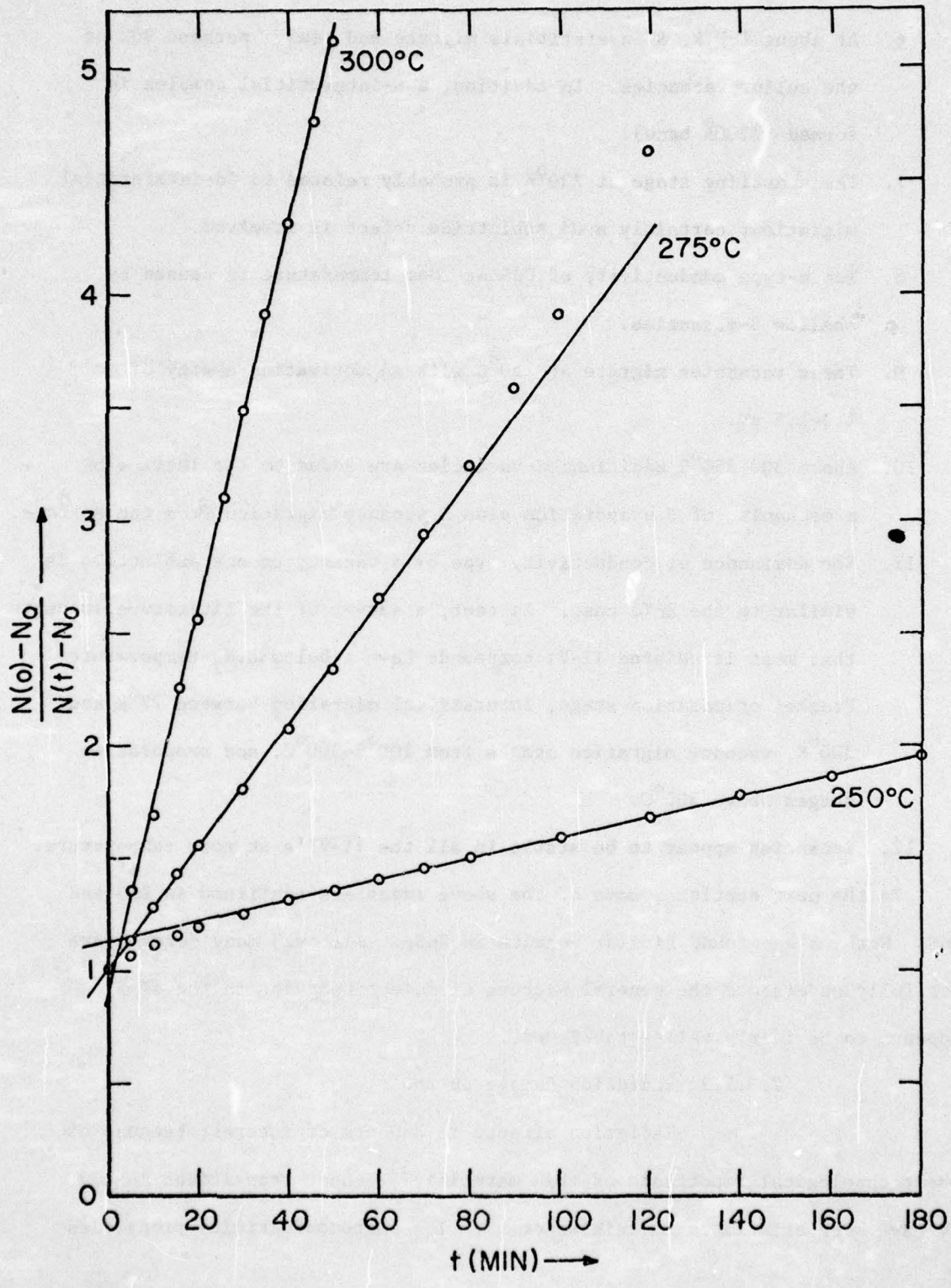

Fig. 2-48. Second-order fit to annealing data in Fig. 2-47.

6. At about 180°K, S interstitials migrate and remove perhaps 90% of the sulfur vacancies. In addition, a S-interstitial complex is formed (7200Å band).
7. The annealing stage at 230°K is probably related to Cd-interstitial migration; certainly a Cd sublattice defect is involved.
8. The n-type conductivity of CdS at room temperature is caused by shallow S-vacancies.
9. These vacancies migrate at 250°C with an activation energy of 1.3-1.5 eV.
10. Above 300-350°C, additional S-vacancies are added to the lattice by a mechanism of S evaporation plus S vacancy migration from the surface.
11. The dominance of conductivity type by a vacancy on one sublattice is similar to the ZnTe case. In fact, a survey of the literature suggests that most irradiated II-VI compounds have a below-L.N_2-temperature Frenkel orientation stage, interstitial migration between 77°K and 300°K, vacancy migration stages from 100°C-300°C, and evaporation stages above 300°C.
12. Vacancies appear to be stable in all the II-VI's at room temperature.

In the next sections, some of the above ideas are confirmed in ZnO and ZnS. Watkins has found similar results in ZnSe. Although many details are not fully understood the general picture of defect behavior in the II-VI's appears to be fairly well established.

2.3.1.3 Radiation Damage in ZnO

Radiation effects in ZnO are of interest because of the technological importance of this material.[33] Laser transitions in the UV have been stimulated in this material. Its photoconductivity properties

form the basis of a copy machine process. ZnO has been used in a variety of light-emission devices, from digital displays to TV picture tubes. ZnO has also been proposed as a useful material for the fabrication of high-frequency delay-line transducers and acoustic amplifiers because of its high electro-mechanical coupling constant and low dielectric constant.

One of the oldest uses of ZnO is as a white paint pigment. Radiation effects on ZnO used in this application are of particular interest since this pigment, in combination with others, has been applied as a thermal paint coating to more spacecraft than any other paint.[33]

Oxides have been found to be some of the most radiation-resistant materials known. Chen et al.[34] have been able to observe, by means of optical absorption, the oxygen displacement threshold in MgO at 330 keV. This value corresponds to a recoil energy T_d = 60 eV. This value is approximately six times as large as the displacement energies observed in the II-VI semiconductors.

In the case of ZnO, early estimates of T_d were much to high when compared with displacement energies in other materials.[35] Vehse, Sibley, Keller and Chen irradiated ZnO with 0.6 MeV and 1.7 MeV electrons. They observed that the optical-absorption coefficient at 4100Å increased for the higher energy irradiation. They were able to correlate this absorption band with the yellow color centers produced by heat treatment of ZnO in Zn-vapor.[35]

They have also shown that elastic collisions are the major source of radiation damage in ZnO. Since they observed no coloration in ZnO for 600 keV irradiation, they assumed that the displacement threshold electron energy, E_d, could be no lower than 600 keV. This corresponds to a recoil energy, T_d, of at least 30 eV for Zn displacements, or 120 eV for oxygen displacements. They argued that 120 eV was too high a value for T_d and therefore assumed that they were observing Zn displacements (a reasonable assumption). They suggested that the

4100Å absorption band was associated with Zn interstitials which were produced either by heat treatment in Zn vapor or by electron irradiation above 600 keV.

It has been difficult to interpret subsequent experiments in terms of the above model. Careful channeling experiments by Appleton and Feldmen on ZnO, additively colored in Zn-vapor, have failed to detect Zn interstitials.[36] More surprisingly, it was found that ionized oxygen vacancies (F^+ centers) could not be observed by EPR for 600 keV electron irradiations.[37] If the Zn threshold is approximately 600 keV, as orginally suggested, then the oxygen threshold should have been much lower because of its lower mass. Therefore, 600 keV irradiations should have produced many oxygen vacancies. Smith and Vehse[37] have also found that the F^+ resonance thermally anneals in the same temperature range as the color center identified in the previous work.[35]

The conclusions concerning the displacement energies in ZnO to be drawn from these early studies are not satisfying. The work of Smith and Vehse, and also that of Appleton and Feldman, suggest that the 4100Å absorption band should be associated with oxygen vacancies, not zinc interstitials. This implies, however, that T_d for oxygen in ZnO must be larger than 120 eV since no EPR resonance for the F^+ center is observed after 600 keV electron irradiation. This conclusion is unsatisfactory since T_d is of the order of 60-80 eV in diamond, a material with a formation energy nearly twice that of ZnO. The work performed under this contract has resolved many of these difficulties. In addition, valuable information has been obtained from which it should be possible to prevent much of the yellowing associated with ZnO paint pigment exposed to a space radiation environment whose degradation is manifested in higher spacecraft cooling system loads.

AD-A032 128 DAYTON UNIV OHIO DEPT OF PHYSICS F/G 20/12
IDENTIFICATION OF DEFECTS IN COMPOUND SEMICONDUCTORS.(U)
OCT 76 D C LOOK, J M MEESE, M M KREITMAN F33615-71-C-1877
UNCLASSIFIED AFAL-TR-76-139 NL

2 OF 3
AD
A032128

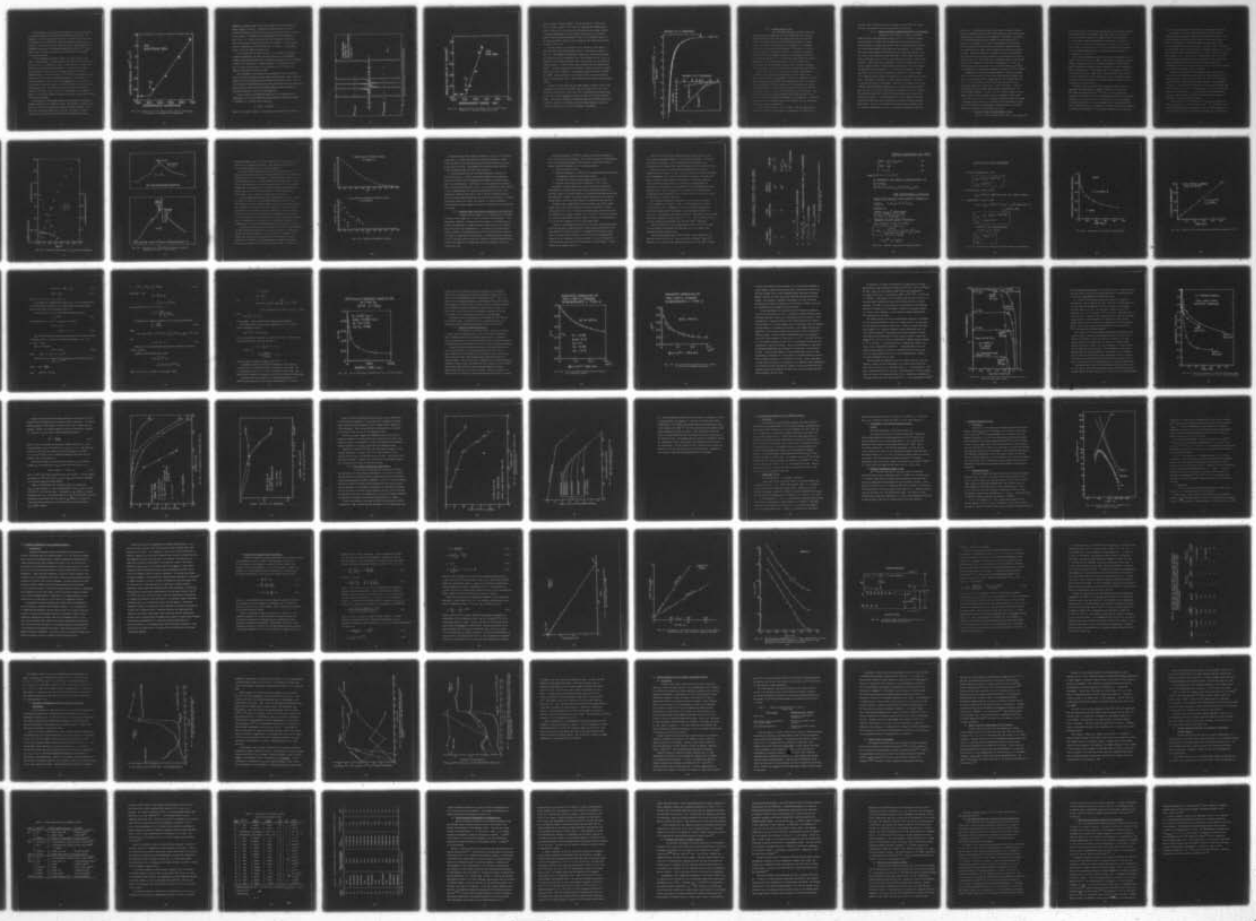

The investigation of irradiation effects began with a study of degradation of electrical properties of ZnO during room-temperature irradiations. The conductivity for fixed beam energies was found to decrease linearly with fluence for fluences up to $3 \times 10^{18} e/cm^2$ so long as the beam power density was kept constant. The carrier removal rate, $dn/d\phi$, was found to vary quadratically with bombardment energy above a displacement threshold of 310 ± 20 keV.[33] This is shown in Fig. 2-49 where the square root of carrier removal rate $(dn/d\phi)^{1/2}$ vs. beam energy is shown.

A second displacement threshold is observed at higher energies by the onset of three phenomena. The samples used in this experiment were irradiated in air for 16 hrs. at 5-10$\mu A/cm^2$ in steps of 50 keV from 0.6 to 1.0 MeV. The EPR spectrum was taken after each irradiation. For energies above 900 keV, a sharp reduction in the free-carrier microwave absorption is observed. Accompanying this, the EPR resonances for Fe^{3+} and Mn^{2+} are observed to increase drastically due to the shift in Fermi level detected by the reduction in microwave absorption. The F^+ center is also observed for the first time and is accompanied by the sample taking on a yellow color due to an increase in the 4100Å absorption band. We emphasize that only F^+ centers (ionized oxygen vacancies) can be seen by EPR. The neutral F center would not be observed if present. It is also not possible to make optical absorption transitions to energy levels which are occupied.

To understand the relationships between these experiments, the crystal was thermally annealed in air at 300°C for 30 min. This procedure is known to remove most of the color centers produced by neutron or electron irradiation. After this anneal, the crystal became clear, indicating the removal of the color centers. The microwave free carrier absorption, did not recover, however,

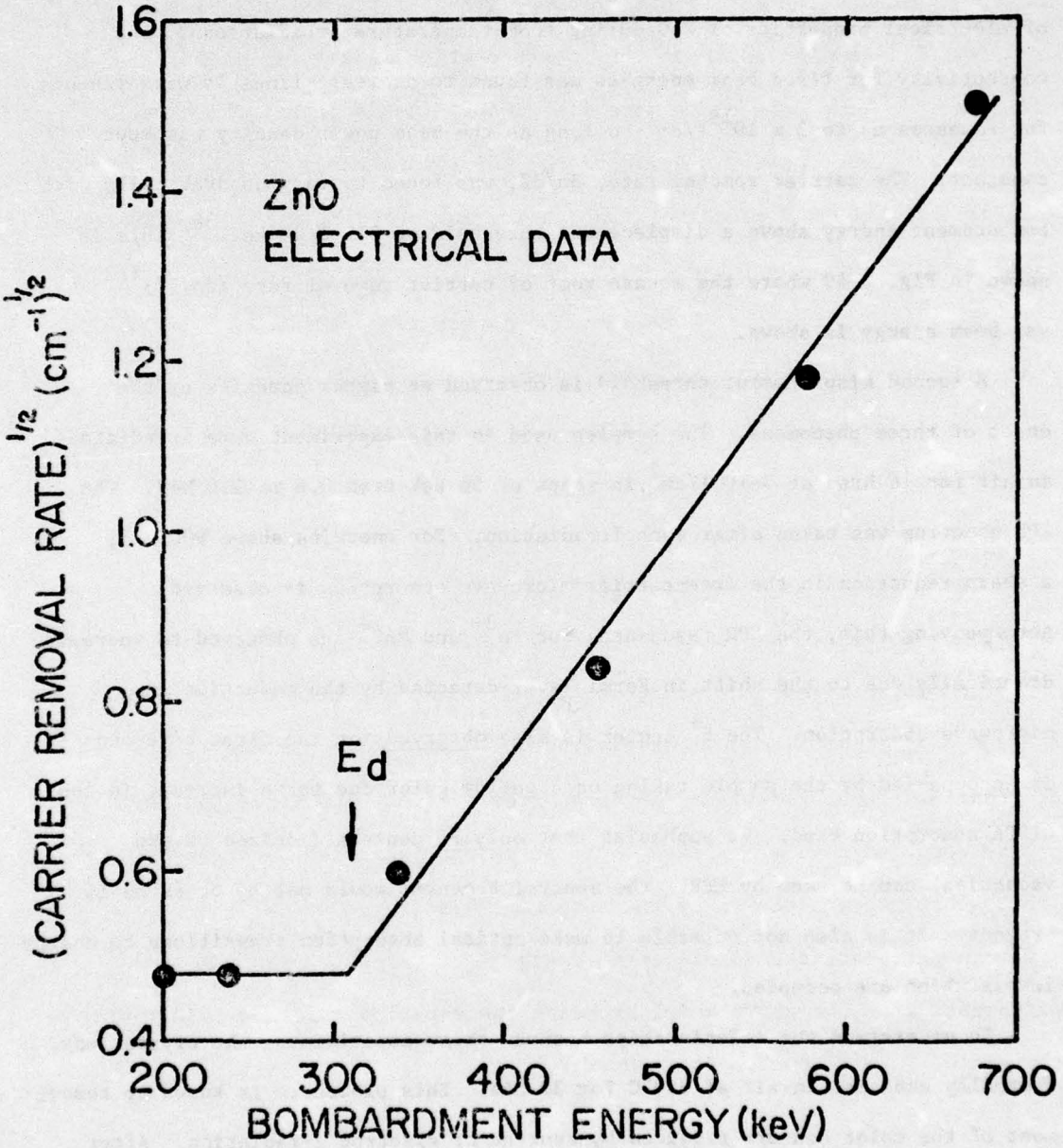

Fig. 2-49. Square root of the carrier removal rate vs. beam energy for ZnO after a room-temperature irradiation.

suggesting a permanent shift in Fermi level caused by irradiation above the second threshold at 900 keV. Subsequent 600 keV irradiation for 16 hrs. at 10μA/cm^2 produced the EPR spectrum shown in Fig. 2-50, as well as a yellow-colored crystal. A discussion of the interpretation of this spectrum is given in Ref. 33. We only state here that the F^+ resonance and its hyperfine structure give conclusive evidence for the existence of oxygen vacancies in ZnO following 600 keV electron irradiation, in contrast to the reported results of Smith and Vehse, and Chen et al.

To demonstrate that the above spectrum is not produced as a result of a bleaching phenomenom, the sample was again annealed and a displacement-threshold experiment performed using the EPR signal strength of the F^+ resonance to monitor the concentration of oxygen vacancies. The results are shown in Fig. 2-51 where the square root of the production rate of F^+ centers is shown vs. beam energy as measured by EPR.

These experiments can be understood by assuming that irradiation above 310 keV (the lower threshold) produces oxygen vacancies which cannot be made paramagnetic until Zinc displacements are produced at 900 keV or above. Either zinc vacancies or interstitials then trap free carriers and force the Fermi level down low enough to make the already present oxygen vacancies paramagnetic. The optical absorption occurs by the same mechanism.

We can calculate the displacement energy T_d for both oxygen and zinc displacements from the above model by using the equation relating beam energy at threshold, E_d, to atomic recoil energy, T_d:

$$T_d = 2(E_d + 2mc^2)E_d/Mc^2$$

where c is the speed of light, m the electron rest mass and M the atomic mass

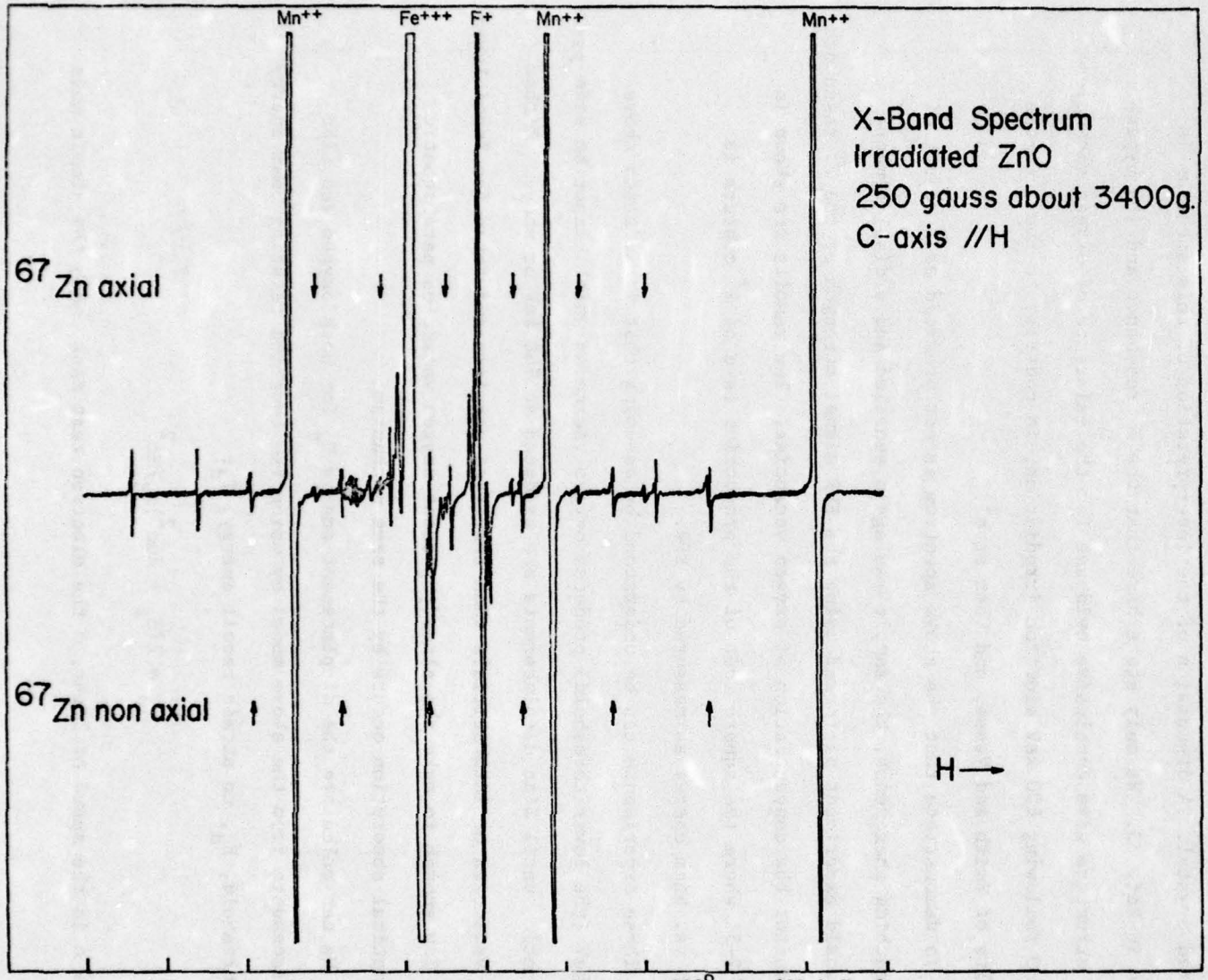

Fig. 2-50. EPR spectrum of ZnO irradiated at 300°K by 600 keV electrons after a previous irradiation at 1 MeV and 300°C thermal anneal.

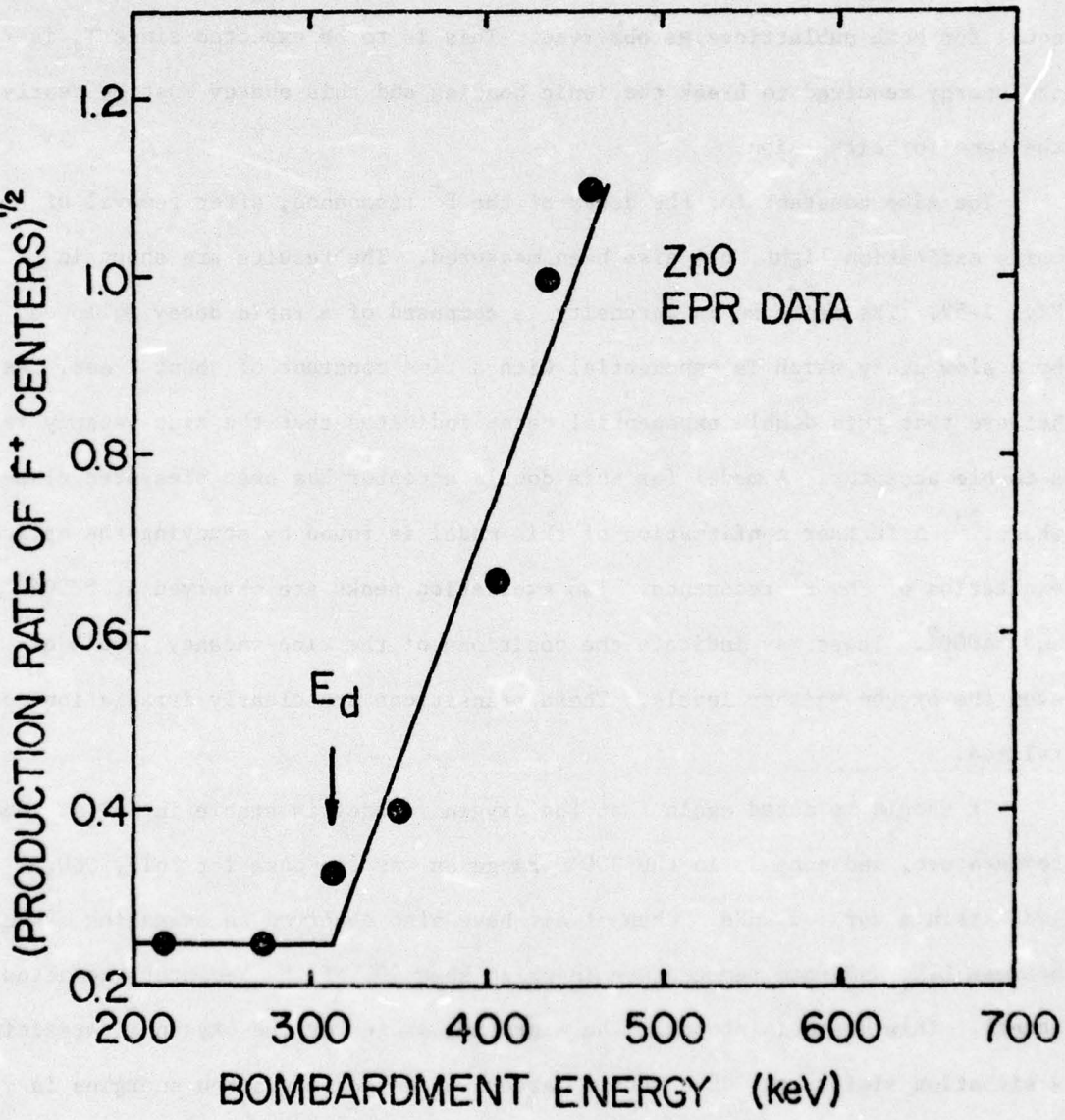

Fig. 2-51. Square root of the production rate of ionized oxygen vacancies (F^+ Centers) versus beam energy.

being displaced. Using E_d (oxygen) = 310 keV and E_d(zinc) ≃ 900 keV, we find that $T_d(O) = T_d(Zn) = 57$ eV. Since T_d represents the maximum kinetic energy transferred to a lattice ion by the minimum electron energy necessary to produced displacements, we would expect the values of T_d to be nearly equal for both sublattices, as observed. This is to be expected since T_d is the energy required to break the ionic bonding and this energy must be nearly the same for either ion.

The time constant for the decay of the F^+ resonance, after removal of white excitation light, has also been measured. The results are shown in Fig. 2-52. The decrease in intensity is composed of a rapid decay followed by a slow decay which is exponential with a time constant of about 1 sec. We believe that this double exponential decay indicates that the zinc vacancy is a double acceptor. A model for this double acceptor has been presented elsewhere.[33] A further confirmation of this model is found by studying the optical excitation of the F^+ resonance. Two excitation peaks are observed at 5300Å and ~4000Å. These may indicate the positions of the zinc-vacancy levels or even the oxygen-vacancy levels. These transitions are clearly irradiation-defect related.

It should be noted again that the oxygen vacancy is stable in ZnO at room temperature, and anneals in the 300°C range as was the case for ZnTe, CdS, and Watkin's work on ZnSe. Chen et al. have also observed an annealing stage between L.N_2 and room temperature in which some 90% of the F-center vacancies anneal. This stage is probably the migration stage for the oxygen interstitial, a situation similar to CdS. Thus a pattern of defect migration energies is beginning to emerge for all the II-VI compounds investigated.

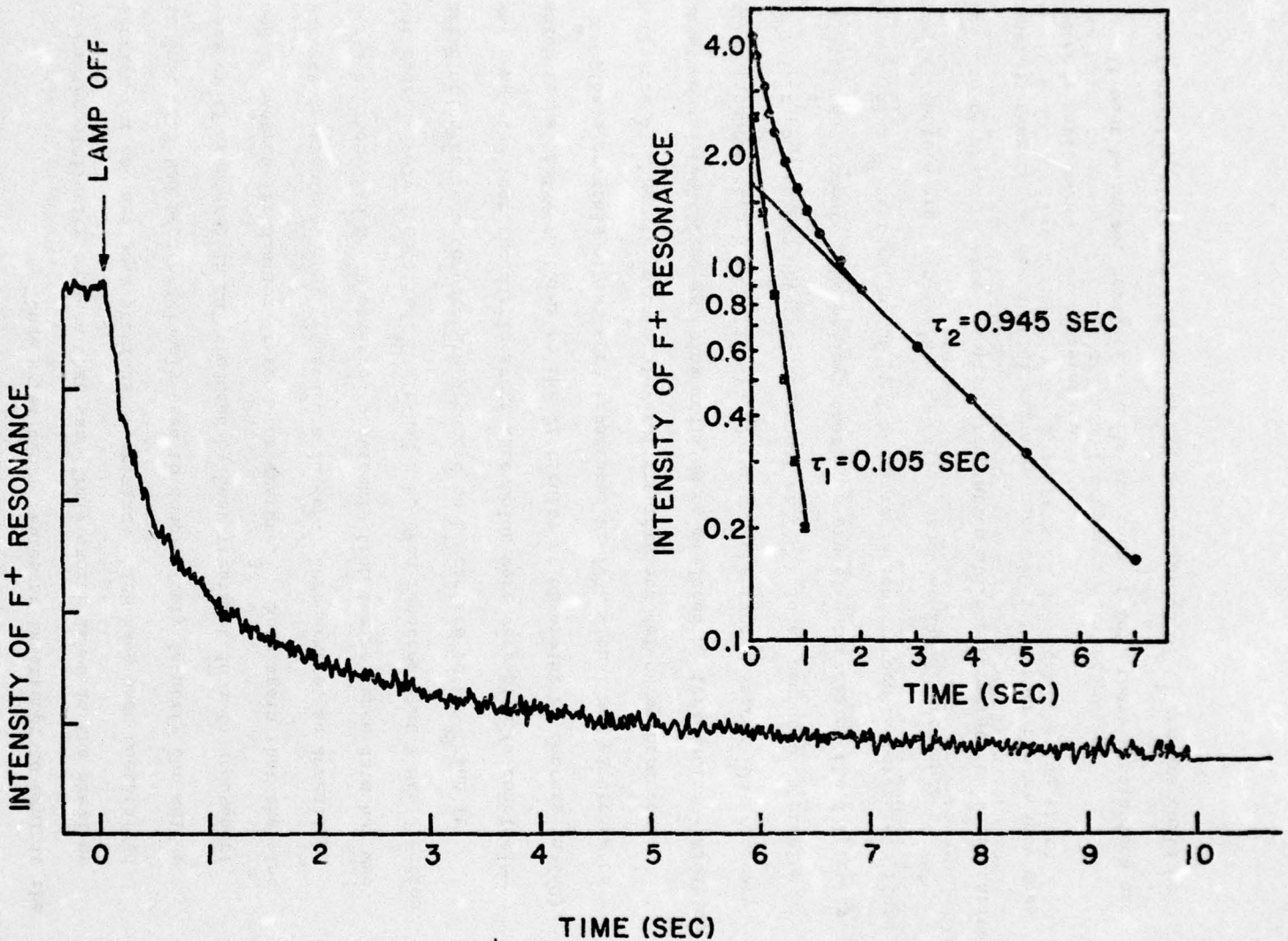

Fig. 2-52. Decay of F^+ resonance at room temperature after the removal of white-light excitation.

2.3.1.4 Radiation Effects in ZnS

These experiments represent an attempt to exploit the suspected similarity between what was firmly exstablished in the previous section for ZnO and some previous experiments which have been unexplained in ZnS. FPR had been previously used to conclusively identify the sulfur vacancy (F^+ centers) in ZnS produced by heat treatment in a Zn atmosphere, and by neutron irradiation at room temperature.[39] Note again that the zinc vacancy is stable at room temperature in ZnS. Furthermore, an annealing stage at about 240°K was observed previously from luminescence data but was not conclusively identified.[40] It had also been reported that 1 Mev electron irradiation at room temperature produced no F^+ centers in ZnS[39] and it was suggested that the displacement thresholds were very high (a conclusion which seems faulty in terms of the difficulty of observing F^+ centers in ZnO).

Single crystals of ZnS were irradiated at 77°K with 1 MeV electrons to a fluence of about $10^{18} e/cm^2$. Several impurity and defect spectra were observed and identified as being modified or produced by irradiation. Additionally, a center though to be the F^+ center was observed. Nearly 100% recovery of this resonance was observed to anneal at 240°K in agreement with previous optical measurements. We believe that this experiment explains the difficulty in obtaining F^+ centers in ZnS by 1 MeV irradiation at room temperature. Since most F^+ centers are lost in this annealing stage at 240°K, but since the F^+ can also be observed after neutron irradiation at room temperature, we tentatively conclude that the S interstitial migrates near 240°K but that the vacancy does not move until above room temperature.

It must be added, however, that in the case of ZnS, these conclusions are very tentative since not a large enough concentration of F^+ centers could be

produced to see the hyperfine structure necessary for positive defect identification. The reasons for this an not understood at this time.

2.3.1.5 Summary of Radiation Damage Experiments in II-VI Compounds

Although much work remains to be done to completely identify all the radiation-produced effects in II-VI's, a pattern of damage effects has begun to emerge. The low-temperature annealing which has been observed below L.N_2 temperatures has been found to be associated with Frenkel-pair reorientation whenever these stages have been observed. It is expected that large recovery stages in which interstitials migrate are found in most of the II-VI's in the temperature range near 200^{o}K. Vacancies have always been found to be stable in the II-VI's at room temperature and begin to migrate from 100-300^{o}C. Beyond this range, evaporation of one of the constitutents of the crystal usually is found. The displacement thresholds in the II-VI compounds are generally in the 8 eV range for T_d. ZnO is the one exception. The very high value of T_d for ZnO can be understood in terms of the unique strength of the oxygen bond which places the thresholds in ZnO near those found for other oxides, regardless of structure. The high radiation hardness of II-VI's can be inferred from the above experiments. Although T_d is generally lower in the compounds than the elemental semiconductors, it is now apparent that Frenkel pairs do exist in the II-VI's and that defect migration is much more difficult. The annealing stages found around 200^{o}K in the compounds tend to have large-percentage recoveries. This is interpreted by us as an indication that most interstitials find their parent vacancies in this stage, through correlated annihilation. This one fact accounts for the high radiation hardness found for compound semiconductor devices. As a comparison, consider the situation

in Ge and Si. In these materials, the interstitials are thought to migrate freely at temperatures as low as 10^{o}K. The vacancies and interstitial separate immediately upon irradiation at room temperature. Furthermore, the vacancies in the elemental semiconductors also migrate below room temperature, as opposed to the compounds. As a result of this migration, Frenkel pairs are not found, vacancies and interstitials have difficulty finding each other, and a whole spectrum of defect impurity complexes form which become difficult to anneal. Additional evidence for this model is found in the experimental fact that Si and Ge can be driven amorphorous by ion implantation more easily than the II-VI's can. This implies that a considerable amount of self-healing occurs in II-VI's which are irradiated at room temperature. In fact, the defect concentrations found in most II-VI's after 1 MeV fluences of $10^{18}e/cm^2$ are comparable to the concentrations produced in Si after only 10^{15} to $10^{16}e/cm^2$.

Although most of the radiation damage community is under the impression that the III-V's in general, and GaAs in particular, should be similar to Ge and Si, strong evidence exists to suggest that the III-VI's behave more like II-VI's. It will be shown in a later section that GaAs solar cells are considerably harder than Si solar cells of similar efficiency. It has also been observed that GaP starlight detectors show no degradation after 10^{9} rad ^{60}Co gamma irradiation. A study of the III-V radiation damage literature suggests that the annealing stages are found in temperature ranges similar to the II-VI's, not Si and Ge! It is apparent that advantages are to be gained by studying radiation effects in a consistent system of semiconductors, such as the II-VI's, since the intercomparisons of defect behaviors are lost when attention is confined to a single element such as Si.

2.3.2 Defect Semiconductor Radiation Damage - In_2Te_3

The III_2-VI_3 binary compounds such as In_2Te_3, Ga_2S_3, Ga_2Se_3, and

Ga_2Te_3 form a class of semiconducting compounds with unusual physical properties. These crystals grow in a tetrahedral phase, based either on the zinc blend or wurtize structures, because of the tendency toward sp^3 hydridization of the crystal bonds. Valency considerations require, however, that there be only two cations for each group of three anions. Because of the tetrahedral crystal habit, this implies that one-third of all available cation sublattice sites are vacant, thereby producing a stiochiometric cation vacant-site concentration of 5.5×10^{21} cm^{-3}.

Since these "stoichiometric vacancies" are a structural component of the crystal, they do not carry a net charge. Nevertheless, this unusual structural element predominates over many of the physical properties of these crystals. These "stoichiometric vacancies" produce an extremely low thermal conductivity which is associated with the high anharmonicity of the asymmetric vibrations of atoms which surround the vacant sites. Even heavily doped In_2Te_3 exhibits intrinsic conductivity to very low temperatures. The stoichiometric vacancies and cations on the In sublattice can be either ordered or disordered but the conductivity of both is intrinsic.

Attempts to alter the conductivity of In_2Te_3 by irradiation near room temperature with large fluences of 100 MeV electrons, 1 MeV neutrons and ^{60}Co gammas have been unsuccessful.[41,42] This is an interesting result suggesting that further study of the radiation-damage properties of these defect compounds could eventually lead to a new approach to the radiation hardening of semiconducting devices. It has been suggested that non-equilibrium point-defect concentrations cannot be preserved in the defect tetrahedral semiconductors by irradiation of quenching.[42] In the present experiments, we have attempted

to test this hypothesis under the conditions of low-temperature irradiation.

The crystals used in the present experiments[43] were polycrystalline In_2Te_3 grown from stoichiometric amounts of very high purity In and Te. The starting material was first reacted in vacuum in a sealed quartz ampoule at 700°C. The temperature of the reacted material was then raised to 800°C for 24 hrs followed by a slow cool at a rate of 2-5°C/hr to 550°C. The ingot was then rapidly cooled to room temperature. The ingot formed was 3 x 1 x 0.5 cm^3 and consisted of dark crystallites about 1 mm^3. Near the center of the ingot, larger single crystals were found with the largest being 1 cm x 3 mm x 3 mm. It was estimated from inspection of the quartz ampoule that the crystals were nearly stoichiometric since the amounts of starting materials were in stiochiometric proportions to better than ± 0.02 atomic % and since no evidence of an unreacted residue was found in the ampoule.

An extensive investigation of the physical proerties was performed to insure that we had indeed grown In_2Te_3 rather than InTe, In_3Te_4, or one of the other stoichiometric combinations of In and Te.[43] Table 2-3 lists physical properties of the α(ordered) and β(disordered) phases of In_2Te_3 compared to our samples. Table 2-4 lists the properties of other possible compounds from In and Te which are likely to form during growth. It is clear from these two tables that our samples were In_2Te_3 and that they possessed some degree of ordering of the vacant sites. Figure 2-53 shows the intrinsic electrical properties of our sample before irradiation.

Figure 2-54 shows the 77°K EPR spectrum of In_2Te_3 before and after 77°K electron irradiation of 1 MeV to a fluence of 10^{17} e/cm^2. In addition to the very broad resonance which is probably the result of a small percentage of In on the vacant sites, four new resonances labeled A, B_1, B_2 and C appear.

Table 2-3. Physical properties of In_2Te_3.

Physical Property	α-Phase	β-Phase	Our Samples
Density	5.79 g/cm^3	5.73 g/cm^3	5.772 g/cm^3
Lattice Constant	18.50 A	6.158 A	6.158 ± .010 A with superstructure lines corresponding to 18.45 A
Cleavage	<111>	<111>	<111>
Electrical Conductivity at 300 K	~$10^{-7}\Omega^{-1}$cm^{-1} (intrinsic)	~$10^{-6}\Omega^{-1}$cm^{-1} (intrinsic)	1.5 X $10^{-7}\Omega^{-1}$cm^{-1} (intrinsic)
Thermal Conductivity at 300 K	2.8 X 10^{-3} cal/cm·sec·deg	1 X 10^{-3} cal/cm·sec·deg	~2 X 10^{-3} cal/cm·sec·deg
Band Gap	1.11 eV	~1.00 eV	1.11 eV
Thermo-Electric Power	0 mV/deg at 59.75 at. % Te -650 mV/deg (59.3 at % Te)	+600 mV/deg 61 at % Te)	<|± 3 mV/deg|
Mobility	~50 ± 10 cm^{2}V^{-1}sec^{-1}		41.2 cm^{2}V^{-1}sec^{-1}

Table 2-4. Physical properties of other possible In_xTe_{1-x} compounds.

MATERIAL	DENSITY (gm/cm^3)	LATTICE CONSTANT (A)	CONDUCTIVITY (Ω-$1cm^{-1}$)
OUR SAMPLE	5.772	6.158 and additional 18.50 lines	1.5×10^{-7}
α-In_2Te_3	5.79	18.50	10^{-7}
β-In_2Te_3	5.73	6.158	10^{-6}
InTe	6.29	8.437 a 7.139 b High pressure phase exists which is cubic with a = 6.16, not stable at STP	14×10^{-3}
In_3Te_4	5.88	4.26	?

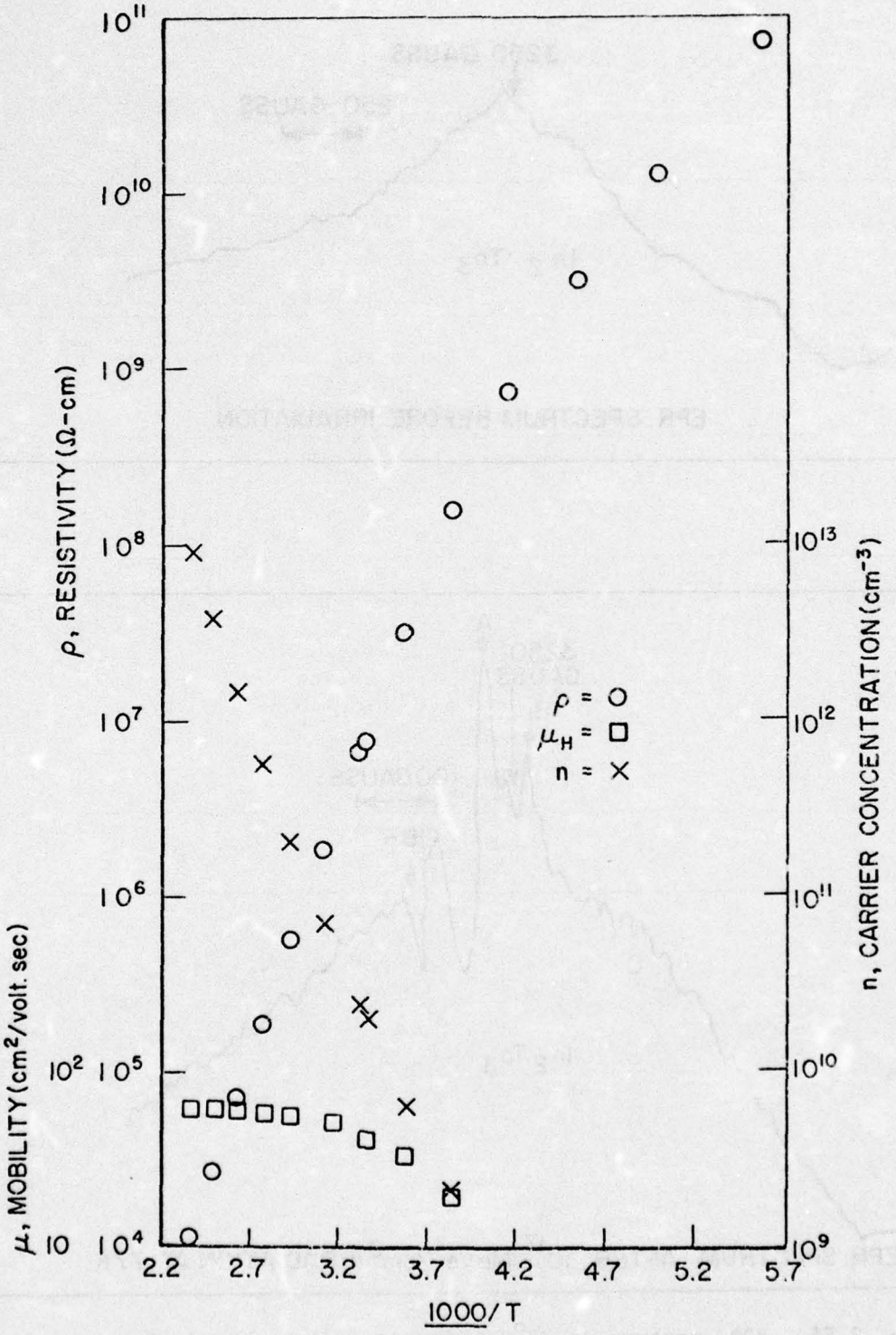

Fig. 2-53. Electrical properties of In_2Te_3 before irradiation.

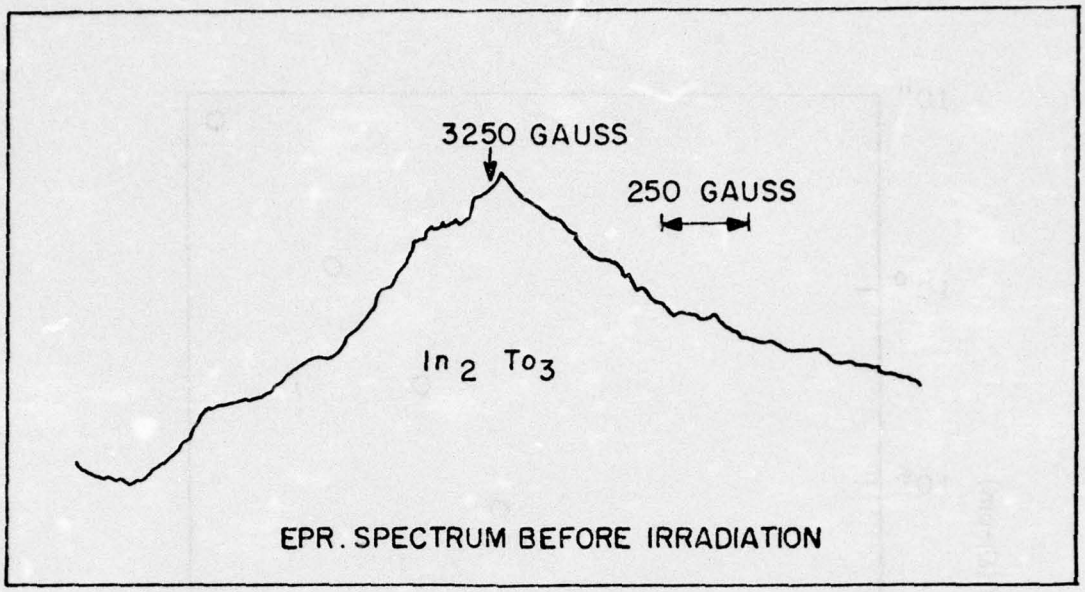

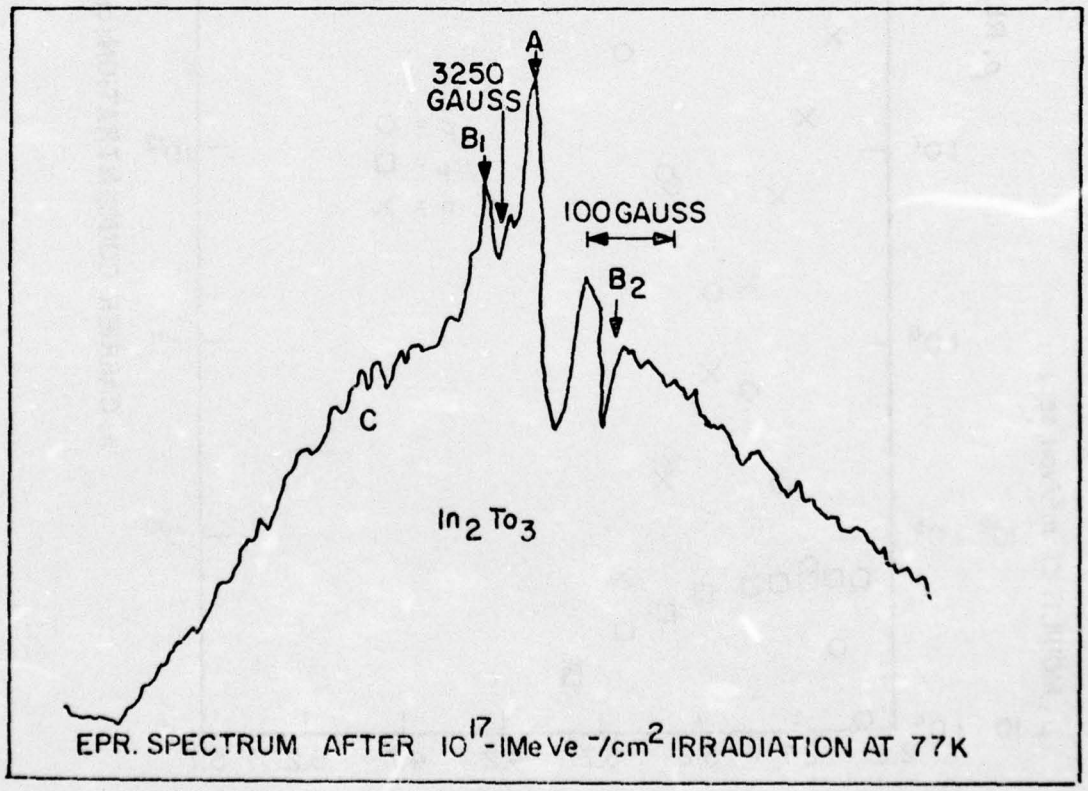

Fig. 2-54. EPR spectrum at 77°K before irradiation and after irradiation with 10^{17} - 1 MeV e/cm^2.

The defect-production rate at 77°K, as estimated from the A resonance, is of the order of 0.1 defects/1 MeV electron. This production rate is typical of 1 MeV defect production rates in other semiconductors.

No positive defect identifications can be made from these EPR spectra because the polycrystalline nature of the sample removes most of the structural information needed for such an analysis. It should be noted, however, that singly charged vacancies on the anion sublattice might be expected to be axial along a [111] direction while the cation vacancies would not. It is therefore possible that the A resonance is a Te vacancy while the other resonances are possibly associated with In sublattice defects. Further investigation of single crystal In_2Te_3 is needed to determine this with certainty.

Isochronal-annealing experiments were conducted from 100 to 300°K. Figure 2-55 shows the recoveries of the resonances labeled in the previous figure. Some annealing of all the resonances possibly occurs at lower temperatures since the intensities all decrease from the 100°K reference. If the stoichiometric vacancies on the cation sublattice tend to preferentially lower the radiation-induced defect stability on this sublattice, then annealing of these defects at a lower temperature is in agreement with the sublattice assignments suggested above. The annealing of the A resonance is extremely broad suggesting that a fundamentally different annealing mechanism may be occurring in this material.

It should be noted that all the resonances have recovered by room temperature, and that at 200°K, only about 20% of the A resonance remains. It should also be noted that no new resonances are formed as a result of annealing. This suggests that long-range defect migration and the formation of new defect complexes is not occurring. These observations also explain why radiation damage was not detected in the previous experiments in Ref. 42 and Ref. 43.

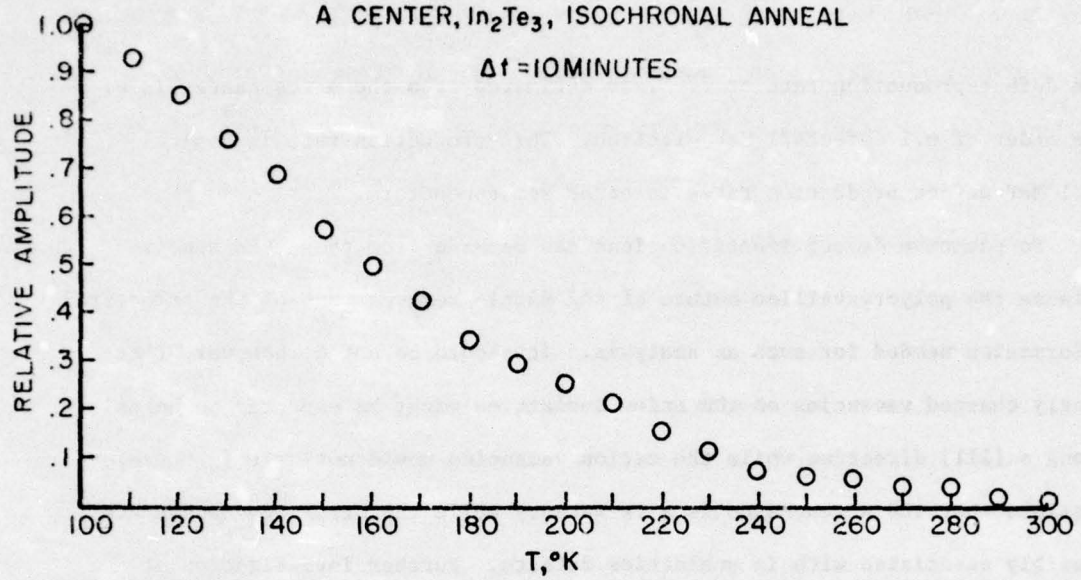

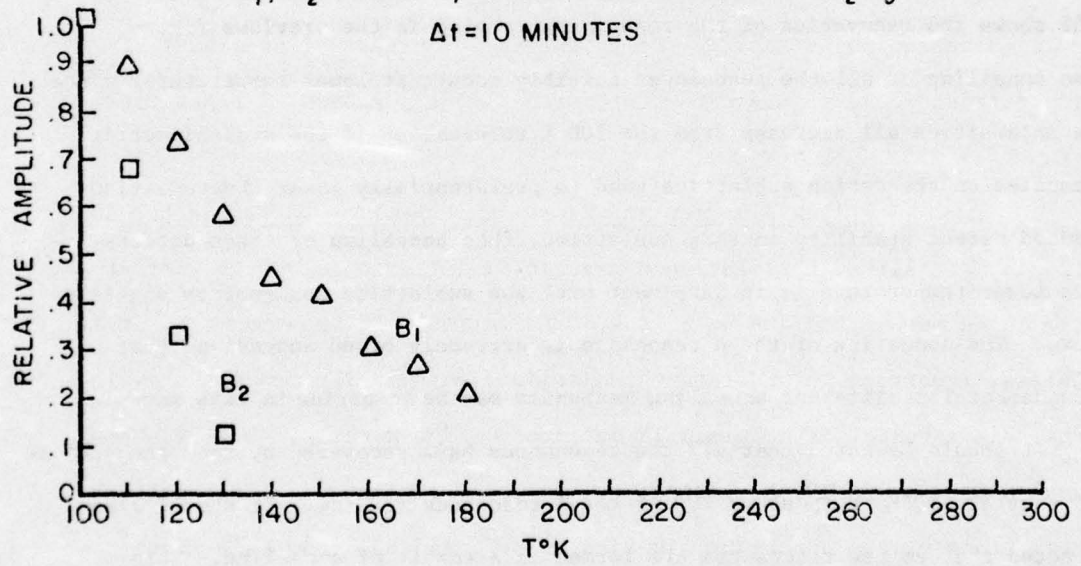

Fig. 2-55. Isochronal annealing of In_2Te_3.

We have shown that 1 MeV electron irradiation of In_2Te_3 at 77°K produces damage centers. We have also observed the isochronal annealing of these defects and find that all the centers anneal below room temperature and that no new centers are found. This suggests that long-range defect migration without annihilation does not occur in this material.

It is quite possible that all the defect tetrahedral semiconductors possess this ability to recover from radiation damage at room temperature since none that have been investigated have been shown to radiation damage easily at room temperature. This could be of future technological importance from a radiation hardening point of view. It is conceivable that solid solutions of defect semiconductors with non-defect semiconductors could lead to new semiconductor materials which will be able to sustain considerable damage, but still possess physical properties suitable for device fabrication. Although difficulties remain to be solved, the potential for orders-of-magnitude harder electronic devices suggests that further consideration of these materials is warranted.

2.3.3 Annealing Kinetics and Radiation Annealing in Si, Ge and GaAs

Although radiation damage in Si is reasonably well understood, the work in Ge has lagged due to a lack of successful EPR experiments. It is, nonetheless, important to understand radiation damage at low temperatures in Ge since this material is a common IR-detector window material in AF systems and is also used as an IR photodetector. In this section, we will briefly outline a study of the annealing kinetics in Ge[44] and show how this model has been useful in understanding the phenomenon of ionization radiation annealing in Si.[45] This model has also been used to predict a radiation annealing effect in GaAs[45] and suggests that forward-bias injection annealing of GaAs solar cells should occur.

When lightly doped ($n = 10^{14}/cm^3$) n-type Ge is electron irradiated at $4.2^{\circ}K$, acceptor levels are produced. These acceptors account for approximately 90% of all the radiation damage in this material. These acceptors can be removed following irradiation by the following mechanisms:

1. Thermal annealing at $65^{\circ}K$.
2. Radiation annealing at $7\text{-}10^{\circ}K$ where the electron-beam energy stimulating the annealing is below the displacement energy.
3. Intrinsic light ($h\omega > E_g$) optical annealing at about $27\text{-}30^{\circ}K$.
4. Extrinsic light ($h\omega < E_g$) optical annealing at $4.5^{\circ}K$ or lower.

Although it has been known for many years that vacancy-interstitial recombination is occurring during these various annealing mechanisms, the particular nature of the defect migration and annealing mechanisms has not been well understood. However, the results outlined above made it clear that the charge states of the defects were important in determining their stability.

Although it was a common belief that these defects were closely spaced Frenkel pairs, which could be annealed by the above mechanisms, in 1970 it was discovered that for all of the above annealing stages, the annealing rates were dependent on the <u>type</u> of n-dopant in the crystal.[46] This result suggested that long-range interstitial migration might be occurring at low temperatures in Ge as had been suggested for Si at a much earlier date.

A model for the annealing kinetics for all the above annealing mechanisms, and based upon defect charge states and a freely migrating interstitial, has been published during this contract.[44] Although several close-pair models exist, the present model is the only one from which all the annealing-rate constants can be calculated from first principles. Only a brief sketch will be presented here, since many of the calculations are quite lengthy. Further details may be obtained from Ref. 44.

Figure 2-56 lists the defects and charge states assumed to play a role in the various annealing mechanisms. In the following treatment, V represents the vacancy concentration, I the free interstitial concentration, and C the concentration of interstitials trapped at impurity sites of concentration i_o.

Figure 2-57 shows the assumed kinetics equations for these various concentrations as a function of time. The rate constant K_1, K_2 and K_3 determine the time dependence of the various concentrations of defects. The object has been to find approximate solutions to the system of differential equations (exact solutions in closed form do not exist) and to calculate the rate constants K_1, K_2 and K_3 from first principles for all the annealing situations mentioned above. That is is possible to accomplish this for the multitude of experimental data available[44] in the literature tends to lend strong support to the essential features of the model.

Two approximate solutions are possible for the fraction of vacancies $f = V/V_o$ remaining as a function of time. The approximations are given as I and II in Fig. 2-57. A comparison of the rate constants calculated from the carrier trapping model[44] is compared to the experimental results[44] in Fig. 2-58. It is clear that the model is capable of predicting the rate constants which can be measured to within a factor of 2 or so. This is remarkable since the rate constants can conceivably vary over many orders of magnitude.

Figure 2-59 shows a fit of the approximate solution I in Fig. 2-57 where the rate constant is calculated from first principles for a typical high-temperature thermal annealing case.

The optical annealing case at 4.5°K for light of lower energy than the band gap is shown in Fig. 2-60. Again, the fit is calculated. Figure 2-61 shows the fit of calculated and experimental annealing data for 30°K intrinsic

DEFECT CHARGE STATES USED IN MODEL

VACANCY (double acceptor)	FREE INTERSTITIAL	GROUP V IMPURITY	COMPLEX
V^{--}	I^{+}	Sb^{+}	$I^{0}Sb^{0} = C^{0}$
V^{-}	I^{0}	Sb^{0}	$I^{0}Sb^{+}$, $I^{+}Sb^{0}$ $\} = C^{+}$
			$I^{+}Sb^{+} \rightarrow$ dissociates

1. $I^{+} + Sb^{+} \xrightarrow{K_1}$ COMPLEX DISSOCIATION
2. $I^{0} + Sb^{+,0} \xrightarrow{K_2}$ C retrapping, assume larger than $I_0 + V \rightarrow$ annihilation
3. $I^{+} + V^{-} \xrightarrow{K_3}$ annihilation

   $I^{+} + V^{--} \xrightarrow{K_3}$ annihilation

Fig. 2-56. Processes and defect charge states for low-temperature annealing in n-type Ge.

KINETICS EQUATIONS FOR MODEL

$$\begin{cases} dC/dt = -K_1 C + K_2 (i_0 - C)\ I & (1) \\ dV/dt = -K_3 I V & (2) \\ V = I + C & (3) \end{cases}$$

where $V = V^0 + V^- + V^{--}$, $I = I^0 + I^+$

K_1 = PROBABILITY FOR COMPLEX DISSOCIATION/UNIT TIME

$K_2 = P_I(o)\,\sigma_C V_I$

$K_3 = \{P_I(+1)\,P_V(-1)\,\sigma_{V(-1)} + P_I(1)\,P_V(-2)\,\sigma_{V(-2)}\}\,V_I$

TWO APPROXIMATE SOLUTIONS

1. STEADY STATE SOLUTION (LARGE RETRAPPING PROBABILITY)

$K_1/K_2 \ll i_0$, $\quad V \ll i_0$ (at $t=0$, $V \leq 0.15\, i_0$)

then $dC/dt \approx 0$

$\rightarrow dV/dt \approx -(K_3/i_0)\,V^3$ (THIRD ORDER)

$$\boxed{f = V/V_0 = \left[1 + (2K_3 V_0^{\,2}/i_0)t\right]^{-1/2}}$$

II. TRANSIENT SOLUTION (NEGLECT RETRAPPING)

near $t=o$, $K_2(i_0 - C)\ I = K_2(i_0 - C)\ (V - C) \approx O$

$$\boxed{f = V/V_0 = \frac{e^{-(u-u_0)}}{1 + u_0 e^{u_0}\left[E_1(u) - E_1(u_0)\right]}}, \quad E_1(x) = \int_x^\infty p^{-1} e^{-p}\, dp$$

$$u = u_0 e^{-K_1 t} \quad u_0 = K_3 V_0 / K_1$$

Fig. 2-57. Kinetics equations for annealing models.

COMPARISON WITH EXPERIMENT

1. RADIATION ANNEALING AT 7-8° K

$$K_{calc} = 2K_3 V_o^2 / i_o = 8.5 \times 10^{-4} \text{ sec}^{-1}$$

$$K_{exp} = 11.2 \times 10^{-4} \text{ sec}^{-1}$$

2. MONOCHROMATIC LIGHT AT 4.2°K

$K_{calc} \simeq 10^{-6} \text{ sec}^{-1}$ or 1000 times slower than radiation annealing

3. MONOCHROMATIC LIGHT AT 30°K

$p \simeq \Delta p = \alpha I_o \tau_p = 5 \times 10^9 \text{ cm}^{-3}$, $\alpha = 5 \text{ cm}^{-1}$ $I_o = 10^4$ photons/cm^2 - sec

$\tau_p \simeq 10^{-5}$ sec at 30° K

$$K_{1_{calc.}} = 1/t_h = p v_h \sigma_h(+) = 2.5 \times 10^{-2} \text{ sec}^{-1}$$

$$K_{1_{exp}} = 1.67 \times 10^{-2} \text{ sec}^{-1}$$

$n = 2 \times 10^{14} \text{ cm}^{-3}$ due to thermal ionization

$P_V(-1) \simeq 1$ $P_I(+1) = 2.5 \times 10^{-8}$

$$u_{o_{calc.}} = K_3 V_o / K_1 = 1.7$$

$$u_{o_{exp}} = 1.0$$

Fig. 2-58. Comparison of calculated and experimental rate constants.

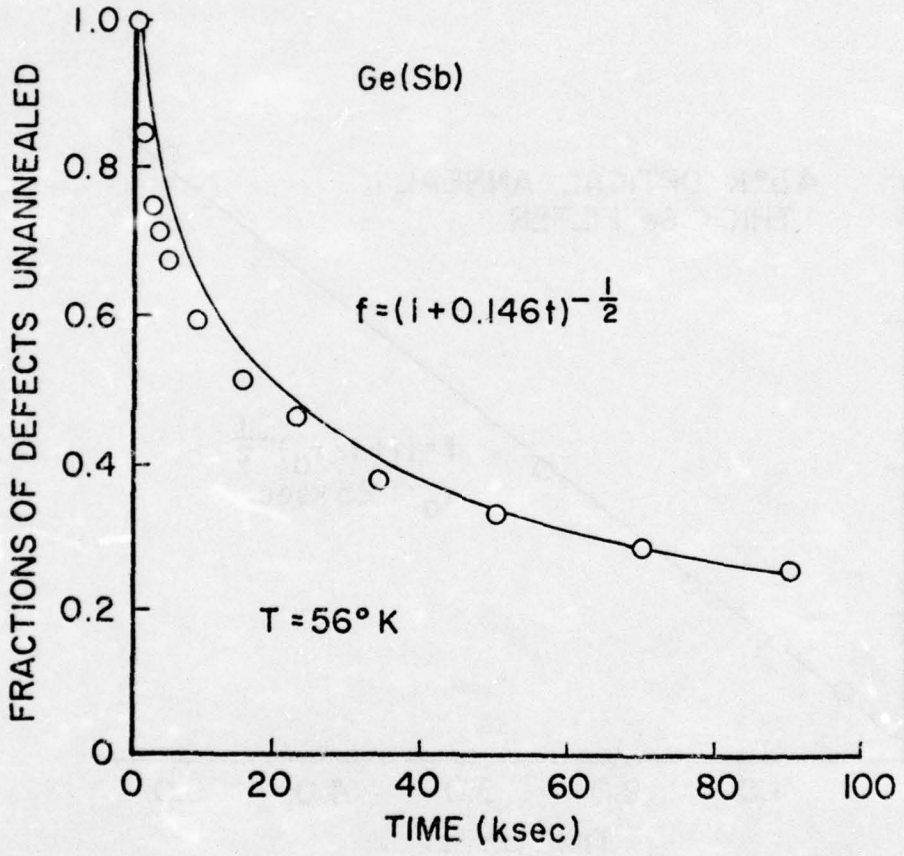

Fig. 2-59. Calculated fit to thermal annealing data.

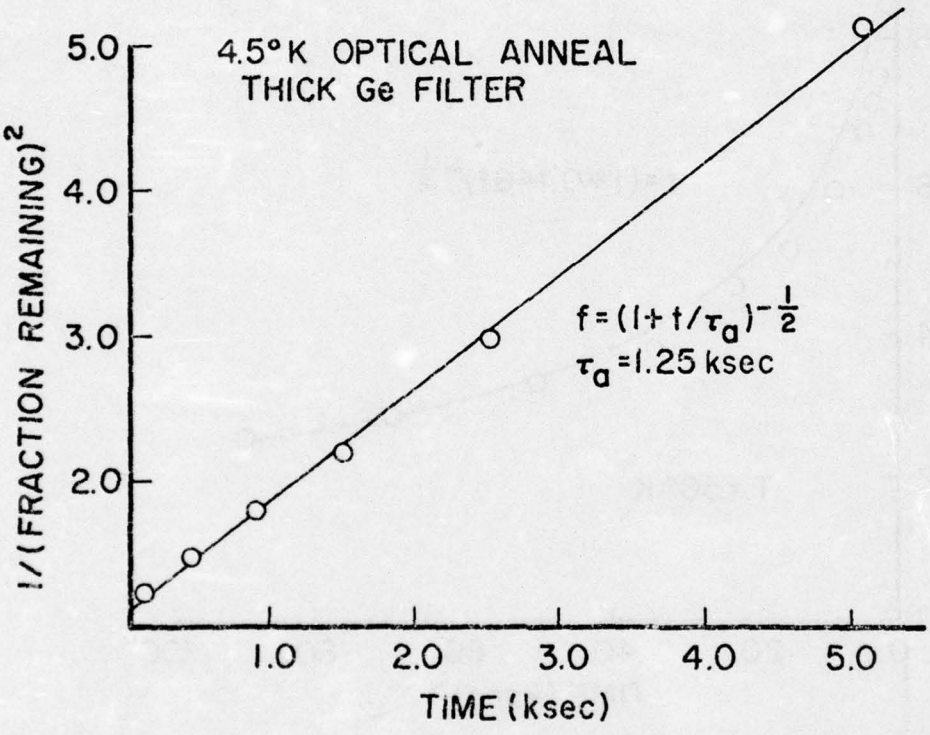

Fig. 2-60. Calculated fit to extrinsic-light optical annealing at 4.5°K.

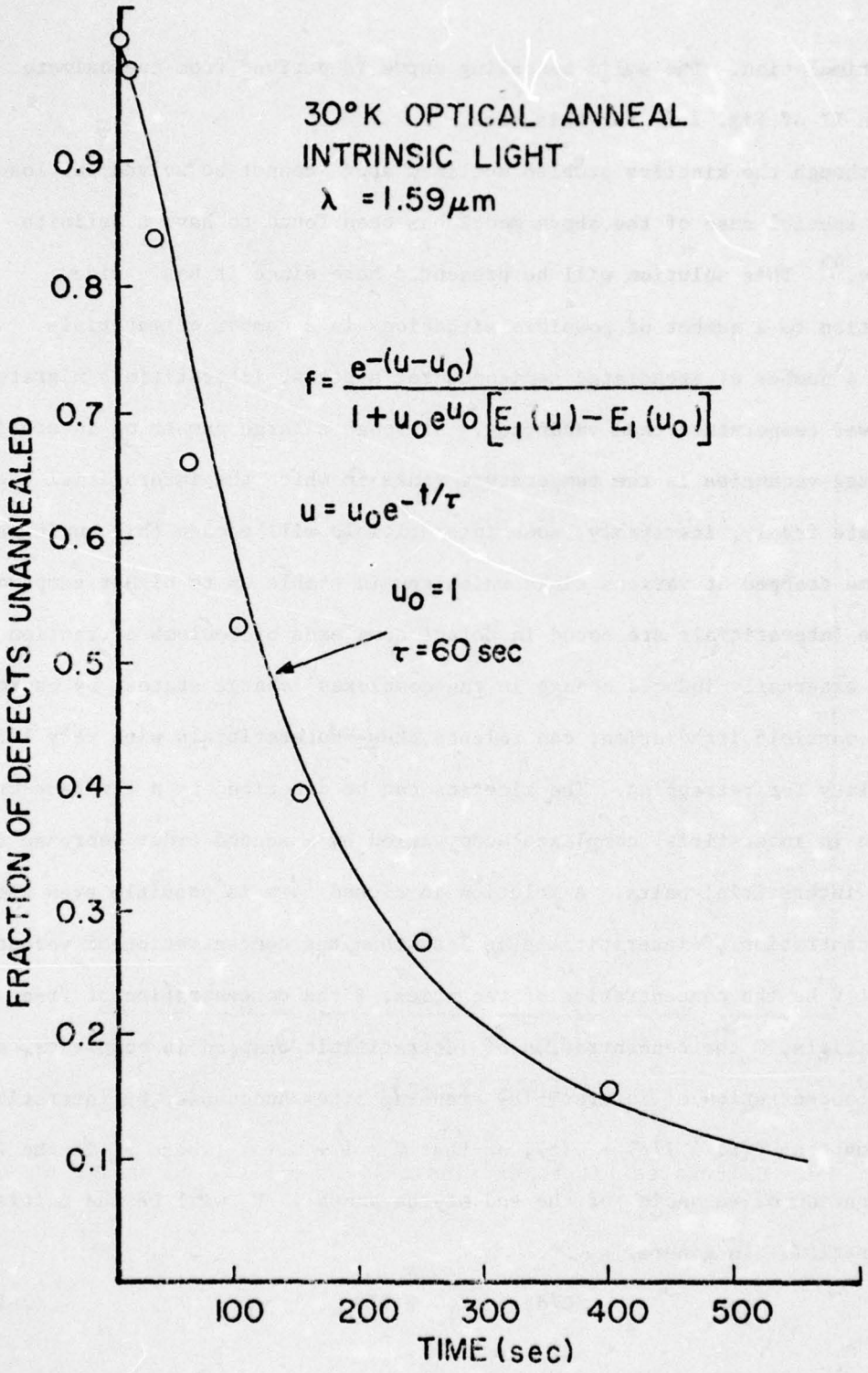

Fig. 2-61. Calculated fit to 30°K intrinsic-light optical annealing.

light stimulation. The solid annealing curve is derived from approximate solution II of Fig. 2-57 for this case.

Although the kinetics problem outlined above cannot be solved in closed form, a special case of the above model has been found to have a definite solution.[45] This solution will be presented here since it has a wider application to a number of possible situations in a number of materials.

In a number of irradiated semiconductor systems, interstitials migrate at a lower temperature than vacancies. Although a large number of interstitials annihilate vacancies in the temperature range in which the interstitial begins to migrate freely, inevitably, some interstitials will escape this annihilation to become trapped at various sinks which remain stable up to higher temperatures. If these interstitials are bound in defect complexes by Coulomb attraction then an externally induced change in the complexes' charge states, by photon or fast particle irradiation, can release these interstitials with very little probability for retrapping. The kinetics can be described by a first-order decrease in interstitial complexes accompanied by a second order decrease in vacancy interstitial pairs. A solution in closed form is possible even when the concentration of interstitials is less than the concentration of vacancies.

Let V be the concentration of vacancies, I the concentration of free interstitials, C the concentration of interstitials trapped in complexes, and N_t the concentration of interstitial trapping sites unoccupied by interstitials. We assume that $V(t) \geq I(t) + C(t)$, or that $V = I + C + V_\infty$ where V_∞ is the final concentration of vacancies of the end of the anneal. V_o will be the initial concentration. In general

$$dC/dt = -K_1 C + KIN_t \qquad (2\text{-}1)$$

$$dI/dt = K_1C - KIN_t - K_2IV \tag{2-2}$$

$$dV/dt = -K_2IV \tag{2-3}$$

where at $t = 0$, $V = V_o$, $C = C_o$, and $I = 0$.

If we assume the retrapping term $+KIN_t$ in Eq. 2-1 can be neglected due to a radiation-induced change in the complex charge state, which drives interstitials away from the complexes, then $K = 0$.

We can now solve Eq. 2-2 at once with the solution given by

$$C = C_o e^{-K_1 t}. \tag{2-4}$$

By substitution of $V = I + C + V_\infty$ into Eq. 2-3 we have

$$dV/dt = -K_2IV$$

$$= -K_2V\,(V - V_\infty - C). \tag{2-5}$$

This is the differential equation which we must solve in order to obtain a complete solution. We make the following substitutions. Let $y = \frac{1}{V}$, $x = K_2t$, $\alpha = K_1/K_2$.

The Eq. 2-5 becomes

$$dy/dx + g(x)y = 1 \tag{2-6}$$

where $g(x) = V_\infty + C(x) = V_\infty + C_o e^{-\alpha x}$.

Equation 2-6 can be separated if we multiply by the integration factor

$$e^{G(x)} = e^{\int g(x)dx}$$

where $g(x) = \frac{dG(x)}{dx}$.

Thus $d[e^{G(x)}y] = e^{G(x)}dx$

or $$e^{G(x)}y - e^{G(o)}y_o = \int_o^x e^{G(x)}dx. \tag{2-7}$$

Since G(0) = 0 and

$$G(x) = \int_o^x g(x)\,dx$$

$$= \int_o^x (V_\infty + C_o\, e^{-\alpha x})\,dx,$$

we can solve Eq. 2-7 for $y^{-1} = V$; i.e.,

$$V = y^{-1} = \frac{e^{G(x)}}{\frac{1}{V_o} + \int_o^x e^{G(x)}dx}\ .$$

We summarize the following solutions for the various concentrations:

$$\frac{V}{V_o} = \frac{e^{G(x)}}{1+R(x)} \tag{2-8}$$

where

$$G(x) = V_\infty x + \frac{C_o}{\alpha}(1 - e^{-\alpha x}),\ R(x) = V_o\int_o^x e^{G(x)}dx,\ \text{and}\ \frac{C}{C_o} = e^{-\alpha x} \tag{2-9}$$

and

$$I = (V - V_\infty) - C\ . \tag{2-10}$$

Therefore, all the concentrations are known as a function of time once R(x) is evaluated.

Consider now the explicit form of R(x):

$$R(x) = \int_o^x e^{G(x)}\,dx$$

$$= \int_o^x e^{[v_\infty \alpha x]}\ e^{-c_o[e^{-\alpha x}-1]}dx$$

where $v_\infty = V_\infty/\alpha$, $c_o = C_o/\alpha$, and $\theta = c_o \exp(-\alpha x)$. Then

$$x = -\frac{1}{\alpha} \ln(c/c_o)$$

$$dx = -\frac{1}{\alpha c} dc$$

and

$$R(x) = R(c) = v_o[c_o]^{v_\infty} \exp[c_o] \int_c^{c_o} z^{-(v_\infty + 1)} e^{-z} dz$$

$$= v_o[c_o]^{v_\infty} \exp[c_o]\{\Gamma[-v_\infty, c(x)] - \Gamma[-v, c_o]\}. \quad (2\text{-}11)$$

Here,

$$\Gamma(a,x) = \int_x^\infty x^{a-1} e^{-x} dx$$

is the incomplete Gamma function which is tabulated in math tables.

The solution takes on a particularly simple form if $V_\infty = 0$. Then we consider integrals of the form

$$\Gamma(0,x) = \int_x^\infty x^{-1} e^{-x} dx = E_1(x)$$

which is the exponential integral, also found in math tables. Closed solution approximations exist for $E_1(x)$ and are given by

$$E_1(x) = \begin{cases} -\ln x + \sum_{i=0}^{5} a_i x^i; & 0 \le x \le 1 \\ x^{-1} \ln x \dfrac{x^2+b_1x+b_2}{x^2+c_1x+c_2}; & 1 \le x \le \infty \end{cases}$$

where the accuracy is better than about 1 part in 10^5.

This model is reapplied to the optical annealing at 30°K to take into account the fact that only an 88% recovery is observed for this stage. This is represented by $V_\infty/V_o = 0.12$. A plot of this model is shown in Fig. 2-62 which should be compared to the results of Fig. 2-61 which assumed a 100% recovery.

This model has also been applied to a radiation-annealing case in Si which has never before been fit by typical annealing kinetics.[47] The data

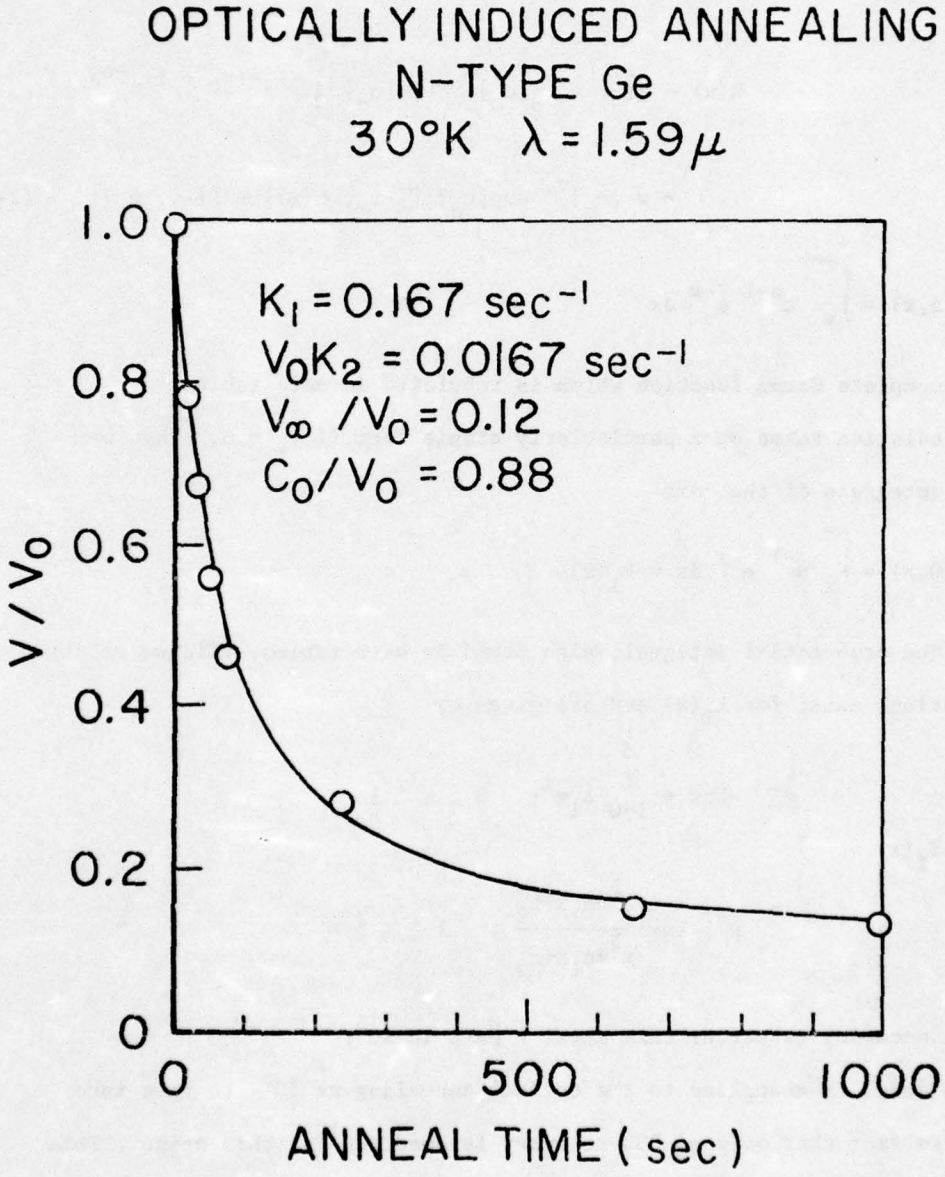

Fig. 2-62. Fit to 30°K optical annealing data in Ge for 80% recovery.

in Fig. 2-63 are for float-zone Si where the trapping site is presumably carbon. Here, the parameters K_1 and K_2 were adjusted to give the best fit and the other listed parameters were from experimental data.[47] Figure 2-64 shows the fit to radiation annealing in a pulled sample of high oxygen content. The percentage recoveries are quite different for these two samples, presumably due to different interstitial trapping-site concentrations and types. The curve in Fig. 2-64 has been fit with no adjustable parameters and although not a perfect fit, it is approaching the accuracy of the experiment.

It has also recently been demonstrated by Kimerling and Lang[48] that GaAs will optically anneal. We believe this to be an important reason for the forward-bias injection annealing demonstrated in GaAs lasers and LED's.

2.3.4 Irradiation Effects in Solar Cells

The objective of this work has been to determine the behavior of various solar cell designs subject to fast (1 MeV) electron bombardment in order to determine which physical parameter changes induced by irradiation will be most detrimental to the useful lifetime of solar cell devices fabricated from these materials and subsequently subjected to a hostile radiation environment.

Silicon solar cells are presently being used as the primary power source for Air Force satellites. There currently exists within the Air Force a need to improve both the efficiency of power conversion of these cells and the device lifetime in orbit (which degrades primarily through Van Allen belt radiation damage). This Air Force need for improvement is based upon anticipated increases in satellite power requirements and orbit lifetimes of future missions, since present mission limits are already dictated primarily by the power output versus orbit time of the solar cell arrays. Because a redesign of the satellite solar cell arrays for higher output, achieved by increases in the number

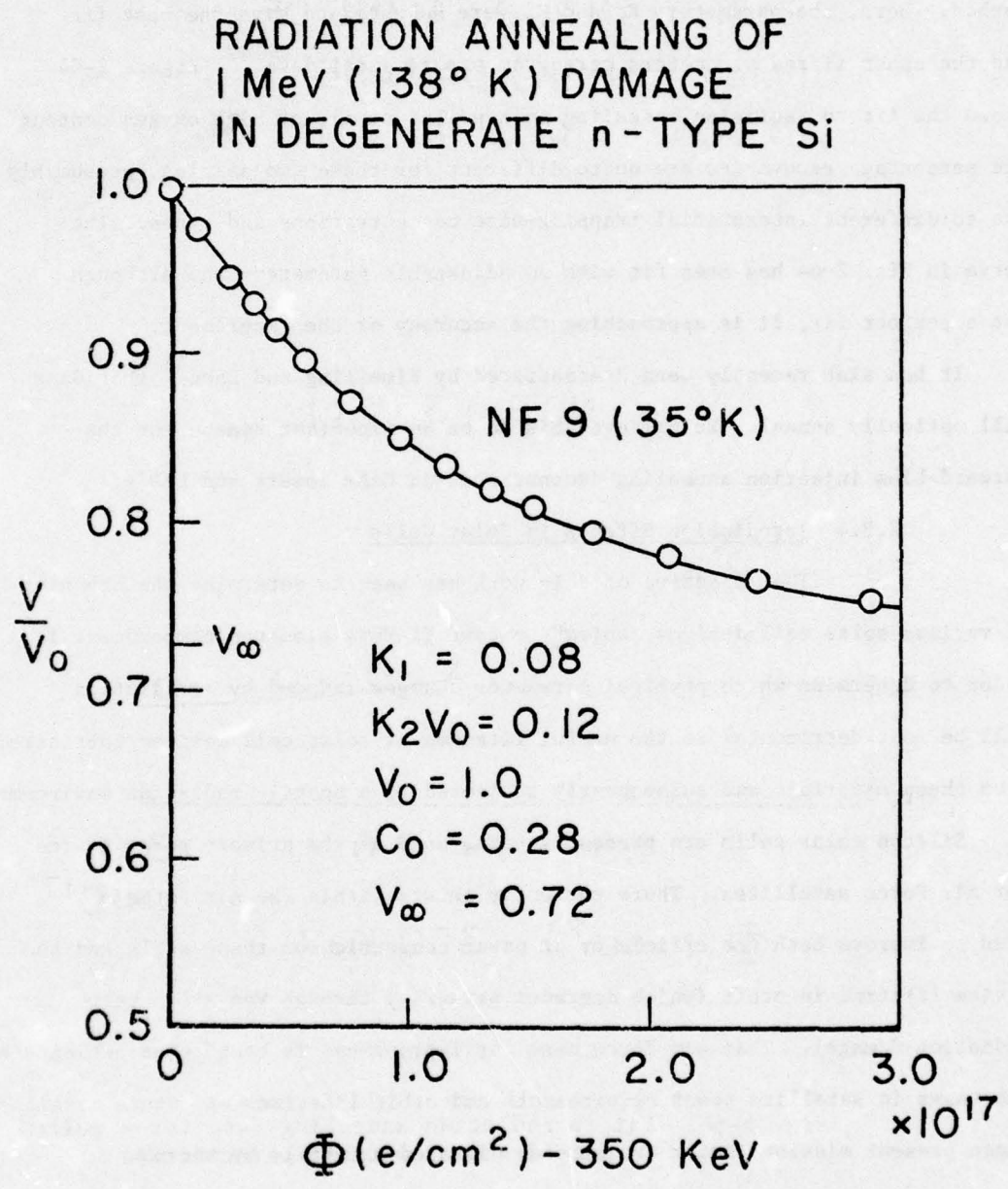

Fig. 2-63. Fit to radiation annealing data in n-type Si for a float-zone sample.

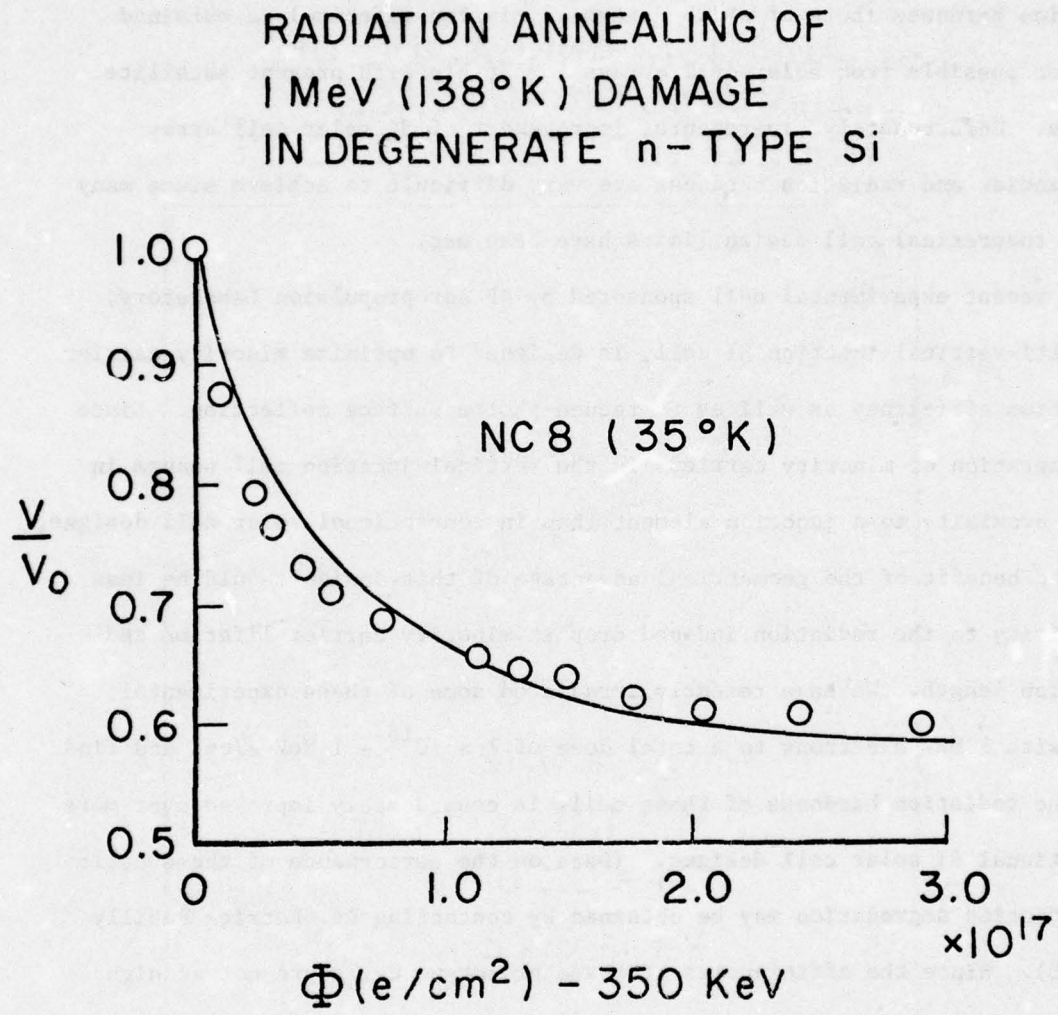

Fig. 2-64. Fit to radiation annealing data for a pulled Si sample (no adjustable parameters).

of cells, would require a major redesign of the total satellite package, at a great expense, economics dictates that higher conversion efficiencies and radiation hardness (both of which determine mission lifetime) be obtained whenever possible from solar cell arrays compatible with present satellite designs. Unfortunately, incremental improvement of Si solar cell array efficiencies and radiation hardness are very difficult to achieve since many of the theoretical cell design limits have been met.

A recent experimental cell sponsored by AF Aeropropulsion Laboratory, the multi-vertical-junction Si cell, is designed to optimize minority-carrier collection efficiency as well as to reduce photon surface reflection. Since the generation of minority carriers in the vertical-junction cell occurs in closer proximity to a junction element than in conventional solar cell designs, an added benefit of the geometrical advantage of this design should be less sensitivity to the radiation induced drop in minority carrier lifetime and diffusion length. We have recently irradiated some of these experimental cells with 1 MeV electrons to a total dose of 1×10^{16} - 1 MeV e/cm^2 and find that the radiation hardness of these cells is considerably improved over more conventional Si solar cell designs. (Data on the performance of these cells and radiation degradation may be obtained by contacting Dr. Patrick Rahilly of AFPL). Since the efficiencies of these prototype cells are not as high as eventually anticipated, it is not possible to precisely assess the improvement in radiation hardness of this design at this time. Further experiments on these cells, particularly, a measurement of the radiation-induced degradation of the minority carrier lifetime and a measure of the unirradiated effective-diffusion length, are planned for the near future as soon as additional cells become available from the vendor.

In addition to the above, approximately 40 Si solar cells of various designs have now been irradiated to fluences of 10^{13}, 10^{14}, 10^{15} and 10^{16} e/cm^2 for AFPL. Also, over 30 Li-doped Si Samples have been irradiated for Dr. Brown of Ohio State, at the request of AFPL, to 10^{14}, 10^{15}, 2×10^{15}, and 3×10^{16} e/cm^2. These samples will be studied by NMR and EPR at Ohio State to determine specific properties of the radiation-induced defects and their annealing. The object of this program is to investigate the self annealing induced by Li doping of Si in an attempt to enhance the radiation hardness of Si cells by this technique. We have therefore completed approximately 310 irradiations for this study.

The recent production of many new semiconductor materials of reasonable size and quality has prompted a search for alternative solar cell materials for both space and terrestrial applications. Based on an ideal diode model, $CuInS_2$ appears to be a material deserving further experimental study for solar energy conversion.[49] The maximum theoretical efficiency for energy conversion has been calculated for $CuInS_2$, using the model of Wysocki and Rappaport,[50] to be 27.4 to 32.1%, corresponding to minority carrier lifetimes of 10^{-8} to 10^{-6} sec. The efficiencies for Si, GaAs, and CdS, based on this model, are 24%, 28%, and 19% respectively. Since both shallow donor and acceptor states appear to be related to lattice defects in $CuInS_2$, solar cells from this material may prove to be more radiation-damage resistant in a space environment than Si cells.

Recent interest has developed in GaAs as a highly efficient solar cell material. Figure 2-65 shows the behavior of a typical Varian GaAlAs-GaAs solar cell as a function of concentration ratio, C'. In this figure, "C' = 312" means a concentration ratio of 312 suns. The efficiences of the GaAlAs window cells have reached 15% unconcentrated and 17% in a concentrator configuration. It should be noted that the current output for C' = 312 is approximately 10A/cm^2.

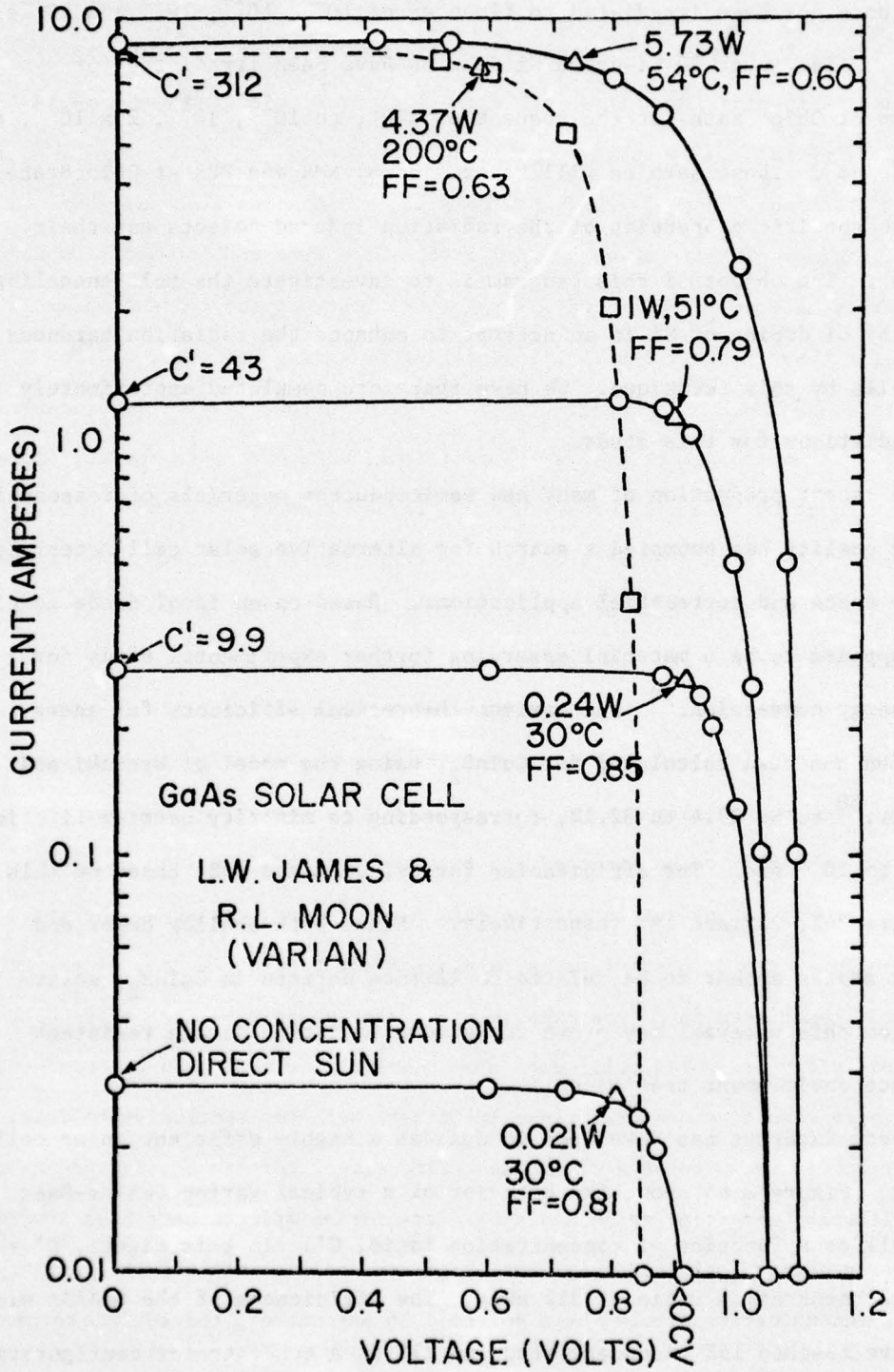

Fig. 2-65. I-V curves for typical GaAs-GaAlAs solar cell for various concentration ratios.

From the radiation-annealing model of the previous section, it might be expected that such large minority-carrier currents might provide an annealing mechanism for radiation damage exposure from the Van Allen Belts.

C. E. Barnes[52] has observed that GaAs laser diodes will anneal when forward biased. This is shown in Fig. 2-66. Note that the forward-bias current is of the same order of magnitude as the output current for concentration GaAs cells shown in Fig. 2-65. The annealing of Barnes was after a ^{60}Co irradiation of 1×10^{7} rad or about 5×10^{14} 1 MeV e/cm^2. Appreciable annealing is seen in 1 hour. Figure 2-67 shows additional data of Barnes for the annealing as a function of diode temperature.[53] Barnes reports that the 230°C annealing stage in GaAs is shifted to room temperature by forward biasing the diodes. Hum and Barry have also assumed this effect on LED's (GaAs) after ^{60}Co, 2 MeV neutrons, and 100 MeV protons.[53]

Since a solar cell is automatically forward biased when illuminated (the injection current of interest is approximately the solar cell short-circuit current), the possibility exists that significant annealing of the space radiation damage is to be expected and that the rate of annealing should increase as the output current of the cell is increased. It should be noted that the damage rate to solar cells in a space environment is many orders of magnitude lower than in Barnes experiment. Experiments have been planned to test this effect in solar cells once some concentrator cells can be obtained. Preliminary results on several 1-sun cells have not been conclusive to date; however, there seems to be a slight annealing effect for lightly damaged cells.

Although GaAs solar cells and their irradiation effects have been studied for over a decade, only recently have large-area cell growth and the very high surface-recombination problem been solved. In particular, the surface recombination

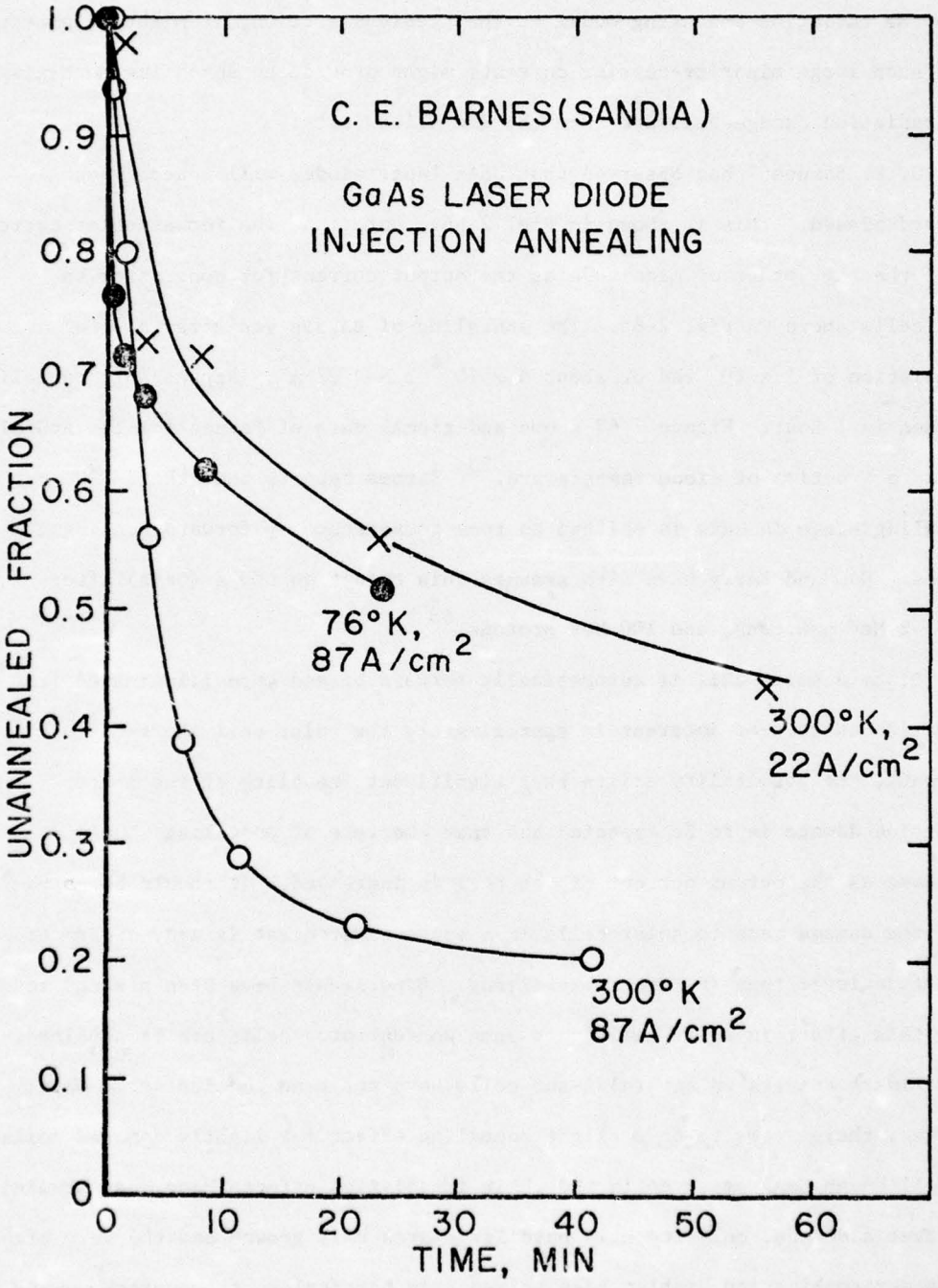

Fig. 2-66. Injection annealing of irradiated GaAs laser diode as a function of time for various forward currents.

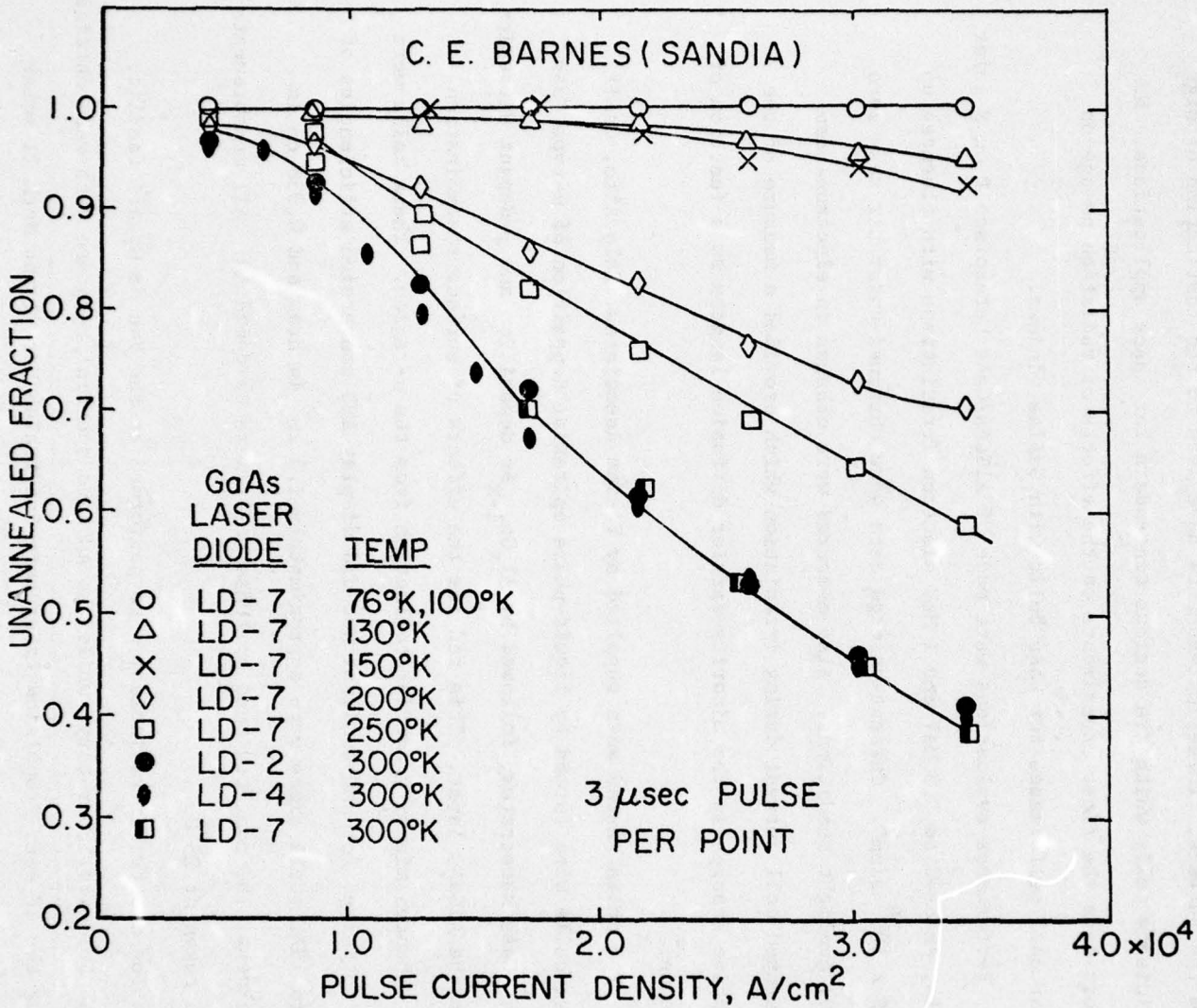

Fig. 2-67. Forward-current annealing for various temperatures.

problem has been overcome by the growth of a layer of greater bandgap GaAlAs over the cell which tends to reflect carriers toward the junction and away from the surface. These improvements have lead to the fabrication of high efficiency cells which are serious contenders for space applications. We report here the first experiments on the effects of radiation damage on solar cell performance for GaAs cells with GaAlAs windows.

Performance evaluations were made of AlGaAs/GaAs heteroface P on N solar cells, exposed to 0.5 MeV and 1 MeV electron irradiations with fluences up to 6×10^{16} e/cm^2. Current-voltage data were obtained under air mass zero (AMO) sunlight conditions. Also measured were changes in electron-beam-generated cell current during irradiation which provided a measure of the relative changes in the minority-carrier diffusion lengths as a function of fluence.

The cells tested were supplied by Varian Associates, Palo Alto, Calif. These cells were formed by liquid-phase epitaxial deposition of n-type GaAs on n^+ GaAs substrates, followed by $Al_xGa_{1-x}As$ deposition and p-dopant diffusion from the AlGaAs layer. This reduces the effects of surface recombination and enhances minority-carrier collection from the p-region. These cells were not optimized for AMO sunlight but did display AMO conversion efficiencies of 12 to 13%. Cell sizes were approximately 1.5 cm^2 in area and 0.038 cm in thickness. The contacts used on these cells were Ge-doped Au. All measurements were taken at 25°C.

The electron irradiations were performed at the Van de Graaff facility at AF Avionics Laboratory, while the AMO and spectral response data were obtained using the AF Aero Propulsion Laboratory Spectralab Mark I and Mark II solar simulators.

Results for the 1 MeV electron-damage experiments are shown in Fig. 2-68. Relative data are presented with initial data given in the insert. The initial diffusion lengths for the minority carriers in the p and n material were not measured. However, the relative changes in the sum of the diffusion lengths $(L_n + L_p)/(L_{n_o} + L_{p_o})$ do follow a simple relationship given by

$$\frac{L}{L_o} = \frac{1}{\sqrt{1 + \beta\phi}} \tag{2-21}$$

where $\beta = L_o^2 K$, K is defined as the electron damage coefficient, ϕ is the electron fluence, and L_o is the value of $L = L_n + L_p$ for $\phi = 0$. The solid line in Fig. 2-68 for (L/L_o) was based on calculations using Eq. 2-12 with $\beta = 3.43 \times 10^{-15}$ cm^2/e; the experimentally determined points were used to obtain β from a least squares fit.

The relative changes in the short-circuit current, I_{sc}, open-circuit voltage, V_{oc}, and maximum power, P_{max}, follow the characterisitc form

$$\text{Relative Value} = 1 - \alpha \ln(1 + \beta\phi) \tag{2-13}$$

until $\phi > 10^{15}$ e/cm^2, where deviations become quite drastic. The data suggest that beyond $\phi = 10^{15}$ e/cm^2, the V_{oc}, I_{sc}, and P_{max} become linearly dependent on the minority-carrier diffusion length.

Figure 2-69 illustrates the voltage and current at maximum power (V_{mp}, I_{mp}) as a function of 1 MeV electron fluence. The V_{mp} drops by nearly 4% after 10^{13} e/cm^2 and then rises. Simultaneously I_{mp} degrades in a manner described by Eq. 2-13. The observed behavior of V_{mp} can be explained by series-resistance effects wherein the rapid drop in I_{mp} reduces the voltage loss across the series resistance, and thus produces the observed increase in V_{mp} at higher fluences.

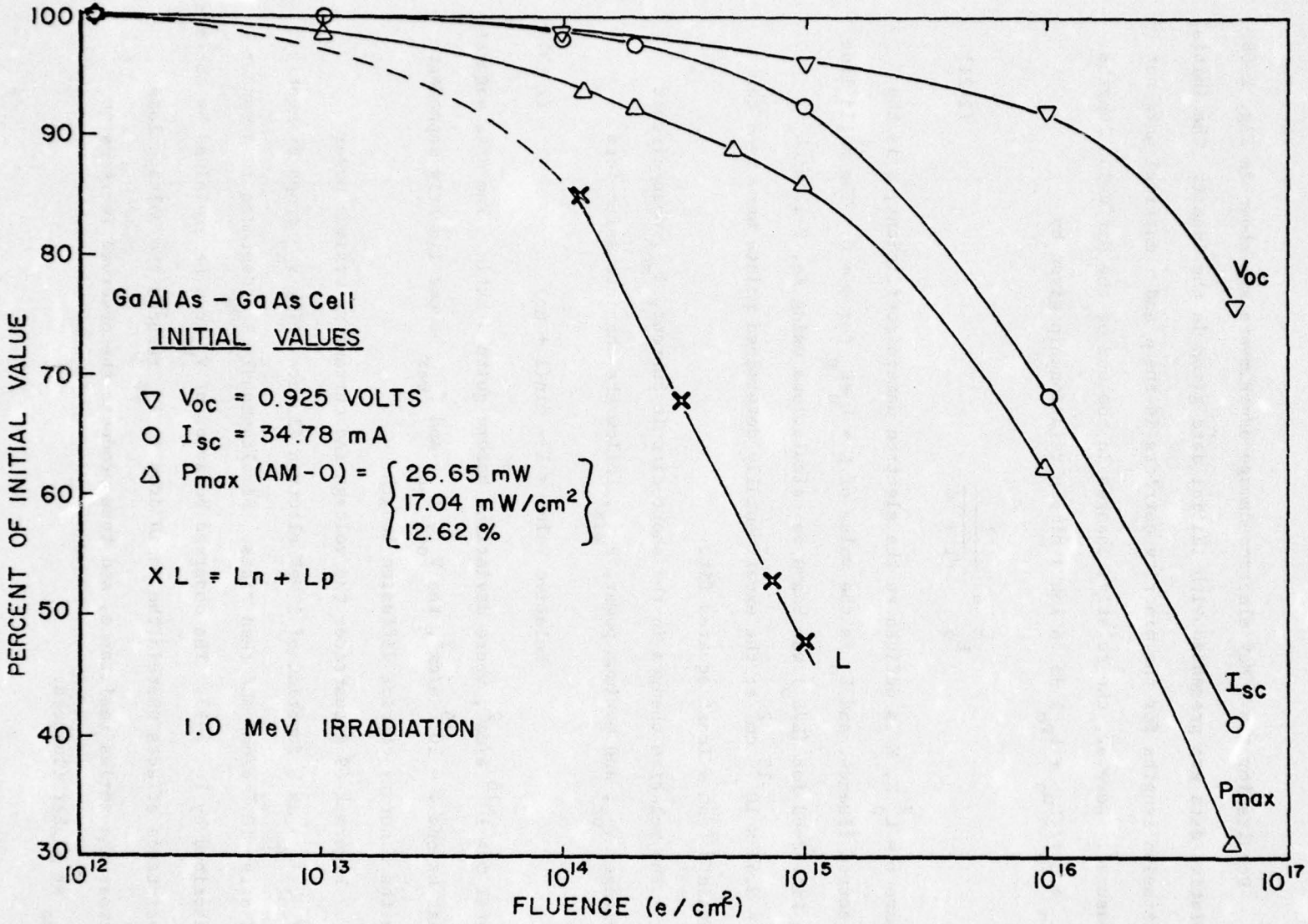

Fig. 2-68. 1 MeV degradation of GaAlAs-GaAs solar cell.

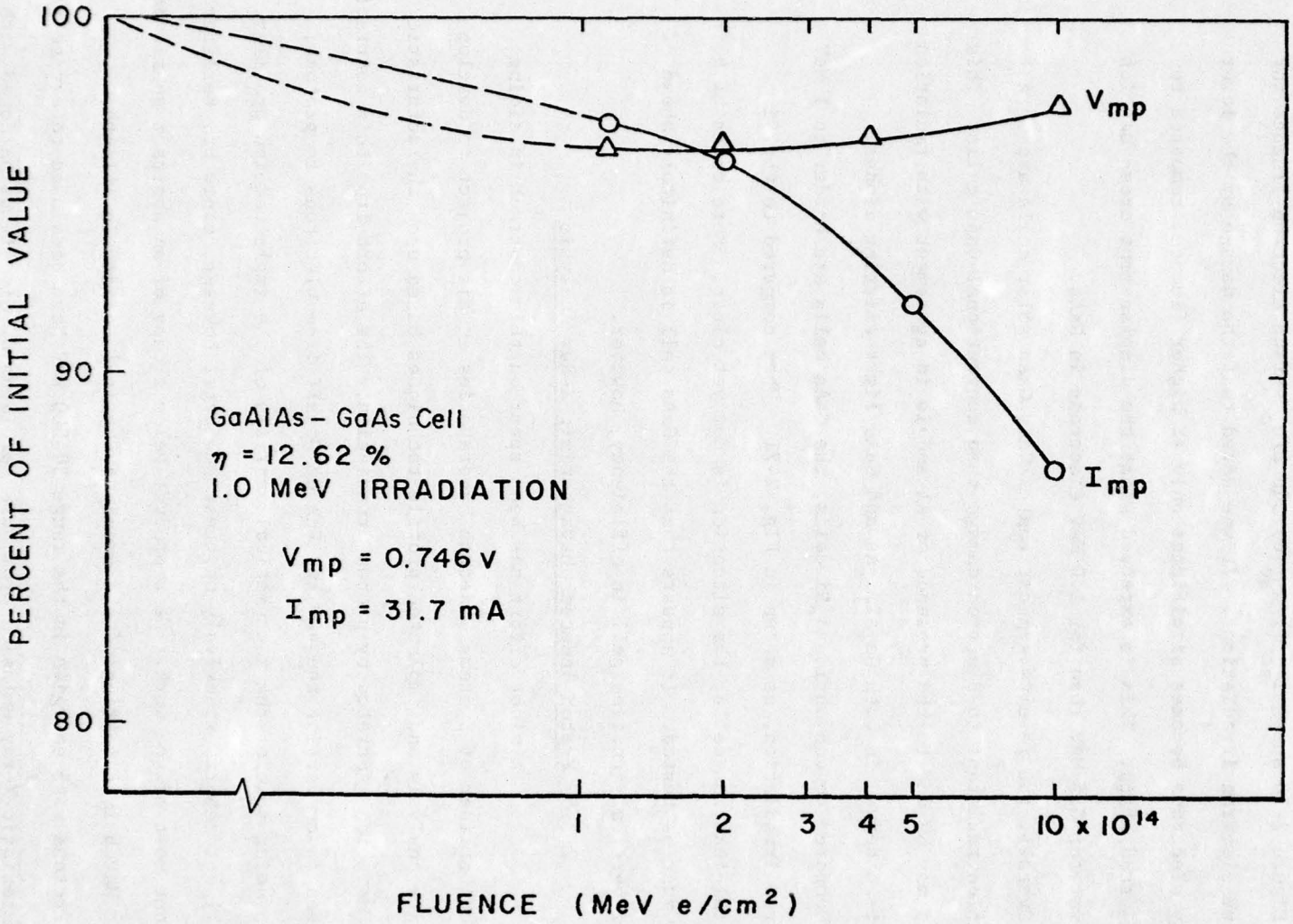

Fig. 2-69. V_{mp} and I_{mp} versus 1 MeV fluence.

Figure 2-70 shows $I_{sc}(\phi)/I_{sc}(0)$ and L/L_o versus electron fluence for 0.5 MeV electron irradiations. It was noted that the damage by the lower energy electrons becomes significant only at higher fluence, compared to 1 MeV irradiation. This is expected since the displacement cross section is lower for 0.5 MeV than for 1.0 MeV electrons in GaAs.

Overall, the results suggest that AlGaAs/GaAs solar cells are more radiation resistant to electron damage than conventional GaAs cells. This effect may be due to the presence of Al and is in agreement with radiation effects observed in both $Ga_xAl_{1-x}As$ and GaAs light-emitting diodes.

Compared to conventional Si cells, the GaAs cells are harder to 1 MeV electron irradiation, as shown in Fig. 2-71. When compared to the Si vertical-junction cells, the situation is not yet clear. More cells of both types must be tested. It appears that the GaAs cell is definitely ahead of the Si vertical-junction cell in efficiency, however.

2.3.5 Proton Induced Characterisic X-Ray Analysis

A minor effort has been spent on this contract in aiding Dr. Ron Berliner of Systems Research Laboratories in his project to develop impurity analysis and implanted profile techniques based upon characteristic x-ray emission generated by proton irradiation. The effort from this contract has been in converting the 400 keV Van de Graaff from electrons to protons, and in doing some of the mathematical analysis of the implanted-ion profiles. We will not report extensively on these subjects, however, since Dr. Berliner has done most of the work. We reproduce below a copy of an abstract submitted to the March 1976 meeting of the American Physical Society in Atlanta.

Protons with energies in the range 50-500 keV have been used to excite characteristic X-ray emission from bulk specimens of Si, diffusion doped with

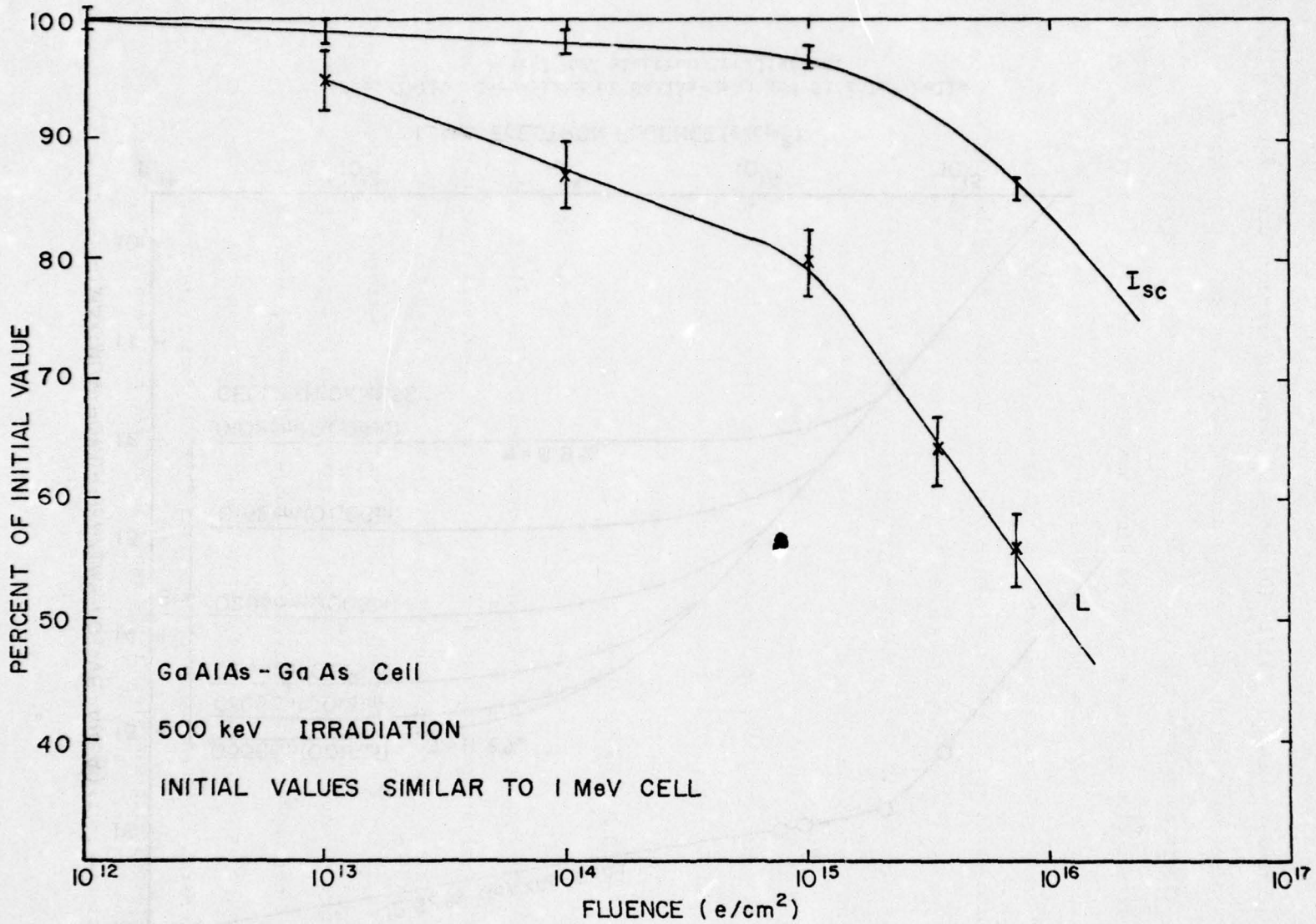

Fig. 2-70. 500 keV degradation of cell, similar to one described in Fig. 2-69.

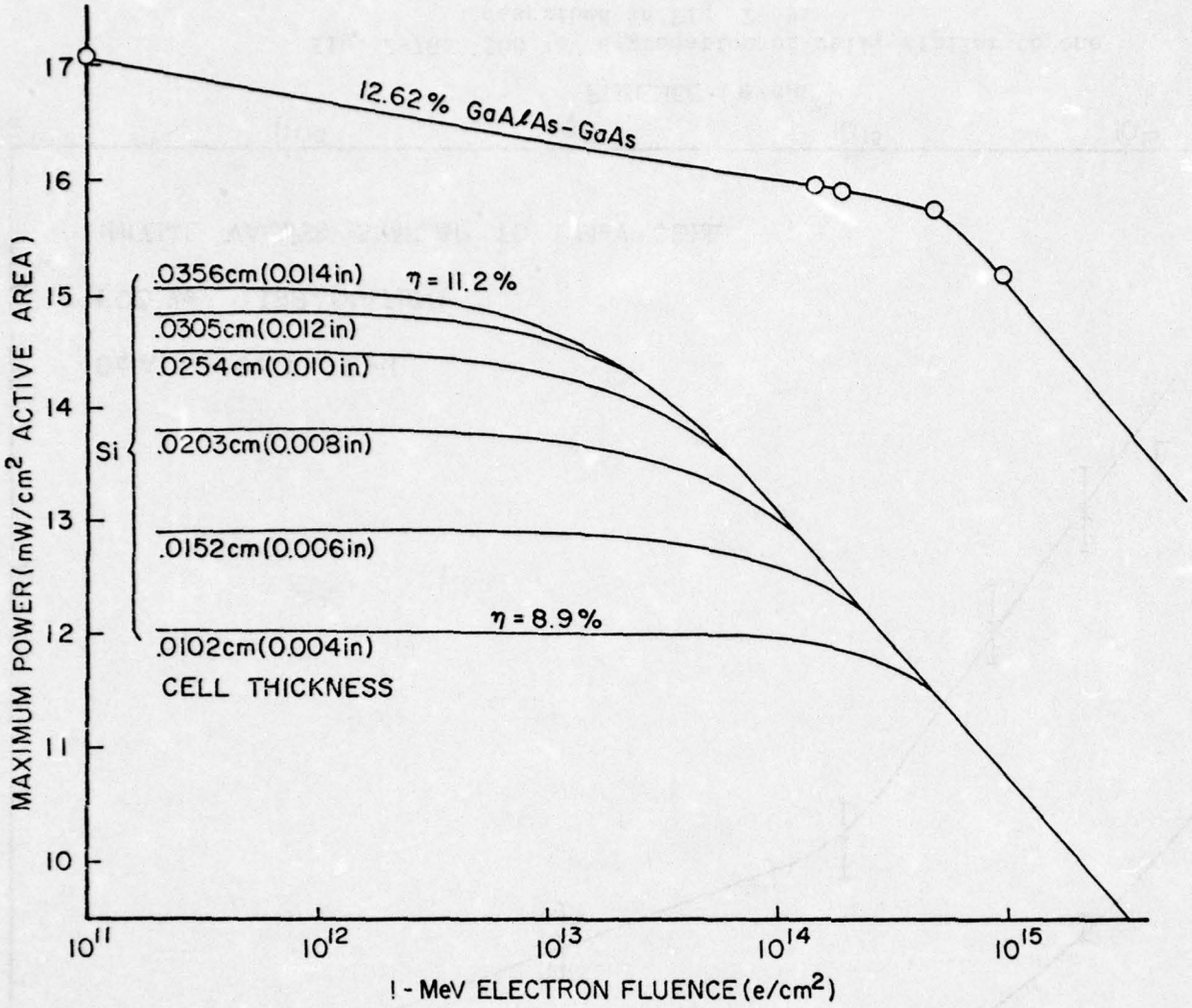

Fig. 2-71. Comparison of GaAlAs-GaAs and Si solar cells after 1 MeV electron irradiation.

As. The X-ray emission from the As-L and Si-K lines, as analyzed by a Si(Li) X-ray spectrometer, was measured as a function of incident proton energy. Decomposition of the strongly overlapping spectra was accomplished by means of the computer code "SAMPO".[54] The X-ray emission from bulk specimens under proton bombardment has been calculated. These calculations include the effects of proton-energy loss and X-ray absorption and can be performed for any impurity profile. The specimen-impurity profile was obtained by fitting, in a least-squares sense, the measured X-ray intensities to the results of the calculations. An X-ray filter was used in certain cases to enhance the detection of the As-L line relative to the Si-K X-ray line. Estimates of the accuracy of these profile determinations will be presented.

3.0 NUCLEAR MAGNETIC RESONANCE IN II-VI COMPOUNDS AND GaAs

3.1 Introduction

Nuclear magnetic resonance (NMR) techniques have been used quite successfully in elucidating some of the conduction-electron, paramagnetic-ion, and chemical-bonding properties of the II-VI compounds, CdS, CdSe, CdTe, and CdO. At least half of the present published literature on this subject has come from this contract effort. We have been able, among other things, to study the semiconductor-to-metal transition as a function of donor doping in CdS.[55] This type of study also leads to values of g*, the effective g-factor of conduction electrons. For example, we were the first to measure g* in CdTe,[56] following unsuccessful attempts by others using EPR techniques. Another area of applicability of NMR techniques involves the study of paramagnetic impurites in the ppm range. For example, 10 ppm of Co^{2+} in CdS will dominate the Cd^{113} nuclear spin-lattice relaxation from 1-300°K.[57] We have also investigated the effects of Cr, Zn, and Te impurites in GaAs. Below we describe the results of several NMR studies. The details of most of these may be found in the published literature.

3.2 Study of Co^{2+} in CdS

The following abstract is reprinted from Ref. 57.

Nuclear spin-lattice relaxation times, T_1, have been measured over a temperature range T = 1.1 - 300°K and frequency range ν = 2 - 15 MHz in a single crystal of CdS doped with 13-ppm cobalt. Minima in T_1 vs T are observed, and absolute values of the effective electron relaxation time, τ_e, may be calculated at the temperatures of the minima; e.g. at 14°K, $\tau_e = 8.0 \times 10^{-8}$ sec. At low temperatures, $T \lesssim 5$°K, τ_e is dominated by a resonant Orbach process involving the two ground-state Kramers doublets ($S = \pm \frac{3}{2}$ and $S = \pm \frac{1}{2}$) which, according to our measurements, are split by $\Delta = (4 \pm 1)$°K at zero magnetic field. At higher temperatures, $T \gtrsim 20$°K, τ_e is dominated by a nonresonant

process, and these data are well fitted from 40 to 300°K by $\tau_e^{-1} \propto T^5 J_4(210/T)$, where J_4 is a transport integral and 210°K is the CdS Debye temperature.

3.3 A Measurement of the Conduction-Electron g-Factor in CdTe

The following abstract is reprinted from Ref. 56.

The effective g-factor, g*, of conduction electrons in degenerate CdTe has been determined by using measurements of the Cd^{113} nuclear spin-lattice relaxation time T_1 and the Knight shift K. It is shown that the magnitude of g* is given by the Korringa product $T_1TK^2 = C(g^*)^2$, where C is a known constant and T is the absolute temperature, and that the sign of g* is given by the sign of K for a spherically symmetric conduction band. The measured value, g* = - 1.1 ± 0.1, is within the range allowed by effective-mass theory. Also, the electronic probability density at the nucleus, normalized to unity in an atomic volume, is calculated to be $|\psi_F(0)|^2 \simeq 6.5 \times 10^{25}$ cm^{-3}, about 70% of that found for the free Cd ion in a $5s^2S_{1/2}$ state.

3.4 Studies of Paramagnetic Dopants in GaAs

The Ga^{69} nuclear spin-lattice relaxation times (T_1) have been measured in GaAs:Te over a temperature range T = 6-300°K and a frequency range ν = 4-16 MHz. Above 60°K T_1 is dominated by quadrupolar interactions while below this temperature the paramagnetic Te are the dominant mechanism. There appear to be minima in T_1 vs T at 8MHz but more data are needed to confirm this. The concentration of Te in this sample is not known, as yet. Relaxation effects have also been seen in Cr- and Zn-doped GaAs ingots. The results of these studies have not been fully analyzed but it is clear that paramagnetic impurities in the ppm range in GaAs can be studied investigated by NMR techniques.

4.0 ELECTRICAL PROPERTIES OF $CuInS_2$

4.1 Introduction

The ternary I-III-VI compounds have recently received much attention because, unlike their binary II-VI analogues, they can often be made usefully both n- and p-type.[58-59] The largest-bandgap I-III-VI compound having this property is $CuInS_2$ ($E_o \simeq 1.5$ eV at room temperature) which has evoked technological interest both as an electroluminescent device[60] (note that the bandgap is close to that of GaAs), and as a photovoltaic device with a high theoretical solar-cell efficiency.[49] In spite of the importance of its electrical properties there have been no studies, to our knowledge, of their temperature dependences, with subsequent identification of donor and acceptor energies, and hole and electron scattering mechanisms. We have attempted to fill this gap by producing both n- and p-type $CuInS_2$, including some oriented single crystals, and then measuring the hole and electron concentrations and mobilities as functions of temperature.

4.2 Experimental Results

The $CuInS_2$ crystals were grown from the melt by sealing stoichiometric quantities of Cu, In, and S in an evacuated quartz tube and heating to 1050, 1125, or 1175°C for about 1 day, and then cooling at a rate of about 2-5°C/hr. Single crystals of approximate dimensions 5mm x 5mm x 1mm could easily be found, especially in the 1175°C growth. Good p-type behavior ($p \sim 1\Omega$-cm, $\mu_p \sim 20$ cm^2/V sec) could then be obtained by annealing at 550°C in a sulfur overpressure, and good n-type characteristics ($p \sim 1\Omega$-cm, $\mu_n \sim 100$-200 cm^2/V sec), by annealing in indium and excess $CuInS_2$ powder at 725-800°C.

In Fig. 4-1 we present μ_p vs. T for a single crystal grown at 1175°C and then annealed at 550°C in a sulfur overpressure. The circles and squares represent two pieces of the same crystal, and the solid lines represent theoretical

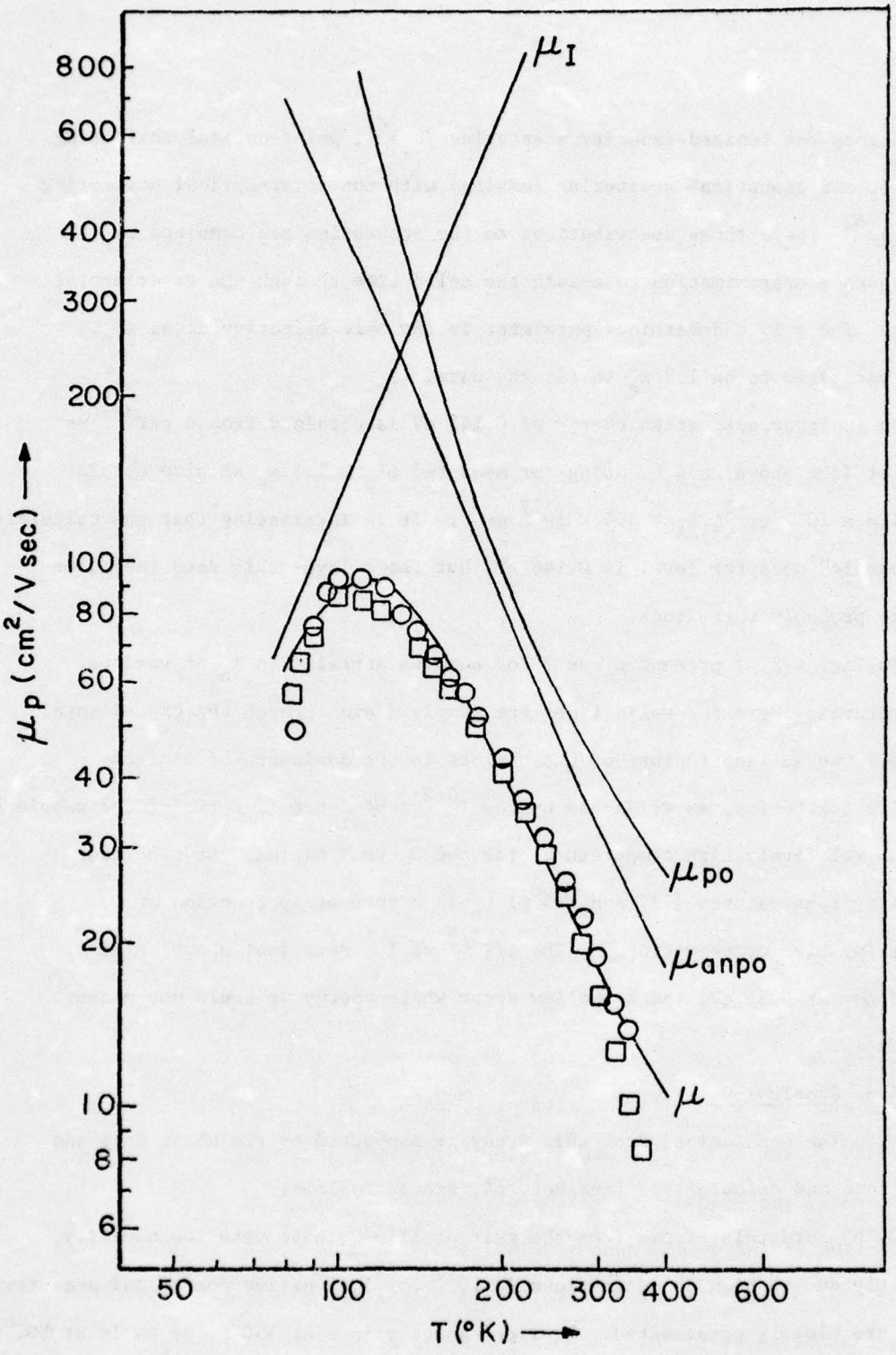

Fig. 4-1. The hole mobility vs. temperature for a single crystal of $CuInS_2$.

expressions for ionized-impurity scattering (μ_I)[61], polar-optical scattering (μ_{po})[61], and acoustical scattering combined with non-polar-optical scattering (μ_{anpo}).[62] These three contributions to the scattering are combined by Mathiessen's approximation to obtain the solid line through the experimental points. The only undetermined parameter is the hole effective mass, m^*_p, which was taken to be 1.3 m_e to fit the data.

An acceptor activation energy of 0.145 eV is obtained from a $p/T^{3/2}$ vs T^{-1} plot (not shown) and by using our measured $m^*_p = 1.3\ m_e$ we also obtain $N_D \simeq 1.6 \times 10^{17}\ cm^{-3}$, $N_A \simeq 3.4 \times 10^{17}\ cm^{-3}$. It is interesting that the calculated "hydrogenic" acceptor level is 0.146 eV, but for a level this deep the agreement is probably fortuitous.

In Fig. 4-2 we present μ_n vs T for samples annealed in I_n at various temperatures. Here the solid lines are simply drawn through the experimental points. One salient feature of these plots is the dominance of ionized-impurity scattering, as evidenced by the $T^{3/2}$ dependence (for two of the samples) and the relatively high temperatures for the μ_n vs T maxima. At the lower annealing temperatures (725 and 745°C) μ_n is a very steep function of T, suggesting high compensation.[63] The $n/T^{3/2}$ vs T^{-1} data (not shown) give a deep donor at 0.35 eV, and a shallow donor whose energy we could not measure accurately.

4.3 Conclusions

The conclusions from this study, as supported by the above data and other data and calculations from Ref. 64, are as follows.

$CuInS_2$ crystals, grown from the melt at 1175°C, have very low mobility, evidently due to high concentrations ($> 10^{18}\ cm^{-3}$) of native donors and acceptors which are closely compensated. However, anneals in S at 550°C, or in In at 800°C,

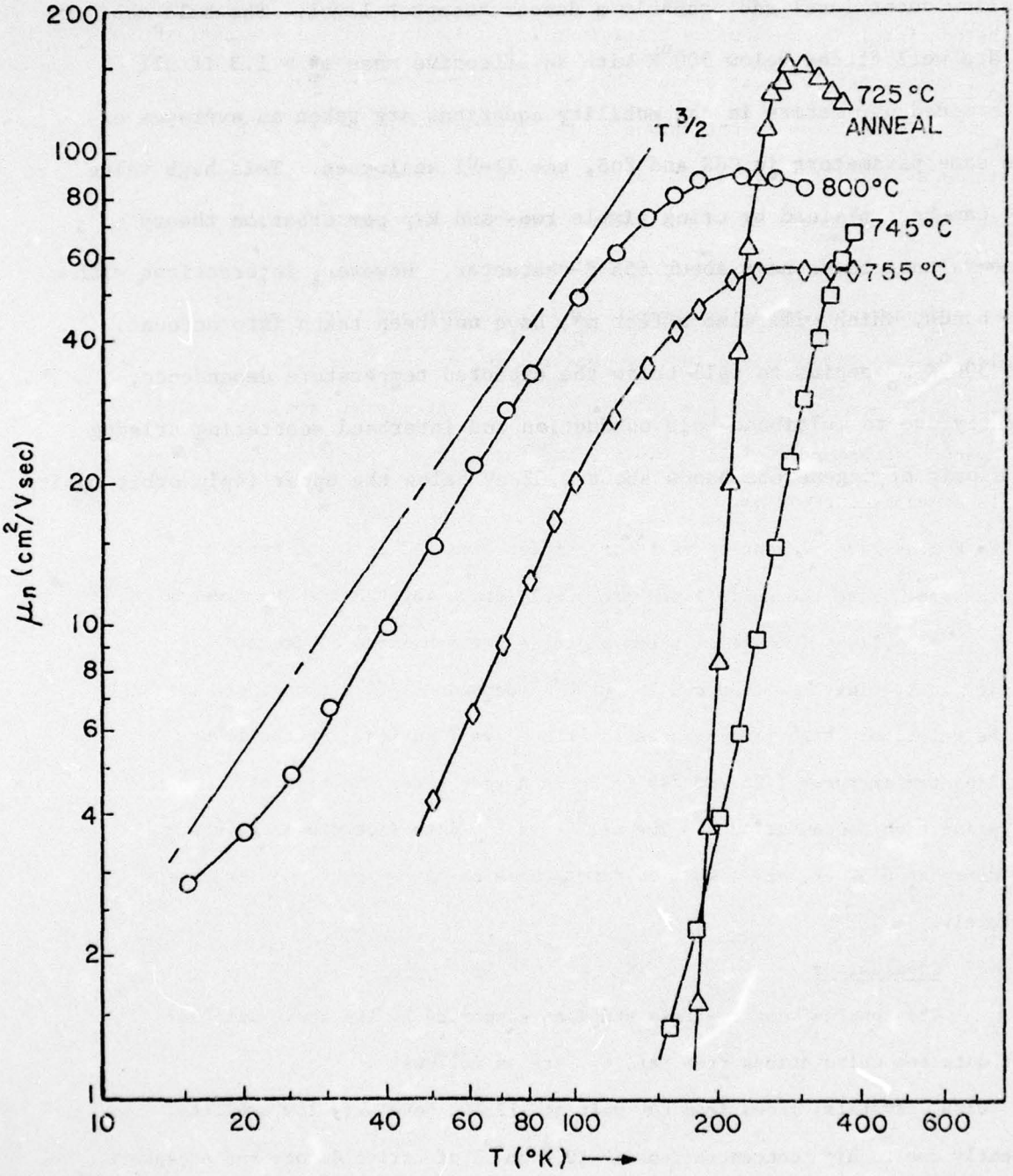

Fig. 4-2. The electron mobilities vs. temperature for several $CuInS_2$ crystals annealed at different temperatures in In.

produce good p- and n-type conductivity, respectively. An acceptor level at 0.15 eV and a donor level at 0.35 eV have been identified, but there also is a shallow donor level and probably a deeper acceptor level. The hole-mobility data are well fitted below 300°K with an effective mass $m_p^* \simeq 1.3$ if all undetermined parameters in the mobility equations are taken as averages of those same parameters in CdS and ZnS, the II-VI analogues. This high value of m_p^* can be explained by using simple two-band k·p perturbation theory if the valence bands have about 65% d-character. However, interactions with other bands, which will also affect m_p^*, have not been taken into account. Above 300°K μ_p begins to fall below the expected temperature dependence, evidently due to multiband hole conduction and interband scattering arising from a pair of degenerate bands about 0.02 eV below the upper (spin-orbit split) band.

5.0 ELECTRICAL PROPERTIES OF GaAs SUBSTRATE MATERIALS

5.1 Introduction

Although semiconductor-device technology is still centered on silicon, the growing need for higher-frequency (> 10 GHz) and higher-temperature devices has stimulated work on compound semiconductor materials with higher mobilities and larger bandgaps than those of Si. By far the most promising of the compound semiconductors at this stage is GaAs, with a bandgap of 1.43 eV and an electron mobility as high as 8,500 cm^2/V sec, at room temperature. Among the other advantages of GaAs are a direct bandgap, easy formation of p-n homojunctions, good solid solution formation with other III-V compounds (to obtain a wide range of bandgaps), and good solubility of deep donor and acceptor centers so that very high-resistivity bulk material (> 10^9 Ω-cm) can be grown. This latter property makes the future of large-scale GaAs integrated cirucits very bright, since the necessary epitaxial layers do not have the disadvantages of being grown on a foreign material or else isolated by a p-n junction, as is the case for Si integrated circuits.

Unfortunately, materials problems are holding back the development of many GaAs devices, especially the microwave devices. It is perhaps easy to understand why industrial sources have not seen fit to invest large sums of money to improve the material purity and stoichiometry since the main commercial application at present, and in the forseeable future, is for light emitting diodes (LED), which do not require especially good material. Thus, during the last two years of this contract period we have carried out a GaAs materials characterization program, using electrical, optical, and magnetic-resonance techniques. The goal has been to identify and help solve material problems in order to produce better microwave devices.

We have concentrated on substrates for reasons outlined below. It is safe to say that virtually every GaAs microwave vendor believes that "poor" substrates are a major, if not the major, cause of poor device performance. Recently, workers at several major industrial and university laboratories have experimentally verified this assertion. For example, one scientist at an industrial laboratory reports that of five substrate (GaAs:Cr and GaAs:O) brands that he has used, one of these brands is the best if a field effect transistor (FET) is fabricated directly onto the substrate surface, and the worst if an epibuffer layer is used for isolation. The reasons are unclear. As another example, a quite definitive study has been performed by J. Barrera,[65] at Hewlett-Packard, in which he closely correlates poor FET performance with the formation of a conduting layer on the surfaces of certain brands of substrates, under liquid-phase-epitaxy (LPE) growth conditions. Barrera and others have also noted gross nonuniformities in dislocation counts (from 10^3 to $10^5/cm^2$ over a set of ingot slices), impurity clustering at dislocations, Cr compound precipitates, and other defects. Furthermore, light irradiation, especially near 1.1μ, can adversely affect FET performance. Barrera has suggested a method of "eliminating" poor substrates by actually measuring the surface layer resistance after a simulated epicycle, and rejecting those substrates that end up with greater than a specified surface conductivity. We have tried to develop some room-temperature methods of quickly and accurately determining the suitability of a particular substrate material for a particular device to be fabricated under particular growth conditions. This goal has not yet been reached, of course, but we believe that we have made substantial progress.

5.2 Hall-Effect and Magnetoresistance Measurements

Probably the singly most applied characterization and research technique for semiconductors is the Hall effect. Briefly stated, a magnetic field ($\vec{B} = B\hat{z}$) applied at right angles to a current ($\vec{I} = I\hat{x}$) in a crystal will produce a voltage (V_H) perpendicular to I and B.[66] Generally, a voltage (V_C) parallel to I is also measured so that the resistivity (ρ), mobility (μ_p), and carrier concentration (n) may be deduced as follows (practical units):

$$\rho = \left(\frac{yz}{x}\right) \frac{V_C}{I} \ (\Omega\text{-cm}) \tag{5-1}$$

$$\mu_n = \frac{10^8}{B} \ \frac{x}{y} \frac{V_H}{V_C} \left(\frac{cm^2}{V\ sec}\right) \tag{5-2}$$

$$n = 6.25 \times 10^{10} \frac{IB}{VHz} \ cm^{-3} \tag{5-3}$$

where x, y, z are, respectively, the crystal length (or points between which V_C is measured), width, and thickness in centimeters, and I is measured in amperes, V_C and V_H in volts, and B in gauss. Here an n-type sample is assumed, but the generalization is obvious.

When the conductivity is mainly of one type, i.e., either n or p, the temperature dependence of the above quantities can be used to deduce donor and acceptor concentrations and energy levels in a nondegenerate crystal, according to well-known relationships.[67] Unfortunately, the carrier concentrations and mobilities in GaAs:Cr, the most useful high-resistivity substrate, are not given by Equations 5-2 and 5-3, and herein lies a common error in the

analyses of these crystals. The reason is that the conductivity is mixed; i.e., both holes and electrons are contributing. Although this fact has long been suspected, it was first proved by our research during this contract. The Hall coefficient, extrapolated to zero B, is given by (if $r_n = r_p = 1$),

$$R = \frac{p\mu_p^2 - n\mu_n^2}{e(p\mu_p + n\mu_n)^2} = 10^8 \frac{V_H z}{IB} \left(\frac{cm^3}{coul}\right) \tag{5-4}$$

and the Hall "mobility" is

$$R\sigma = \frac{p\mu_p^2 - n\mu_n^2}{e(p\mu_p + n\mu_n)} = \frac{10^8}{B} \frac{x}{y} \frac{V_H}{V_C} \left(\frac{cm^2}{V\ sec}\right) \tag{5-5}$$

where $\sigma = 1/\rho$. Thus, since $\mu_n/\mu_p > 1$, it is evident that if an acceptor is dominant, the apparent mobility, $R\sigma$, could be either positive (p-type) or negative (n-type), depending upon the value of n/p. It is also evident that we cannot obtain four quantities, n, p, μ_n, and μ_p, from two measurements, V_H and V_C. The resolution of this problem lies in measuring R and σ (i.e., V_H and V_C, with I constant) as a function of B. For example, it is known[68] that

$$R = \frac{R_n^2\sigma_n^2 + R_p^2\sigma_p^2 + R_n R_p \sigma_n^2 (R_n + R_p)B^2}{(\sigma_n + \sigma_p)^2 + \sigma_n^2\sigma_p^2(R_n + R_p)^2 B^2} \tag{5-6}$$

where $\sigma_n = ne\mu_n$, $\sigma_p = ne\mu_p$, $R_n = r_n(ne)^{-1}$, and $R_p = r_p(pe)^{-1}$. A similar equation can be written for $\sigma(B)$. During this contract period we have formulated a systematic method of obtaining μ_n, μ_p, n, and p from the measurements.[69] The results are:

$$A = \frac{2 + T(1 + \beta^{-2})}{1 - T/\beta}, \quad T \equiv \frac{(R_o\sigma_o)^2}{S_\rho} \tag{5-7}$$

$$b \equiv \frac{\mu_n}{\mu_p} = \frac{1}{2\alpha} \{A + \sqrt{A^2 - 4}\} \tag{5-8}$$

$$c \equiv \frac{n}{p} = \frac{1 + \alpha b \beta}{b(\alpha b + \beta)} \tag{5-9}$$

$$\mu_n = \frac{1 + \beta^{-1}}{1 - (\alpha b)^{-1}} \frac{(-R_o \sigma_o)}{r_n} \tag{5-10}$$

$$\mu_p = \mu_n / b \tag{5-11}$$

$$p = \frac{\sigma_o^{-1}}{e\mu_n (c + b^{-1})}, \quad n = cp, \quad n_i = \sqrt{np} \tag{5-12}$$

where β is the x-intercept of an R versus $\Delta\rho/\rho$ (magnetoresistance) plot, S_ρ is the slope of $1/B^2$ versus $\rho_o/\Delta\rho$ plot, r_n and r_p are, respectively, the Hall factors for electrons and holes, $\alpha = r_n/r_p$, n_i is the intrinsic concentration, and the subscript zero denotes a measurement at B = 0. The quantities r_n, r_p, and α are close to unity and can be taken as such if they are not explicitly known. Figures 5-1 and 5-2 illustrate the process for sample A.

More can be learned from the temperature dependence of these quantities, especially μ_n and p, shown in Fig. 5-3. For thermally activated holes, well below the exhaustion region ($p \ll N_D$, $N_A - N_D$), p should be given by

$$p \simeq \left(\frac{N_A}{N'_D} - 1\right) \frac{N_v}{g_v} e^{-E_A/kT} \tag{5-13}$$

where N_A and N'_D are the acceptor (chromium) and <u>net</u> donor concentrations, respectively, g_v is the degeneracy factor, and $N_v = 2(2\pi m_p^* kT)^{3/2}/h^3$ is the valence-band density of states. Here $N_D - N'_D$ ($\equiv N_A^s$) is the concentration of <u>all</u> acceptors lying <u>below</u> the chromium level. The quantities N_v and g_v are known reasonably well, and E_A can be determined from a plot of ln p versus T^{-1}, thus leaving N_A, N_D, and N_A^s as unknowns. The various relationships, to be discussed later, are illustrated in Fig. 5-4. For most samples we can ignore the upper Cr level shown in Fig. 5-4 and we will also assume that if oxygen is

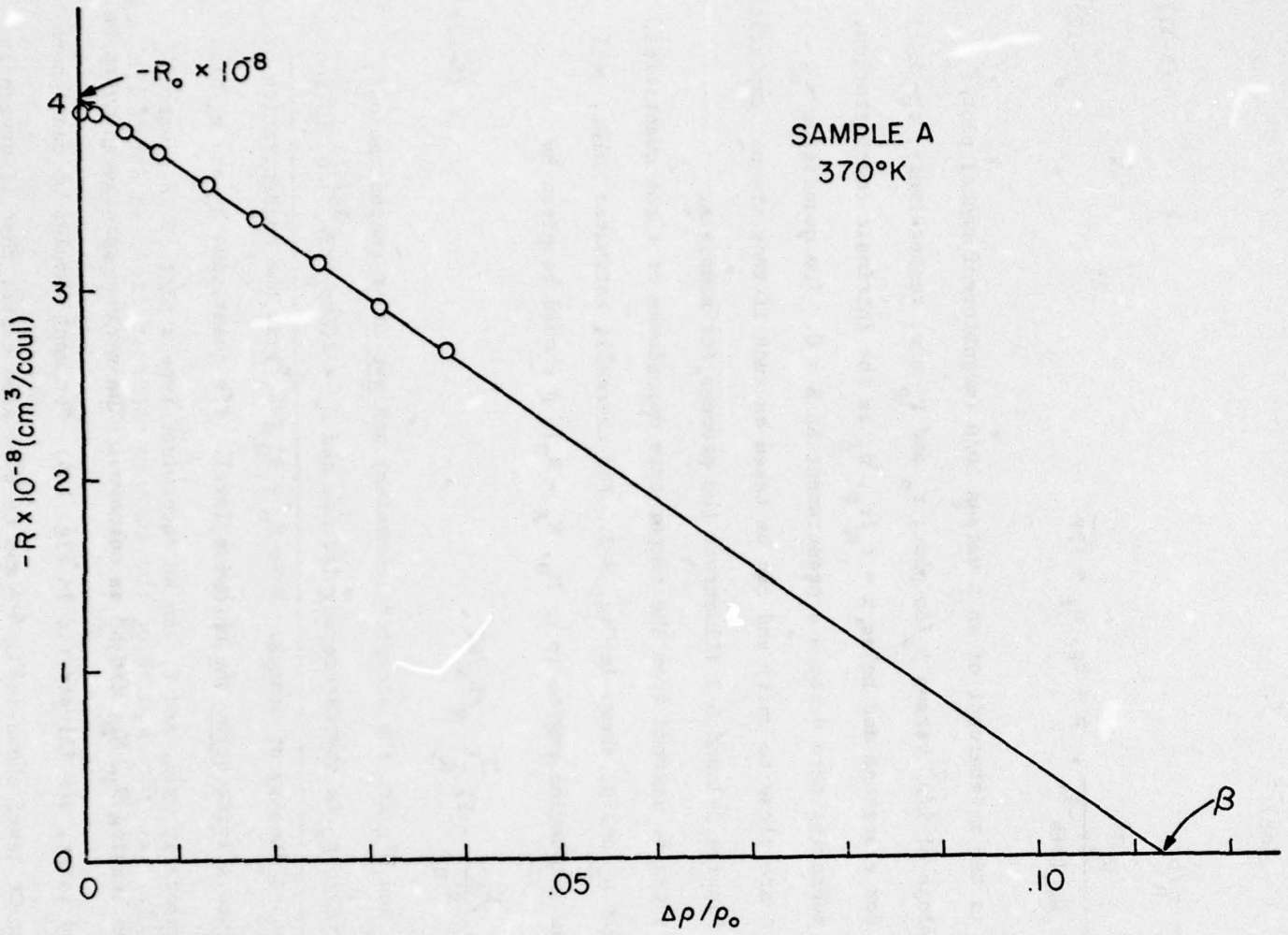

Fig. 5-1. The Hall coefficient R vs. the magnetoresistance $\Delta\rho/\rho_o$ for GaAs:Cr Sample A at 370°K.

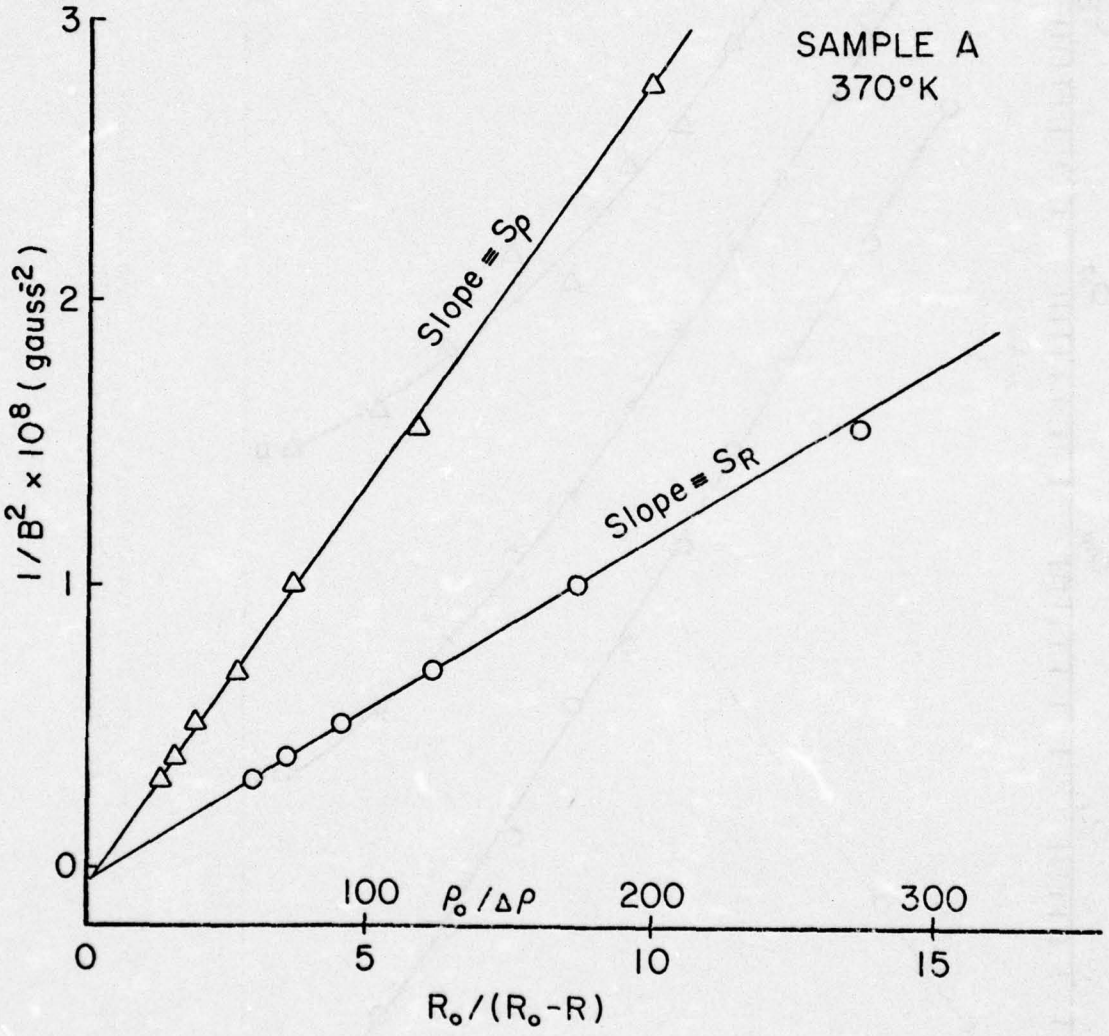

Fig. 5-2. The square of the inverse magnetic field strength $1/B^2$ vs. $R_o/(R_o-R)$ and vs. $\rho_o/\Delta\rho$ for GaAs:Cr Sample A at 370°K.

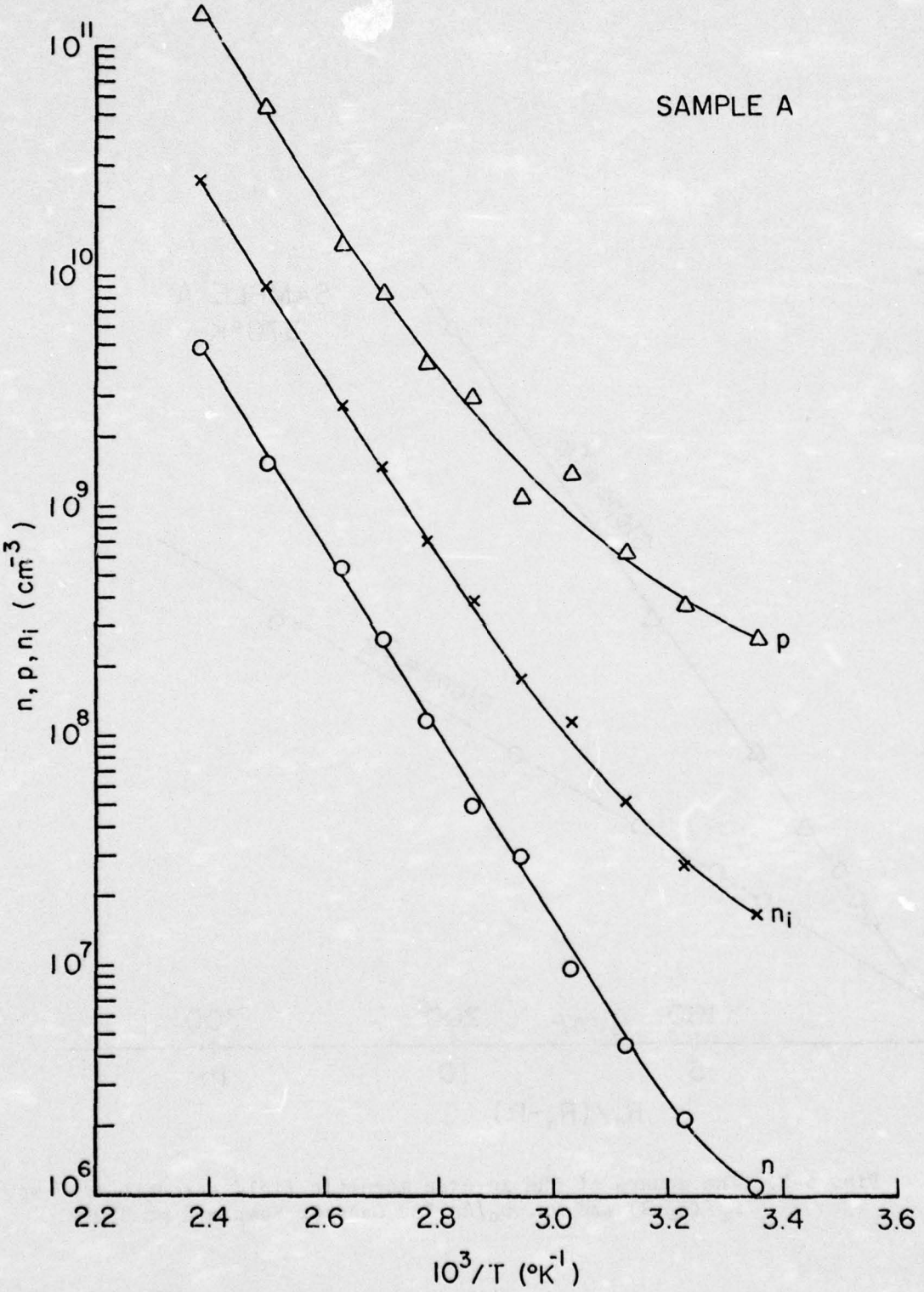

Fig. 5-3. The temperature dependences of the carrier concentration, n and p, and the intrinsic concentration, n_i. (The curvature at low temperature is caused by surface conduction).

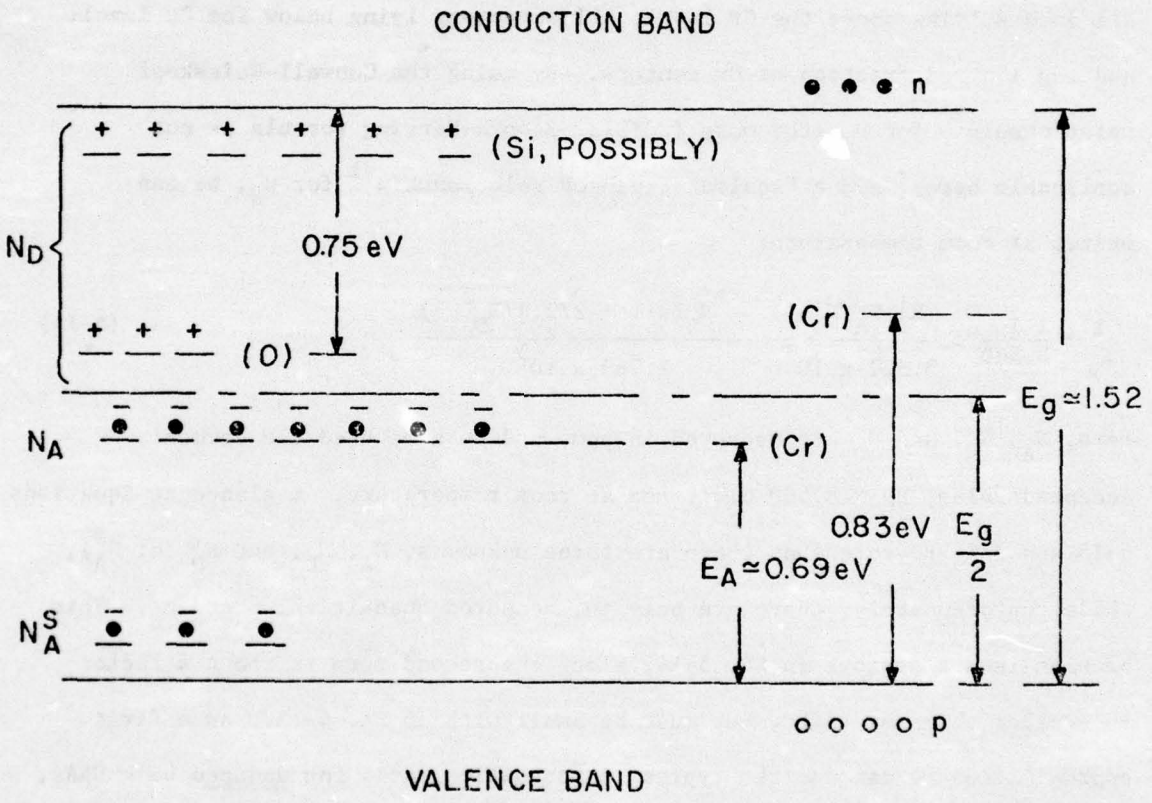

Fig. 5-4. A proposed energy diagram for GaAs:Cr at T = 0. The energy levels are tentative.

present its levels are mostly empty.

Further information may be obtained from the electron mobility, which in Mathiessen's approximation is given by $\mu^{-1} \simeq \mu_L^{-1} + \mu_N^{-1} + \mu_I^{-1}$, where μ_L is the contribution of lattice modes to the electron scattering, μ_N is the contribution of neutral Cr centers (the Cr level is only partially filled with electrons), and μ_I is the contribution of ionized centers, including all donors lying above the Cr level, all acceptors lying below the Cr level, and the ionized fraction of Cr centers. By using the Conwell-Weisskopf relationship[70] for μ_I (the more familiar Brooks-Herring formula is not applicable here), and a "scaled" Erginsoy relationship[71] for μ_N, we can write, at room temperature,

$$\frac{1}{\mu_n} = \frac{1}{8{,}500} + \frac{N_D'(N_A/N_D'-1)}{3.627 \times 10^5} + \frac{N_D \ln(1 + 273.4/N_D^{2/3})}{1.769 \times 10^5} \qquad (5\text{-}14)$$

Here, N_A, N_D, and N_D' are measured in ppm, and we have used the commonly accepted value, $\mu_L \simeq 8{,}500$ cm^2/V sec at room temperature. A glance at Equations 5-13 and 5-14 reveals that there are three unknowns, N_A, N_D, and N_D' (or N_A^s), while, unfortunately, there are only two measured quantities, p and μ_n. This problem is not serious in Eq. 5-14, since the second term is about a factor 10 smaller than the third, but must be dealt with in Eq. 5-13. As a first approximation we can use the typical compensation ratio for undoped bulk GaAs, $N_D/N_A^s \simeq 0.5$. Then, using Equations 5-7 through 5-14, it is possible to estimate N_A (the chromium concentration) and N_D (often silicon and oxygen). To our knowledge we are the first group to obtain such data, although many groups have previously investigated the electrical properties of GaAs:Cr. We illustrate the method below.

For one sample (A), an $p/T^{3/2}$ versus T^{-1} plot gives $E_A \simeq 0.69$ eV from the valence band (This is a T = 0 value if $E_A(T) = E_A(0) + \alpha T$). Then p and μ_p are measured only at room temperature for other samples (B, C, D, and E) and N_A and N_D are calculated. The results are shown in Table 5-1 along with spark-source mass spectrographic (SSMS) data obtained on Samples B, D, and E. The SSMS data are considered accurate to within only a factor three. It is clear that for even our simple model, which can be improved, the results are consistent with the SSMS data. The data for each sample may be accumulated and analyzed with a hand calculator in less than 1-1/2 hours from receipt of the sample and thus the cost is less than one-tenth that of SSMS. Of course, SSMS gives a "total" spectrum of elements, whereas our method gives only Cr and the total donor content. In this illustration, the data are of particular interest because they show that the bottom ends of the boules (D and E) contain higher Cr concentrations than the top ends (B and C).

Because both epigrowth and post-ion-implantation annealing require high temperatures (700-900°C), it is important to know whether or not the GaAs:Cr substrates retain their high resistivity after exposure to such temperatures. Several groups, as mentioned earlier, have already investigated this problem, at least from a practical point of view.[65] To check, we heated Sample A for 10 minutes at 600°C in an Ar atmosphere and the resistivity dropped from 8×10^8 to $2 \times 10^7 \Omega$-cm. Upon removal of about 20μ, the resistivity returned to its initial high value. In an independent study we have shown that heating "undoped" GaAs ingots in vacuum for 24 hours at 600 or 700°C produces a p-type sample with an acceptor level at 0.14 eV from the valence band. We believe that this center is associated with a Ga vacancy, although further work needs to be done to verify this.

Table 5-1 The reisitivity (ρ), electron mobility (μ_n), hole concentration (p), donor (N_D), and acceptor (N_A) concentrations (calculated from Hall-effect measurements), and Si(N_{Si}), O(N_O) and Cr(N_{Cr}) concentrations (measured by mass spectroscopy). Here, 1 ppm = 2.21×10^{16} atoms/cm^3.

				Hall Meas.		Mass Spec.	
Sample	$\rho(\Omega\text{-cm})$	$\mu_n(\frac{cm^2}{V\ sec})$	$p(cm^{-3})$	N_D(ppm)	N_A(ppm)	$N_{Si}+N_O$(ppm)	N_{Cr}(ppm)
A	0.93×10^9	3.65×10^3	4.5×10^6	7	7	(not measured)	
B	1.63	3.24	3.9	7	6	7	4
C	1.21	3.11	3.2	7	6	(not measured)	
D	1.04	2.82	8.5	9	13	7	13
E	1.69	2.53	3.8	11	10	18	10

The apparatus necessary to perform the Hall-effect and magnetoresistance measurements on high-resistivity samples has been completed and working for about 1-1/2 years. It makes use of electrometers, operated in a unity gain mode, guarding each voltage contact. Triaxial cable is employed with the inner shield of each cable held at its respective center-lead potential to effectively reduce cable capacitances. The system can measure 10^{13} ohms with 1 percent accuracy, limited by a time constant of only 10 seconds at this resistance. Our He exchange-gas dewar can operate between 5.5 and 600°K with an efficient cool-down period of 45 minutes.

5.3 Photomagnetoelectric Measurements

The photomagnetoelectric effect is essentially the Hall effect of a diffusion current. If light $\vec{I}_o$ is absorbed near one surface, the created holes and electrons will diffuse toward the opposite face. If a magnetic field $\vec{B}$ is applied perpendicular to $\vec{I}_o$, the carriers will experience a force perpendicular to both $\vec{B}$ and $\vec{I}_o$ and we can measure a short-circuit current I_{PME}, or an open-circuit voltage V_{PME}^{oc} in this perpendicular direction. These quantities depend, of course, upon the intensity of the light and the conversion efficiency, both hard quantities to determine accurately. One way to circumvent this problem is to measure the photoconductivity under the same conditions. Then, it can be shown[72] that

$$\frac{\varkappa B I_{pc}}{I_{PME}} \left(\frac{1}{V_{pc}^{\ell}} - \frac{1}{V_{pc}^{d}}\right) = \frac{\tau}{L}\left(1 + \frac{1}{\alpha L^{*}}\right) \qquad (5\text{-}15)$$

where

$$L^{*} = \frac{L}{1+S\tau/L} \qquad (5\text{-}16)$$

Here I_{pc} is the photoconductivity current, held constant, V_{pc}^{ℓ} and V_{pc}^{d} are the PC voltages in the light and dark, respectively, between two points a

distance x apart, τ is the carrier lifetime, and L the diffusion length, assumed equal for holes and electrons, α is the absorption constant, and S is the front-surface recombination velocity. We are assuming here that $\alpha d >> 1$, where d is the sample thickness in the light direction.

At high light intensities V_{PME}^{oc} approaches a constant, $V_{PME}^{oc,\ sat}$; it can be shown that

$$V_{PME}^{oc,sat} = \frac{xBL}{\tau} \quad \frac{1}{1+(\alpha L^*)^{-1}} \tag{5-17}$$

The quantities L and τ are related by $L = \sqrt{D\tau}$ where D, the ambipolar diffusion constant, is given by

$$D = \frac{n + p}{n/D_p + p/D_n} \tag{5-18}$$

For the nondegenerate case, $D_n = (kT/e)\mu_n$, and $D_p = (kT/e)\mu_p$, the Einstein relationships. Note that for an n-type sample, $D = D_p$, and for p-type, $D = D_n$; i.e., this is a minority carrier effect. From plots of either $(I_{pc}/I_{PME})(1/V_{pc}^{\ell} - 1/V_{pc}^{d})$ or $V_{PME}^{oc,\ sat}$ versus α, we can obtain L (or τ) and S.

In case trapping centers are present, $\tau_n \neq \tau_p \neq \tau$ and $\tau_{pc} \neq \tau_{PME}$. It can be shown[73] that Eq. 5-15 can be revised by letting $\tau \rightarrow \tau_{pc}^{\ 2}/\tau_{PME}$, where $\tau_{PME} = (\tau_n + c\tau_p)/(1 + c)$ and $\tau_{pc} = (b\tau_n + \tau_p)/(1 + b)$. Since in Eq. 5-17, $\tau = \tau_{PME}$, the measurement of <u>all</u> of the quantities I_{PME}, $V_{PME}^{oc,\ sat}$, I_{pc}, and V_{pc} will give τ_{pc} and τ_{PME}, by Equations 5-15 and 5-17, and thus τ_n and τ_p.

The apparatus we have been using for the investigation of the PC and PME effects includes the electrical-measurement system, described in the previous paragraphs, along with a high-intensity B&L monochromator with a lens. The monochromator is capable of providing a constant 1×10^{15} photons/cm^{2}sec over the wavelength range 0.7 to 1.6μ, with a resolution of about 0.02 eV.

For Sample A (Table 5-1) we have performed detailed measurements of I_{PME}, I_{pc}, and V_{pc} as a function of wavelength (or α). The results are: $\tau_n \simeq \tau_p \simeq 1.4 \times 10^{-8}$ sec and $S \simeq 5 \times 10^4$ cm/sec. We have also measured τ for a total of 10 other GaAs:Cr samples and have found values from 5×10^{-9} to 3×10^{-5} sec. Some of the samples exhibit trapping effects. Considering this range of τ values it seems clear that the PME technique is sensitive to the differing properties of the substrate materials and should be valuable as a characterization tool.

5.4 Photo-Hall, Photomagnetoresistance, and Photoconductivity Measurements

In the presence of light irradiation, new equilibrium concentrations of holes and electrons will be established, and consequently all of the quantities discussed in Sec. 5.2 may be affected. In this section we show how the various effects can be isolated and we present a model for the deep levels in GaAs which is consistent with our present results. However, more data will be necessary to confirm the model.

Most of the GaAs:Cr wafers which we have analyzed yield room-temperature photoconductivity (PC) and photo-Hall (PH or Rσ) curves similar to those shown in Fig. 5-5. For this sample the PC increases from a threshold at about 0.72 eV, with perhaps another threshold existing between 0.8 and 0.9 eV. Then the intrinsic (above-band-gap) PC takes over above 1.4 eV. In a mixed-conductivity system like this, an increase in PC could be due to increases in p, n, μ_p, or μ_n, or even some complicated combination of increases and decreases of these quantities. Usually, it is assumed that this threshold is due to electrons being excited from a deep impurity level to the conduction band, but in most cases this is wrong. The Rσ data help to clarify the situation

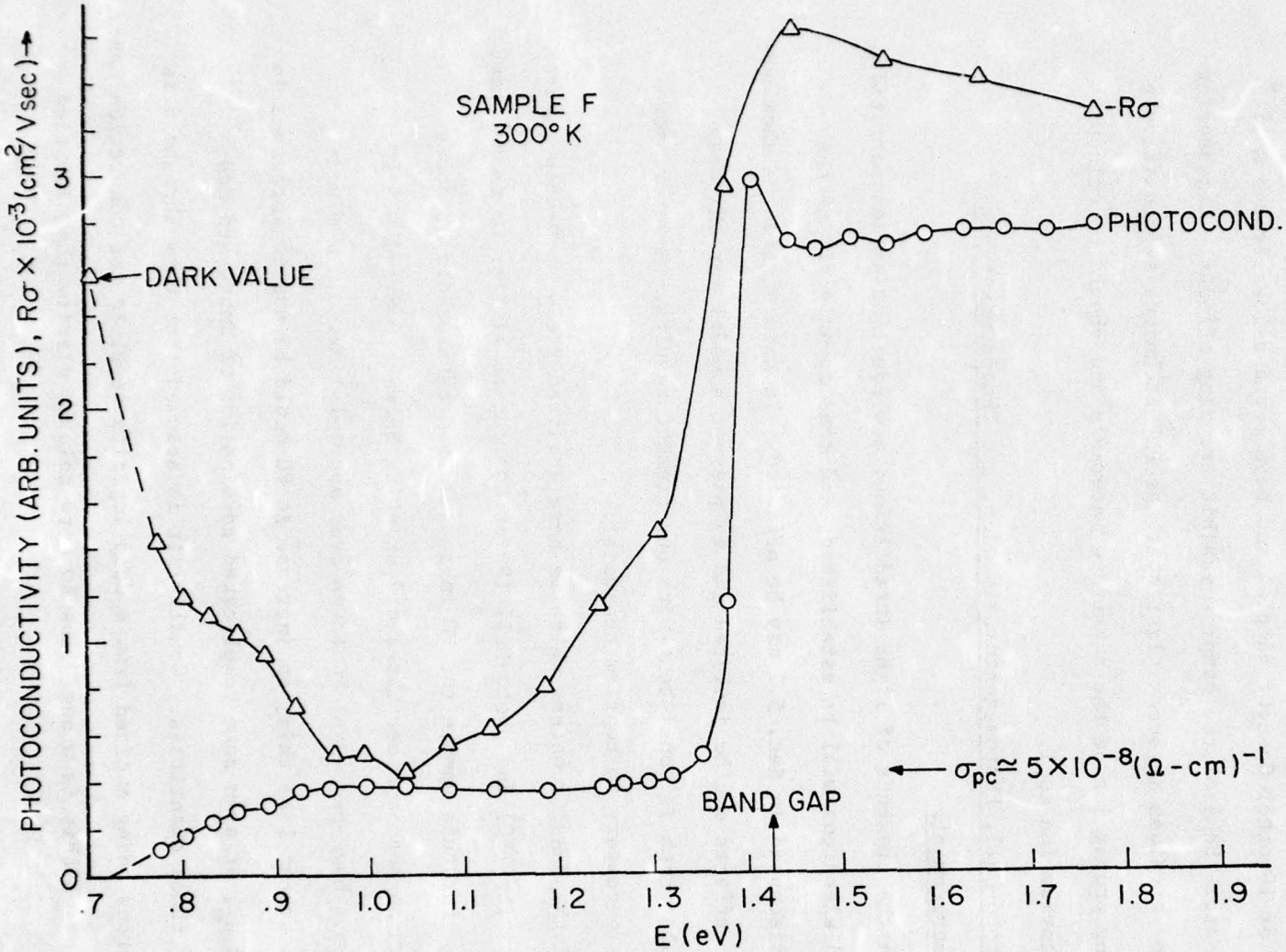

Fig. 5-5. The photoconductivity and photo-Hall mobility (Rσ) vs. light energy for GaAs:Cr Sample F at 300°K.

somewhat by showing that this sample is more p-type (i.e., $R\sigma$ is less negative) in above-threshold light than in the dark. It is doubtful that this could occur if the threshold corresponds to electrons being excited to the conduction band.

Amother sample, with similar $R\sigma$ data (not shown), is illustrated in Fig. 5-6. Here two thresholds at 0.72 and 0.81 eV are clearly seen. Also, p and p/n (not shown) are rapidly increasing, and μ_n is decreasing as the light energy is increased. These results are consistent with electrons being excited from the valence band to acceptor levels, thus increasing p and decreasing μ_n, since the acceptors are becoming ionized. For this sample, $p/T^{3/2}$ vs T^{-1} data give an acceptor level at 0.83 eV above the valence band. Even though this is a T = 0 value of E_A, still it is natural to identify it with the 0.81 eV level measured by the room temperature PC. On two other GaAs:Cr samples, $p/T^{3/2}$ vs T^{-1} measurements have yielded $E_A \simeq 0.69$-0.72 eV, which probably corresponds to the PC value of 0.72 eV. If this model is correct, then the two Cr centers must remain relatively fixed to the valence band as a function of temperature. It is probable that one of the two levels is Cr^{3+} on a Ga site (becoming Cr^{2+} after accepting on electron) while the other may be an interstitial or complex. Further speculation must await more data.

A few samples, such as Sample B shown in Fig. 5-7, exhibit differences compared with those in Figures 5-5 and 5-6. One difference is a lower threshold energy, about 0.68 eV, on the average. Another difference is that $R\sigma$ is more n-like at the threshold, than in the dark, and n/p is increasing. A third difference is a relatively low σ_{pc} at the impurity maximum. These features are all consistent with the presence of a significant amount of oxygen, which

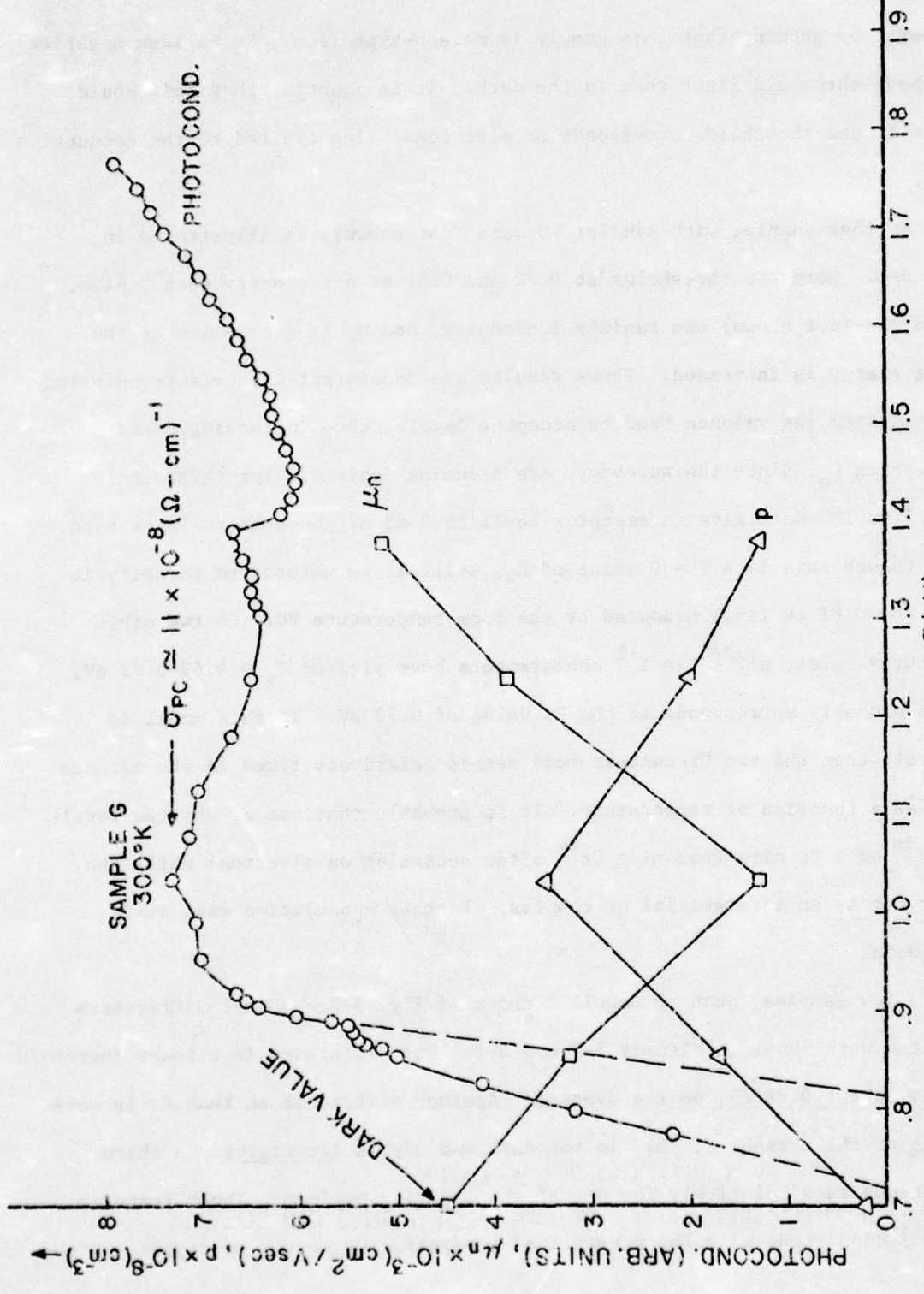

Fig. 5-6. The photoconductivity, electron mobility (μ_n), and hole concentration (p) vs. light energy for GaAs Sample G at 300°K.

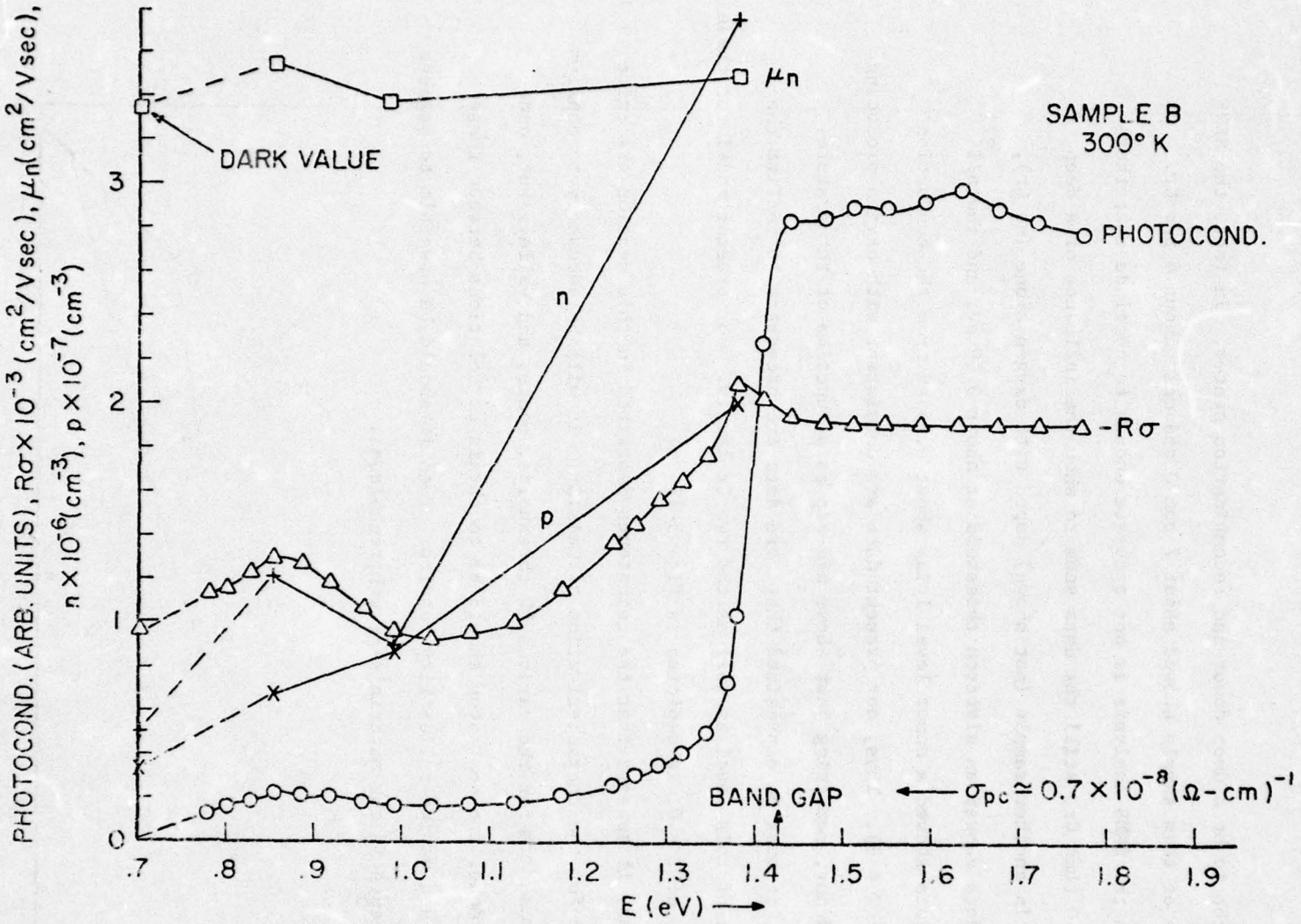

Fig. 5-7. The photoconductivity, photo-Hall mobility (Rσ), electron mobility (μ_n), electron concentration (n), and hole concentration (p) vs. light energy for Sample B at 300°K.

is thought to be a deep donor and recombination center. In fact, the SSMS analysis of this sample showed about 7 ppm O and only about 4 ppm Cr. Although the SSMS analysis is not accurate enough to conclude that there is more O than Cr, still the data seem to show the influence of a deep donor. In another sample (not shown) doped with oxygen alone (no Cr), the PC data showed an electron threshold at about 0.69 eV, and the $n/T^{3/2}$ vs T^{-1} data showed a donor level lying about 0.75 eV from the conduction band (at T = 0). Thus, our present data are consistent with oxygen producing a deep donor, remaining just above mid-gap as a function of temperature. However, it must be emphasized that more data are necessary to confirm the location of this level as well as the two Cr levels. Our present model for these centers, at T = 0, is depicted in Fig. 5-4.

Thus, it appears that the techniques described in this section are quite valuable for the characterization of GaAs:Cr. It will be necessary to confirm the explanations for the various PC thresholds, peaks, and valleys but, once this is done, the next step should be to obtain correlations between these results and device-reliability results. Then it should be possible to suggest improvements in the materials-growth techniques.

6.0 THERMAL PROPERTIES OF II-VI COMPOUNDS AND RELATED MATERIALS

6.1 Introduction

Studies of the thermal conductivity of II-VI type crystals are important in their own right since this type of information is most necessary for the engineer concerned with device applications, especially in a variable temperature environment. Additionally, the use of low-temperature thermal conductivity changes as a probe in studies of the character of lattice imperfections induced by radiation has been well-known for several decades. However, partly because of the nonavailability of good crystal specimens, such research on almost all of the II-VI compounds has been neglected. Another reason for this neglect is, of course, the fact that much of the early work was confined to the elemental semiconductors such as Ge and Si because of the less complicated associated problems. Many of the conclusions of these preliminary studies indicate the advantages of extending this method to other classes of materials. It has been predicted with confidence that many interesting and important findings will be made in compound semiconductors, in particular, in the II-VI materials.[74]

Thermal conductivity theory indicates that this property is particularly sensitive to impurities and defects in the temperature region where the thermal conductivity is a maximum. Although in some cases the maximum is near room temperature, for most dielectric solids the important temperature region is below 50°K. Thus, low-temperature techniques are desirable.

Radiation produces an additional thermal resistance and to a first approximation this addition can be regarded as a quantity which is additive to the normal lattice resistance. In quartz, for example, the additional thermal resistance has a minimum at approximately 15°K. Above 15°K it increases directly with the temperature and it has been suggested that in this region the resistance is caused by the presence of single lattice defects.

Below 15°K the radiation-induced increase in the thermal resistance increases more rapidly than 1/T and it is believed that the cause is due to the presence of large defects at lower temperatures.

The effectiveness of the thermal conductivity tool results from the ability of the different types of lattice defects to produce corresponding temperature-dependent differences in the phonon-scattering probabilities. For example, the several well-known behaviors and defects may be tabulated as follows:

Table 6-1 Thermal resistance behaviors of various defect types

Lattice Defect	Thermal Resistance Behavior
Point defect	Increase is proportional to temperature, T
Dislocations, elongated disorders, etc., linear regions	Increase is inversely proportional to T
Two-dimensional boundaries	Increase is inversely proportional to T^3

Since any physical or chemical defect can be a source of phonon scattering, those materials which have the fewest defects are best suited for extensive thermal conductivity measurements. In recent years small single crystals of some of the II-VI compounds have been prepared in a high purity state. Feedback from thermal conductivity measurements on these crystals has aided in the development of better growth techniques. At the same time such measurements are important because of their ability to form a basis for comparing thermal conductivity results on irradiated crystals and, thereby, identify radiation-induced defects. Such results give information on the nature and properties of the interstitial, the role of impurities, and perhaps help to identify the temperature at which long-distance defect migration begins to take place.

Furthermore, thermal conductivity measurements can provide much insight in differentiating between various possible processes. For example, by measuring the change in thermal resistance along different crystallographic directions, before and after irradiation and after temperature pulses of an isochronal anneal, the presence of anisotropic defects as well as the preferential alignment of these defects can be detected. This is because such defects are anisotropic phonon-scattering centers which produce an anisotropic increase in the thermal resistance of the sample. The anihilation of interstitials at vacancy sites can also be detected as a decrease in the thermal resistance. Thermally-induced defect clustering would produce, on the other hand, an increase in thermal resistance. Such defects might have a preferential orientation in a wurtzite structure or might be preferentially oriented by an externally applied strain in the case of zinc-blende lattices. Thermal conductivity measurements are, therefore, vital to a complete understanding of the defect structures produced as a result of bombardment and annealing. By combining this technique with NMR, luminescence, optical absorption, and electrical measurements, a much better understanding of the irradiation defects in semiconductors is possible.

6.2 Thermal Properties Equipment

The equipment with which the absolute thermal conductivity measurements have been made has undergone modifications[75,76] which have permitted it to be used to make measurements of magnetic susceptibility,[77-79] (some of these measurements have been carried out on samples at temperatures below $0.1^{o}K$[80]), magnetoresistance,[81] and the specific heat of various II-VI compounds.[82-88] Preliminary thermal conductivity experiments have also

been made on CdS with different concentrations of magnetic impurity.[89] In addition, the experimental apparatus has been used to obtain absolute thermal conductivity results for thermal insulators such as nylon[90] and thermal bonding agents,[91] such as Cry-Con and the Apiezon greases.[92-96] These results have been especially useful in the research since it is necessary to know the thermal transport properties of the technological materials when they are used to support the experimental specimens. Furthermore, anomalies observed in the heat conduction of thermal greases have special application[97] when grease is used as a thermal bond. Likewise, information on methods of establishing low-temperature mechanical contacts with the II-VI compounds has also been useful.[98] Other improved aspects of the equipment, such as the incorporation of a superfluid value[99] into a variable temperature dewar[100], have been useful in helping to carry out cryogenic experiments.

6.3 Thermal Conductivity Measurements on II-VI Compounds

Thermal conductivity results at room temperature on undoped polished single crystals of ZnO, ZnS, ZnSe, ZnTe, CdS, CdSe, CdTe, HgS and crystals with Li, In, Co, and Mn impurities have been obtained with a thermal comparator. Although the duration of each measurement was approximately less than 10 to 20 seconds, numerous readings were taken in order to obtain statistical information on the reliability of the data. In most cases the percent probable error associated with the reproducibility of a measurement was found to be in the neighborhood of 1%, and the results are in reasonable agreement, though slightly higher than previous experimental work. The higher conductivities are interpreted as due to the more recent availability of better crystals.[101]

Because it is not always possible to use large samples, we have explored the use of the comparative method of measuring the thermal conductivity of small samples. Plexiglass disks are used to hold various II-VI compounds mounted in woodsmetal. The crystals are ordinarily mounted this way for polishing and no further preparation is necessary for a conductivity measurement. We have kept the samples on a large copper plate in a room where the temperature drifts and air currents are minimized. A sample is lifted by tongs to the sample stage of the comparator. The arm trip lever is depressed and the probe assembly is released and comes into contact with the sample.

The probe is kept at some temperature about 20°C above room temperature. When the sensing tip comes into contact with the sample, heat is extracted from the probe at a rate which is dependent on the thermal conductivity of the sample. The response of the probe produces a microvolt reading which is recorded. The entire operation takes about 15 seconds. Standards used for calibration are armco iron, stainless steel, titanium alloy, quartz, glass, and ebonite.

After taking a reading on a sample, we have found it convenient to move the sample slightly on the stage so that the probe may come into contact with another point of the sample's surface. Normally this second reading should be lower because of the warming of the sample during the first reading. If the second reading is larger, it may imply that the contact of the probe with the surface is not good and in this case both readings are discarded. With a properly polished surface, less than 10% of the readings need to be discarded when this technique is used.

Table 6-2 illustrates some results on zinc compounds. Note that the ratio of successful readings to total reading, using the criteria just mentioned, varies from 1 to about 0.5. The ZnSe mounted crystal had small cracks, and these and other surface defects could have decreased its ratio.

The reproducibility of the remaining readings is often better than 1 percent and seldom worse than 1.5 percent, as can be seen in the table.

Table 6-3 shows our results on zinc oxide along with those of Koenig,[102] Slack,[103] and Martin and Wolf.[104] Martin and Wolf appear to have the highest value at 300°K. Table 6-3 also compares data for additional zinc compounds. It is expected that polycrystalline and hot-pressed materials should have lower conductivity values and this is borne out by the comparison. Martin and Wolf have reported their results on ZnO recently.

Table 6-4 gives results for some cadmium compounds. There is very good agreement with CdS. Our CdS crystal was analyzed by Bell and Howell and it was found to have 6.3 ppm carbon, 2.9 ppm H, and 2.0 ppm V. All other impurities found were less than 1 ppm.

6.4 Thermal Conductivity Results from Comparator Measurements on CdTe Crystals

The work described in this section is partly representative of a coupling effort of the Solid State Physics Laboratory of the Aerospace Research Laboratories with the Laser Window group of the Materials Laboratory. The latter supplied the CdTe crystals upon which the measurements reported below were measured. Comparator results on other II-VI compounds have been reported above.

The thermal conductivity of 15 different CdTe samples was measured and the highest value observed, 0.117 ± 0.007 $Wcm^{-1}K^{-1}$ @ 298 K was obtained on

Table 6-2. Thermal-comparator results on Zn compounds at 300°K

Sample	λ ($Wcm^{-1}K^{-1}$)	Reproducibility* (%)	Successful Reading / Total Reading
ZnO (Litton)	0.36±5.5%	0.5	4/4
ZnS (Mounted)	0.27±7.0%	1.0	39/42
ZnS (CC)	0.22±9.3%	1.1	7/7
ZnS (183 EP)	0.19±7.4%	0.8	6/8
ZnSe (Mounted)	0.23±6.8%	1.0	23/40
ZnSe (188 EP)	0.18±8.1%	1.2	23/27
ZnSe (P. Coors)	0.15±8.2%	1.5	17/24
ZnSe (P. Raytheon)	0.14±7.4%	1.0	5/7
ZnTe (Melt, E. P.)	0.22±5.9%	0.9	12/16

* See Ref. 127 for a discussion of this factor.

Table 6-3. Thermal conductivities of Zn compounds at 300°K

(L designates the linear-heat-flow method, and C, the comparator method)

Crystal	$\lambda(Wcm^{-1}K^{-1})$	Method, Crystal Data, Source	Reference
ZnO	0.31 (extra-polated)	---, Yellow color, Rutgers U.	Koeing (1953)[102]
	0.25	---, Grey color, Rutgers U.	Koenig (1953)[102]
	0.54	L, Single, colorless, N.J. Zinc	Slack (1966)[103]
	0.58	L, Single, hydrothermal, Ventron	Martin & Wolf (1972)[104]
	0.62	Li doped	Martin & Wolf (1972)[104]
	~0.8 (extra-polated)	L, Single, vapor, 3M	Martin & Wolf (1972)[104]
	0.36±6%	C, Single, hydrothermal, slight yellow color, Litton Ind.	Present Results[101]
ZnS	0.265	L, Natural Cubic	Eucken & Kuhn (1928)[105]
	0.27	L, Single, vapor, colorless, G.E.	Slack (1966)[103]
	0.27±7.0%	C, Single, melt, mounted, E.P.	Present Results[101]
	0.22±9.3%	C, Single, melt, 1 cm cube, E.P.	Present Results[101]
	0.19±7.4%	C, Single, melt, #833, E.P.	Present Results[101]
ZnSe	0.14	Polycrystalline, hot-pressed	Ioffe & Ioffe (1960)[106]
	0.13@ 327K	Polycrystalline, hot-pressed	Ladd (1963)[107]
	0.19	L, Single, vapor, lemon-yellow, G.E.	Slack (1966)[103]
	0.23±6.8%	C, Single, melt, 321 (M7102 BQ),E.P.	Present Results[101]
	0.18±8.1%	C, Single, melt, P-188 (M7103 ER)E.P.	Present Results[101]
	0.15±8.2%	C, Polycrystalline, Coors	Present Results[101]
	0.14±7.4%	C, Polycrystalline, vapor, Raytheon	Present Results[101]
ZnTe	0.17		Kelemen et.al. (1965)[108]
	0.18	L, Single, vapor, red-brown, G.E.	Slack (1966)[103]
	0.22±5.9%	C, Single, melt, E.P.	Present Results[101]

Table 6-4. Thermal conductivities of Cd compounds at 300°K

Crystal	λ(Wcm^{-1}K^{-1}	Method, Crystal Data, Source	Reference
CdS	0.20	L, Single, Vapor, ARL	Holland (1964)[115]
	0.2	L, Single, Clevite	Vook (1968)[116]
	0.20±8.4%	C, Single, melt, semi-elements	Present Results[101]
CdSe	0.043 (cubic)	---, Polycrystalline, hot-press	Ioffe & Ioffe (1960)[106]
	0.063	---, Polycrystalline, hot-press (at 280°K)	Ioffe & Ioffe (1960)[106]
	0.12±6.2%	C, Single, Vapor, ARL	Present Results[101]
CdSe:Li	0.11±7.3%	C, Single, Vapor 10 ppm Li, ARL	Present Results
CdTe	0.052	---, Polycrystalline, hot-press	Ioffe & Ioffe (1960)[106]
(Cubic)	0.075	L, Single, melt, G.E.	Slack Galginaitis (1964)[117]
	0.09	L, Single	Holland (1964)[115]
	0.016-0.035	L, Single	Horch & Nieke (1965)[118]
	0.11±5%	C. Single, ARL	Present Results[101]
	0.087±4%	C, Single, Hughes	Present Results[101]
CdTe:In	0.10±6%	C, Single, 100 ppm In, ARL	Present Results[101]

an undoped single crystal. Other single crystal samples which also gave high conductivity values contained small amounts of Ga (20 ppm) or In (10 ppm). The largest conductivity values for polycrystalline samples were observed to lie below 0.100 $Wcm^{-1}K^{-1}$. The data were obtained using a commercial instrument with a capability of making a measurement on a polished sample surface within a duration of approximately 10 seconds. Out of a total of 302 measurements, 267 or 91% were found acceptable (according to criteria adapted to eliminate erroneous readings) and the average reproducibility of all of these measurements was calculated to be $\pm$ 0.92%. The average value for the precents of error for the 15 samples was determined to be 5.3%.[119]

Table 6-5 describes 15 CdTe crystals which were measured. Eleven of the CdTe crystals are designated as single crystals in the table. However, this means that they contain large single crystal parts about 1 cm^2 in area. The results of thermal conductivity measurements on these CdTe crystals by the comparator method are shown in Table 6-6. As is expected, single crystals, either pure, or compensated with small amounts of gallium or indium, yield the highest conductivities.

The criteria adopted to eliminate poor readings can be illustrated with sample number 18. (See the top of the table.) Only 27 out of 31 sets of measurements were accepted. The remaining 4 sets were discarded because the second reading in each set was larger than the first. And this was taken as an indication that the probe had not come to rest on a good spot on the crystal.

In general, it might be inferred that the condition of the surface is related to the percentage of measurements accepted. For all of the CdTe

Table 6-5. Description of CdTe samples measured by the thermal-comparator method

Sample Number	Material	Nominal Dopant	Crystal-linity	Size Diam.	(mm) Thick	Original Source
17	CdTe	Undoped	~ Single	48	7	Gould[109]
18	CdTe	Undoped	~ Single	54	10	Gould[109]
23	33Ge55Se12As	Chalcogenide	Glass TI-20	25	6	Tex. Inst.[110]
25	28Ge60Se12Sb	Chalcogenide	Glass TI-1173	25	7	Tex. Inst.[110]
29	ZnSe	Undoped	Poly	39	6	Coors[111]
36	CdTe	Undoped	Poly	39	4	Coors[111]
38	CdTe	10ppmIn	~ Single	27	2	Hughes[112]
39	CdTe	10ppmIn	~ Single	27	2	Hughes[112]
40	CdTe	10ppmIn	~ Single	28	13[a]	Hughes[112]
42	CdTe	1500ppmIn	Poly	49	4	Tyco[113]
43	CdTe	Undoped	~ Single	38	4	Gould[109]
44	CdTe	20ppmGa	~ Single	49	8	Gould[109]
45	CdTe	20ppmGd	~ Single	49	11	Gould[109]
56	CdTe	1500ppmIn	Poly	50	4	Tyco[113]
58	CdTe	100ppmCl	Poly	51	10	Tyco[113]
68	ZnSe	Undoped	Poly[b]	26	2	Ratytheon[114]
86	CdTe	Undoped	~ Single	47	4	Gould[109]
87	CdTe	20ppmGa	~ Single	48	6	Gould[109]
88	CdTe	20ppmGa	~ Single[c]	48	7	Gould[109]

[a] Maximum dimension of edge. The crystal was in the shape of a frustrum of a cone.

[b] Irregular area.

[c] Etched surface.

Table 6-6. Thermal-comparator measurements on CdTe samples described in Table 6-5

Sample Number	Material	Number of Measurements / Number of Attempts	$\lambda \pm$P.E. ($Wcm^{-1}K^{-1}$)	Reproducibility* (%)	P.E. (%)
18	CdTe	27/31	0.117±0.007	1.1	6.0
45	CdTe+20ppmGa	20/22	0.113±0.008	1.2	7.3
44	CdTe+20ppmGa	19/21	0.112±0.006	0.90	5.4
40	CdTe+10ppmIn	29/32	0.109±0.007	1.0	6.3
88	CdTe+20ppmGa	8/9	0.108±0.004	0.51	3.7
17	CdTe	25/30	0.102±0.006	0.89	5.5
87	CdTe+20ppmGa	9/9	0.098±0.002	0.34	2.0
58	CdTe+100ppmCl	29/30	0.098±0.006	1.0	5.7
43	CdTe	28/30	0.095±0.005	0.83	4.9
86	CdTe	7/9	0.094±0.003	0.55	3.2
56	CdTe+1500ppmIn	3/5	0.094±0.006	1.3	6.4
36	CdTe	24/25	0.088±0.003	0.78	3.8
42	CdTe+1500ppmIn	29/30	0.088±0.004	0.91	4.9
39	CdTe+10ppmIn	10/10	0.081±0.004	1.0	5.4
38	CdTe+10ppmIn	9/9	0.074±0.004	0.97	5.3

* See Ref. 127 for a discussion of this factor.

crystals included here there was a total of 302 sets of measurements and 276 or 91.4% of these were acceptable. The average reproducibility was within 0.92% and the average error was within 5.3%.

6.5 Thermal Comparator Measurements on Ion-Implanted CdS

Work on the thermal conductivity of ion-implanted samples of CdS was initiated during the report period in order to aid a probe of the physical characteristics of the implanted layers. This work was carried out with the collaboration of Y. S. Park and W. R. Woody. D. E. Johnson assisted by orientating, cutting and polishing the crystals. A paper[120] on the subject of this section was presented at the XII International Conference on Thermal Conductivity in Birmingham, Alabama. A summary[126] of the work follows.

Recently, a growing interest has been generated in type-converting II-VI compound semiconductors.[121] Ion-implantation techniques appear to be particularly attractive for II-VI compound semiconductors, because of the difficulty of achieving type conversion and p-n junction formation by thermal diffusion and/or other conventional growth and doping techniques. Furthermore the accomplishment of such transformations in the electrical characteristics when combined with the typically large band gaps associated with this group of semiconductors offers the promise of optoelectronic devices associated with electroluminescence in the visible range. However, in order to use the ion-implantation technique to its best advantage, many questions such as the extent of radiation damage, the lattice location, and the penetration depth of the implanted ions remain to be answered. In the past, thermal comparators have been used for comparative thickness determinations of materials and surface deposits.[122-125] We have used the thermal comparator to observe changes in the thermal conductivity of the implanted layers in CdS in the hope that these measurements may contribute to the understanding and to the

characterization of the profile of the implants. A dose of singly-ionized atomic nitrogen (N^{14}) ions, measured to be 10^{15} ions/cm^2, was implanted at 90 KeV into a polished CdS surface, the normal to which was parallel to the c-axis of the crystal. Thermal conductivity measurements on this crystal and on three other unimplanted, but otherwise identical, crystals were taken and a statistical summary of the results produced the conclusion that the thermal conductivity of the implanted sample decreased by approximately 25%. A second experiment produced a similar result. A third experiment, in which the unimplanted area adjacent to the implanted area was tested, resulted in a thermal conductivity similar to the unimplanted samples. The results of the preliminary measurements were encouraging because they demonstrated the potential of this technique. They show that the comparator technique can easily detect the presence of an implant.

In order to expedite the study of the physical properties of implanted layers, thermal conductivity measurements have been carried out on single-crystal cadmium sulfide samples implanted along the c-axis direction with doses of 90 KeV N^+ ranging from 5×10^{14} to 5×10^{15} ions per cm^2. The electrical resistivity, mobility, and carrier concentration were found to be 5.32 Ω-cm, 292 cm^2/Volt-sec, and 4.03×10^{15} cm^{-3}, respectively, typical of the n-type base material. The thermal conductivity was measured by the comparator method which, prior to implantation, gave a value of 0.20 W cm^{-1} K^{-1}, in good agreement with published values. The decrease in thermal conductivity, occurring with an increase in dose, was observed to be equal to 12.5% for a dose of 5×10^{14} ions per cm^2 and 25% for a dose of 10^{15} ions per cm^2. A sample having a dose of 5×10^{15} ions per cm^2 was annealed in vacuum for 15 minutes at 500°C. While the annealing removed to darkened region left by the implantation, subsequent observations on the annealed sample disclosed that most of the implant damage (as measured by the remaining thermal resis-

tance) was still present. More recent measurements on similar samples indicate identical results for an annealing temperature of 250°C. It is possible that the nitrogen impurities, left within the implanted layers, may be responsible for that part of the increased thermal resistance left after the annealing. Argon- and nitrogen-implanted CdS crystals have been investigated to uncover differences. ZnTe implanted with Al has also been scanned.

It was concluded that the comparator method of measurement offers good potential as a useful tool in the study of implanted layers. A detailed summary of the use of the comparator to obtain thermal conductivity data on II-VI compounds has been published during the report period.[127]

6.6 Thermal Conductivity of Support Materials

The necessity of knowing the thermal properties of technological materials such as nylon and greases has already been mentioned in Section 6.2. Preliminary experiments on such materials have already led to thermal conductivity[90-96] and heat capacity[97] data. Some of this research was completed during the period of this report. Although these studies do not involve II-VI semiconductor compounds directly they may be considered as valuable spin-off connected with the research since the results have not only aided in the research on II-VI compounds but they have also helped all similar research. They are mentioned briefly in the next few paragraphs.

Measurements of the temperature dependence of the thermal conductivity of nylon have been carried out over a temperature range from liquid helium temperatures up to 350°K. A maximum $\lambda_{max} = 0.371\ Wm^{-1}K^{-1}$ was observed at the glass-transition temperature, $T_g = 330°K$. Because the results gave values which were significantly larger than previous results at room temperatures, and because the data were obtained by using the linear-heat-flow method instead of methods based on a radial flow of heat, it was suspected

that orientation anisotropy in the nylon (possibly due to extrusion effects) could account for the difference. Although measurements by a comparator method on sample surfaces cut perpendicular and parallel to the direction of extrusion failed to show any anisotropy, all of the results were in reasonable agreement with thermal conductivity results obtained by the linear-heat-flow method. Use was made of $\lambda_{max.}$ to compare thermal transport of nylon with that of other polymers. In particular, the dependence of $\lambda/\lambda_{max.}$ on T/T_c for nylon, natural rubber, silicon rubber, poly (methyl methacrylate) and poly (vinyl chloride), was determined and it was observed that the tendency for the curves to peak at $T = T_c$ was common. During the report period a paper on this subject was presented at the XII International Conference on Thermal Conductivity in Birmingham, Alabama. The work reported was performed in collaboration with T. Ashworth of the Physics Department at the School of Mines and Technology in South Dakota. Summaries of this work have been published.[128]

Greases are often used to bring about improved thermal contact between experimental components such as thermometers, samples, heat sinks, and shields over a temperature range extending from less than $1^{o}K$ up to their melting points. A study of the effectiveness of these materials has also been published.[129]

The work described in this paragraph involves a coupling effort with Mr. J. Becsey of the ARL Chemistry Laboratory and workers in the Avionics Laboratory who were searching for a suitable heat-sink liquid. The thermal conductivity of the organic dimethylsulfite is of interest because of its potential use as a nonaqueous battery solvent owing to its stability with high energy density electrodes and its ability to dissolve electrolytes.

Mahefkey and Kreitman[130] have noted that the important thermal related properties of battery performance, viz., cell cycle life, and cell capacity, as well as electrical efficiency, can be strengthened by operation at lower battery temperatures which they achieve with the introduction of an intercell heat pipe. The removal of waste heat from a battery is an important design characteristic and therefore the thermal conductivity of the electrolyte solution is a significant factor in the design and operation of a battery. However, very little information exists on the thermal properties of dimethyl sulfite. In order to help fill this gap, a thermal comparator was used to obtain measurements on the room-temperature thermal conductivity of a liquid sample of dimethylsulfite using a liquid-cell adapter and the basic thermal comparator apparatus described elsewhere.[127] Mr. Becsey supplied the dimethylsulfite sample and a number of the calibration standards, i.e., H_2O, glycerol, methanol, and CCl_4. The value obtained for the thermal conductivity of dimethylsulfite was 0.00178 $Wcm^{-1}K^{-1}$. For more detailed information the reader is referred to the published article.[131]

6.7 Some Notes on the Comparator Method

We have used the comparator method on many other crystals and, aside from its advantages, there are definite problems that the user should be aware of. One problem is the necessity of sufficient and clean calibrating standards. This is particularly true when measuring CdTe which has a conductivity between stainless steel and armco iron. Because of a bend in the calibration curve in this region more calibrating standards are necessary. Another difficulty with some standards, such as armco iron, is the oxidation which affects its surface. It may be possible to replace such standards with II-VI compounds. Our results show that the reproducibility of readings on CdS, for example, is much higher than that for the iron or the stainless steel.

The thermal comparator appears to yield its highest reproducibility when measuring plastics.[127]

6.8 Linear-Heat-Flow Measurements on ZnSe and Type 316 Stainless Steel

With a modified form of the apparatus used to measure the thermal conductivity of nylon and greases (described in reference 95), a number of linear-heat-flow measurements have been carried out on bar samples of ZnSe and type 316 stainless steel, from room temperatures down to pumped nitrogen temperatures. The former material was supplied by the Laser Window Group of the Materials Laboratory. Mr. D. Locker of the Solid State Physics Laboratory collaborated in the measurements.

The results of our linear-heat-flow measurements on the ZnSe bar (dimensions 0.62 cm x 5.32 cm x 0.28 cm) yield room-temperature values differing (by more than our limits of error) with the literature values of ZnSe. Although the addition of insulating powder and increased vacuum were observed to decrease the disparity, a significant variance remained. In order to test the accuracy of the modified linear-heat-flow apparatus a bar of type 316 stainless steel was machined and measured in place of the ZnSe. In addition, a disc of the same 316 material was machined and polished to the dimensions of the 316 calibration standard of the thermal comparator instrument. The results of comparator measurements on the 316 sample were found to be identical to those on the comparator 316 calibrating standard, yielding a room temperature conductivity of approximately 0.14 $Wcm^{-1}K^{-1}$ for the 316 test bar and thus validating its use as a means of checking the modified linear-heat-flow apparatus. Subsequent linear-heat-flow measurements on the 316 test bar yielded thermal conductivity data slightly larger than its accepted value. In other experiments, insulating powder (to reduce radiation losses) and increased vacuum have also been observed

to reduce the discrepancy in the stainless steel data. Although the experiment had to be terminated in order to attend to the other investigations (below) it appeared that the preliminary results of the measurements indicated a ZnSe thermal conductivity which was slightly higher than that found by Slack[103] in Table 6-3.

6.9 Debye θ and Heat Capacity Studies in II-VI Compounds

The II-VI compounds have aroused a good deal of interest over the past few years for a variety of reasons. In order to analyze the vibrations in these compounds and to analyze properties of the vibrational frequency spectra, knowledge of the specific heat, thermal expansion, and elastic constants are required, ideally over a wide range of low temperatures. An examination of the available thermodynamic data for the oxides, sulfides, selenides, and tellurides of zinc, cadmium, and mercury reveals the existence of a large number of gaps. Only for zinc oxide and zinc sulfide do sufficiently complete sets of data exist to justify thermodynamic analysis, and even in these cases the analyses can only be embarked upon with reservations.[132]

Furthermore, theoretical studies of low-temperature specific heat anomalies arising from simultaneous effects of exchange and magnetic fields had been initiated to study factors which influence impurity peaks in the low-temperature specific heat of samples in zero and non-zero magnetic fields. One conclusion was that the simultaneous presence of exchange interactions and external magnetic fields on doped crystals may lead to two peaks in the low-temperature dependence of the heat capacity. These two peaks may best be seen when the ratio of the magnetic energy to the exchange energy is close to, but not equal to, certain integers, the number of which varies directly as the spin of the magnetic atoms in a pair system. Further information may be obtained from the work which was published during the report period.[133] The application or test of these ideas rests on attempts to approximate a dilute state of magnetic material by adding magnetic atoms to a diamagnetic lattice, and describing the resulting magnetic

cooperative phenomena by the cluster method,[134] which considers the magnetic impurity atoms in various nearest neighbor, next-nearest neighbor, and/or higher order clusters.[135]

In order to satisfy a need for more experimental data on II-VI compounds and on low-temperature heat-capacity anomalies, work had been initiated on CdS. During the report period work on the specific heat and Debye θ of CdS:0.45% Mn was completed. Experimental heat-capacity measurements permitted values of Debye θ to be tabulated down to 3.32°K. The low-temperature limiting value of $\theta_{thermal}$ (T = 0) = 216 $\pm$ 4°K was found to correspond satisfactorily with an experimental value of 215°K obtained by Gerlich[136] from low-temperature elastic constant data on CdS. This result differed by 7.4% with the theoretical value of 200°K obtained by Goel and Singh[137] based on a simple model involving a radial nearest-neighbor approximation. A theoretical value of 263°K published by Nusimovici et.al.,[138] was found to be 19.2% different. Additional information may be obtained from our published work.[139]

AD-A032 128 DAYTON UNIV OHIO DEPT OF PHYSICS F/G 20/12
IDENTIFICATION OF DEFECTS IN COMPOUND SEMICONDUCTORS.(U)
OCT 76 D C LOOK, J M MEESE, M M KREITMAN F33615-71-C-1877
UNCLASSIFIED AFAL-TR-76-139 NL

3 OF 3
AD
A032128

END

DATE
FILMED
1-77

7.0 OPTICAL INVESTIGATIONS IN II-VI COMPOUNDS AND RELATED MATERIALS

Optical absorption studies can be used to give important information. Although the chief interest in the effects produced by irradiation of semiconductors is generally agreed to lie in the area of electrical properties, studies of the optical absorption (as well as other spectroscopic methods) can give detailed information related to the microscopic character of the defects. Irradiation normally produces a variety of new absorption bands which can be divided into "Localized Vibrational Bands" and "Electronic Excitations". The identification of the defects associated with the bands could help in solving many unanswered questions. Such studies have led to information about the local symmetry of particular defects.[140] Once identified, the band can serve as a tool for monitoring the damage. Optical spectra can also give information about the excited states to which a transition is made.

7.1 Raman Scattering in ZnTe

Work in this area of research was initiated in order to carry out electron-spin-flip scattering measurements and study the associated physical parameters of II-VI semiconductors. In one experiment, measurements were carried out on a ZnTe crystal at 4.2°K in various magnetic fields up to 89 kG, approximately. At least 3 clear spin-flip peaks were observed to occur at short distances from the laser line in the spectra, for slit widths less than 50 μ. Other experimental work performed within the report period has been at liquid-helium temperatures and in magnetic fields up to 90 kG with scattered light from an argon laser line. This work has disclosed (possibly for the first time) what appears to be second-, third-, and possibly fourth-order stokes and antistokes lines. Time was also devoted to aligning and replacing components in a

krypton laser system. In addition, the vacuum system associated with this experimentation area was modified. Part of this effort involved setting up a 69 kG superconducting magnet system and designing metal and glass parts to complement and improve various experiments with a 100 kG magnet system.

7.2 Infrared Absorption in ZnS and ZnSe

Studies in infrared absorption were initiated in order to examine the near and far-infrared absorption of ZnSe:Co, ZnSe:Al, ZnS:Co, GaAs, and certain other crystals with alkali-metal dopings as a function of temperature, including cryogenic temperatures, with the aim of sorting out and identifying host-lattice native defects and impurity defects having potential possibilities leading to the production of better infrared detectors from the large-band-gap compounds.

Taken with a 60-inch grating spectrometer, absorption measurements in the near- and far-infrared on single crystals of pure and aluminum doped ZnSe, have revealed the presence of multiphonon processes along with localized vibrational modes, the latter arising from the Al doping. ZnSe interference phenomena displayed at ~30μ from crystal temperatures of 300, 100 and 40°K make possible a determination of the index of refraction.

Near-infrared measurements on undoped ZnS samples and 4 ZnS:Co samples have revealed large absorptions in the regions 1.30 to 1.86 μ, and 2.4 to 3.0 μ, approximately, corresponding to $^4T_1(F)$ and $^4T_2(F)$ levels of cobalt (d^7) in cubic ZnS with a crystalline field parameter, D_q, of approximately 375. At liquid-helium temperatures sharp absorption lines appear in both the 3 and 1 μ grating spectra of those crystals having significant cobalt impurity. Data have been obtained on various experimental samples in the wavelength regions offered by the 1, 3, 18, 30 and 45 μ gratings, and, after zero-corrections are made, the results are in approximate agreement with those cases where published

results appear in the literature. Water vapor-lines were used to check the calibration of the spectrometer.

7.3 Infrared Absorption in α-HgS

7.3.1 Introduction

Mercury sulfide is a wide bandgap semiconductor which is of considerable interest because its unique properties offer excellent potential for non-linear optics and laser-technology devices. It is the most optically active of all known mineral compounds, possessing the greatest birefringence, a remarkable rotary power, and strong piezoelectric properties.

Sapriel[141] has reported that α-HgS has the highest acousto-optical figure of merit of any known crystal, making it an efficient material for acousto-optical applications, such as transducers, light modulators, deflectors, delay lines, etc. Ultrasonic attenuation and the elastic and photoelastic constants in α-HgS have been measured.[142] Sapriel and Lancon[143] have pointed out that, since the electromechanical coupling coefficients of cinnabar are approximately two times larger than those of quartz, piezoelectric α-HgS transducers, bonded on a parallelpiped cinnabar crystal would realize perfect accoustical matching and therefore yield wide bands for acousto-optical deflection. Thus α-HgS should serve well as a good deflectior of laser light. For example, if one assumes a frequency bandwidth of 250 MHz for a transducer made of cinnabar, and an acoustic beam 1/2 mm square, it may be shown that only 210 mW of acoustic power is necessary to deflect all of the incident light of a He-Ne laser beam into 62,500 different positions with an access time of 1 μs.

Measurements[144] on the red-colored α-phase of synthetic and good natural crystals indicate a transparency of more than 50% between 0.6 and 14 μ at 300°K. Residual absorption in the transparent region is known to be less tha 1 cm^{-1}

for good quality natural crystals.[145-146] Large indices of refraction have been measured[147] over the range 0.62-11 μ. The proximity of the upper limit of the transparent region to the 6328Å He-Ne laser line, and the large temperature dependence of the HgS absorption edge (~9×10^{-4} eV/C), has already been exploited[148] for thermal modulation of the laser line (by the thermoabsorption of cinnabar).

Photoelectronic properties of α-HgS have been studied, chiefly in the more available, good quality, natural crystals and these studies reveal a close similarity to those of other II-VI compounds. Some results[149] in synthetic crystals include a peak photoconductivity at ~6000Å (300°K) for HgS (~10^{12} Ωcm); the existence, within the energy gap, of localized levels of electrons (0.62 eV) and holes (1.08 eV) from the conduction band; and thresholds (0.67 eV and 1.08 eV) for optical quenching. In other studies[150] the conductivity of illuminated natural crystals has been observed to increase by 6 orders of magnitude. Furthermore the mobility in a direction perpendicular to the c-axis has been determined[151] to originate from electrons at 10 $cm^2 V^{-1} s^{-1}$ while others[150] have noted a photo-Hall mobility of 38 $cm^2 V^{-1} s^{-1}$ in a crystal which may not have been oriented.

The strong non-linear properties of cinnabar are also important for integrated optical circuits, parametric oscillator upconversion, difference-frequency generation, tunable lasers, and other applications. For example, Martin and Thomas[152] have suggested that the stimulated Raman effect be combined with the non-linear electro-optic effect[153] in HgS in order to conveniently generate pulses of radiation between 9 and 15 μ. They utilize the non-linear electro-optic effect to generate a beat frequency between a Nd^{3+}/glass laser and the laser-activated, stokes Raman emission. The difference frequency is equal to the molecular vibrational frequency of the Raman process.

The successful future utilization of all of these devices, and the exploration and study of these and additional properties of α-HgS, rests heavily on the growth of good quality single crystals, which, until recently, has been very difficult. Below we report optical measurements which help to confirm the yield of good cinnabar crystals. These results form part of a presentation at the Conference on Optical Properties of Highly Transparent Solids at Waterville Valley, New Hampshire, in 1975, the proceedings of which have been published by Plenum Press.[154] A preliminary report of this work was reported earlier.[155]

7.3.2 Results

Some of the larger cinnabar crystals, grown by the iodine vapor-transport methods[141], were used as samples for optical investigations in the visable and infrared spectral regions. A typical measured value of crystal thickness was 330 μ. In one study, a 2-meter spectrograph was employed to take photographic plates (4 Å/mm) of the edge absorption of a number of crystals on which a tungsten source was focused. In this arrangement the crystals were mounted on a rod within a fixed temperature dewar and measurements were carried out at room temperature and at 4.2°K. A densitometer analysis of the photographic plates enabled values of the wavelength at zero absorption to be tabulated with the exposure times and this led to an extrapolation of the wavelength corresponding to zero-exposure time and a value of 6115 Å for the approximately || absorption edge at 300°K with a decrease of approximately 2.0 Å/K on cooling to 4.2°K. Additional transmission data taken on a Cary spectro-photometer were used to verify this value for the edge. A value of the reflection at 0.63 was calculated as 26%. The observed temperature dependence is in rough agreement with a literature value[156] of 1.8 Å/K, the difference being

easily attributed to the pronounced dichroism of the α-HgS edge. In fact, because of the small size and delicate nature of the crystals, use was made of this anisotropy to check the orientation of the crystal after mounting.

Although we did not thoroughly search for it at very low absorption levels,[145] we did not observe any discrete structure near the edge at 4.2°K. Typical values of resistivity for our samples were approximately 2 x 10^9Ωcm which may be compared to 10^{12}Ωcm obtained by Roberts, Lind and Davis[149] for their undoped synthetic cinnabar. Their high resistivity crystals, of mm dimensions, were grown at temperatures just below the polymorphic transition temperature by a reaction of the HgS elements in sealed quartz ampoules containing 200-400 mm Hg pressure at room temperature.

Infrared measurements were performed with the crystals at temperatures of 32, 92, and 300°K in a metal cryostat and mounted on a cold finger, instrumented with Ge, Pt, and carbon thermometry. The tail and barrel of the dewar were enclosed within a vacuum spectro-photometer having a focal length of 60 inches. The spectrometer has Czerny-Turner optics and utilizes interchangeable 7" x 9", kinematically mounted reflection gratings, blazed at 1, 3, 9, 18, 30, 45, 60 and 100 μ with associated spectral reststrahlen filter plates, filters, choppers, and I.R. sources together with a Golay cell detector. Sapphire, ZnSe and polyethelene dewar windows were employed for the low-temperature measurements and at 30 μ a typical value of the inverse linear dispersion was experimentally computed to vary between 0.028-0.030 μ/mm for a range of grating angles.

Measurements of the infrared transmission were carried out in vacuum over a wavelength range which extends from the fundamental absorption to beyond the restrahlen edge beginning at approximately 27 μ. Some typical experimental data representing some of the more prominent absorption peaks which we have observed are presented in Table 7-1 for comparison with the work of others.[157]

Table 7-1 Low temperature I-R data on α-HgS phonon frequencies.

E		A	E			
T	L	T	T	L	T(K)	Source
285	290	334	340	348	32	Present work, ARL
283	290	340	344	350	300	Barcello, et. al.[152]
277	287	333	338	346	90	Zallen, et. al.[153]
284		345			77	Riccius, et.al.[154]
280		335	343		300	Poulet, et. al.[155]

From the data comparisons summarized above it may be concluded that the optical measurements verify the growth of α-HgS crystals and that the iodine transport method and its associated techniques merit further study and development. Furthermore it appears that when the cinnabar growth methods have been developed to the extent that large single crystals are available in sufficient supply, that α-HgS, because of its unique properties, will be in great demand as a device material.

7.4 Characterization of GaAs Samples by Infrared Spectroscopy

7.4.1 Introduction

The need to achieve a more complete characterization and identification of defects in compound semiconductors is an important and urgent response to the demands for improved solid-state microwave and optoelectronic, III-V semiconductor devices. It has now become widely accepted that the goals of long-term stability, low cost, and reliable predictions of performance of these devices can be met only with a thorough materials characterization program, which will not only provide feedback of the usual characterization information to the materials growth technology, but will also investigate and utilize new procedures for materials characterization and combine these with the established methods. Infrared spectroscopy, utilizing observations of photoconductivity,

reflection, luminescence, and transmission, are valuable measurement techniques that can be used in order to provide new material characterization data which can be recognized and evaluated as having to do with the materials' intrinsic properties and can be separated from those parameter changes which are introduced by the effects of device processing. Infrared spectroscopy cannot only detect the presence of electrically inactive impurities such as oxygen or carbon, but with proper resolution (accomplished by cryogenic techniques), it can also distinguish between the kinds of impurites present.

7.4.2 Infrared Photoconductivity of GaAs:O

The results of a series of characterization experiments on a GaAs:O sample demonstrated, as erroneous, a set of unusual conclusions drawn by H. L. Stocker in his publication[158] entitled, "Probable Observation of Unusual Local Vibrational Modes in the Oscillatory Photoconductivity of Semi-insulating GaAs." Our work was concerned chiefly with the characterization of sample 76-3, a GaAs:O sample which was reported to be an oxygen-doped substrate material.

The results of photoconductivity observations at 300°K under a 300 V D.C. bias indicated a gradual increase in photoconductivity response beginning at approximately 0.7 eV and extending to a maximum of about 3nA at the silicon-filter cut off near 1.0 eV. Difficulties experienced at nitrogen temperatures with crystal breakdown-voltage oscillations were eliminated when the bias voltage was decreased to 50 V D.C. At 300°K with the new 50 V bias (and without the silicon filter), the bandgap energy was observed to be represented by 2 peaks separated by 33 meV, and occurring at 1.42 and 1.39 eV.

Some sharp structure in the photoconductive response near the bandgap was traced to gas pressure and eliminated by vacuum improvements. Since silicon impurity has been observed in the analysis of GaAs samples and since silicon is known to occur as an acceptor with an energy of 0.03 eV, it is possible that one of these levels near the bandgap is related to the presence of silicon.

At temperatures near 30°K oscillations were observed on the high-energy side of the bandgap. The bandgap threshold is approximately 1.51 eV and the average value of the period of the oscillation was measured to be roughly 37.9 meV. The oscillations, of course, may be seen in second order near 0.75 eV and therefore they have led to the publication of erroneous information by Stocker, who concluded: (1) that they represent a period of 20.9 meV; (2) that they are associated with the 0.75 eV oxygen impurity level in GaAs, and (3) that they involve multiple emission of a local vibrational mode associated with the 0.75 eV defect. Stocker's data have been reproduced by our data (calculated is second order). Since Stocker did not realize that he was looking at a second-order spectrum his calculations are in error and his three conclusions are unfortunately wrong. This observation not only helps to clear up certain implications and questions generated by erroneous conclusions, but it also sheds light on the characterization effort, as far as GaAs:O is concerned. It can be shown, using the positions of the minima, that the observed oscillation of intrinsic photoconductivity is caused by a strong coupling of the longitudinal optical (LO) phonon with the photoexcited electrons to produce oscillations on the high-energy side of the bandgap, E_g. Since there is a direct relationship between the intensity of the intrinsic oscillations and the quality of the substrate material the oscillations could be used to monitor crystal quality and hence aid in the characterization of the material. Parameters which could be evaluated are m_e/m_h, ε, or even a more precise value of the LO.

I-R photoconductivity measurements were also made on a Sumitomo semi-insulating GaAs substrate furnished by R.C.A. Photoconductive response data, taken with a silicon filter, revealed a broad band at 300°K with a long wavelength tail stretching to energies less than 0.65 eV. The broad band persisted

at nitrogen temperatures and, unlike other GaAs samples measured previously, the band remained even at temperatures below 30°K. However, at these cryogenic temperatures there was some improvement in resolution, suggesting a central valley and hinting at the possibility that the band was predominantly due to two chief levels, with transition energies of 0.80 and 0.89 eV. It may be concluded from these and other measurements that: 1) the sample contains chromium in substantial amounts; 2) other physical or chemical impurities must also exist; and 3) that the quality of this crystal is relatively poor. In order to become more familiar with the characteristics of the oxygen level it would be beneficial to investigate GaAs material containing only oxygen as a significant dopant.

7.4.3 I-R Photoconductivity of GaAs:Cr

Near-infrared photoconductivity spectra have been taken on a number of GaAs:Cr samples at various temperatures and it has been observed that there are significant differences between groups of crystals from different manufacturers as well as important differences between the results of individual samples within each group. The results on one group of samples are summarized in Table 7-2 which lists the maximum photoconductivity and the threshold energy observed for these materials at temperatures ranging between 300°K and 25°K. In Table 7-2 the samples are grouped according to their photoconductive response at various experimental temperatures. The four Cr-doped substrates gave similar data in that each sample displayed an infrared photoconductive spectrum, the intensity of which decreased with a decrease of sample temperature. In addition, on cooling to approximately nitrogen temperature, each spectrum resolved itself into a single peak due to the chromium impurity. At approximately helium temperature the single peak had decreased slightly in intensity and had shifted slightly to a higher energy.

Table 7-2. Photoconductivity results in several GaAs:Cr samples[+]

	Sample	Threshold	Peak Current	Temp.	Threshold	Peak Current	Temp.	Threshold	Peak Current	Temp.
++	47-B	0.74 eV	0.73 nA	300°K	0.82 eV	771 nA	105°K	----	1023 nA	32°K
								0.82 eV	950 nA	30°K
	9-B	0.74 eV	0.84 nA	300°K	0.82 eV	0.55 nA	108°K	0.84 eV	0.50 nA	32°K
‡	54-B	0.73 eV	0.83 nA	300°K	0.81 eV	----	105°K	0.83 eV	----	32°K
					----	0.28 nA	101°K	----	0.15 nA	35°K
	4-B	0.76 eV	0.80 nA	300°K	0.81 eV	----	97°K	0.83 eV	0.04 nA	27°K
					----	0.10 nA	106°K			
	49-B	0.72 eV	0.12 nA	300°K	*	0.02 nA	115°K	0.81 eV	0.02 nA	30°K
								0.77 eV		

+ For a 1.75 mm slit and a 300 V D.C. Bias

* About the same as above but too weak to measure accurately.

The resolution at about 0.9 eV is calculated to be ~ ± 0.01 eV for a 1.75 mm slit and spectra of good intensity.

++ Normalized to 1.75 mm slit and a 300 V Bias from a 1/2 mm slit and a 50 V D.C. Bias.

‡ This crystal was received in a broken and over-etched condition.

Differences between the results of the four Cr-doped substrate samples were chiefly in the intensity of the observed photoconductive response. Sample 9B and broken Sample 54B yielded the greatest intensity at all temperatures but particularly so at cryogenic temperatues where the ratios of the photoconductive maxima of Samples 9B and 54B to those of Samples 4B and 49B, respectively, grew from more than 5 at temperatures near 100°K to greater than 10 at temperatures close to 30°K. Comparing 9B with 54B one might conclude from their cryogenic spectra that they have approximately the same amount of chromium and that it is the only impurity. Perhaps 9B has slightly more Cr but the fact that Sample 54B was broken and overetched may invalidate this conclusion.

Although Sample 49B exhibited the least photoconductive response, a chromium peak or band was easily seen at cryogenic temperatures. If one uses the intensity of the chromium peak as an indication, it appears that there is significantly more chromium in Samples 9B and 54B than in Sample 4B and 49B.

Sample 47B gave interesting and quite different results. It was known to be an LPE buffer on a semi-insulating substrate. On cooling to 105°K the intensity of the photoconductive response increased over three orders of magnitude as the broad 300°K band resolved itself into a narrow band due to chromium. A further increase in intensity was noted when the sample was cooled to approximately 30°K.

Furthermore the intensity of the maximum of the photocurrent response at cryogenic temperatures was so large that the spectrometer slits had to be closed to 1/2 mm. Even then, at temperatures near 30°K and with a 300 volt D.C. bias, corresponding to a maximum photoconductivity of approximately 6 μA, current oscillations and breakdown effects were observed. To avoid these effects the bias voltage was reduced to 50 volts. The results for Sample 47B

were normalized to a 300 volt bias and a 1.75 mm slit width in Table 7-2.

The photoconductive results of this group of samples differ in some respects from the results of other groups of samples. For example, in a group of Laser Diode Samples SI-3-10, 3-1, 6-10, and 6-1 two peaks were observed near nitrogen temperature, whereas in the present samples only one peak or band is observed over the entire low-temperature range.

In particular there was no evidence in the group of samples of Table 7-2 for an oxygen peak in the photoconductivity. The threshold for the photoconductivity peak in Sample 9B, for example, was measured at 35 and 32^{o}K as 0.83 eV, in excellent agreement with the value obtained for the chromium threshold at approximately the same temperature in the Laser Diode Samples SI-3-10 and SI-6-10.

REFERENCES

1. L. Katz and A. S. Penfold, Rev. Mod. Phys. 24, 28 (1952).
2. A. T. Nelms, Energy Loss and Range of Electrons and Positrons, N.B.S. Circular 577, July 26, 1956.
3. B. A. Kulp and R. H. Kelley, J. Appl. Phys. 31, 1057 (1960).
4. F. J. Bryant and A. F. J. Cox, Proc. Roy. Soc. A310, 319 (1969).
5. C. N. Elsby and J. M. Meese, J. Appl. Phys. 43, 4818 (1972).
6. C. N. Elsby and J. M. Meese, I.E.E.E. Trans. Nuc. Sci. NS-21, 14 (1974).
7. B. A. Kulp, Phys. Rev. 125, 1965 (1962).
8. W. M. Carra, J. E. Ehret and J. M. Meese, Rev. Sci. Instrum. 44, 835 (1973).
9. W. M. Carra, J. E. Ehret, D. R. Locker and J. M. Meese, Rev. Sci. Instrum. 44, 1407 (1973).
10. W. E. Vehse, W. A. Sibley, F. J. Keller, and Y. Chen, Phys. Rev. 167, 828 (1968).
11. J. M. Smith and W. E. Vehse, Phys. Lett. 31A, 147 (1970).
12. F. J. Bryant and A. F. J. Cox, Proc. R. Soc. A310, 319 (1969).
13. J. M. Meese, Appl. Phys. Lett. 19, 86 (1971).
14. F. J. Bryant and A. F. J. Cox, J. Phys. C 1, 1734 (1968).
15. W. R. Woody, R. A. House II, J. M. Meese, Bull. Am. Phys. Soc. 16, 859 (1971).
16. M. Aven and B. Segall, Phys. Rev. 130, 81 (1963).
17. R. E. Nahory and H. Y. Fan, Phys. Rev. 156, 825 (1967).
18. J. M. Meese and Y. S. Park, in The Int. Conf. on Defects in Semiconductors, (Inst. of Physics, Reading, 1973) p. 51.

19. W. R. Woody and J. M. Meese, Bull. Am. Phys. Soc. 20, 811 (1975).

20. W. R. Woody and J. M. Meese, Bull. Am. Phys. Soc. 20, 319 (1975).

21. W. R. Woody and J. M. Meese, (To be presented at the 1976 Ion Implantation Conference, Boulder, Colo.).

22. I. Broser and K. H. Frank, J. Phys. Chem. Solids 26, 1013 (1965).

23. G. D. Watkins, in Radiation Effects in Semiconductors, ed. by J. W. Corbett and G. D. Watkins, (Gordon and Breach, London, 1971) p. 301.

24. C. Kikuchi, Rad. Effects 8, 249 (1971).

25. C. N. Elsby and J. M. Meese, I.E.E.E. Trans. Nuc. Sci. NS-21, 14 (1974).

26. F. L. Vook, Phys. Rev. B 3, 2022 (1971).

27. M. Kitagawa and T. Yoshida, App. Phys. Lett. 18, 41 (1971).

28. A. L. Taylor, G. Filipovich and G. K. Lindeberg, Solid State Commun. 9, 945 (1971).

29. K. Morigaki and T. Hoshina, J. Phys. Soc. Japan 24, 120 (1968).

30. K. Morigaki, S. Toyotomi and Y. Toyatomi, J. Phys. Soc. Japan 31, 511 (1971).

31. D. C. Look and J. M. Meese, Rad. Effects 22, 229 (1974).

32. D. C. Look, J. Appl. Phys. 45, 492 (1974).

33. D. R. Locker and J. M. Meese, I.E.E.E. Trans. Nuc. Sci. NS-19, 257 (1972).

34. Y. Chen, D. L. Trueblood, O. E. Schow and H. T. Tohver, J. Phys. C. 3, 2501 (1970).

35. W. E. Vehse, W. A. Sibley, F. J. Keller and Y. Chen, Phys. Rev. 167, 828 (1968).

36. B. R. Appleton and L. C. Feldman, J. Phys. Chem. Solids 33, 507 (1972).

37. J. M. Smith and W. E. Vehse, Phys. Lett. 31A, 147 (1970).

38. D. R. Locker and J. M. Meese, Bull. Am. Phys. Soc. 20, 319 (1975).

39. J. Schneider and A. Räuber, Sol. State Commun. 5, 779 (1967).

40. F. J. Bryant and P. S. Manning, Sol. State Commun. 10, 501 (1972).

41. L. P. Gal'chenetskii, V. M. Koshkin, et al., Sov. Phys.-Solid State 14, 554 (1972).

42. V. M. Koshkin, L. P. Gal'chinetskii, et al., Solid State Commun. 13, 1 (1973).

43. H. Swenson, D. R. Locker, J. M. Meese, J. C. Manthuruthil, I.E.E.E. Trans. Nuc. Sci. NS-21, 40 (1974).

44. J. M. Meese, Phys. Rev. B 9, 4373 (1974).

45. J. M. Meese, Bull. Am. Phys. Soc. 20, 317 (1975).

46. J. M. Meese and J. W. MacKay, in International Conf. on Radiation Effects in Semiconductors, (Gordon and Breach, London, 1971), p. 51.

47. L. Sivo, Ph.D. Thesis, Purdue University (1967).

48. L. C. Kimerling and D. V. Lang, Bull. Am. Phys. Soc. 20, 317 (1975).

49. J. M. Meese, J. C. Manthuruthil and D. R. Locker, Bull. Am. Phys. Soc. 20, 696 (1975).

50. J. J. Wysocki and P. Rappaport, J. Appl. Phys. 31, 571 (1960).

51. L. W. James and R. L. Moon, Appl. Phys. Lett. 26, 467 (1975).

52. C. E. Barnes, Phys. Rev. B 1, 4735 (1970).

53. R. H. Hum and A. L. Berry, I.E.E.E. Trans. Nuc. Sci., Dec., 1975.

54. J. T. Routti, UCLRL Report No. 19452 (U of Calif Lawrence Radiation Lab., Berkeley, Calif., 1969).

55. F. D. Adams, D. C. Look, L. C. Brown, and D. R. Locker, Phys. Rev. B 4, 2115 (1971).

56. D. C. Look and D. L. Moore, Phys. Rev. B 5, 3406 (1972).

57. D. C. Look and D. R. Locker, Phys. Rev. B 6, 713 (1972).

58. B. Tell, J. L. Shay and H. M. Kasper, J. Appl. Phys. 43, 2469 (1972).

59. For a general review of I-III-VI compounds, see L. I. Berger and V. D. Prochukhan, Ternary Diamond-Like Semiconductors (Consultants Bureau, New York, 1969).

60. P. M. Bridenbaugh and P. Migliorato, App. Phys. Lett. 26, 459 (1975).

61. E. H. Putley, The Hall Effect and Semiconductor Physics, (Butterworth, London, 1960).

62. J. D. Wiley and M. DiDomenico Jr., Phys. Rev. B 2, 427 (1970).

63. D. Redfield and R. S. Crandall, in Proc. 10th Int. Conf. on Phys. of Semicond. (U.S. Atomic Energy Comm., Oak Ridge, Tenn. 1970) p. 574.

64. D. C. Look and J. C. Manthuruthil, J. Phys. Chem. Solids 37, 173 (1976).

65. J. Barrera, in Proc. of the 5th Cornell Conf. on Active Semiconductor Devices (to be published).

66. Ref. 61, Ch. 2.

67. Ref. 61, p. 124.

68. Ref. 61, p. 88.

69. D. C. Look, J. Phys. Chem. Solids 36, 1311 (1975).

70. E. Conwell and V. F. Weisskopf, Phys. Rev. 77, 388 (1950).

71. T. C. McGill and R. Baron, Phys. Rev. B 11, 5208 (1975).

72. See, for example, F. Adduci, et al., J. Appl. Phys. 45, 5000 (1974). We have revised their Eq. 6 somewhat.

73. R. N. Zitter, Phys. Rev. 112, 852 (1958).

74. J. H. Crawford, Jr., in Radiation Effects in Semiconductors, ed. by F. L. Vook, (Plenum Press, New York, 1967) p. 477. See also G. D. Watkins, ibid., p. 77.

75. M. M. Kreitman, Rev. Sci. Instrum. 35, 749 (1964).

76. M. M. Kreitman and D. Cooper, J. Vac. Sci. and Tech. 3, 221 (1966).

77. M. M. Kreitman, F. J. Milford, and J. G. Daunt, in Proc. of the 9th International Conference on Low Temperature Physics (Plenum Press, New York, 1965) p. 909.

78. M. M. Kreitman and J. G. Daunt, Bull. Am. Phys. Soc. 9, 255 (1964).

79. M. M. Kreitman, F. J. Milford, R. P. Kenan, and J. G. Daunt, Phys. Rev. 144, 367 (1966).

80. M. M. Kreitman, Bull. Am. Phys. Soc. 10, 586 (1965).

81. M. M. Kreitman, in Proc. of the 9th International Conference on Low Temperature Physics (Plenum Press, New York, 1965) p. 914.

82. M. M. Kreitman and J. J. Kosiewiez, Bull. Amer. Phys. Soc. 13, 958 (1968).

83. M. M. Kreitman, J. J. Kosiewicz, and R. Schultz, Bull. Amer. Phys. Soc. 14, 559 (1969).

84. M. M. Kreitman, J. Thieman, I. Gessel and J. Callahan, Bull. Amer. Phys. Soc. 15, 127 (1970).

85. G. J. Svenconis and M. M. Kreitman, Bull. Amer. Phys. Soc. 15, 847 (1970).

86. M. M. Kreitman, B. Yates, Bull. Amer. Phys. Soc. 15, 811 (1970).

87. J. J. Kosiewicz, M. S. Thesis, University of Dayton, 1968.

88. J. T. Callahan and M. M. Kreitman, Bull. Amer. Phys. Soc. 16, 857 (1971).

89. R. Roedersheimer, M. S. Thesis, University of Dayton, 1967.

90. M. M. Kreitman, J. J. Kosiewicz, and R. J. Roedersheimer, Bull. Amer. Phys. Soc. 13, 1453 (1968).

91. A. C. Anderson, R. B. Rauch, and M. M. Kreitman, Rev. Sci. Instrum. 41, 469 (1970).

92. M. M. Kreitman, Rev. Sci. Instrum. 40, 1562 (1969).

93. M. M. Kreitman and E. U. Oldham, Bull. Amer. Phys. Soc. 14, 799 (1969).

94. M. M. Kreitman, in 9th Conference on Thermal Conductivity (USAEC Conf, 691002, 1970) p. 712.

95. M. M. Kreitman and J. T. Callahan, Cryogenics 10, 155 (1970).

96. J. T. Callahan, M. Blasius and M. M. Kreitman, Bull. Amer. Phys. Soc. 15, 126 (1970).

97. M. M. Kreitman, in Advances in Cryogenic Engineering, Vol 16, ed. by K. D. Timmerhaus (Plenum Press, New York, 1971) p. 51. M. M. Kreitman T. Ashworth and M. Rechowicz, Cryogenics 12, 32 (1972).

98. M. M. Kreitman and D. Wilkening, Rev. Sci. Instrum. 40, 1411 (1969).

99. M. M. Kreitman, Rev. Sci. Instrum. 40, 1249 (1969).

100. M. M. Kreitman, in Advances in Cryogenic Engineering, Vol. 16, ed. by K. D. Timmerhaus (Plenum Press, New York, 1971) p. 282.

101. M. M. Kreitman, Bull. Amer. Phys. Soc. 17, 290 (1972).

102. J. H. Koening, Rutgers Univ., N.J., Ceramic Res. Sta., Progress Rept. No. 3, AD 19833 (Defense Documentation Center, Wash. D.C., 1953).

103. G. A. Slack, General Electric Report No. 66-C-481, December, 1966.

104. J. J. Martin and M. W. Wolf, personal communication. See also, Bull. Amer. Phys. Soc. 17, 282 (1972).

105. A. Eucken and G. Kuhn, Z. Physik. Chem. 134, 193 (1928).

106. A. V. Ioffe and A. F. Ioffe, Sov. Phys. Sol. State 2, 719 (1960).

107. L. S. Ladd, AD 42148, (Defense Documentation Center, Wash. D.C., 1963).

108. F. Kelemen, E. Cruveano and D. Niculescv, Phys. Stat. Sol. 11, 865 (1965).

109. Gould Laboratories, 540 E. 105th St., Cleveland, Ohio 44108.

110. Texas Instruments, Inc., Corporate Research Labs, P.O. Box 5636, Dallas, Texas 75222.

111. Coors Porcelain Co., Golden, Colorado 80401.

112. Hughes Research Laboratories, 3011 Malibu Road, Malibu, California, 90265.

113. Tyco Laboratories, Corporate Research Center, 16 Hickory Dr., Waltham, Mass. 02154.

114. Raytheon Research Division, 28 Seyon St., Waltham, Mass. 02154.

115. M. G. Golland, Phys. Rev. A 134, 471 (1964).

116. F. L. Vook, App. Phys. Letters 13, 25 (1968).

117. G. A. Slack and S. Galginaitis, Phys. Rev. A 133, 253 (1964).

118. R. Horch and H. Nieki, Ann. Physik 16, 289 (1965).

119. M. M. Kreitman, Bull. Am. Phys. Soc. 17, 814 (1972).

120. M. M. Kreitman, W. R. Woody and Y. S. Park, in Proc. of the 12th International Conference on Thermal Conductivity (Birmingham, Alabama, September, 1972).

121. Y. Shiraki, T. Shimada, and K. F. Komatsubara, J. Appl. Phys. 43, 711 (1972); W. W. Anderson and J. T. Mitchell, Appl. Phys. Letters 12, 334 (1968); Y. S. Park and C. H. Chung, Appl. Phys. Letters 18, 99 (1971).

122. R. W. Powell, Progress in Non-Destructuve Testing 1, 199 (1958).

123. R. W. Powell, Mem. Sci. de la Revue de Metallurgie 56, 181 (1959).

124. R. W. Powell, Techniques of Non-Destructive Testing (Butterworth, London, 1960) p. 175.

125. R. W. Powell, in Proc. Symposium on Physics and Non-Destructive Testing (Gordon and Breach, London, 1967) p. 455.

126. M. M. Kreitman, Y. S. Park, and W. R. Woody, Bull. Am. Phys. Soc. 18, 890 (1973).

127. M. M. Kreitman, in Proc. of the 6th Symposium on Thermophysical Properties, ed. by P. E. Liley (ASME, New York, 1973) p. 286.

128. T. Ashworth, L. R. Johnson, C. Y. Hsuing, and M. M. Kreitman, Cryogenics 13, 34 (1973).

129. T. Ashworth, J. E. Loomer, and M. M. Kreitman, in Advances in Cryogenic Engineering Vol. 18, ed. by K. D. Timmerhaus (Plenum Press, New York, 1973) p. 271.

130. E. T. Mahefkey, M. M. Kreitman, J. Electrochem. Soc. 118, 1382 (1971).

131. M. M. Kreitman, J. Chem. Eng. Data 21, 11 (1976).

132. B. Yates, R. F. Cooper, and M. M. Kreitman, Phys. Rev. B 4, 1314 (1971).

133. M. M. Kreitman and J. T. Callahan, in Dynamical Aspects of Critical Phenomena, ed. by J. I. Budnick and M. P. Kawatra, (Gordon and Breach, New York, 1972) p. 359.

134. J. S. Smart, in Magnetism, Vol. 3, ed. by G. T. Rado and H. Suhl, (Academic Press, New York, 1963).

135. M. M. Kreitman and A. O'Hare, Bull. Amer. Phys. Soc. 11, 728 (1966).
M. M. Kreitman and D. L. Barnett, J. Chem. Phys. 43, 364 (1965).
M. M. Kreitman and F. Hamaker, J. Chem. Phys. 45, 2396 (1966).

136. D. Gerlich, J. Phys. Chem. Solids 28, 2575 (1967); D. Gerlich, Personal Communications.

137. N. S. Goel and R. P. Singh, Ind. J. Pure and Appl. Phys. 1, 343 (1963).

138. M. A. Nusimovici and J. L. Birman, in II-VI Semiconducting Compounds, ed. by D. J. Thomas, (W. A. Benjamin, New York, 1967) p. 1204;
M A. Nusimovici, Ph.D. Thesis, University of Paris, 1968;
M A. Nusimovici, M. Balkanski, and J. L. Birman, Phys. Rev. B 1, 595 (1970).

139. M. M. Kreitman, G. J. Svenconis, J. J. Kosiewicz and J. T. Callahan, in Low Temperature Physics, Lt 13, Vol. 4, ed. by K. D. Timmerhaus, W. J. O'Sullivan, and E. F. Hammel, (Plenum Press, New York, 1974) p. 449.

140. M. M. Kreitman, Bull. Amer. Phys. Soc. 14, 294 (1967); M. M. Kreitman H. J. Richter, and R. N. Euwema, Bull. Amer. Phys. Soc. 11, 446 (1966); H. J. Richter and M. M. Kreitman, Bull. Amer. Phys. Soc. 10, 475 (1965).

141. J. Sapriel, Appl. Phys. Letters 19, 533 (1971).

142. J. Sapriel, L. Rivoallan, and J. L. Ribet, J. de Physique 33, 96 (1972).

143. J. Sapriel and R. Lacon, Proc. IEEE 61, 678 (1973).

144. Y. Toudic and R. Aumont, J. Crystal Growth 10, 170 (1971).

145. R. Zallen, in II-VI Semiconducting Compounds, ed. by D. G. Thomas, (Benjamin, New York, 1967) p. 877.

146. G. G. Roberts and R. Zallen, J. Phys. C (Sol. State Phys.) 4, 1890 (1971).

147. W. L. Bond, G. D. Boyd and H. L. Carter, Jr., J. Appl. Phys. 38, 4090 (1967).

148. M. Abkowitz, G. Pfister, and R. Zallen, J. Appl. Phys. 43, 2442 (1972).

149. G. G. Roberts, E. L. Lind, and E. A. Davis, J. Phys. Chem. Solids 30, 833 (1969).

150. C. Verolini, and H. Diamond, J. Appl. Phys. 36, 1791 (1965).

151. M. Tabak and G. G. Roberts, J. Appl. Phys. 39, 4873 (1968).

152. M. D. Martin and E. L. Thomas, IEEE J. Quant. Electron QE-2, 196 (1966).

153. E. H. Turner, IEEE J. Quant. Electron QE-3, 695 (1967).

154. M. M. Kreitman, S. P. Faile, C. W. Litton, and D. C. Reynolds, in Optical Properties of Highly Transparent Solids, ed. by S. S. Mitra and B. Bendow (Plenum Press, New York, 1975) p. 179.

155. M. M. Kreitman, S. P. Faile, R. S. Harmer, and D. G. Wilson, Bull. Am. Phys. Soc. 20, 221 (1975).

156. Y. O. Dovgii and B. F. Bilenkii, Sov. Phys.-Sol. State 8, 1280 (1966).

157. J. Barcelo, M. Galtier, and A. Montaner, Comp. Rend. (Paris), 274-B, 1410 (1972); R. Zallen, G. Lucovsky, W. Taylor, A. Pinczuk, and E. Burstein, Phys. Rev. B 1, 4058 (1970); H. D. Riccus and K. J. Siemsen, J. Chem. Phys. 52, 4090 (1970); H. Poulet and J. P. Mathieu, Comp. Rend. (Paris), 270-B, 708 (1970).

158. H. J. Stocker, Solid State Comm. 16, 525 (1975).

PUBLICATIONS

1. J. M. Meese and D. R. Locker, "Oxygen Displacement Energy in ZnO," Solid State Commun. 11, 1547 (1972).
2. D. R. Locker and J. M. Meese, "Displacement Thresholds in ZnO," IEEE Trans. on Nuc. Sci. NS-19, 237 (1972).
3. C. N. Elsby and J. M. Meese, "Cd Displacement Threshold in CdS at Liquid Helium Temperatures," J. Appl. Phys. 43, 4818 (1972).
4. D. C. Look and D. L. Moore, "NMR Measurement of the Conduction-Electron g-Factor in CdTe," Phys. Rev. B 5, 3406 (1972).
5. D. C. Look, "NMR Chemical Shifts in CdS, CdSe, and CdTe," Phys. Stat. Sol. (b) 50, K97 (1972).
6. D. C. Look and D. R. Locker, "NMR Study of Co^{2+} in CdS," Phys. Rev. B 6, 713 (1972).
7. M. M. Kreitman, T. Ashworth, and M. Rechowicz, "A Correlation Between Thermal Conductance and Specific Heat Anomalies and the Glass Temperature of Apiezon N and T Greases," Cryogenics 12, 32 (1972).
8. M. M. Kreitman and J. T. Callahan, "Low Temperature Specific Heat Anomalies Arising from Simultaneous Effects of Exchange and Magnetic Fields," in Dynamical Aspects of Critical Phenomena, ed. by J. I. Budnick and M. P. Kawatra (Gordon and Breach, New York, 1972) p. 359.
9. W. M. Carra, J. E. Ehret, D. R. Locker, and J. M. Meese, "Beam Scanner for a 1 MeV Van de Graaff," Rev. Sci. Instr. 44, 1407 (1973).
10. W. M. Carra, J. E. Ehret, and J. M. Meese, "Low Cost Beam Current Integrator," Rev. Sci. Instr. 44, 835 (1973).

11. J. M. Meese and Y. S. Park, "The Zn Displacement Threshold and Zn Vacancy Luminescence in Electron Irradiated ZnTe," in Intern. Conf. on Defects in Semiconductors, (Institute of Physics, Reading, 1973) p. 51.

12. M. M. Kreitman, "Thermal Comparator Measurements on II-VI Compound Semiconductors," in Proc. of the 6th Symposium on Thermophysical Properties, ed. by P. E. Liley (ASME, New York, 1973) p. 286.

13. T. Ashworth, J. E. Loomer and M. M. Kreitman, "Thermal Conductivity of Nylon and Apiezon Grease," Advances in Cryogenic Engineering 18, 271 (1973).

14. T. Ashworth, L. R. Johnson, C. Y. Hsiung, and M. M. Kreitman, "Use of the Linear Heat Flow for Poor Conductors and its Application to the Thermal Conductivity of Nylon" Cryogenics 13, 34 (1973).

15. C. N. Elsby and J. M. Meese, "Luminescence in Electron-Irradiated CdS," IEEE Trans. Nuc. Sci. NS-21, 14 (1974).

16. H. Swenson, D. R. Locker, J. M. Meese, and J. C. Manthuruthil, "Electron Damage in In_2Te_3-A Defect Tetrahedral Semiconductor," IEEE Trans. Nuc. Sci. NS-21, 40 (1974).

17. J. M. Meese, "Low-Temperature Recovery of Irradiation Defects in n-type Ge," Phys. Rev. B 9, 4373 (1974).

18. D. C. Look, "High-Temperature Annealing in Electron-Irradiated CdS," J. Appl. Phys. 45, 492 (1974).

19. B. K. Shin, Y. S. Park, and D. C. Look, "Electrical Characteristics of Al-Implanted ZnSe," Appl. Phys. Lett. 24, 435 (1974).

20. D. C. Look and J. M. Meese, "Room Temperature Electron Damage in CdS," Radiation Effects 22, 229 (1974).

21. Y. S. Park, B. K. Shin, D. C. Look, and D. L. Downing, "Properties of Al and P Ion-Implanted Layers in ZnSe," in Proc. of the 4th International Conf. on Ion Implantation, Japan, 1974 (in press).

22. M. M. Kreitman, G. J. Svenconis, J. J. Kosiewicz, and J. T. Callahan, "Specific Heat and Debye θ of CdS:0.45% Mn," in Low Temperature Physics - LT 13 Vol. 4, ed. by K. D. Timmerhaus, W. J. O'Sullivan and E. F. Hammel (Plenum Press, New York, 1974) p. 449.

23. B. K. Shin, D. C. Look, and Y. S. Park, "Ohmic Contacts on Al-Implanted ZnSe," J. Electrochemical Soc. 122, 450 (1975).

24. D. C. Look, "Mixed Conduction in GaAs:Cr," J. Phys. Chem. Solids, 36, 1311 (1975).

25. M. M. Kreitman, S. P. Faile, C. W. Litton, and D. C. Reynolds, "Optical Transmission in Iodine Transported α-HgS" in Optical Properties of Highly Transparent Solids, ed. by S. S. Mitra and B. Bendow (Plenum Press, New York, 1975) p. 179.

26. D. C. Look and J. C. Manthuruthil, "Electron and Hole Conductivity in $CuInS_2$," J. Phys. Chem. Solids 37, 173 (1976).

27. M. M. Kreitman, "Thermal Comparator Measurements on Dimethyl Sulfite," J. Chem. Eng. Data 21, 11 (1976).

28. W. R. Woody and J. M. Meese, "Photoluminescence in ZnTe," (accepted in J. Appl. Phys.).

29. J. J. Santiago, S. A. Scyzak, and J. M. Meese, "Effects of Stellar Irradiation on Interstellar Grains," (accepted in J. of Astrophys.).

30. B. K. Shin, D. C. Look, Y. S. Park, and J. E. Ehret, "Hall-Effect Measurements in Cd-Implanted GaAs," (accepted in J. Appl. Phys.).

☆ U. S. GOVERNMENT PRINTING OFFICE: 1976 — 757-001/22